

# On-line Temperature Monitoring of Permanent Magnet Synchronous Machines



**Shuai Xiao, *BEng., MSc***

A thesis submitted for the degree of Doctor of Philosophy  
Department of Electronic and Electrical Engineering  
The University of Sheffield, 3 Solly Street  
Sheffield, S1 4DE  
United Kingdom

April 2019

# ABSTRACT

The use of electric machines can be found in many applications such as household appliance, machine tools, vehicles and railways, due to their indispensable role in converting energy. Most recently, permanent magnet synchronous machines have been increasingly employed in electrical/hybrid electrical vehicles, industrial servo drives and wind power generators for their high power density and good efficiency. There is a growing trend towards the inclusion of thermal management in permanent magnet synchronous motors by monitoring their internal temperatures during real-time operation, because high temperatures can significantly shorten the lifetime of the motor components. Whilst temperature sensors are suitable for measuring stator temperatures, fixing them on rotating permanent magnets is difficult in practice. As a result, model-based temperature estimation methods are preferable.

A practical and computationally efficient system for the estimation of the critical temperatures in permanent magnet synchronous machines is introduced, based on a low-order lumped parameter thermal network which represents stator iron, stator winding and permanent magnet. The parameterization of the network requires an accurate rotor temperature measurement, which is provided by a PWM-based estimation algorithm predicting rotor temperature via permanent magnet flux linkage.

The proposed temperature estimation system is validated in simulation, including offline simulation in Matlab/Simulink, and online simulation utilizing the Hardware-in-the-Loop technique, which performs the emulation of motor and control in two real-time platforms. Comprehensive experimental validation is also conducted on a three-phase surface-mounted permanent magnet servo motor, with motor temperature estimation error less than 6°C.

The main contributions of the research work include: a) A three-node thermal network for motor temperature estimation, which is simple to implement — detailed knowledge of motor dimensions, material properties is not needed, as the thermal parameters are derived from a measurement-based recursive parameter identification procedure, based on the recursive Kalman Filter, b) A simplified and accurate PWM-based rotor temperature estimation method without using signal injection, which is a commonly-employed approach for temperature estimation and disturbs motor operation. It is also insensitive to practical implementation errors, such as inverter nonlinearity, c) The integration of the rotor temperature estimation method and the thermal network. As a result direct rotor temperature measurement which can be expensive and troublesome is avoided.

# ACKNOWLEDGEMENTS

I would like to show my sincere appreciation to my project supervisors, Dr. Antonio Griffo and Prof. Jiabin Wang of the Department of Electronic and Electrical Engineering, the University of Sheffield, for their continuous encouragement and guidance in the course of my study. I would not have been able to complete this project without their support.

My thanks also to the colleagues of the Electrical Machines and Drives Research Group, for helping me solve the technical difficulties I encountered throughout the years, and providing a lively and friendly working atmosphere.

I also would like to express my gratitude towards my family, particularly my parents, for their unconditional financial and moral support, without which this journey would not have been possible.

# Table of contents

<b>ABSTRACT</b> .....	<b>1</b>
<b>ACKNOWLEDGEMENTS</b> .....	<b>2</b>
<b>LIST OF FIGURES</b> .....	<b>6</b>
<b>NOMENCLATURE</b> .....	<b>13</b>
<b>ABBREVIATIONS</b> .....	<b>20</b>
<b>CHAPTER 1: INTRODUCTION AND LITERATURE REVIEW</b> .....	<b>22</b>
1.1 INTRODUCTION .....	22
1.2 LITERATURE REVIEW .....	25
1.2.1 A Review of Temperature Measurement Techniques .....	25
1.2.2 Temperature Estimation Methods Based on Electrical Parameters .....	31
1.2.2.1 Stator Temperature.....	31
1.2.2.2 Rotor Temperature .....	31
1.2.3 Temperature Estimation Methods Based on Thermal Modelling.....	44
1.2.3.1 Loss Prediction.....	45
1.2.3.2 High-Order Thermal Model .....	49
1.2.3.3 Low-order Thermal Model .....	54
1.3 CONCLUSION.....	60
<b>CHAPTER 2: TEMPERATURE ESTIMATION FOR PERMANENT MAGNET SYNCHRONOUS MOTORS BASED ON A LOW-ORDER THERMAL NETWORK</b> 61	
2.1 INTRODUCTION .....	61
2.2 FUNDAMENTAL THEORY .....	61
2.2.1 Model Structure .....	62
2.2.2 Loss Modelling .....	62
2.2.3 Thermal Capacitance and Resistance.....	63
2.2.4 State-space Representation .....	63
2.2.5 Model Discretization.....	65
2.2.6 Parameter Identification.....	66
2.3 OFFLINE VALIDATION.....	71
2.3.1 Validation at Single Speed and Current.....	72
2.3.2 Validation at Multiple Speeds and Currents .....	78

2.3.3	Loss Error Analysis.....	85
2.3.3.1	Copper Loss .....	85
2.3.3.2	Iron Loss .....	86
2.3.3.3	Magnet Loss.....	87
2.3.3.4	Loss Effect on Temperature Estimation .....	87
2.4	CONCLUSION.....	89
<b>CHAPTER 3: PWM-BASED FLUX LINKAGE AND ROTOR TEMPERATURE ESTIMATIONS FOR PERMANENT MAGNET SYNCHRONOUS MACHINES.....90</b>		
3.1	INTRODUCTION .....	90
3.2	FUNDAMENTAL THEORY.....	91
3.3	OFFLINE VALIDATION.....	95
3.4	REAL-TIME SIMULATION .....	99
3.4.1	Experimental Setup.....	99
3.4.2	Steady-state Test .....	102
3.4.3	Transient Test.....	104
3.5	PRACTICAL IMPLEMENTATION ERROR ANALYSIS .....	107
3.5.1	Sampling Time.....	108
3.5.2	Inverter Dead-time Effect .....	109
3.5.3	PM Flux Linkage Harmonics.....	110
3.5.4	Inductance Saturation.....	111
3.5.5	Non-zero d-axis Current .....	113
3.6	EXPERIMENTAL VALIDATION.....	115
3.6.1	Experimental Setup.....	115
3.6.2	Validation at Room Temperature.....	120
3.6.3	Validation at Constant Temperatures.....	123
3.6.4	Rotor Temperature Estimation.....	126
3.7	CONCLUSION.....	129
<b>CHAPTER 4: A PWM-BASED LOW-ORDER THERMAL NETWORK FOR CRITICAL TEMPERATURES ESTIMATIONS FOR PERMANENT MAGNET SYNCHRONOUS MOTORS.....130</b>		
4.1	INTRODUCTION .....	130
4.2	EXPERIMENTAL VALIDATION.....	130

4.2.1	Loss Modelling .....	130
4.2.2	Experimental Setup .....	132
4.2.3	Validation at Single Speed and Current .....	134
4.2.4	Validation at Multiple Speeds and Currents .....	139
4.3	CONCLUSION.....	143
<b>CHAPTER 5: CONCLUSION AND FUTURE WORK .....</b>		<b>144</b>
5.1	CONCLUSION.....	144
5.2	FUTURE WORK .....	145
<b>APPENDICES .....</b>		<b>147</b>
APPENDIX A: LIST OF PUBLICATIONS .....		147
APPENDIX B: PARAMETER IDENTIFICATION OF THREE-NODE THERMAL NETWORK .....		148
APPENDIX C: VOLTAGE CALCULATION OF THE PWM-BASED FLUX LINKAGE AND ROTOR TEMPERATURE ESTIMATIONS.....		152
<b>REFERENCE .....</b>		<b>156</b>

## List of figures

Fig. 1-1: (a) circular window on the tested motor (b) Thermal image through the window and (c) Schematic of the image (b) [18] .....	25
Fig. 1-2: Schematic of the temperature monitoring system [15] .....	27
Fig. 1-3: Rotor temperature monitoring system: a) mechanical assembly diagram and b) demonstration of the physical instruments [15].....	28
Fig. 1-4: Mechanical assembly of the presented measurement system [14].....	30
Fig. 1-5: Method implementation schematic [18].....	33
Fig. 1-6: Estimation progress block diagram [18] .....	33
Fig. 1-7: Voltage-injection scheme based on three-phase inverter switching pattern [25] ....	34
Fig. 1-8: Practical implementation of the presented method [26] .....	36
Fig. 1-9: Adaline NN algorithm structure [26] .....	37
Fig. 1-10: (a) stator resistance estimator subnet and (b) PM flux linkage estimator subnet [26] .....	39
Fig. 1-11: Estimation process flow chart [26] .....	39
Fig. 1-12: Schematic of the zero-voltage vector injection method [28] .....	40
Fig. 1-13: $q$ -axis current variation under the zero-voltage vector injection scheme [28].....	41
Fig. 1-14: Flux linkage observer structure [8] .....	42
Fig. 1-15: $dq$ -axis circuits considering the iron loss effect [54] .....	51
Fig. 1-16: Schematic of the proposed computationally efficient motor model [54].....	51
Fig. 1-17: Schematic of the proposed machine model taking into account the temperature effect [6].....	52
Fig. 1-18: Schematic of the electro-thermal system [6].....	53
Fig. 1-19: Structure of the proposed LPTN [6].....	53
Fig. 1-20: Structure of the four-node LPTN [60] .....	54
Fig. 1-21: Thermal model with two temperature nodes [56].....	58
Fig. 2-1: Schematic graph of the three-node LPTN.....	62

Fig. 2-2: Extended Kalman Filter algorithm block diagram.....	69
Fig. 2-3: Schematic of the PMSM used for offline validation.....	71
Fig. 2-4: Thermal resistances estimated by the EKF.....	73
Fig. 2-5: Node temperatures estimated by the EKF.....	73
Fig. 2-6: Temperature estimation errors in Fig. 2-5.....	73
Fig. 2-7: Three-node temperature estimations using the identified thermal resistances.....	74
Fig. 2-8: Temperature estimation errors for the open-loop test.....	74
Fig. 2-9: Node temperatures estimated by the Levenberg-Marquardt algorithm, the power losses, the cooling system and ambient temperatures.....	76
Fig. 2-10: Values of the cost function $S$ before the iteration stops.....	76
Fig. 2-11: Thermal resistances estimated by the Levenberg-Marquardt and extended Kalman filter algorithms.....	76
Fig. 2-12: Open-loop temperature estimations with the results in Fig. 2-11.....	77
Fig. 2-13: Temperature estimation errors in Fig. 2-12.....	77
Fig. 2-14: Thermal resistances estimated by the Levenberg-Marquardt algorithm with different initial conditions and the extended Kalman filter algorithm.....	78
Fig. 2-15: Estimated node temperatures with the results in Fig. 2-14.....	78
Fig. 2-16: Temperature estimation errors in Fig. 2-15.....	78
Fig. 2-17: Thermal resistances estimated at $\omega r = 1000rpm, 2000rpm, 3000rpm, 4000rpm, 5000rpm,$ and $6000rpm$ and maximum current.....	79
Fig. 2-18: Thermal resistance estimated at $I = 40A, 70A, 100A, 130A, 160A,$ and $189A$ and maximum speed.....	79
Fig. 2-19: $RFes - C$ estimated at various speeds and currents.....	80
Fig. 2-20: $RW - Fes$ estimated at various speeds and currents.....	80
Fig. 2-21: $RPM - Fes$ estimated at various speeds and currents.....	81
Fig. 2-22: $RPM - W$ estimated at various speeds and currents.....	81
Fig. 2-23: $RPM - A$ estimated at various speeds and currents.....	81

Fig. 2-24: Speed and current profiles of the transient test .....	82
Fig. 2-25: Thermal resistances in response to the driving cycle.....	82
Fig. 2-26: Temperature estimation results according to the driving cycle .....	83
Fig. 2-27: Temperature estimation errors for the transient test .....	83
Fig. 2-28: Load profile based on the WLTP Class 3 driving cycle .....	84
Fig. 2-29: Thermal resistances for temperature estimations.....	84
Fig. 2-30: Temperature estimations and the corresponding measurements.....	84
Fig. 2-31: Temperature estimation errors under the transient profiles .....	85
Fig. 2-32: Thermal resistances estimated with different copper losses $PW$ applied .....	86
Fig. 2-33: Thermal resistances estimated with different iron losses $PFes$ applied.....	86
Fig. 2-34: Thermal resistances estimated with different magnet losses $PPM$ applied.....	87
Fig. 2-35: Maximum node temperature errors with different $PW$ applied.....	88
Fig. 2-36: Maximum node temperature errors with different $PFes$ applied .....	88
Fig. 2-37: Maximum node temperature errors with different $PPM$ applied.....	88
Fig. 3-1: The values of $\alpha\beta r$ at each temperature region for the tested motor.....	90
Fig. 3-2: Hexagon state vector diagram.....	92
Fig. 3-3: Gate signals PWM1, PWM3, PWM5, and the corresponding current variation in a single switching period .....	93
Fig. 3-4: Flux linkage estimations (top) and the corresponding errors (bottom) at 400rpm, 800rpm, 1000rpm, and 1200rpm rotor speeds .....	96
Fig. 3-5: Flux linkage estimations (top) and the corresponding errors (bottom) at $i_q = 10A$ , 30A, 40A, and 50A.....	97
Fig. 3-6: Command and PWM voltages (top) and their differences (bottom) at 400rpm, 800rpm, 1000rpm, and 1200rpm rotor speeds .....	97
Fig. 3-7: Command and PWM voltages (top) and their differences (bottom) at $i_q = 10A$ , 30A, 40A, and 50A.....	98

Fig. 3-8: Flux linkage (top) and rotor temperature (bottom) estimations according to the step-based profile.....	98
Fig. 3-9: HIL implementation scheme .....	99
Fig. 3-10: Phase current at $i_q\_command = 2.9A$ .....	100
Fig. 3-11: Rotor angle in OPAL-RT .....	100
Fig. 3-12: Delay between the voltage (green) and current (yellow) in the first-order RL circuit test due to myRIO .....	101
Fig. 3-13: Delay times due to myRIO and OPAL-RT .....	101
Fig. 3-14: PWM1, PWM3, PWM5 and the corresponding $q$ -axis current variation within one switching period in real-time simulation .....	102
Fig. 3-15: Flux linkage estimation at $1000rpm$ rotor speed and rated torque ( $I = 54A$ ) ...	102
Fig. 3-16: Flux linkage estimations at $1000rpm$ , $800rpm$ , and $400rpm$ rotor speeds .....	103
Fig. 3-17: Flux linkage estimations at $35.5Nm$ , $20Nm$ , and $10Nm$ electromechanical torques .....	103
Fig. 3-18: Flux linkage (top) and rotor temperature (bottom) estimations at the rated torque and $500rpm$ rotor speed, according to the transient test cycle .....	104
Fig. 3-19: Flux linkage (top) and rotor temperature (bottom) estimation errors for the test in Fig. 3-18.....	105
Fig. 3-20: Load profile.....	105
Fig. 3-21: Flux linkage (top) and rotor temperature (bottom) estimations, according to the test duty cycle used on the simplified three-node thermal network .....	106
Fig. 3-22: Flux linkage (top) and rotor temperature (bottom) estimation errors in Fig. 3-21 .....	106
Fig. 3-23: Flux linkage estimations (top) and the corresponding errors (bottom) at $1\mu s$ , $2\mu s$ , $5\mu s$ , $10\mu s$ , and $20\mu s$ sampling times .....	108
Fig. 3-24: Command and PWM voltages (top) and their corresponding errors (bottom) at $1\mu s$ , $2\mu s$ , $5\mu s$ , $10\mu s$ , and $20\mu s$ sampling times.....	109

Fig. 3-25: Flux linkage estimations (top) and the corresponding errors (bottom) with $0.5\mu s$ , $1\mu s$ , $2\mu s$ , $5\mu s$ , and $10\mu s$ dead-times applied.....	110
Fig. 3-26: Flux linkage estimations (top) and the corresponding errors (bottom) when $m = 0.01, 0.02, 0.05, 0.08$ , and $0.1$ .....	110
Fig. 3-27: Values of $Ld$ and $Lq$ in a wide range of currents.....	111
Fig. 3-28: Values of $Ld$ and $Lq$ after the modification.....	111
Fig. 3-29: Flux linkage estimations (top) and the corresponding errors (bottom) at $iq\_command = 0.5A, 1A, 2A, 3A$ , and $3.8A$ .....	112
Fig. 3-30: Flux linkage estimations (top) and the corresponding errors (bottom) using (3-32) and (3-33).....	113
Fig. 3-31: Flux linkage estimations (top) and the corresponding errors (bottom) at $id\_command = -0.5A, -1A, -1.5A, -2A$ , and $-3A$ .....	114
Fig. 3-32: Flux linkage estimations (top) and the corresponding errors (bottom) post-compensation.....	114
Fig. 3-33: (a) Tested motor, microcontroller and three-phase inverter and (b) motor control schematic diagram.....	115
Fig. 3-34: Data acquisition unit OPAL-RT 5600.....	116
Fig. 3-35: Method implementation block diagram.....	116
Fig. 3-36: Phase current signal(s) (a) on oscilloscope and (b) in the data acquisition unit at $id = 0$ and $iq = 4A$ .....	117
Fig. 3-37: Phase voltage at $\omega r = 3500rpm$ .....	118
Fig. 3-38: Rotor angle and its relationship with motor fundamental frequency.....	119
Fig. 3-39: Three-phase PWM signals and the corresponding $q$ -axis current variation in one switching period in experimental testing.....	120
Fig. 3-40: PWM and its complementary signals implementing $1\mu s$ dead-time.....	121
Fig. 3-41: Phase current applying (a) $1\mu s$ and (b) $10\mu s$ dead-times.....	121

Fig. 3-42: Flux linkage estimations (top) and the corresponding errors (bottom) with $0.5\mu s$ , $1\mu s$ , $2\mu s$ , $5\mu s$ , and $10\mu s$ dead-times implemented experimentally at $i_q = 3.6A$ and $\omega_r = 3000rpm$ .....	122
Fig. 3-43: Voltage commands with $0.5\mu s$ , $1\mu s$ , $2\mu s$ , $5\mu s$ , and $10\mu s$ dead-times implemented experimentally at $i_q = 3.6A$ and $\omega_r = 3000rpm$ .....	122
Fig. 3-44: (a) Motor wrapped with heater mat and (b) kit wrapped with insulation material .....	124
Fig. 3-45: Flux linkage estimation (top) and back-EMF measurements (bottom) at $4000rpm$ and $25^\circ C$ motor temperature.....	125
Fig. 3-46: Flux linkage estimations at $4000rpm$ and rising temperatures.....	125
Fig. 3-47: Flux linkage errors at $1000rpm$ , $2000rpm$ , $3000rpm$ , $4000rpm$ , and rising temperatures.....	126
Fig. 3-48: Rotor temperature estimation and winding temperature measurement at $T_{setpoint} = 60^\circ C$ .....	127
Fig. 3-49: Rotor temperature estimations (top) and the corresponding errors (bottom) at $T_{setpoint} = 60^\circ C$ , $90^\circ C$ , and $120^\circ C$ .....	127
Fig. 3-50: Motor stator temperature profile during transient testing .....	128
Fig. 3-51: Motor speed and current profiles of the transient testing.....	128
Fig. 3-52: Flux linkage (top) and rotor temperature (bottom) estimations under the transient profiles .....	129
Fig. 4-1: (a) test rig and (b) thermocouple locations .....	132
Fig. 4-2: EKF algorithm implementation block diagram.....	133
Fig. 4-3: Estimated thermal resistances at $\omega_r = 3200rpm$ and $I = 3.4A$ .....	134
Fig. 4-4: Estimated three node temperatures at $\omega_r = 3200rpm$ and $I = 3.4A$ .....	134
Fig. 4-5: Temperature estimation errors in Fig. 4-4.....	135
Fig. 4-6: Estimated node temperatures using the results in Fig. 4-3.....	135
Fig. 4-7: Temperature estimation errors in Fig. 4-6.....	136

Fig. 4-8: Three-node temperatures predicted by the Levenberg-Marquardt algorithm, the power losses, the cooling system (natural convection) and ambient temperatures .....	136
Fig. 4-9: Cost function values during the estimation process .....	137
Fig. 4-10: Identified thermal resistances using the Levenberg-Marquardt and extended Kalman filter algorithm .....	137
Fig. 4-11: Node temperatures estimated with the results in Fig. 4-10 .....	138
Fig. 4-12: Temperature errors in Fig. 4-11 .....	138
Fig. 4-13: Thermal resistance estimations under the conditions of $\omega r = 2000rpm, 2400rpm, 3200rpm,$ and $3800rpm$ and their corresponding currents .....	139
Fig. 4-14: Estimated thermal resistance $RFes - C$ at different speeds and load conditions	140
Fig. 4-15: Estimated thermal resistance $RW - Fes$ at different speeds and load conditions .....	140
Fig. 4-16: Estimated thermal resistance $RPM - Fes$ at different speeds and load conditions .....	140
Fig. 4-17: Estimated thermal resistance $RPM - W$ at different speeds and load conditions .....	141
Fig. 4-18: Estimated thermal resistance $RPM - A$ at different speeds and load conditions	141
Fig. 4-19: Rotor speed and stator current profiles of the transient testing.....	141
Fig. 4-20: Estimated thermal resistances according to the driving cycle .....	142
Fig. 4-21: Open-loop temperature estimations based on the transient driving cycle.....	142
Fig. 4-22: Temperature estimation errors in Fig. 4-21.....	143

# Nomenclature

$a$	The Steinmetz constant
$a_e$	The eddy-current component of open-circuit iron loss
$a_{exc}$	The excess component of open-circuit iron loss
$a_h$	The hysteresis component of open-circuit iron loss
$A$	The state matrix of state-space model
$A_T$	One tooth section area
$b_e$	The eddy-current component of short-circuit iron loss
$b_{exc}$	The excess component of short-circuit iron loss
$b_h$	The hysteresis component of short-circuit iron loss
$B$	The input matrix of state-space model
$B_e$	Flux density
$B_i$	The $i^{th}$ harmonic component of flux density $B_e$
$B_m$	The peak of flux density
$C$	The output matrix of state-space model
$C_{Fes}$	Stator iron thermal capacitance
$C_{PM}$	Permanent magnet thermal capacitance
$C_W$	Stator winding thermal capacitance
$d$	The measured output of the Adaline estimator
$D$	The feedthrough matrix of state-space model
$e(\text{tooth})$	The Back-EMF per tooth
$e_x$	The state variable estimation error
$f_r$	Electrical frequency
$f_{rated}$	Rated electrical frequency
$f_{sw}$	PWM switching frequency
$f_{system}$	System frequency
$F_k$	The state-transition Jacobian of state-space model
$G_{PM-Fes}$	The thermal conductance between permanent magnet and stator iron
$G_{W-Fes}$	The thermal conductance between stator winding and stator iron

$H_k$	The observation Jacobian of state-space model
$i$	Motor phase
$i_d$	$d$ -axis current
$i_{da}$	The $d$ -axis current associated with armature reaction
$i_{dFe}$	The equivalent current incurring loss in the equivalent resistor across $d$ -axis induced voltage
$i_{dN}$	The $d$ -axis current with negative pulse injection
$i_{dqsc}^s$	The high-frequency current
$i_q$	$q$ -axis current
$i_{qa}$	The $q$ -axis current associated with armature reaction
$i_{qFe}$	The equivalent current incurring loss in the equivalent resistor across $q$ -axis induced voltage
$i_{qN}$	The $q$ -axis current with negative pulse injection
$I$	Stator current
$I_{abc\_peak}$	The peak of phase current
$I_{base}$	Stator base current
$I_{rated}$	Rated stator current
$I_{RMS}$	RMS current
$k$	Sampling index
$k_{ch}$	The correction term considering minor hysteresis loop effect
$k_{ce}$	The correction term considering harmonics effect
$k_e$	Eddy-current constant
$k_{exc}$	Excess loss constant
$k_h$	Hysteresis constant
$K_k$	The optimal Kalman gain
$K_N$	The conversion ratio for current sensor
$L^*$	Differential inductance
$\Sigma L$	The high-frequency inductance
$L_d$	$d$ -axis inductance
$L_{dd}$	$d$ -axis self-inductance

$L_{dq}$	Mutual inductance
$L_q$	$q$ -axis inductance
$L_{qd}$	Mutual inductance
$L_{qq}$	$q$ -axis self-inductance
$m$	The ratio of the peak of the harmonic component to that of the fundamental component
$M_o$	The observability matrix of state-space model
$n$	The number of sampling points in one PWM switching period
$n_{so}$	The order of state-space model
$N$	The number of minor loops
$N_T$	The number of turns for the wire wrapped around current sensor
$O(W_i, X_i)$	The activation function of Adaline neural network output
$p$	Pole pairs
$p_c$	The iron loss per unit weight
$p_e$	The eddy-current loss per unit weight
$p_{exc}$	The excess loss per unit weight
$p_h$	The hysteresis loss per unit weight
$P_{CP}$	On-load iron loss associated with the main magnetizing flux path
$P_{CT}$	On-load iron loss associated with the field weakening flux path
$P_{Cu}$	Resistive (copper) loss
$P_{fe_d}$	$d$ -axis iron loss
$P_{fe_q}$	$q$ -axis iron loss
$P_{Fe}$	Iron loss
$P_{Fes}$	The loss generated by the stator iron node in LPTN
$P_{k k}(P_{k-1 k-1})$	The ‘a posteriori’ state estimate error covariance matrix
$P_{k k-1}$	The ‘a priori’ state estimate error covariance matrix
$P_{OC}$	The iron loss for open-circuit condition
$P_{PM}$	The loss generated by the permanent magnet node in LPTN
$P_{resid}$	Residual (excess) loss

$P_{SC}$	The iron loss for short-circuit condition
$P_{ST}$	The loss generated by the stator teeth node in LPTN
$P_{Total}$	The total heat losses generated in a motor
$P_W$	The loss generated by the winding node in LPTN
$Q_k$	The covariance of the process noise
$R_{Fe\_d}$	The equivalent resistor across $d$ -axis induced voltage
$R_{Fe\_q}$	The equivalent resistor across $q$ -axis induced voltage
$R_{Fes-C}$	The thermal resistance between stator iron and cooling system
$R_k$	The covariance of the measurement noise
$R_{PM-A}$	The thermal resistance between permanent magnet and ambient
$R_{PM-Fes}$	The thermal resistance between permanent magnet and stator iron
$R_{PM-ST}$	The thermal resistance between permanent magnet and stator teeth
$R_{PM-W}$	The thermal resistance between permanent magnet and stator winding
$R_{rc}$	The high-frequency rotor resistance
$R_{resistor}$	The resistance of the resistor connected to current sensor
$R_s$	Stator resistance
$R_{sc}$	The high-frequency stator resistance
$R_{ST-Fes}$	The thermal resistance between stator teeth and stator iron
$R_{ST-W}$	The thermal resistance between stator teeth and stator winding
$R_{W-Fes}$	The thermal resistance between stator winding and stator iron
$S$	The sum of the squares of the deviations between the model curve $y_\beta$ and the observations
$S_k$	The measurement residual covariance matrix
$t_a, t_b$	The intervals the two adjacent active state vectors are applied
$t_{switching}$	PWM switching period
$t_0$	The interval zero-voltage vector is applied
$T$	Motor temperature
$T^e$	Estimated temperature
$T^m$	Measured temperature
$T_A$	Ambient temperature

$T_{count}$	The sampling time in FPGA clock ticks
$T_C$	Cooling system temperature
$T_{dead\_count}$	The dead-time in system count
$T_{dead\_count}$	The dead-time in second
$T_{em}$	Electromagnetic torque
$T_{Fes}$	Stator iron temperature
$T_k$	The sampling rate for discrete-time thermal model
$T_L$	Load torque
$T_{PM}$	Permanent magnet temperature
$T_s$	The sampling rate for the PWM-based method
$T_{second}$	The sampling time in second
$T_{setpoint}$	Set-point temperature
$T_{ST}$	Stator teeth temperature
$T_w$	Stator winding temperature
$T_0$	Reference temperature
$u(u_k)$	The input vector of state-space model
$v(tooth)$	The imaginary voltage induced in a single-turn stator winding coil wound around a stator tooth
$v_{abc}$	Three-phase voltages
$v_{avg}$	The average PWM output voltage
$v_d$	$d$ -axis voltage
$v_{dqs}^s$	The high-frequency voltage
$v_k$	The measurement noise of state-space model
$v_{load}(tooth)$	The current-induced-EMF per tooth
$v_q$	$q$ -axis voltage
$v_\alpha$	$\alpha$ -axis voltage
$v_\beta$	$\beta$ -axis voltage
$\bar{V}^*$	The reference voltage vector
$\bar{V}_a, \bar{V}_b$	The components of $\bar{V}^*$ aligned in the directions of the two adjacent active state vectors on the hexagon diagram

$V_d^*$	The demagnetization field equivalent voltage
$V_{dc}$	The DC link voltage for the inverter
$V_{emf}$	Back-EMF
$V_m$	The terminal voltage without the voltage drop across stator resistance
$V_o$	The voltage signal representing temperature measurement
$V_{resistor}$	The voltage across the resistor connected to current sensor
$V_{0...7}$	The active and zero state vectors on the hexagon diagram
$w_k$	The process noise of state-space model
$W_i$	The net weight of the Adaline NN mathematical model
$x, x_k, x_{k-1}$	The state vector of state-space model
$x_{k k}(x_{k-1 k-1})$	The ‘a posteriori’ state estimate
$x_{k k-1}$	The ‘a priori’ state estimate
$X_A, X_B$	Quadrature encoder output channels producing relative rotor angular position
$X_i$	The input of the Adaline NN mathematical model
$X_Z$	Quadrature encoder index channel
$y$	The output vector of state-space model
$y_k$	The measurement residual
$y_\beta$	Nonlinear model curve
$z_k$	The measurement of the state variable in state-space model
$Z_{dqs}^s$	The high-frequency impedance
$\alpha$	The location of the reference voltage vector on the hexagon diagram
$\alpha_{cu}$	The temperature coefficient for stator winding
$\alpha_{Fes}$	The temperature coefficient for stator iron
$\alpha_{Fes-C}$	The coefficient for the convection effect between stator and cooling system
$\alpha_{mag}$	The magnet resistive temperature coefficient
$\alpha_{\beta r}$	The temperature coefficient for PM magnetic field
$\beta$	The parameters of the nonlinear model curve $y_\beta$
$\beta_{Cu}$	The skin and proximity effect coefficient

$\Delta B_i$	The small flux density variation around a hysteresis minor loop
$\Delta v$	The voltage error due to inverter dead-time effect
$\Delta \psi_{dq}$	The $dq$ -axis flux linkage estimation error
$\eta$	The convergence factor adjusting the convergence of $W_i$
$\theta$	Rotor angular position
$\theta_{offset}$	A constant value added to the relative rotor angular position
$\theta_r$	Relative rotor angular position
$\lambda_d$	Damping factor controlling the minimization of the cost function $S$
$\lambda_{emf}$	EMF constant
$\psi_d$	$d$ -axis flux linkage
$\psi_d^*$	Demagnetization field
$\psi_m$	Permanent magnet flux linkage
$\hat{\psi}_m$	Permanent magnet flux linkage estimation
$\psi_{m\_ph}$	Three-phase flux linkage
$\psi_q$	$q$ -axis flux linkage
$\omega_{base}$	Rotor base speed
$\omega_c$	The high-frequency carrier frequency
$\omega_r$	Rotor speed
$\omega_{1,2,3\dots}$	The electrical speed of the first/second/third-order $\dots$ harmonic

# Abbreviations

AC	Alternating current
ADC	Analogue-to-digital converter
BLAC	Brushless AC machine/drive
DC	Direct current
EKF	Extended Kalman Filter
EMF	Electromotive force
FE	Finite element
FEA	Finite element analysis
FEM	Finite element method
FOC	Field-oriented control
FPGA	Field-programmable gate array
GaAs	Gallium Arsenide
HIL	Hardware-in-the-Loop
IM	Induction machine
I/O	Input/output
IPMSM	Interior permanent magnet synchronous machine
IrDA	Infrared Data Association
LED	Light-emitted diode
LMS	Least mean square
LPTN	Lumped parameter thermal network
LUT	Look-up table
MOSFET	Metal-oxide-semiconductor field-effect transistor
NdFeB	Neodymium iron boron magnet
NI	National Instrument
NN	Neural network
OC	Open-circuit
PC	Personal computer
PI	Proportional-integral

PM	Permanent magnet
PMSM	Permanent magnet synchronous machine
PSO	Particle swarm algorithm
PWM	Pulse width modulation
RAM	Random-access memory
Ref	Reference
RK1	Explicit Euler method
RL	Resistor-inductor
RLS	Recursive least square
RMS	Root mean square
RTD	Resistance temperature detector
SC	Short-circuit
SiFe	Silicon-Iron material
SIR	Serial Infrared scheme
SPMSM	Surface-mounted permanent magnet synchronous machine
SQP	Sequential quadratic programming
SV-PWM	Space-vector pulse width modulation
3-D	Three-dimensional
TI	Texas Instruments
UART	Universal Asynchronous Receiver Transmitter
WLTP	Worldwide harmonized light-duty vehicles test procedure

# Chapter 1: Introduction and Literature Review

## 1.1 Introduction

Permanent magnet synchronous machines (PMSMs) are widely popular in servo and traction applications due to their high torque and power density. Their use in applications where high reliability must be guaranteed requires careful online condition monitoring of the motor [1]-[5]. The performance of a PMSM is strongly affected by its internal temperatures, due to the dependence of the stator winding and permanent magnet remanence on temperature [6], [93]. More importantly, temperature is typically the main environmental stressor which may cause motor state-of-health degradation and ultimately failure. With regard to the motor stator, the temperature limit normally occurs in stator winding insulation, which is classified according to maximum allowable stator winding operating temperature. Thermal overload can significantly shorten stator insulation lifetime [7]. In addition, excessive thermal stress increases the risk of partial, or even total irreversible demagnetization of rotor magnet, especially with the motor operated in flux weakening mode [8]. Besides, high temperature may lead to a shortened device lifespan [60]. Therefore, thermal monitoring of PMSMs is particularly significant.

Several direct and indirect temperature monitoring techniques are well established. Temperature sensors such as thermocouples and thermistors can be relatively easily embedded into machine stators during the manufacturing process. However, the requirement for additional sensors may increase costs. Rotor temperatures are difficult to measure in practice, as the motor rotating shaft can only be accessed through slip rings [9]-[10], infrared [11]-[12], or other wireless sensors [13]-[14], making direct measurement unrealistic in most applications. In addition, rotor temperature measurement technique is limited to laboratory use, because specific instruments are selected for a particular motor [15]. Hence model-based methods, have been investigated in the past decades.

It is possible to determine motor temperatures via temperature dependent electrical parameters [16]-[38]. In [16]-[21], rotor temperature is estimated by measuring the response to the injection of a pulsating high-frequency current signal to the  $d$ -axis of the PMSM noting that the resulting high-frequency resistance varies with the rotor temperature. Ref. [22]-[25] propose the detection of variations in the slope of the  $d$ -current response to a voltage pulse applied in the  $d$ -axis of the motor, which is an indicator of the magnetization level variation of the PM. Rotor temperature can also be potentially acquired indirectly from the estimation of

rotor magnet flux linkage, using the fact that (NdFeB) PM loses 0.11% to 0.12% remanence per one degree Celsius temperature rise. An online method [26] to estimate stator resistance and rotor PM flux linkage under constant load torque with two sets of  $dq$ -axis voltage equations corresponding to  $i_d = 0$  and the injection of a  $i_d \neq 0$  test signal [27], is proposed. Likewise, by utilizing a zero-voltage injection scheme, flux linkage is directly determined with the measurement of the average value of the voltage commands which are the outputs of current loop PI controllers of the standard field-oriented control (FOC) at different rotor speeds [28]. In both methods, the  $dq$ -axis inductance terms are cancelled during the derivations of the methods, resulting in a parameter-independent estimation. However, these signal injection-related methods are not desirable because the additional signal disturbs the motor performance by producing additional current and thus additional torque ripples and additional losses. The use of a rotor flux linkage model-based observer is proposed in [8], [29]-[31], where the variation in the flux linkage due to the temperature change is retrieved from the difference in the  $dq$ -axis currents between the measurement and an accurate PMSM model considering saturation effect. Nevertheless, this method is difficult to apply practically, because of the necessity of a precise modelling for motor and inverter — the model-related errors otherwise will be misinterpreted as temperature changes.

Another most commonly used approach uses thermal models usually based on a lumped parameter equivalent thermal network (LPTN). It can be the basis for a thermal ‘observer’ which, combined with loss models, is capable of providing accurate temperature estimation during real-time operation. A handful of multi-node thermal models for induction motors (IMs) and PMSMs are presented in [39]-[49]. They are able to predict the temperatures in a number of locations within the machine. However, the models require information on the internal topology, materials, and interfaces between them which might not be directly available in practical applications. Additionally, accurate estimation of losses and characterization of boundary conditions, e.g. heat transfer coefficients are not straightforward and empirical functions [50]-[53] need to be used. One such high-fidelity electro-thermally coupled model for interior PMSM (IPMSM) was introduced in [6], [54]. The motor temperatures can be predicted by an appropriate thermal network represented by a set of state-space equations, with the losses provided by a robust IPMSM model, which takes into account saturation, harmonics, iron loss and temperature effects. Low-order LPTNs [7], [31], [55]-[60] lump large regions of the machine in few nodes and detailed knowledge of the motor internal topology, materials and dimensions might not be required if measurement-based parameter identification procedures,

which determine the values of the thermal parameters based on the minimization of a specified cost function, are used.

Considering the significance of temperature monitoring from the perspective of prolonging the life spans of PMSMs and the challenges facing temperature measurement, this thesis aims for presenting a simple, accurate and robust three-node LPTN suitable for the online estimations of the critical temperatures in PMSMs. The primary objectives of the thesis are: a) to study the indirect temperature monitoring techniques, particularly the use of LPTNs with low model orders, b) to establish a three-node LPTN and conduct validation in offline simulation, c) to investigate the rotor temperature estimation methods using the thermal properties of motor electrical parameters, due to the difficulty in acquiring a rotor temperature measurement for the modelling of the LPTN, d) to develop a PWM-based method for predicting the PM flux linkage and rotor temperature and examine its validity through a series of simulation and experimental tests, e) to evaluate the performance of the LPTN integrated with the rotor temperature estimation method, f) to conclude, and outline the direction for future research — combining the system with a stator temperature estimation approach.

The thesis is structured as follows: an in-depth literature review of motor temperature measurement and estimation approaches is presented in the following section. Chapter 2 proposes a three-node thermal model for the prediction of the critical temperatures in PMSMs, and chapter 3 introduces a PWM-based estimation method serving as a rotor temperature measurement for the thermal model. Finally, the estimated temperatures of the experimentally-tested motor combining the methodologies introduced in the previous chapters are shown in chapter 4.

Two major factors motivate the research work undertaken in this PhD project. First, compared to the conventional electromagnetic design, there is a dearth of study on the thermal management of an electrical machine. Second, motor temperature affects motor electromagnetic performance and relates to motor safe operation. This thesis will be of good value for motor designers, as the knowledge of motor critical temperatures provides the designers with the opportunities to significantly improve motor output and efficiency. In addition, the methods allow users to monitor the temperatures of a PMSM online, which prevents unexpected motor shutdowns and extends the motor lifespan.

## 1.2 Literature Review

### 1.2.1 A Review of Temperature Measurement Techniques

Knowledge of motor temperatures is significant particularly from the perspective of safe motor operation. The most accurate approach to access temperature information is through measurement techniques. Also, despite the fact that model-based temperature estimation method has been at the centre of research interest, validation of the obtained results still requires temperature measurements. Stator temperature can be acquired by means of temperature sensors, such as thermocouples and thermistors, which can be installed directly into stator slot or winding and are commonly used in commercial PMSMs, particularly in applications where the reliability of temperature data is crucial. The measurement of rotor temperature remains a challenge as a result of rotation. In general, rotor temperature monitoring can be achieved by adopting contact or non-contact measuring techniques.

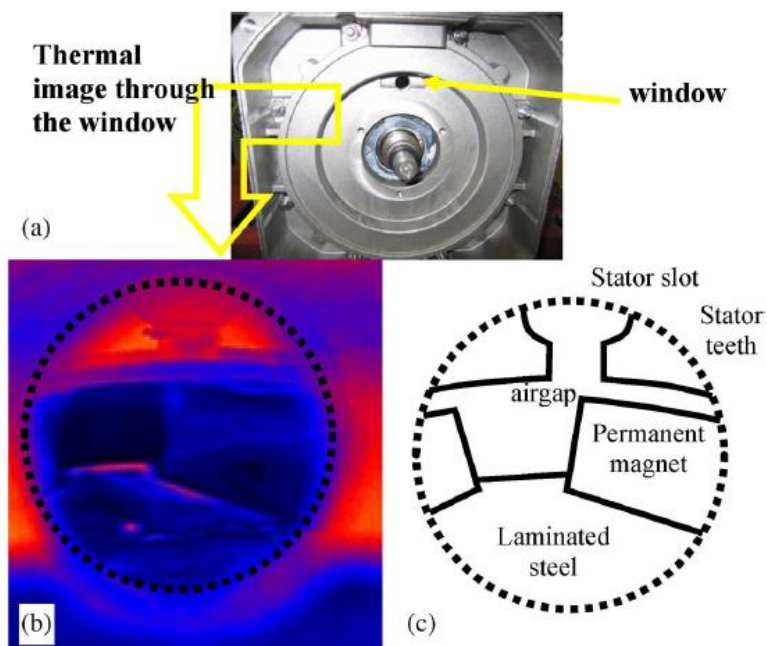


Fig. 1-1: (a) circular window on the tested motor (b) Thermal image through the window and (c) Schematic of the image (b) [18]

Non-contact measurement techniques are relatively simple to apply, because temperature information can be obtained directly from the temperature-sensing device employed and thus the data transmission from motor rotating part is avoided. The use of an infrared camera is presented in [18], in which the temperature of the side surface of the PM is captured, as illustrated in Fig. 1-1. However, the temperature towards the centre of the machine is unmeasurable. Furthermore, a circular slot is cut on the motor end frame in order for the camera

to access the PM, which inevitably affects the motor operation and robustness. Ref. [11] introduces a similar setup. Instead of an infrared camera, a thermometer is placed into the slot for the rotor temperature measurement. The same limitation applies, in spite of the cost being reduced.

Other non-contact techniques include the use of the fibre-optic conveyed, laser-induced fluorescence of a thermographic phosphor [61], and Gallium Arsenide (GaAs) chip [62] which is a temperature-sensitive detector able to be fixed onto rotor surface. Both methods however are flawed as only average rotor temperature can be obtained. Besides, this type of approach suits only large-sized motors rotating at lower speeds.

On the other hand, contact measurement techniques involve the use of a rotating instrumentation collecting temperature data from the sensors and a transmission strategy allowing the data to be communicated to a stationary receiver, and therefore to a certain degree resolves the issue regarding non-contact techniques, because it allows multiple measurement points along the axial and radial directions of the PM which guarantees a better precision.

Contact measurement techniques can be categorized based on sensor type and data transmission procedure. The thermocouple, as one of the most common types of temperature sensing device, is employed in a variety of monitoring systems [63]-[66]. Compared with resistance temperature detector (RTD) [9], [67]-[68], which operates on the principle that the electrical resistance of a material is temperature-dependent, thermocouple is more desirable as current or voltage supply is not required. In addition, they have relatively good linearity and are not limited by size.

The data collected by sensors is transmitted from rotor to a stationery platform. Several methods are available, including slip rings, light transmission, and radio telemetry. With regard to slip rings, ref. [10] presents a system reading and processing the temperature data through eleven shaft-mounted brush slip-rings. This method discloses several issues such as limited number of rings, electrical noise and suitable motor operating speed range. Nevertheless, it is among the most effective methods from the point of view of the requirement of motor disassembly [9]. Ref. [63]-[65], [67] demonstrate a few applications in which the temperature data transmission is achieved by light, and the results are highly reliable and immune to noise. However, the location where the light emitter has to be situated determines that only a hollow shaft encoder can be used. In [13] and [68], an approach using radio telemetry is introduced, where a wireless module which operates at a high carrier frequency is adopted. The main

drawback of this particular strategy is electromagnetic interference, as up to 10% packet loss is possible during data transmission due to strong magnetic field. Although amplifying wireless transmission power can eliminate electromagnetic interference, it increases the level of the power consumption.

A state-of-the-art rotor temperature monitoring system taking into consideration the defects of the proposed methods is introduced in [15]. The instruments comprise a dozen thermocouples for the rotor temperature measurement, a microcontroller for the data processing, and optical link transmitting the data between the rotor and a host PC. The schematic diagram of the system is demonstrated in Fig. 1-2.

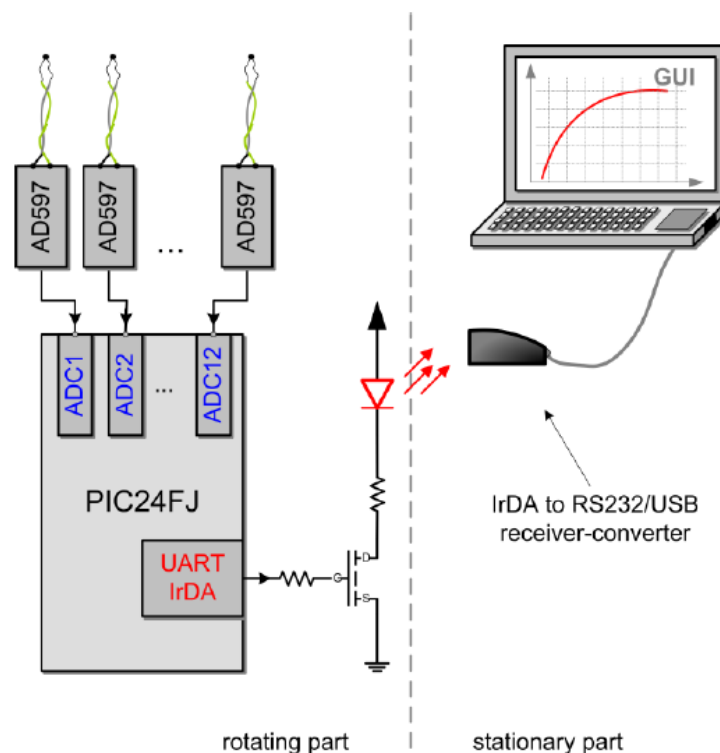


Fig. 1-2: Schematic of the temperature monitoring system [15]

Twelve K-type thermocouples are placed at various positions on the rotor surface in order to obtain the temperature distribution in axial and radial directions. Each thermocouple connects with a single integrated circuit AD597, where the amplification and cold junction compensation of the thermocouple output voltage is implemented. The analogue voltage output is then digitized by the analogue-to-digital converter (ADC) of a PIC24FJ-family microcontroller. The data collected from all twelve sensors is packed and transferred to a Universal Asynchronous Receiver Transmitter (UART) on-chip module. It receives data bytes and transmits the individual bit sequentially. The transmitted data is used to control the switching state of a LED.

Ref. [15] selects the Infrared Data Association (IrDA) for the data transmission protocol because a) it is UART-supported, and b) it significantly reduces the power consumption.

The mechanical assembly of the system is shown in Fig. 1-3. Two printed circuit boards (PCB) for the thermal conditioners AD597 and the microcontroller integrated with the power electronic are adopted, in order to minimize the diameter of the board. The PCBs are then fitted into two aluminium frames which are separated by a plastic battery container. Also, a no less than  $5\text{mm}$  slot into the motor shaft is required leading the thermocouples through to the instruments from the rotor.

In conclusion, the rotor temperature estimation system in [15] is capable of measuring the temperatures at various locations on the rotor surface, and withstanding tangential and centrifugal forces at  $6000\text{rpm}$  rotating speed thanks to the slim circuit design. It presents relatively high immunity to electromagnetic interference, as the aluminium frame can provide the circuits with an electrostatic shield. In addition, a low-pass filter is applied to each ADC channel to acquire a smooth and stable temperature signal. With the power saving protocol IrDA SIR, long-hour operation can be warranted.

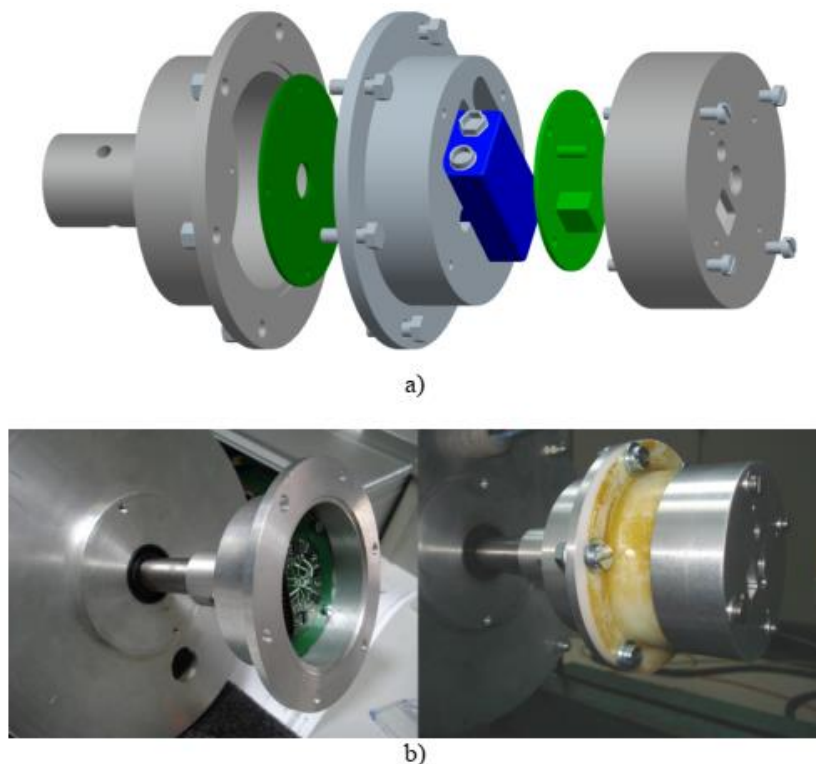


Fig. 1-3: Rotor temperature monitoring system: a) mechanical assembly diagram and b) demonstration of the physical instruments [15]

Ref. [14] presents a wireless PM temperature measurement system for PMSMs with high spatial resolution and low sampling rate. The magnetic field is monitored synchronously with the PM temperature, which provides a platform to evaluate the risks of partial or global demagnetization of the PM, and the relationship between the field and magnet, and to validate the already-existing estimation methods. Similarly to [15], the temperature and field measurements are performed using sensors, and the microcontrollers undertake data collection and manipulation processes. The temperature and field measurements are transmitted to a central PC via *WiFi* link and are later assessed.

Fifteen temperature sensors and fifteen field sensors are installed on the rotor surface. TMP100 digital temperature sensors are employed and connected with a PIC24FJ64GA004 microcontroller denoted as ‘Slave  $\mu$ Controller’ through an  $I^2C$  bus. The magnetic field is measured by GaAs sensors, which output analogue voltages. They are converted into digital signals in the Slave  $\mu$ Controller following a suitable modification. The Slave  $\mu$ Controllers interact via *SPI* with a Master  $\mu$ Controller, which collects the temperature measurements from the Slave  $\mu$ Controllers and transmits them to a central PC using *WiFi*, and a *SPI SRAM* memory with a faster data transmission rate is used for the collection and transmission of the field measurement data.

The practical implementation of the measurement system is illustrated in Fig. 1-4. The temperature and field sensors are distributed in a  $3 \times 5$  style as shown in Fig. 1-4(a), and are attached onto a flexible PCB (Fig. 1-4(b)). The flexible PCBs’ are installed in the motor during the rotor assembly (Fig. 1-4(c)) and then mounted on a connection PCB shown in Fig. 1-4(d), which is fixed onto the shaft (Fig. 1-4(e)). As can be seen from Fig. 1-4(f)-(h), the  $I^2C$  buses connect with the Slave  $\mu$ Controllers, which are assembled along with the filtering and conditioning devices, Master  $\mu$ Controllers, *SPI SRAM* memories, and *WiFi* module into an aluminium box through a hollow shaft. The box is then fitted onto the motor shaft.

The wireless temperature-field measurement system is advantageous because it overcomes the limitation of the positioning of the large number of sensors and meets the requirement of high data acquisition and transmission rates. Also, it is able to measure magnetic field simultaneously with rotor temperatures using field sensors, which are not included in the other systems.

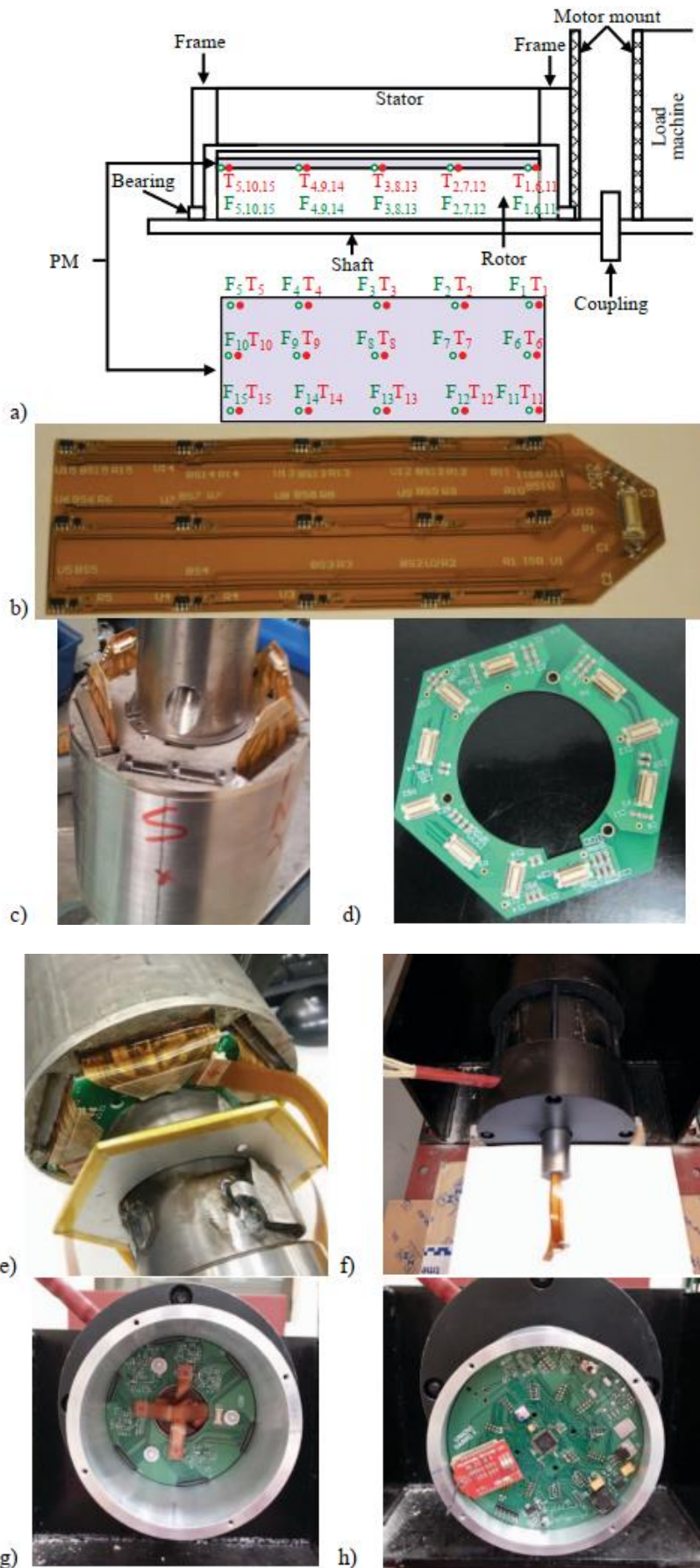


Fig. 1-4: Mechanical assembly of the presented measurement system [14]

## 1.2.2 Temperature Estimation Methods Based on Electrical Parameters

Regardless of higher accuracy and reliability, the hindrances to the use of temperature measurement systems are evident, considering costs and some practical difficulties facing rotor temperature measurement. As a result, immense effort has been put into developing the methodologies in which rotor temperature can be derived from most-common motor parameters, such as voltage and current in recent years.

### 1.2.2.1 Stator Temperature

While stator temperature monitoring techniques are well established, the search for the estimation methods without the involvement of sensors continues. Stator winding temperature can be predicted based on its linear relationship with stator resistance. In [69]-[71], the methods suitable for stator resistance estimation are presented. By superposing intermittently a DC voltage offset in one or more motor phases, winding resistance estimation is dependent on the variations in rotor flux linkage and inductances. Nevertheless the disturbance of the DC voltage injection to the system stability is not taken into consideration. Signal injection technique is also applied in [72], where stator resistance is estimated at low motor speed based on the combination of a speed-adaptive observer and a high-frequency voltage injection. Ref. [26] proposes an online method to estimate stator resistance under constant load torque condition, with two sets of  $dq$ -axis voltage equations obtained at  $i_d = 0$  and  $i_d \neq 0$ . Compared to [32], [35], [73]-[75], it does not require the knowledge of parameter nominal values, and its accuracy is not affected by the variation in motor parameters due to  $i_d \neq 0$ . In addition, ref. [76] introduces a new estimation scheme involving the use of the recursive least square (RLS) algorithm. The value of stator resistance as a result can be updated continuously in real-time.

### 1.2.2.2 Rotor Temperature

The research into rotor temperature estimation is of greater value, because high temperature could lead to local or even global rotor magnet demagnetization. Besides, measuring rotor temperature is not practically applicable in most applications due to rotor spin, and it may interfere with motor operation. In general, two approaches based on signal injection and flux observer are frequently employed, both of which predict rotor temperature using the thermal properties of electrical parameters such as winding resistance, and PM flux linkage. However, this type of method requires particularly accurate modelling for high-power and high-efficiency

motors, as their PMs are not temperature-sensitive, and their resistive voltage drops compared to the terminal voltages are rather small. Also, the signal injected generates ripples and losses, which could affect motor performance. PM flux linkage can also be estimated with assistance from some measuring instruments [18], [77]-[79], such as a digital power meter, which measures motor armature current and voltage. However such instruments are expensive.

Ref. [18] proposes an estimation method using a high-frequency injection signal, as the resulting resistance changes with PM temperature. A simplified high-frequency model can be obtained, following the injection of a high-frequency carrier rotating voltage vector to the stator windings:

$$v_{dqs\ c}^s = V_c e^{j(\omega_c t)} \quad (1-1)$$

$$v_{dqs\ c}^s = Z_{dqs}^s i_{dqs\ c}^s \quad (1-2)$$

$$Z_{dqs}^s = \Sigma R + j\omega_c \Sigma L \quad (1-3)$$

$$\Sigma R = R_{sc} + R_{rc} \quad (1-4)$$

The variations in the motor temperatures lead to the variations in the stator resistance and rotor resistance, which represents the eddy-current magnet loss as a result of the high-order harmonics of the stator current [80]. Additionally, the  $d$ -axis and  $q$ -axis inductances of the motor also vary with the rotor temperature, as a result of the change in the magnet field which is nonlinearly related to the overall saturation level of the motor. In spite of the fact that the rotor temperature could be predicted potentially by either the inductance or resistance, the use of resistance is preferable due to the linear relationship between resistance and temperature. Therefore, the PM temperature can be estimated based on the following equations:

$$\Sigma Z = \Sigma R + j\omega_c \Sigma L = \frac{v_{dqs\ c}^s}{i_{dqs\ c}^s} \quad (1-5)$$

$$\Sigma R_{(T_W, T_{PM})} = |\Sigma Z_{(T_W, T_{PM})}| \cos(\varphi \Sigma Z) \quad (1-6)$$

$$\Sigma R_{(T_W, T_{PM})} = R_{sc}(T_0)[1 + \alpha_{cu}(T_W - T_0)] + R_{rc}(T_0)[1 + \alpha_{mag}(T_{PM} - T_0)] \quad (1-7)$$

$$T_{PM} = T_0 + \frac{\Sigma R_{(T_W, T_{PM})} - R_{rc}(T_0) - R_{sc}(T_0)[1 + \alpha_{cu}(T_W - T_0)]}{R_{rc}(T_0)\alpha_{mag}} \quad (1-8)$$

and:

$$\varphi_{\Sigma Z} = \tan^{-1} \left( \frac{\omega_c \Sigma L}{\Sigma R} \right) \quad (1-9)$$

The implementation of the PM temperature estimation method is shown in Fig. 1-5. The carrier signal is injected intermittently in order to avoid undesired interference to normal motor operation. The voltage injection process takes place during a period of  $t_1$ , while a short blank interval is applied prior to the measurement of the motor current, allowing the initial transient respond to disappear. Fig. 1-6 presents the block diagram of the estimation process. Two state filters are employed to eliminate the negative sequence components in the voltage and current signals.

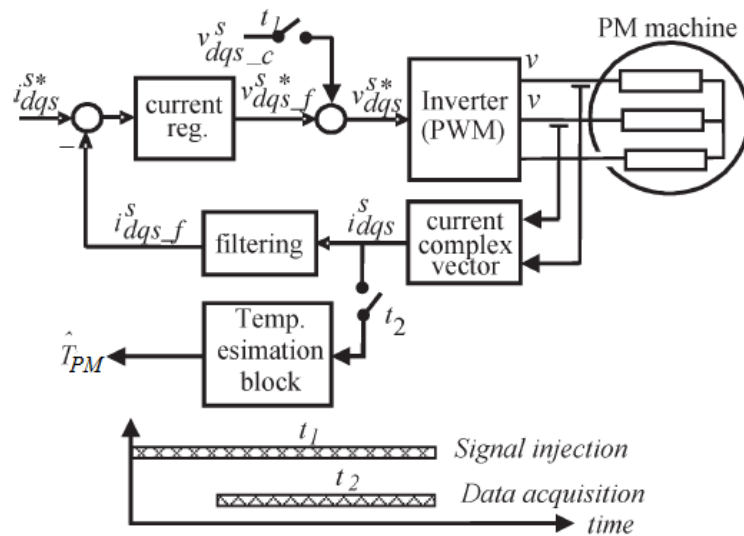


Fig. 1-5: Method implementation schematic [18]

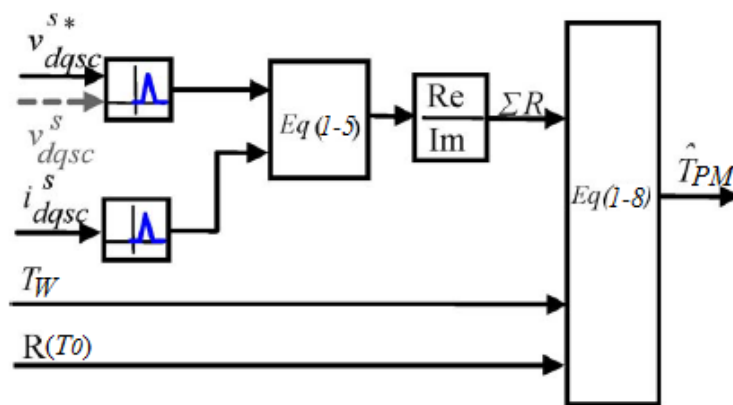


Fig. 1-6: Estimation progress block diagram [18]

In [25], a novel technique is presented, which estimates PM temperature through the detection of the changes in the  $d$ -axis saturation level of a PMSM (SPMSM/IPMSM) due to the variations

in the PM magnetization level. The changes can be observed in the slope of the  $d$ -axis current responding to a voltage pulse injected into the  $d$ -axis of the motor.

The  $q$ -axis current is set to be zero such that the  $d$ -axis current response  $di_d/dt$  is dependent predominantly on the excitation signal and the PM flux linkage. It can be achieved with a three-phase two-level bridge inverter, for which the switching combination generates a  $d$ -axis voltage pulse, with the angle between stator and rotor reference frames being one of the six space vector angles ( $0^\circ, 60^\circ, 120^\circ, 180^\circ, 240^\circ, 300^\circ$ ). Zero angle is used for simplicity — the voltage injection therefore can be applied in phase A of the motor as the rotor moves past zero electrical position. The implementation of this injection-based scheme is demonstrated in Fig. 1-7.

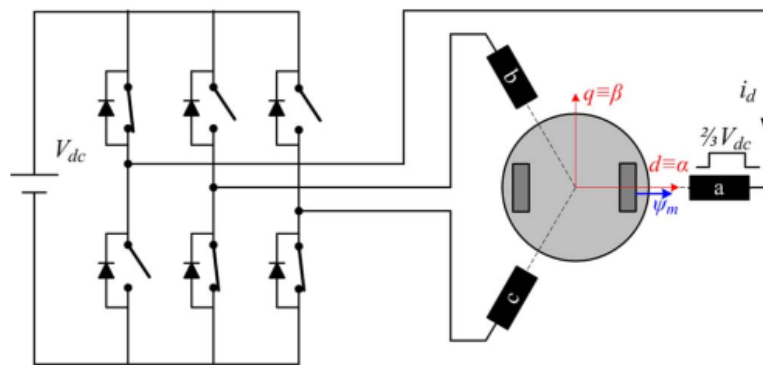


Fig. 1-7: Voltage-injection scheme based on three-phase inverter switching pattern [25]

In the rotor reference frame, the  $dq$ -axis voltage equations of the motor are given as:

$$v_d = R_s i_d + L_{dd}^* \frac{di_d}{dt} + L_{dq}^* \frac{di_q}{dt} - \omega_r L_{qq} i_q - \omega_r L_{qd} i_d \quad (1-10)$$

$$v_q = R_s i_q + L_{qq}^* \frac{di_q}{dt} + L_{qd}^* \frac{di_d}{dt} + \omega_r L_{dd} i_d + \omega_r L_{dq} i_q + \omega_r \psi_m \quad (1-11)$$

$L^*$  represents the differential inductance with respect to the motor currents:

$$L_{dd}^* = L_{dd} + \frac{dL_{dd}}{di_d} i_d \quad (1-12)$$

$$L_{dq}^* = L_{dq} + \frac{dL_{dq}}{di_q} i_q \quad (1-13)$$

$$L_{qq}^* = L_{qq} + \frac{dL_{qq}}{di_q} i_q \quad (1-14)$$

$$L_{qd}^* = L_{qd} + \frac{dL_{qd}}{di_d} i_d \quad (1-15)$$

Assuming the motor is connected in star connection, the  $dq$ -axis voltages  $v_d$  and  $v_q$  after the injection of the voltage pulse are:

$$v_d \approx v_\alpha = \frac{2}{3}V_{dc} \quad (1-16)$$

$$v_q \approx v_\beta = 0 \quad (1-17)$$

Therefore rearranging (1-10) yields:

$$L_{dd}^* \frac{di_d}{dt} = \frac{2}{3}V_{dc} - R_s i_d - L_{dq}^* \frac{di_q}{dt} + \omega_r L_{qq} i_q + \omega_r L_{qd} i_d \quad (1-18)$$

The differential inductance  $L_{dd}^*$  has a strong dependency on the  $d$ -axis saturation level. Thus the value of  $di_d/dt$  can be used as an indicator of the PM magnetization level which is linearly dependent on the rotor temperature. Nonetheless, at high motor speed the  $q$ -axis current  $i_q$  varies during the voltage injection process, in order to cancel out the back-EMF term  $\omega_r \psi_m$  in (1-11) as the  $q$ -axis voltage  $v_q$  is set to zero. This unfortunately affects the  $d$ -axis current response  $di_d/dt$  in (1-18), introducing an error in the estimated rotor temperature.

A negative voltage pulse is injected into the  $d$ -axis, which leads to:

$$L_{dd}^* \frac{di_{dN}}{dt} = -\frac{2}{3}V_{dc} - R_s i_{dN} - L_{dq}^* \frac{di_{qN}}{dt} + \omega_r L_{qq} i_{qN} + \omega_r L_{qd} i_{dN} \quad (1-19)$$

By subtracting (1-19) from (1-18), the effect of  $i_q$  can be eliminated from the  $d$ -axis current response, under the conditions that the inductances are independent on the voltage pulses and  $i_q = i_{qN}$ .

$$L_{dd}^* \left( \frac{di_d}{dt} - \frac{di_{dN}}{dt} \right) = \frac{4}{3}V_{dc} - R_s (i_d - i_{dN}) + \omega_r L_{qd} ((i_d - i_{dN})) \quad (1-20)$$

The voltage terms relating to stator resistance and rotor speed in (1-20) are not taken into account to simplify the estimation.

The information of rotor temperature can also be extracted from PM flux linkage, as PM remanence decreases with rotor temperature. A parameter estimation method is proposed in [26], which is capable of predicting stator winding resistance and PM flux linkage simultaneously. At steady state, the  $dq$ -axis voltage equations of a PMSM are expressed as:

$$v_d(k) = R_s i_d(k) - L_q \omega_r(k) i_q(k) \quad (1-21)$$

$$v_q(k) = R_s i_q(k) + L_d \omega_r(k) i_d(k) + \psi_m \omega_r(k) \quad (1-22)$$

in which  $k$  represents the  $k^{th}$  sampling instant,. It is obvious that the parameters  $R_s$ ,  $L_d$ ,  $L_q$ , and  $\psi_m$  are unsolvable as the rank of the equations is less than the number of the variables. As a result, a current pulse is injected into the  $d$ -axis of the motor which provides a different set of voltage equations. The schematic of the data acquisition processes is presented in Fig. 1-8.

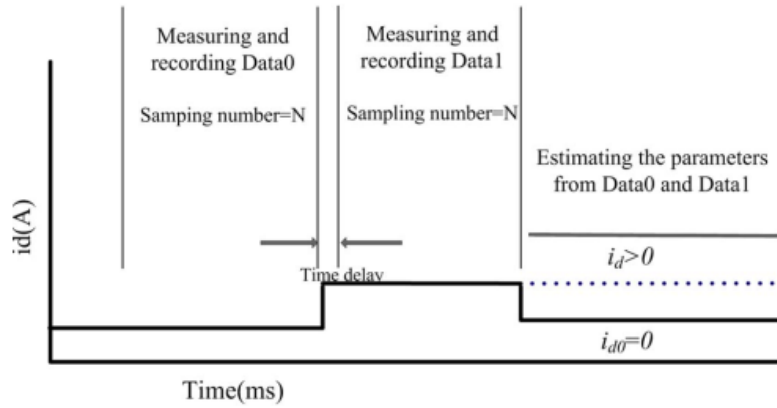


Fig. 1-8: Practical implementation of the presented method [26]

The  $d$ -axis current is controlled to be zero before and after the pulse injection. A short time delay is applied to avoid the sampling of the step transient resulting from the injection. Two sets of data correspond to two sets of equations, which can be written as:

$$v_{d0}(k_0) = -L_{q0}\omega_r(k_0)i_{q0}(k_0) \quad (1-23)$$

$$v_{q0}(k_0) = R_s i_{q0}(k_0) + \psi_{m0}\omega_r(k_0) \quad (1-24)$$

$$v_d(k_1) = R_s i_d(k_1) - L_q \omega_r(k_1) i_q(k_1) \quad (1-25)$$

$$v_q(k_1) = R_s i_q(k_1) + L_d \omega_r(k_1) i_d(k_1) + \psi_m \omega_r(k_1) \quad (1-26)$$

where the subscript 0 and 1 denote  $i_d = 0$  and  $i_d \neq 0$  operating conditions, respectively. Due to the electrical time constant of a PMSM being significantly smaller than its mechanical and temperature constants, it is assumed that the stator resistance and motor rotating speed remain unaffected during the signal injection period, which is kept short to reduce its influence on the motor performance. With the motor under constant load torque, and speed being constant, the electromagnetic torques at  $i_d = 0$  and  $i_d \neq 0$  are identical:

$$T_{em}(k_0) = \frac{3}{2} p \psi_{m0} i_{q0}(k_0) \quad (1-27)$$

$$T_{em}(k_1) = \frac{3}{2} p [\psi_m i_q(k_1) + (L_d - L_q) i_d(k_1) i_q(k_1)] \quad (1-28)$$

$$T_{em}(k_0) = T_{em}(k_1) \quad (1-29)$$

From (1-27) to (1-29), the rotor flux linkage can be derived as:

$$\psi_m = \psi_{m0} \frac{i_{q0}(k_0)}{i_q(k_1)} + (L_q - L_d)i_d(k_1) \quad (1-30)$$

Substituting (1-30) into (1-26) gives:

$$v_q(k_1) = R_s i_q(k_1) + \left( \psi_{m0} \frac{i_{q0}(k_0)}{i_q(k_1)} + L_q i_d(k_1) \right) \omega_r(k_1) \quad (1-31)$$

Multiplied by  $i_q(k_1)$ , equation (1-31) becomes:

$$v_q(k_1)i_q(k_1) = R_s i_q^2(k_1) + \left( \psi_{m0} i_{q0}(k_0) + L_q i_d(k_1)i_q(k_1) \right) \omega_r(k_1) \quad (1-32)$$

Multiplying (1-25) by  $i_d(k_1)$  produces:

$$v_d(k_1)i_d(k_1) = R_s i_d^2(k_1) - L_q \omega_r(k_1)i_q(k_1)i_d(k_1) \quad (1-33)$$

Adding (1-33) to (1-32):

$$v_q(k_1)i_q(k_1) + v_d(k_1)i_d(k_1) = R_s \left( i_q^2(k_1) + i_d^2(k_1) \right) + \psi_{m0} i_{q0}(k_0) \omega_r(k_1) \quad (1-34)$$

Therefore, the stator resistance and PM flux linkage can be estimated using (1-34) and (1-24), in which only two parameters are unknown due to the elimination of the inductance terms  $L_d$ ,  $L_{d0}$ ,  $L_q$ , and  $L_{q0}$ .

The parameter estimation procedure is performed adopting the Adaline NN algorithm. Its mathematical model can be represented by the following equation:

$$O(W_i, X_i) = \sum_{i=0}^n W_i X_i \quad (1-35)$$

The structure of the algorithm is shown in Fig. 1-9.

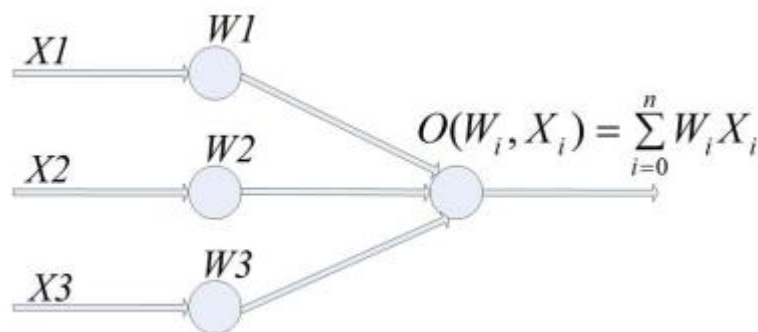


Fig. 1-9: Adaline NN algorithm structure [26]

Assuming the measured system output to be  $d(k)$ , the update of  $W_i$  can be obtained through the LMS algorithm [81]:

$$W_i(k+1) = W_i(k) + 2\eta X_i(d(k) - O(k)) \quad (1-36)$$

Multiplying (1-24) by  $i_{q0}(k_0)$  yields:

$$v_{q0}(k_0)i_{q0}(k_0) = R_s i_{q0}^2(k_0) + \psi_{m0}\omega_r(k_0)i_{q0}(k_0) \quad (1-37)$$

With  $\omega_r(k_0)$  equal to  $\omega_r(k_1)$ , subtracting (1-37) from (1-34) gives:

$$\begin{aligned} v_q(k_1)i_q(k_1) + v_d(k_1)i_d(k_1) - v_{q0}(k_0)i_{q0}(k_0) \\ = R_s \left( i_q^2(k_1) + i_d^2(k_1) - i_{q0}^2(k_0) \right) \end{aligned} \quad (1-38)$$

The same structure as shown in Fig. 1-9 can be depicted for the winding resistance estimator under the following assumptions:

$$W_i(k) = \hat{R}_s(k) \quad (1-39)$$

$$d(k) = v_q(k_1)i_q(k_1) + v_d(k_1)i_d(k_1) - v_{q0}(k_0)i_{q0}(k_0) \quad (1-40)$$

$$O(k) = \hat{R}_s(k) \left( i_q^2(k_1) + i_d^2(k_1) - i_{q0}^2(k_0) \right) \quad (1-41)$$

$$X_i = i_q^2(k_1) + i_d^2(k_1) - i_{q0}^2(k_0) \quad (1-42)$$

in which  $\hat{R}_s(k)$  is the predicted stator resistance. Therefore, the stator resistance Adaline estimator can be described as:

$$\begin{aligned} \hat{R}_s(k+1) = \hat{R}_s(k) \\ + 2\eta \left( i_q^2(k_1) + i_d^2(k_1) - i_{q0}^2(k_0) \right) \left( v_q(k_1)i_q(k_1) + v_d(k_1)i_d(k_1) \right. \\ \left. - v_{q0}(k_0)i_{q0}(k_0) - \hat{R}_s(k) \left( i_q^2(k_1) + i_d^2(k_1) - i_{q0}^2(k_0) \right) \right) \end{aligned} \quad (1-43)$$

Likewise, the subnet of the PM linkage estimator derived from (1-24) can be expressed as in Fig. 1-9 by assuming:

$$W_i(k) = \hat{\psi}_{m0}(k) \quad (1-44)$$

$$d(k) = v_{q0}(k_0) - \hat{R}_s(k)i_{q0}(k_0) \quad (1-45)$$

$$O(k) = \hat{v}_{q0}(k) - \hat{R}_s(k)i_{q0}(k_0) = \hat{\psi}_{m0}(k)\omega_r(k_0) \quad (1-46)$$

$$X_i = \omega_r(k_0) \quad (1-47)$$

where  $\hat{\psi}_{m0}(k)$  is the predicted PM flux linkage. The PM flux linkage estimator thus is written as:

$$\hat{\psi}_{m0}(k + 1) = \hat{\psi}_{m0}(k) + 2\eta\omega_r(k_0) (v_{q0}(k_0) - \hat{v}_{q0}(k)) \quad (1-48)$$

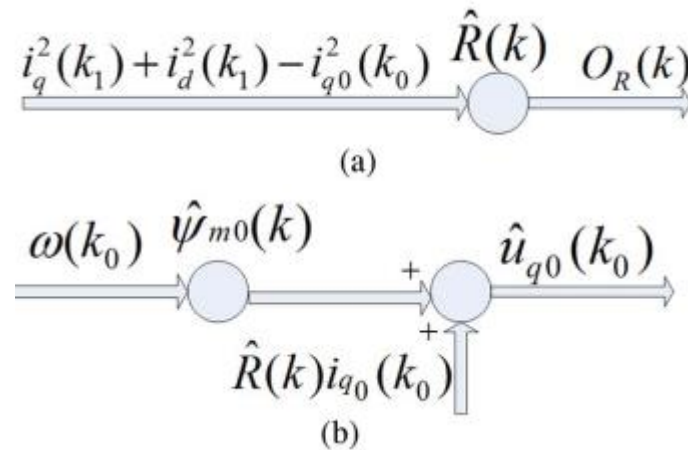


Fig. 1-10: (a) stator resistance estimator subnet and (b) PM flux linkage estimator subnet [26]

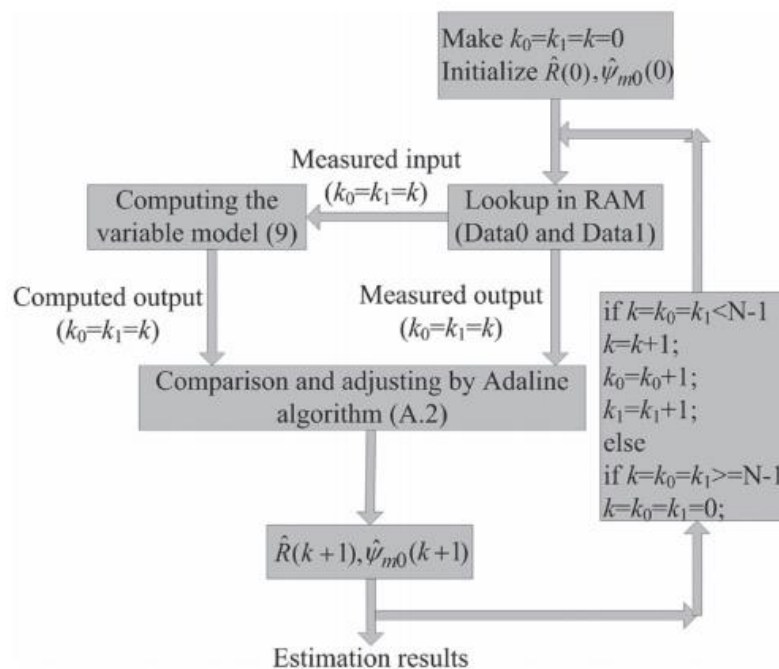


Fig. 1-11: Estimation process flow chart [26]

The estimation process is plotted in a flow chart shown in Fig. 1-11. The data acquisition takes place before the estimation, and a RAM is employed to collect two sets of data corresponding to  $i_d = 0$  and  $i_d \neq 0$ . The synchronization of  $k_0$  and  $k_1$  can be achieved by setting the initial time step to be zero, and ensuring the data sets being transmitted simultaneously to the estimation method for the iterative computation.

According to [28], PM flux linkage can also be estimated with a zero-voltage vector injection scheme, where an additional zero-voltage vector switching period is imposed between the PWM periods controlled by PI controllers, as demonstrated in Fig. 1-12.

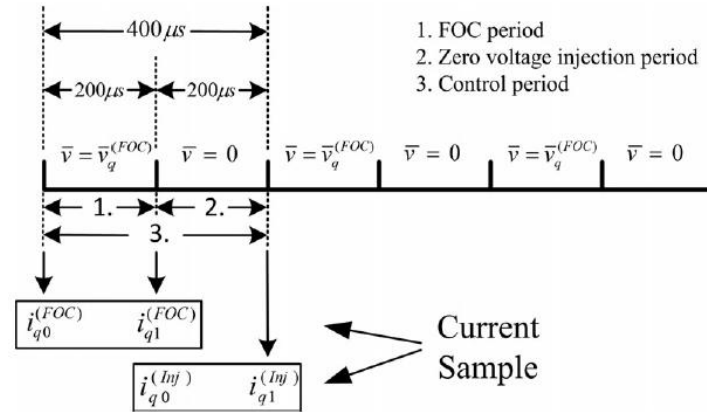


Fig. 1-12: Schematic of the zero-voltage vector injection method [28]

The  $q$ -axis voltage equations of a PMSM during the ‘FOC period’ and ‘zero-injection period’ shown in Fig. 1-12 are expressed as:

$$v_q^{(FOC)} = R_s i_{q0}^{(FOC)} + L_q \frac{d}{dt} i_q^{(FOC)} + \omega_r L_d i_{d0}^{(FOC)} + \omega_r \psi_m \quad (1-49)$$

$$0 = R_s i_{q0}^{(Inj)} + L_q \frac{d}{dt} i_q^{(Inj)} + \omega_r L_d i_{d0}^{(Inj)} + \omega_r \psi_m \quad (1-50)$$

With the motor operating at steady-state, the speed loop PI controller ensures the  $q$ -axis current command is constant. In response, the current loop PI controller regulates the  $q$ -axis current feedback ( $i_{q0}^{(FOC)}$ ) at the beginning of each PWM switching period such that they remain unchanged. This means the current variation during the FOC period is opposite to that during the adjacent zero-voltage injection period, as is seen in Fig. 1-13. In other words:

$$\frac{d}{dt} i_q^{(FOC)} = -\frac{d}{dt} i_q^{(Inj)} \quad (1-51)$$

Adding (1-49) to (1-50), and taking account of  $i_d = 0$  gives:

$$v_q^{(FOC)} = v_q^* + \Delta v = R_s \left( i_{q0}^{(FOC)} + i_{q0}^{(Inj)} \right) + 2\omega_r \psi_m \quad (1-52)$$

the voltage error  $\Delta v$  due to inverter dead-time effect can be minimized by applying (1-52) to two different speed conditions:

$$v_{q1}^* + \Delta v = R_s \left( i_{q01}^{(FOC)} + i_{q01}^{(Inj)} \right) + 2\omega_{r1}\psi_m \quad (1-53)$$

$$v_{q2}^* + \Delta v = R_s \left( i_{q02}^{(FOC)} + i_{q02}^{(Inj)} \right) + 2\omega_{r2}\psi_m \quad (1-54)$$

Assuming the  $q$ -axis current is independent of rotor speed at constant (no) load motor operation:

$$i_{q01}^{(FOC)} = i_{q02}^{(FOC)} \quad (1-55)$$

$$i_{q01}^{(Inj)} = i_{q02}^{(Inj)} \quad (1-56)$$

Subtracting (1-53) from (1-54) leads to:

$$v_{q2}^* - v_{q1}^* = 2(\omega_{r2} - \omega_{r1})\psi_m \quad (1-57)$$

Hence the PM flux linkage can be predicted with the measurements of the voltage command  $v_q^*$  and rotor speed  $\omega_r$ . The knowledge of the motor inductance and the compensation of the inverter-induced voltage errors are not required.

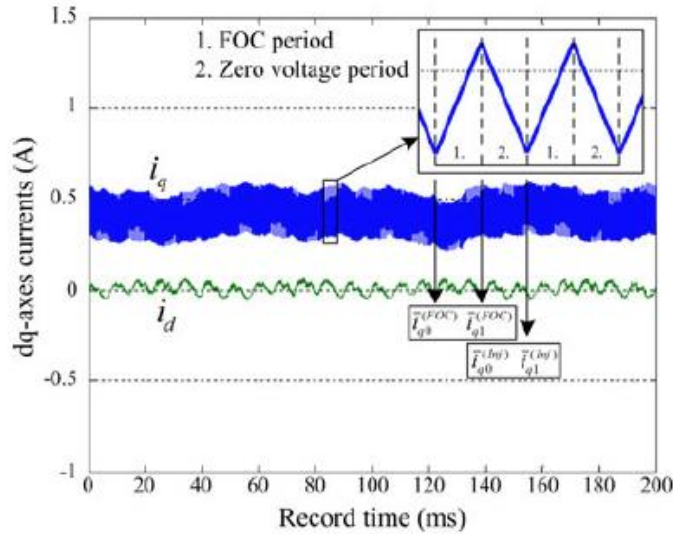


Fig. 1-13:  $q$ -axis current variation under the zero-voltage vector injection scheme [28]

Alternatively, PM flux linkage observer [8] can be used for the retrieval of rotor temperature. It does not require signal injection which could be invasive to a normally operated motor. The model of a PMSM expressed in  $dq$ -reference frame is given as:

$$v_{dq} = R_s(T_W)i_{dq} + \dot{\psi}_{dq} + J\omega_r\psi_{dq}(T_{PM}) \quad (1-58)$$

and:

$$\psi_{dq} = \begin{pmatrix} \psi_m(T_{PM}) + L_d i_d \\ L_q i_q \end{pmatrix} \quad (1-59)$$

$$J = \begin{pmatrix} 0 & -1 \\ 1 & 0 \end{pmatrix} \quad (1-60)$$

The nonlinear relationship between the stator current and flux linkage as a result of the saturation effect is considered and represented by the function  $f$ , which is formulated with look-up tables (LUT) where the data is measured at the motor reference temperature. The estimated stator currents therefore can be written as:

$$\hat{i}_{dq} = f \left( \int v_{dq} - R_s(T_W) \hat{i}_{dq} - J \omega_r (\psi_{dq}(T_{PM}) + \Delta \psi_{dq}) \right) \quad (1-61)$$

The estimation error  $\Delta \psi_{dq}$  tunes the observer:

$$\Delta \psi_{dq} = k_v \int \Delta i_{dq} \quad (1-62)$$

Assuming the rotor temperature variation only reflects on  $\Delta \psi_d$ :

$$T_{PM} = T_{0,PM} + \frac{\Delta \psi_d}{\psi_m(T_{0,PM}) \alpha_{Br}} \quad (1-63)$$

The schematic of the flux linkage observer is shown in Fig. 1-14.

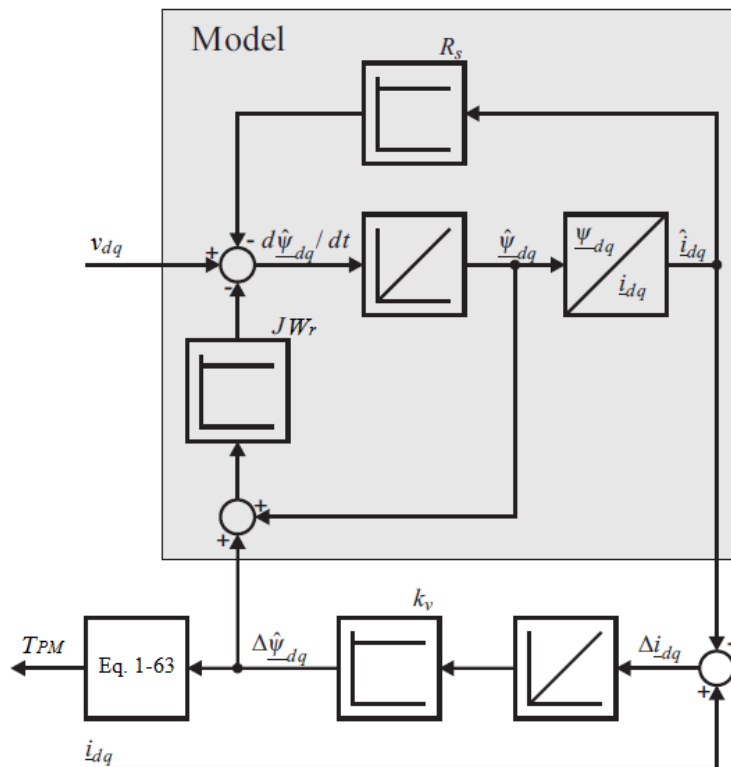


Fig. 1-14: Flux linkage observer structure [8]

Due to the small temperature-dependent coefficient, a discretization approach with high precision is required. Ref. [29] and [30] discover that discretizing the motor model in stationary  $\alpha\beta$ -reference frame prior to the  $\alpha\beta$ - $dq$  transformation leads to considerably improved estimation results, compared to discretizing the model in  $dq$ -reference frame directly. The observer in Fig. 1-14 has two inputs: stator current and PWM voltage. Stator current can be accurately measured by current sensor. However the measurement of stator terminal voltage is uncommon in most industrial applications. Even though the information of voltage command is available, the estimation may still be subject to inverter nonlinearity, for instance. In [30], an inverter model is proposed which takes into consideration the main sources of the deviation between PWM voltage and voltage command, such as dead-time effect. The temperature estimation results after replacing the voltage measurement with this advanced voltage model are relatively accurate.

This section introduces five methods for the estimations of motor temperature and temperature-dependent electrical parameters. In [18], rotor temperature is predicted using the fact that the resistance resulting from a pulsating high-frequency signal injected into the  $d$ -axis of a PMSM varies with the rotor temperature. Ref. [25] retrieves rotor temperature information from the slope of the  $d$ -axis current response to a voltage pulse injection into the  $d$ -axis of a motor, which reflects the magnetization level of the PM. An online method is proposed in [26], where the PM flux linkage and stator resistance are estimated using a full-rank motor model corresponding to  $i_d = 0$  and an injected  $i_d \neq 0$  test signal. According to [28], PM flux linkage can be determined with only the voltage commands of the standard FOC at two rotor speeds after the injection of a zero-voltage vector between the two adjacent active vectors. Signal-injection-based approaches are in general more accurate and robust and do not require additional sensors or cabling. However they produce undesired ripples and losses disturbing motor operation. Observer-based method [8] is a desirable alternative. Nevertheless, the machine and inverter parameters need to be accurately identified in order to avoid flux linkage observation errors. These references offer a promising method for the prediction of rotor temperature using the thermal properties of motor parameters, such as PM flux linkage, which will be further developed in chapter 3.

### 1.2.3 Temperature Estimation Methods Based on Thermal Modelling

As mentioned earlier, despite being able to produce reliable estimation result, the methods for retrieving motor temperatures from temperature-dependent electrical variables are imperfect due to the requirement of high modelling precision. Besides, the use of signal injection technique, which has an interfering character, increases the risk of machine malfunction. A more preferable alternative is a lumped parameter thermal network, in which the heat exchange in a motor is abstracted and can be described by a circuit diagram similar to an electric circuit. Table I encapsulates the analogy between them:

Table I: Analogy between electric circuit and LPTN

Electrical Quantities	Thermal Quantities
Voltage ( $V$ )	Temperature Difference ( $^{\circ}\text{C}$ )
Current ( $A$ )	Heat Dissipation ( $W$ )
Electrical Resistance ( $\Omega$ )	Thermal Resistance ( $^{\circ}\text{C}/W$ )
Electrical Capacitance ( $F$ )	Thermal Capacitance ( $J/^{\circ}\text{C}$ )

In general, LPTNs can be classified according to their complexity [59]. The thermal networks with a high number of temperature nodes are modelled solely, or mainly based on the material and geometrical information of the machine, which is not directly accessible in practice. Furthermore, an accurate prediction of motor losses, and the analytical derivations of thermal parameters, which may require the knowledge of the heat transfer coefficients obtained from empirical equations, are rather complicated. On the other hand, reduced-order LPTNs only consider the most significant heat paths in the motor, and therefore can be modelled with less physical knowledge of the motor. In this case, most thermal parameters are computed in a measurement-based identification process, and accurate estimations of the critical temperatures in the motor can be obtained, as the results shown in [56], [59]-[60] suggest.

The accuracy of the loss model for a LPTN determines that of the temperature estimation. A loss model includes loss coefficients, which cannot be derived correctly without precise information of the overall losses of the motor. Therefore, a review of the most commonly employed methods for the calculation of motor losses will be presented first in the following section, followed by a comprehensive evaluation of the existing thermal models with different modelling depth.

### 1.2.3.1 Loss Prediction

The heat losses generated in an electric motor can be defined as:

$$P_{Total} = P_{Cu} + P_{Fe} + P_{resid} \quad (1-64)$$

The resistive loss is produced by the motor winding (end-winding) and can be calculated as:

$$P_{Cu} = \sum R_{si}(T_W)I_i^2 \quad (1-65)$$

where  $i = 1, 2, 3$ . The temperature dependence of the winding temperature  $T_W$  must be considered in order to prevent the winding loss being underestimated.

Iron loss occurs in armature iron core, due to the current induced by a sinusoidally varying magnetic field [82]-[91]. The total core power loss per unit weight  $p_c$  is commonly expressed by the empirical Steinmetz's equation:

$$p_c = p_h + p_e = k_h \omega_r B_m^a + k_e \omega_r^2 B_m^2 \quad (1-66)$$

All the parameters are dependent on motor lamination material and can be determined by manufacturers' loss curves.

However, the iron loss expression (1-66) assumes perfect sinusoidal variation of magnetic field, which is not realistic for most PM motors. In [82], two correction terms  $k_{ch}$  and  $k_{ce}$  taking into account the effects of minor hysteresis loop and harmonics on hysteresis and eddy-current losses are introduced:

$$k_{ch} = 1 + \frac{c}{B_e} \sum_{i=1}^N \Delta B_i \quad (1-67)$$

$$k_{ce} = \left(\frac{B_1}{B_e}\right)^2 \sum_{i=1}^N \left(\frac{iB_i}{B_1}\right)^2 \quad (1-68)$$

in which  $c$  is a constant with the value between 0.6 and 0.7.  $B_i$  is the  $i^{th}$  harmonic component of flux density  $B_e$ , whose fundamental component is donated as  $B_1$ . Therefore, equation (1-66) after the modification becomes:

$$p_c = k_{ch} k_h \omega_r B_m^n + k_{ce} k_e \omega_r^2 B_m^2 \quad (1-69)$$

Calculating hysteresis loss is relatively simple as  $p_h$  only depends on the peak of the fundamental component of flux density, as long as minor hysteresis loops are not considered, which is acceptable in some applications. However, the accuracy of eddy-current loss may be

affected significantly by the disregard of the harmonic components of magnetic field. Ref. [83]-[84] presents an alternative formula, in which eddy-current loss density is calculated using the derivative term  $dB_e/dt$ . Assuming:

$$B_e = B_m \sin(\omega_r t) \quad (1-70)$$

therefore:

$$\frac{dB_e}{dt} = \omega_r B_m \cos(\omega_r t) \quad (1-71)$$

$$\left(\frac{dB_e}{dt}\right)_{avg}^2 = \left(\frac{\omega_r B_m}{\sqrt{2}}\right)^2 = \frac{(\omega_r B_m)^2}{2} \quad (1-72)$$

Substituting (1-72) into (1-66):

$$p_e = 2k_e \left(\frac{dB_e}{dt}\right)_{avg}^2 \quad (1-73)$$

Due to the use of this particular expression, the harmonic effect on eddy-current loss is inherently included. Nevertheless, as (1-72) indicates, this method only provides reasonably accurate average loss predictions over one electrical cycle, suggesting errors may occur in the calculation of instantaneous loss.

Based on (1-73), an analytical model for iron loss estimation is proposed in [85], in which motor flux is decomposed into a radial and a circumferential components. Eddy-current loss as a result relies on the variations in these two orthogonal flux densities. The effect of motor geometry is also taken into consideration, by introducing a correction factor which is the difference between the losses estimated using the approximation model and Finite Element method (FEM). This method is of good value particularly because of its simplicity.

According to [86], eddy-current loss can be related to a fictitious voltage signal. The eddy-current loss per weight unit of one stator tooth considering fundamental and harmonic magnetic flux excitations is given as:

$$p_c(\text{tooth}) = k_e(\omega_1^2 B_{m1}^2 + \omega_2^2 B_{m2}^2 + \omega_3^2 B_{m3}^2 + \dots) \quad (1-74)$$

in which  $B_{m1}, B_{m2}, \dots$  are the peaks of flux density harmonics per tooth. Multiplied and divided by the square of one tooth section area  $A_T$ , equation (1-74) becomes:

$$p_c(\text{tooth}) = k_e[(\omega_1 \psi_{m1})^2 + (\omega_2 \psi_{m2})^2 + \dots] / A_T^2 \quad (1-75)$$

where  $\psi_{m1}, \psi_{m2}, \dots$  are the amplitudes of magnetic flux linkage harmonics per tooth. Therefore  $(\omega_1\psi_{m1}), (\omega_2\psi_{m2}), \dots$  can be interpreted as the amplitudes of the harmonic components of an imaginary voltage  $v(\text{tooth})$  induced in a single-turn stator winding coil wound around a stator tooth, and the sum  $[(\omega_1\psi_{m1})^2 + (\omega_2\psi_{m2})^2 + \dots]$  equals to twice the square of the RMS value of the voltage  $V(\text{tooth})_{RMS}$ . The analysis shown in [87]-[88] verifies that the eddy-current loss induced in stator yoke can also be evaluated via  $v(\text{tooth})$  — the overall stator eddy-current loss therefore can be determined. Furthermore, this approach is suitable under no-load condition, where the voltage  $v(\text{tooth})$  is the back-EMF per tooth  $e(\text{tooth})$ , whereas under loaded condition, the voltage component  $v_{load}(\text{tooth})$  generated from current-induced flux should also be considered:

$$v(\text{tooth}) = e(\text{tooth}) + v_{load}(\text{tooth}) \quad (1-76)$$

An extended version of the Steinmetz's equation including an additional term of excess loss is proposed most recently by Bertotti [89]:

$$p_c = p_h + p_e + p_{exc} = k_h \omega_r B_m^n + k_e \omega_r^2 B_m^2 + k_{exc} \omega_r^{1.5} B_m^{1.5} \quad (1-77)$$

The excess loss constant  $k_{exc}$  can be retrieved from an experimentally-verified iron loss measured at a particular frequency and sinusoidal flux density amplitude. To be specific:

$$k_{exc} = \frac{p_c - p_h - p_e}{\omega_r^{1.5} B_m^{1.5}} \quad (1-78)$$

Ref. [82] modifies (1-77) to a practical form given as:

$$p_c = k_{ch} k_h \omega_r B_m^n + 2k_e \left( \frac{dB_e}{dt} \right)_{avg}^2 + 2^{0.75} k_{exc} \left( \frac{dB_e}{dt} \right)_{avg}^{1.5} \quad (1-79)$$

It is clear that the hysteresis minor loop effect is accounted for by the introduction of the correction factor  $k_{ch}$ . Eddy-current and excess losses are computed using the average loss density in an electrical revolution (i.e.  $t = 2\pi$ ), which compensates the losses of the harmonic components of motor magnetic flux.

Using (1-77), the core loss of a motor can be correctly estimated with the precisely calculated parameters  $k_h, k_e, k_{exc}$ , and  $a$ . A model-fitting procedure is described in [90], where these coefficients can be identified based on the minimization of the error between loss measurements and losses predicted by the proposed model over a wide scale of frequencies and flux densities. The results show that the hysteresis loss coefficients  $k_h$  and  $a$  vary with both frequency and flux density, whilst the eddy-current and excess loss coefficients  $k_e$  and

$k_{exc}$  are only dependent on flux density. This results in lower error in loss estimation, compared to adopting the conventional models in which these parameters are assumed to be constant.

In [91], the calculation of iron loss is based on the assumption that the total loss is the superposition of two motor operating modes associated with two distinct flux paths — the main magnetizing flux path flowing through stator back iron and stator teeth and coupling stator winding coils, and the field weakening path in which PM flux flows across the tooth tip region. The iron losses corresponding to these two flux paths are linked to the terminal voltage  $V_m$  after the subtraction of the voltage drop across the stator resistance, and the equivalent voltage  $V_d^*$  of demagnetization field and are described as:

$$P_1 = g_1(V_m) \quad (1-80)$$

$$P_2 = g_2(V_d^*) \quad (1-81)$$

The two functions are determined using the Finite Element Analysis (FEA) with motor operating at open-circuit (deriving  $g_1$ ) and short-circuit (deriving  $g_2$ ) conditions. As a result, stator iron loss is obtained as:

$$P_{OC} = P_h^{OC} + P_e^{OC} + P_{exc}^{OC} = a_h f_r + a_e f_r^2 + a_{exc} f_r^{1.5} \quad (1-82)$$

$$P_{SC} = P_h^{SC} + P_e^{SC} + P_{exc}^{SC} = b_h f_r + b_e f_r^2 + b_{exc} f_r^{1.5} \quad (1-83)$$

In (1-82) and (1-83), the iron losses are separated into the hysteresis, eddy-current and excess components. It is noted that friction and windage losses are not considered. The parameters can be calculated at a constant frequency  $f_r$  which is randomly chosen:

$$a_h = \frac{P_h^{OC}}{f_r} \quad (1-84)$$

$$b_h = \frac{P_h^{SC}}{f_r} \quad (1-85)$$

$$a_e = \frac{P_e^{OC}}{f_r^2} \quad (1-86)$$

$$b_e = \frac{P_e^{SC}}{f_r^2} \quad (1-87)$$

$$a_{exc} = \frac{P_{exc}^{OC}}{f_r^{1.5}} \quad (1-88)$$

$$b_{exc} = \frac{P_{exc}^{SC}}{f_r^{1.5}} \quad (1-89)$$

The frequency term in (1-82) and (1-83) can be used to retrieve the motor EMF constant:

$$\lambda_{emf} = \frac{V_{emf}}{f_r} \quad (1-90)$$

where  $V_{emf}$  is calculated by performing open-circuit FEA. Now replacing  $f_r$  in (1-82) and (1-83) with  $\lambda_{emf}$ , the loss functions (1-80) and (1-81) become:

$$P_1 = g_1(V_m) = \frac{a_h}{\lambda_{emf}} V_m + \frac{a_e}{\lambda_{emf}^2} V_m^2 + \frac{a_{exc}}{\lambda_{emf}^{1.5}} V_m^{1.5} \quad (1-91)$$

$$P_2 = g_2(V_d^*) = \frac{b_h}{\lambda_{emf}} V_d^* + \frac{b_e}{\lambda_{emf}^2} V_d^{*2} + \frac{b_{exc}}{\lambda_{emf}^{1.5}} V_d^{*1.5} \quad (1-92)$$

### 1.2.3.2 High-Order Thermal Model

A plethora of the publications in regard to the thermal modelling of electric motors exists in literature. Most of the proposed LPTNs are analytically modelled based on heat transfer theory and require detailed dimensional and material information of motors. However, a thermal network with high complexity ensures a high resolution of temperature distribution, which is vitally important in applications where the motors have particularly complex construction and cooling [45].

A high-fidelity, computationally-efficient electro-thermally coupled model is introduced in [6], which integrates a temperature-dependent electromagnetic model taking into account the magnetic saturation, spatial harmonics and iron loss effects, with a LPTN derived from the FE software containing numerous temperature nodes. A flux-linkage-based model for a PMSM is adopted, in which the stator current nonlinearly relates to the flux linkage:

$$v_d = \frac{d\psi_d}{dt} + R_s i_d - \omega_r \psi_q \quad (1-93)$$

$$v_q = \frac{d\psi_q}{dt} + R_s i_q + \omega_r \psi_d \quad (1-94)$$

$$\psi_d = f(i_d, i_q, \theta) \quad (1-95)$$

$$\psi_q = g(i_d, i_q, \theta) \quad (1-96)$$

$$T_{em} = \frac{3}{2} \left( \frac{p}{2} \right) (\psi_d i_q - \psi_q i_d) \quad (1-97)$$

in which two nonlinear functions  $f$  and  $g$  extracted from the FEA describe the relationship between the flux linkage and stator current. Therefore, the saturation and harmonic effects can be intrinsically included in the model. Also, instead of performing the derivative calculations in (1-93) and (1-94),  $\psi_d$  and  $\psi_q$  are obtained by the following integrations:

$$\psi_d = \int (V_d - R_s i_d + \omega_r \psi_q) dt \quad (1-98)$$

$$\psi_q = \int (V_q - R_s i_q - \omega_r \psi_d) dt \quad (1-99)$$

The inverse of (1-95) and (1-96) leads to:

$$i_d = f^{-1}(\psi_d, \psi_q, \theta) \quad (1-100)$$

$$i_q = g^{-1}(\psi_d, \psi_q, \theta) \quad (1-101)$$

It is noted that (1-97) does not account for the cogging torque, which is non-zero even with zero current. Thus the electromagnetic torque is assumed to be a function of the current and angle:

$$T_{em} = T(i_d, i_q, \theta) \quad (1-102)$$

The iron loss in a machine operating as a motor decreases its active power, and therefore changes the effective stator current with a constant voltage supply. The iron loss is computed in a computationally-efficient manner by (1-91) and (1-92) and is split into the  $d$ -axis and  $q$ -axis components expressed as:

$$P_{fe\_d} = \frac{\psi_q^2}{\psi_d^2 + \psi_q^2} P_1 + P_2 \quad (1-103)$$

$$P_{fe\_q} = \frac{\psi_d^2}{\psi_d^2 + \psi_q^2} P_1 \quad (1-104)$$

The iron loss effect can be viewed as the equivalent currents  $i_{dFe}$  and  $i_{qFe}$  which result in the equivalent resistors  $R_{Fe\_d}$  and  $R_{Fe\_q}$  across the  $d$ -axis and  $q$ -axis induced voltages generating losses, as illustrated in Fig. 1-15. Hence the impact of the iron loss on the stator current is given in the form:

$$i_d = i_{da} + i_{dFe} = i_{da} + \frac{P_{fe\_d}}{v_d - R_s i_d} \quad (1-105)$$

$$i_q = i_{qa} + i_{qFe} = i_{qa} + \frac{P_{fe\_q}}{v_q - R_s i_q} \quad (1-106)$$

Fig. 1-16 shows the diagram of the machine model considering the aforementioned effects.

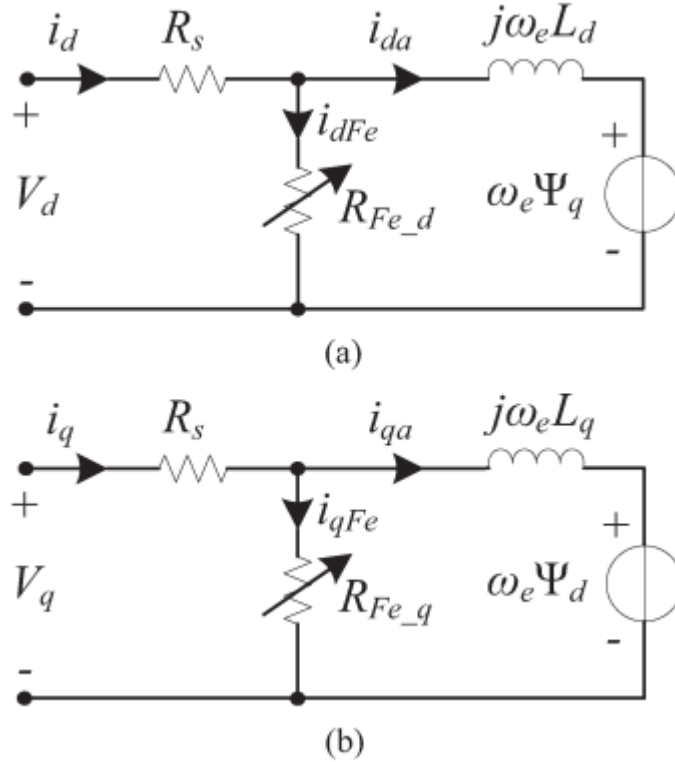


Fig. 1-15:  $dq$ -axis circuits considering the iron loss effect [54]

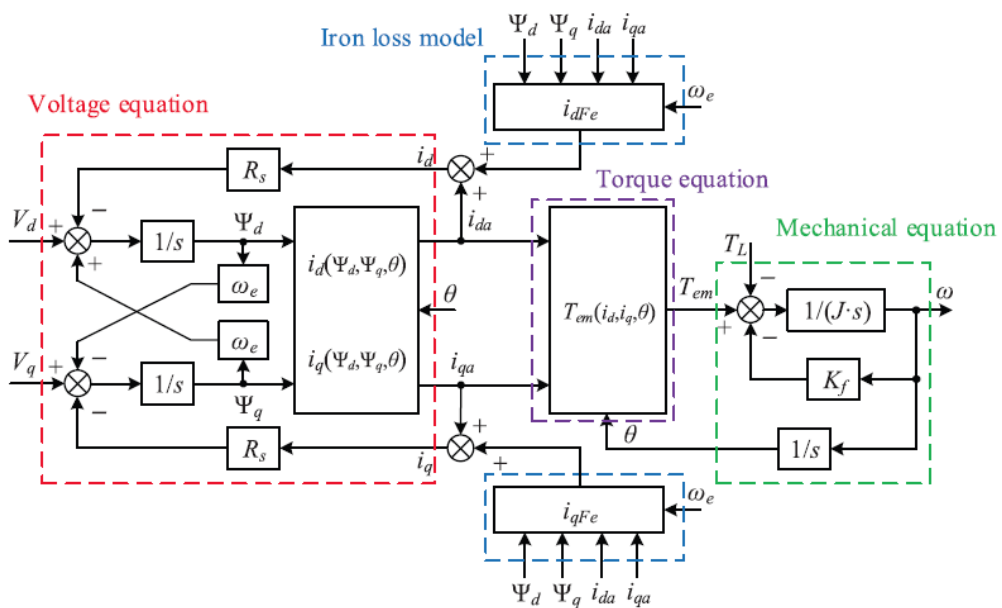


Fig. 1-16: Schematic of the proposed computationally efficient motor model [54]

The change in the winding temperature affects the stator resistance, which can be described by a linear function. The PM temperature influences the magnet remanence, which reflects on the variations in both  $d$ -axis and  $q$ -axis flux linkages as a result of the saturation-induced cross-coupling, and this influence is dependent on current and rotor position, according to [6]. Therefore, the temperature effect on the motor model proposed in the previous section is considered, and accordingly, the three 4-D functions  $i_d(\psi_d, \psi_q, \theta, T_{PM})$ ,  $i_q(\psi_d, \psi_q, \theta, T_{PM})$  and  $T_{em}(i_d, i_q, \theta, T_{PM})$  should be substituted for the 3-D functions (1-97), (1-98) and (1-99). However, a simplified method based on the Taylor's expansion is adopted in order to reduce the model order, and  $i_d$ ,  $i_q$  and  $T_{em}$  can be estimated by:

$$i_d(\psi_d, \psi_q, \theta, T_{PM}) = i_d(\psi_d, \psi_q, \theta, T_0) + \Delta i_d(\psi_d, \psi_q, \theta)(T_{PM} - T_0) \quad (1-107)$$

$$i_q(\psi_d, \psi_q, \theta, T_{PM}) = i_q(\psi_d, \psi_q, \theta, T_0) + \Delta i_q(\psi_d, \psi_q, \theta)(T_{PM} - T_0) \quad (1-108)$$

$$T_{em}(i_d, i_q, \theta, T_{PM}) = T_{em}(i_d, i_q, \theta, T_0) + \Delta T_{em}(i_d, i_q, \theta)(T_{PM} - T_0) \quad (1-109)$$

The terms  $\Delta i_d(\psi_d, \psi_q, \theta)$ ,  $\Delta i_q(\psi_d, \psi_q, \theta)$ , and  $\Delta T_{em}(i_d, i_q, \theta)$  are the first-order slopes of  $i_d$ ,  $i_q$  and  $T_{em}$ , respectively and can be derived from calculating the deviations in  $i_d(\psi_d, \psi_q, \theta)$ ,  $i_q(\psi_d, \psi_q, \theta)$ , and  $T_{em}(i_d, i_q, \theta)$  at two arbitrary rotor temperatures. The iron loss model also varies with the rotor temperature, because the equivalence resistors in Fig. 1-15 are temperature-dependent due to their relations to flux linkage. The proposed model including the temperature effect is shown in Fig. 1-17.

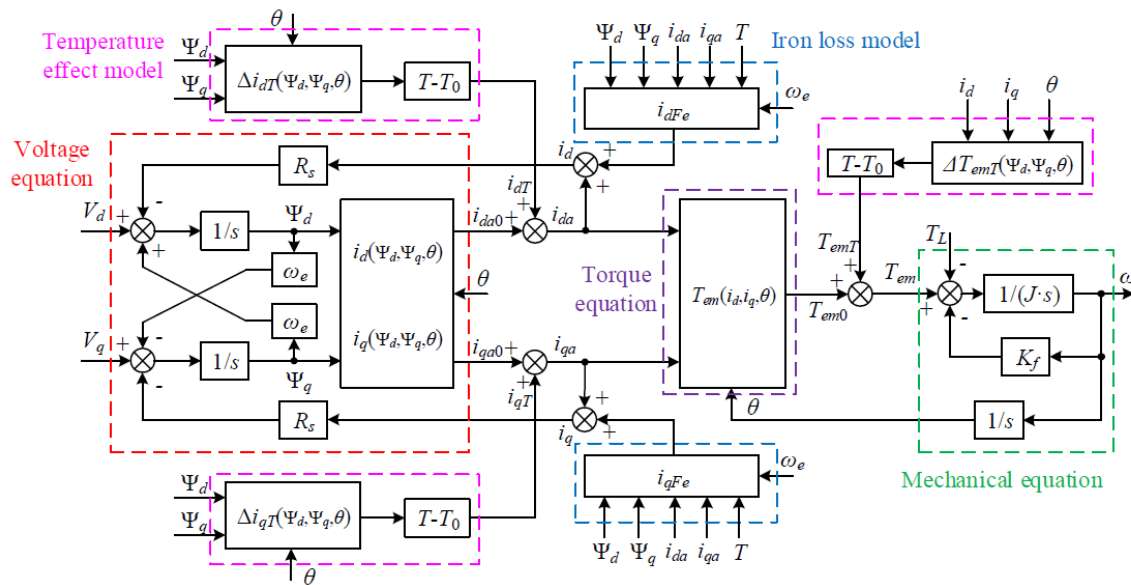


Fig. 1-17: Schematic of the proposed machine model taking into account the temperature effect [6]

As can be seen in Fig. 1-18, the motor model is paired with a thermal model to establish an electro-thermal system able to monitor the motor temperatures with high fidelity. The copper loss and iron loss are computed by the electromagnetic model shown in Fig. 1-17, and passed on to the thermal model represented by state-space equations. The estimated winding and rotor temperatures are then communicated to the machine model where the temperature effect is taken into consideration.

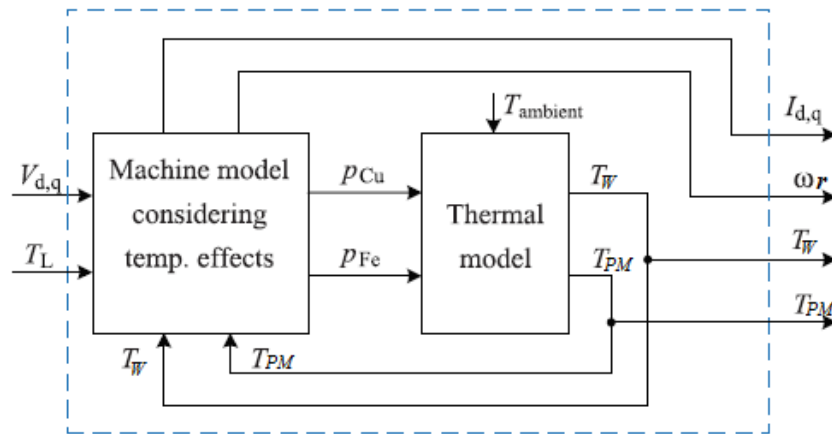


Fig. 1-18: Schematic of the electro-thermal system [6]

The thermal model is based on the detailed LPTN developed in the FE software Motor-CAD and contains 48 nodes including the housing, stator tooth, stator back iron, winding, magnet, rotor back iron, shaft, bearing, and etc. As a result, the overall losses consist of 48 components forming a loss vector. The copper loss is allocated into the winding and end-winding nodes depending on their physical lengths, whereas the iron loss is distributed into the stator back iron, stator tooth, magnet pole and rotor back iron nodes. The magnet loss is also included. The state-space thermal model calculates and outputs the temperature variations of the 48 nodes, which are added to the ambient temperature in order to acquire the node temperatures. In addition, the cooling effect is considered by assuming a varying thermal resistance between the housing and ambient. Fig. 1-19 shows the structure of the LPTN.

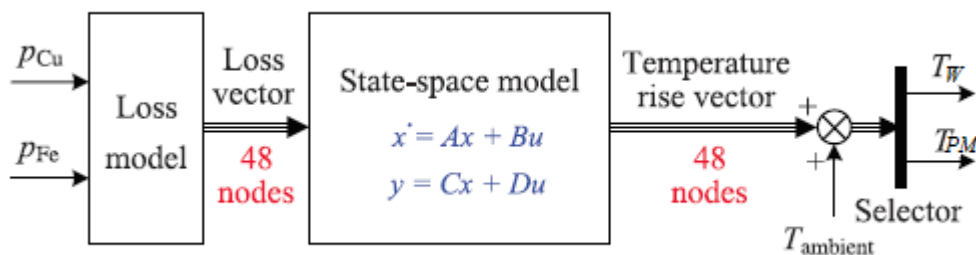


Fig. 1-19: Structure of the proposed LPTN [6]

### 1.2.3.3 Low-order Thermal Model

In contrast, the critical temperatures in a motor can be predicted with high precision using thermal models with lower orders. Despite only considering the averaged motor region temperatures due to the strongly abstracted network, this type of thermal model simplifies the motor parameterization, which can be performed based on the use of a set of experimental training data. It can be applied in different motor operating conditions and its utilization is not limited to certain PMSM designs, showing a great level of robustness.

One such example is introduced in [59]-[60], where the critical temperatures of an automotive traction PMSM are estimated through a four-node LPTN representing the stator back iron ( $T_{Fes}$ ), stator winding ( $T_W$ ), stator teeth ( $T_{ST}$ ), and PM ( $T_{PM}$ ). Fig. 1-20 shows the circuit diagram of the presented LPTN.

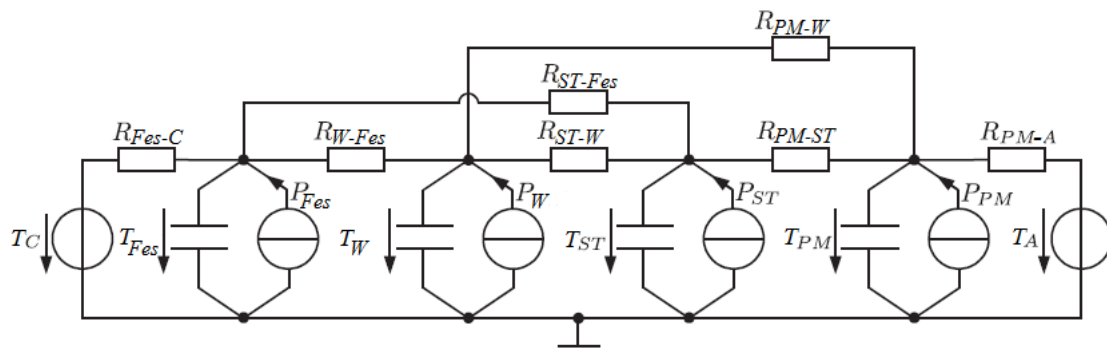


Fig. 1-20: Structure of the four-node LPTN [60]

Each temperature node is connected to a thermal ground through a thermal capacitance which models the thermal dynamics. The cooling liquid and ambient temperatures  $T_C$  and  $T_A$  are the temperature sources measured with sensors. Seven thermal resistances taking into account thermal conduction and convection effects are denoted as  $R_{i-j}$  meaning the heat flows from node  $i$  into node  $j$ . The losses produced by different temperature regions  $P$  are also included as heat sources.

A measurement-based approach for the loss modelling replaces the conventional FEA simulation which requires enormous effort in loss calculation mainly due to the consideration of the switching inverter characteristics and current control behaviour [92]. The total losses  $P(\omega_r, I)$  of the motor are measured at a reference temperature and data saved in a LUT. Assuming the stator winding loss equals to the copper loss calculated with the stator current and resistance:

$$P_{Cu} = P_W = 3I^2R_s(T_W, \omega_r) \quad (1-110)$$

$$R_s(T_W, \omega_r) = R_s(T_{0,W})f_1(T_W)f_2(\omega_r) \quad (1-111)$$

$$f_1(T_W) = 1 + \alpha_{Cu}(T_W - T_{0,W}) \quad (1-112)$$

$$f_2(\omega_r) = 1 + \beta_{Cu,1}\left(\frac{\omega_r}{\omega_{r,max}}\right) + \beta_{Cu,2}\left(\frac{\omega_r}{\omega_{r,max}}\right)^2 \quad (1-113)$$

The stator resistance  $R_s$  is considered temperature-dependent and speed-dependent due to the skin effect and proximity effect. In order to reduce the amount of unknown parameters, only  $\beta_{Cu,1}$  and  $\beta_{Cu,2}$  are estimated in the parameter identification process, whilst  $R_s(T_0)$  is obtained from the manufacture datasheet and  $\alpha_{Cu}$  assumed to be 0.39%/°C.

The iron loss is regarded as the difference between the copper loss and total losses:

$$P_{Fe} = P(\omega_r, I) - P_{Cu}(\omega_r, I, T_{0,W}) \quad (1-114)$$

The loss  $P_{Fe}$  is then separated into the rest of the nodes via:

$$P_{stator} = k_1(\omega_r, I)P_{Fe} \quad (1-115)$$

$$P_{rotor} = P_{PM} = [1 - k_1(\omega_r, I)]P_{Fe} \quad (1-116)$$

$$P_{Fes} = k_2(\omega_r, I)P_{stator} \quad (1-117)$$

$$P_{ST} = [1 - k_2(\omega_r, I)]P_{stator} \quad (1-118)$$

$P_{Fe}$  is split into a rotor and a stator portions using a first-order polynomial function  $k_1(\omega_r, I)$  written as:

$$k_1(\omega_r, I) = k_{1,0} + k_{1,1}\omega_r + k_{1,2}I + k_{1,3}\omega_r I \quad (1-119)$$

where  $0 \leq k_1 \leq 1$ . This assumption is based on the fact that iron loss is dependent on motor frequency and flux density associated with current amplitude and its harmonics. The stator iron loss is assigned into the stator iron and stator teeth nodes through  $k_2(\omega_r, I)$ , which is similarly formulated:

$$k_2(\omega_r, I) = k_{2,0} + k_{2,1}\omega_r + k_{2,2}I + k_{2,3}\omega_r I \quad (1-120)$$

with  $0 \leq k_2 \leq 1$ . The coefficients  $k_{1,j}$  and  $k_{2,j}$  ( $j = 0,1,2$ ) need to be identified.

The temperature effect on the iron loss is also included and expressed as:

$$P_{PM}(T_{PM}) = P_{PM}[1 + \alpha_{Fes}(T_{PM} - T_{0,PM})] \quad (1-121)$$

$$P_{Fes}(T_{Fes}) = P_{Fes}[1 + \alpha_{Fes}(T_{Fes} - T_{0,Fes})] \quad (1-122)$$

$$P_{ST}(T_{ST}) = P_{ST}[1 + \alpha_{Fes}(T_{ST} - T_{0,ST})] \quad (1-123)$$

The temperature coefficient  $\alpha_{Fes}$  has a negative value because the increase in temperature leads to the decrease in iron loss. Due to its dependency on material and motor design,  $\alpha_{Fes}$  is difficult to calculate. Instead, it is predicted during the parameter identification.

In addition, the identification of the thermal capacitances and resistances are required as a result of the lack of information regarding the motor dimensions. However they are roughly pre-computed using the empirical formulas in order to limit the search room. With respect to the thermal resistances, it is assumed that  $R_{W-Fes}$ ,  $R_{ST-W}$ , and  $R_{ST-Fes}$  which describe the heat transmission due to conduction, are constant. The resistance  $R_{Fes-C}$  represents the heat convection from the stator back iron to the cooling system, as well as the heat conduction between the stator iron and housing. Therefore, it is defined as the sum of a constant and temperature-varying resistances:

$$R_{Fes-C}(T_C) = R_{Fes-C}(T_{0,C})[1 + \alpha_{Fes-C}(T_C - T_{0,C})] \quad (1-124)$$

in which  $\alpha_{Fes-C}$  is determined in the identification procedure. The convection effect is influenced by the kinematic viscosity of the water, which decreases with the rising cooling system temperature. This means  $\alpha_{Fes-C}$  is negative. The resistances  $R_{PM-W}$ ,  $R_{PM-ST}$  model the heat flow through the air gap, whereas  $R_{PM-A}$  takes into account the thermal connection between the rotor shaft and the ambient. A speed-dependent expression is derived for these three parameters based on the analytical formulas presented in [51] and [93]:

$$R_{i-j}(\omega_r) = R_{i-j}(T_0)e^{-\frac{\omega_r}{\omega_r,max} \frac{1}{b_{i-j}}} + a_{i-j} \quad (1-125)$$

with:

$$0 \leq R_{i-j}(T_0) \leq R_{i-j,max}(T_0) \quad (1-126)$$

$$0 \leq a_{i-j} \leq a_{i-j,max} \quad (1-127)$$

$$0 \leq b_{i-j} \leq b_{i-j,max} \quad (1-128)$$

Where  $R_{i-j,max}(T_0)$ ,  $a_{i-j,max}$ , and  $b_{i-j,max}$  are calculated using the analytical equations, and  $R_{i-j}(T_0)$ ,  $a_{i-j}$ , and  $b_{i-j}$  are identified along with the other unknown parameters/coefficients.

The LPTN is described in the state-space form:

$$\dot{x} = A(\omega_r)x + B(T, \omega_r, I)u(\omega_r, I) \quad (1-129)$$

$$y = Cx + Du \quad (1-130)$$

with:

$$x = [T_{Fes} \quad T_W \quad T_{ST} \quad T_{PM}] \quad (1-131)$$

$$u = [P_{Cu} \quad P_{Fe} \quad T_C \quad T_A] \quad (1-132)$$

$$A = \mathbb{R}^{4 \times 4}, B = \mathbb{R}^{4 \times 4}, C = I^{4 \times 4}, D = 0 \quad (1-133)$$

where the node temperatures are assumed to be the state variables, and the system inputs are the loss components and measurements of the cooling liquid and ambient temperatures. The system (state-transition) and control-input models  $A$  and  $B$  are two matrices with four rows and four columns, which are dependent on motor speed, stator current and state estimate (temperature).  $C$  and  $D$  are identity and zero matrices, such that  $y$  outputs the predicted states. For the forthcoming parameter identification and validation, the thermal model is discretized using the explicit Euler method (RK1), which is less computationally demanding compared to the standard discretization method. The discrete-time model is thereby given as:

$$\frac{1}{T_k}(x[k+1] - x[k]) = A[k]x[k] + B[k]u[k] \quad (1-134)$$

The identification problem can be interpreted as the search for the parameters that minimise the output error  $e = \vartheta - \tilde{\vartheta}$ . A cost function normally is required which leads to a highly accurate model. Regarding the presented thermal network with multiple inputs and outputs, the function that meets this requirement is the covariance of the output error. Therefore the optimization task can be summarized as:

$$\hat{p} = \min_p cov(e), \quad s. t. \quad g(p) \leq 0, h(p) = 0 \quad (1-135)$$

where  $g$  and  $h$  are the boundary conditions.

A global optimization algorithm is innovatively applied to identify the parameters, combining a particle swarm algorithm (PSO) with the sequential quadratic programming (SQP). The first step is for the PSO to identify several potential parameter sets. In the second step, the ‘inertia weight’ method conducts an additional exploration within the entire search room, and a reduced number of parameter sets is then passed to the SQP algorithm for an accurate local identification. Nonetheless, it is impossible to confirm the identified parameters are the global optimums.

An even more simplified thermal network proposed in [56] is also capable of predicting motor winding and PM temperatures. The schematic of the thermal model is shown in Fig. 1-21.

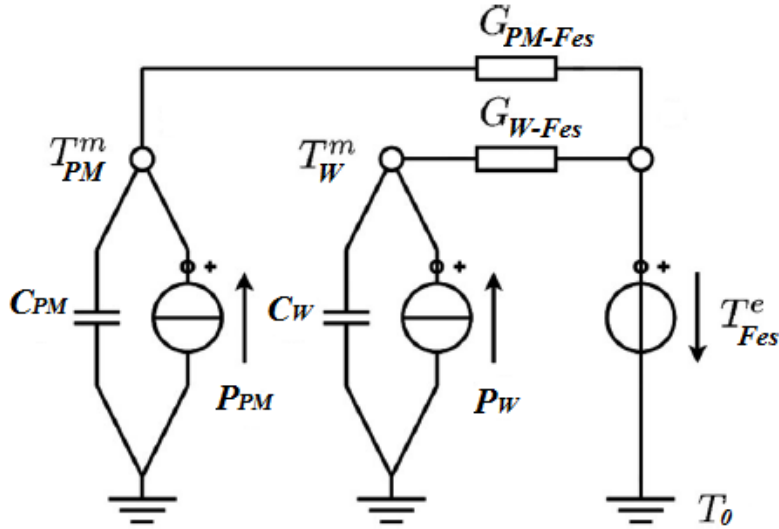


Fig. 1-21: Thermal model with two temperature nodes [56]

This LPTN consists of two temperature nodes corresponding to stator winding  $T_W$  and rotor PM  $T_{PM}$ . Stator core temperature  $T_{Fes}$  is an input quantity measured by a temperature sensor, which ensures that cooling system is immanently taken into account in the model. Stator core is connected to stator winding via a conductance  $G_{W-Fes}$  representing the thermal conduction through copper and iron core, and to PM by means of a conductance  $G_{PM-Fes}$  which considers the heat conduction through solid motor components and the heat convection from stator to rotor.

Stator loss  $P_W$  is determined by RMS current  $I_{RMS}$  and temperature-dependent stator resistance  $R_s$ :

$$P_W = 3R_s(T_W)I_{RMS}^2 \quad (1-136)$$

The heat flowing between rotor to stator due to heat conduction and convection effects changes with current and frequency and is modelled in the following form:

$$\frac{P_{PM}}{P_{rated}} = \left(\frac{f_r}{f_{rated}}\right)^{b_1} \left(\frac{I}{I_{rated}}\right)^{b_2} \quad (1-137)$$

In which  $f_{rated}$ ,  $I_{rated}$  and  $P_{rated}$  are pre-defined constants. The parameters  $b_1$  and  $b_2$  are calculated in a data-fitting process, with rotor losses  $P_{PM}$  obtained from the 2-D FEA at various speed and load conditions.

Similarly to the previously introduced thermal model, the parameters  $C_{PM}$ ,  $C_W$ ,  $G_{W-Fes}$ , and  $G_{PM-Fes}$  are estimated in an identification procedure aiming to minimize the sum of the squared temperature deviations:

$$\Delta T^2 = \frac{1}{t_{max}} \int_0^{t_{max}} ((T_{PM}^e - T_{PM}^m)^2 + (T_W^e - T_W^m)^2) dt \quad (1-138)$$

using an optimization software. In (1-138),  $T^e$  and  $T^m$  denote estimated and reference/measured temperatures, respectively, and  $t_{max}$  is the time period of testing.

The thermal conductance  $G_{PM-Fes}$  is assumed to be linearly dependent on frequency due to convection effect:

$$G_{PM-Fes} = G_{PM-Fes,0} + \Delta G_{PM-Fes} \frac{f_r}{f_{rated}} \quad (1-139)$$

in which two parameters  $G_{PM-Fes,0}$  and  $\Delta G_{PM-Fes}$  are to be determined. By performing the identification at two different rotor speeds:

$$G_{PM-Fes,f_{r1}} = G_{PM-Fes,0} + \Delta G_{PM-Fes} \frac{f_{r1}}{f_{rated}} \quad (1-140)$$

$$G_{PM-Fes,f_{r2}} = G_{PM-Fes,0} + \Delta G_{PM-Fes} \frac{f_{r2}}{f_{rated}} \quad (1-141)$$

the two parameters can be derived from the two independent equations.

This section focuses on the temperature estimation methods based on the use of a lumped parameter thermal network. A summary of the analytical models for iron loss calculation is presented at the beginning, due to its significant contribution to motor overall losses. Iron loss can be estimated using the empirical Steinmetz's equation or its extended version Bertotti equation. Ref. [82]-[89] present the modified iron loss expressions which take into account the minor hysteresis loop and harmonic effects, whereas a curve-fitting procedure is performed to identify the iron loss coefficients in [90]. A simplified voltage-based loss model catering for constant torque and constant power operations is proposed in [91] and two finite element solutions corresponding to open-circuit and short-circuit operations are required for the derivation of the coefficients in the model. Motor temperatures can be predicted by a 48-node LPTN coupled with a loss model with high fidelity and considering temperature effect, according to [6]. Nevertheless, high-order LPTNs require detailed motor geometrical and material information, which might not be available. Two low-order LPTNs presented in [56], [59]-[60] summarise only the most significant heat exchange processes in a motor. Detailed

motor physical knowledge is not needed because the thermal parameters can be identified with the curve-fitting algorithms. However, the practical implementation of the reduced-order LPTN is challenging as a result of the difficulty in obtaining rotor temperature measurement directly from temperature sensors for the identification of the unknown parameters. Chapter 4 provides a solution to this issue by demonstrating a temperature monitoring ‘system’, which combines a three-node LPTN with a simple and accurate model-based method replacing rotor temperature measurement.

### **1.3 Conclusion**

A research into the commonly-adopted temperature monitoring techniques is conducted. In spite of its reliability and accuracy, temperature measurement is not favoured in most applications because installing temperature sensors on the motor rotating part is particularly difficult. Besides, carrying out such measurements can be expensive. An alternative to measuring motor temperatures is estimating them via the electrical parameters changing with temperatures, such as flux linkage. However this approach requires the parameters of the machine and inverter to be precisely determined, and the use of signal injection in some methods may be disruptive to motor operation. A detailed LPTN provides important insights into the heat transfer processes in a motor and therefore is able to predict motor temperatures accurately. Nevertheless, it is modelled solely based on the knowledge of motor geometry and material properties, and the derivation of thermal parameters remains a difficult task. The use of a low-order LPTN in recent years has arisen, which does not demand high design effort, as only the major heat paths of a motor are considered, and therefore is the main focus of this PhD project.

# **Chapter 2: Temperature Estimation for Permanent Magnet Synchronous Motors Based on a Low-order Thermal Network**

## **2.1 Introduction**

It is concluded in the previous chapter that, from the temperature estimation point of view, a low-order LPTN may be able to achieve accurate temperature estimations with the least modelling effort and without detailed knowledge of the dimension and material of an electric motor. This chapter presents a simplified three-node thermal model predicting the critical temperatures in PMSMs. A set of state-space equations is used to describe the heat transfer processes between the motor components. The motor losses are calculated via the Finite Element software Motor-CAD, and are distributed into different temperature nodes according to their sources. The thermal capacitances are assumed to be constant and can also be derived from the Finite Element software. The thermal resistances are estimated in a recursive parameter identification procedure to avoid the rather complicated analytical derivation process.

After an introduction of the basic concept, the proposed method is verified using the Nissan LEAF motor. The identification of the thermal resistances is carried out at different motor operating conditions in order to take into account the dependency of the resistances on rotor speed and current due to the model-fitting nature of the algorithm. The performance of the temperature estimation method is cross-validated with two independent motor driving cycles, demonstrating a small estimation error. In practice, inevitable errors in the modelling of losses may lead to the reduction of the model accuracy. This effect is evaluated in depth subsequently.

## **2.2 Fundamental Theory**

A low-order LPTN will be presented in the following section, which consists of three temperature nodes including stator iron, stator winding and PM. This particular LPTN requires minimum knowledge of motor dimension and material, and takes into consideration the most important heat transfer paths in a PMSM. Due to the highly simplified thermal structure, the modelling process can be reduced to the identification of only the five unknown thermal resistances, making this thermal network suitable to implement online in an embedded system.

## 2.2.1 Model Structure

A reduced-order LPTN with three nodes and considering only the most dominant heat-flow mechanisms in the motors is introduced for real-time temperature estimation for PMSM. As illustrated in Fig. 2-1, the nodes correspond to stator iron, stator winding, and rotor permanent magnets. The thermal resistance between stator iron and stator winding  $R_{W-Fes}$  represents the heat conduction through the solid regions of a motor. The heat convections through ambient, air gap, and cooling system are described by  $R_{PM-A}$ ,  $R_{PM-Fes}$ ,  $R_{PM-W}$  and  $R_{Fes-C}$ , respectively. Each node is also connected to a heat source representing the heat losses of the respective region of the motor, as well as a thermal capacitance, which is the product of the specific heat capacity and the mass of the respective motor component and therefore is assumed to be constant.

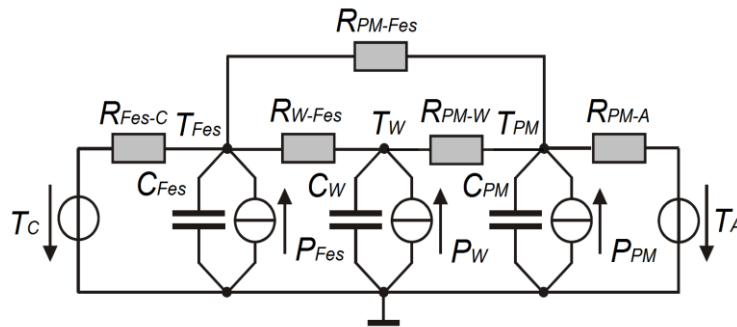


Fig. 2-1: Schematic graph of the three-node LPTN

It is important that the thermal resistance  $R_{PM-A}$  is considered. This physically represents the heat flow from rotor to ambient through the shaft. The rotor temperature otherwise may be overestimated in cases where both the stator iron and stator winding temperatures are higher than the rotor temperature, because there is no power outlet for the PM node.

## 2.2.2 Loss Modelling

An accurate modelling of motor losses is of great significance because it describes the heat generation in the motor and thus affects the motor thermal behaviour. In the following, motor losses are calculated with analytical and Finite Element software-based tools. The total losses mainly consist of DC stator copper loss, iron loss and windage loss. Copper loss calculation is based on  $P_w = I^2 R$ , where resistance  $R$  varies with stator winding temperature, whereas iron loss is determined by either Steinmetz's or Bertotti's equation. Windage loss is optional and can be easily added.

For the presented LPTN shown in Fig. 2-1, the winding loss  $P_w$  is assumed to be the temperature-dependent copper loss which is split into the winding and end-winding components based on their relative effective conductor lengths. The stator iron loss  $P_{Fes}$  contains the stator back iron and stator teeth losses. With respect to the rotor loss  $P_{PM}$ , it is considered to be the sum of the rotor back iron loss and the magnet loss. Windage loss due to air turbulence as stator and rotor move past each other appears in the form of stator surface and rotor surface losses, and can be allocated evenly into the stator and rotor nodes. However it sometimes is not taken into consideration.

### 2.2.3 Thermal Capacitance and Resistance

The thermal capacitance of each motor component is defined by its specific heat capacity and mass, and can be calculated with a knowledge of the motor topology. The precise calculation of the value of the thermal capacitance for each node in Fig. 2-1 is difficult because some uncertainties exist, for instance, the information regarding stator slot such as epoxy configuration and insulation thickness is normally unknown.

As a result, the node capacitance is roughly estimated on the basis that the capacitance of each node is the sum of the capacitances of all the motor components this node represents. Specifically, the stator iron node capacitance consists of stator housing, stator back iron, stator tooth, and flange mounted plate capacitances, etc. The winding node capacitance contains stator winding and end-winding capacitances. Due to the lumped modelling of rotor, the PM node should be viewed as the ‘rotor node’ and therefore the capacitance of each component located in rotor should be lumped together.

The proposed structure only takes into account the major heat transfer processes in a motor, which are summarized in five thermal resistances. Instead of deriving the analytical formulas for the thermal resistances, which require the detailed knowledge of the motor geometry and the thermal properties of the materials, the thermal resistances are estimated in the parameter identification process introduced in the following section, along with the node temperatures.

### 2.2.4 State-space Representation

As with the voltage node equations for electrical circuit, the temperature node equations for the presented ‘thermal circuit’ can be described as:

$$P_{Fes} - C_{Fes} \frac{d}{dt} T_{Fes} = \frac{T_{Fes} - T_C}{R_{Fes-C}} + \frac{T_{Fes} - T_W}{R_{W-Fes}} + \frac{T_{Fes} - T_{PM}}{R_{PM-Fes}} \quad (2-1)$$

$$P_W - C_W \frac{d}{dt} T_W = \frac{T_W - T_{Fes}}{R_{W-Fes}} + \frac{T_W - T_{PM}}{R_{PM-W}} \quad (2-2)$$

$$P_{PM} - C_{PM} \frac{d}{dt} T_{PM} = \frac{T_{PM} - T_{Fes}}{R_{PM-Fes}} + \frac{T_{PM} - T_W}{R_{PM-W}} + \frac{T_{PM} - T_A}{R_{PM-A}} \quad (2-3)$$

The thermal behaviour of the LPTN based on the above description therefore can be expressed in the form of a set of state-space equations:

$$\dot{x} = Ax + Bu \quad (2-4)$$

$$y = Cx + Du \quad (2-5)$$

in which:

$$x = [T_{Fes}, T_W, T_{PM}]^T \quad (2-6)$$

$$u = [P_{Fes}, P_W, P_{PM}, T_C, T_A]^T \quad (2-7)$$

$$A = \mathbb{R}^{3 \times 3} \quad (2-8)$$

$$A_{11} = -\frac{1}{C_{Fes}} \left( \frac{1}{R_{Fes-C}} + \frac{1}{R_{W-Fes}} + \frac{1}{R_{PM-Fes}} \right) \quad (2-9)$$

$$A_{12} = \frac{1}{C_{Fes} R_{W-Fes}} \quad (2-10)$$

$$A_{13} = \frac{1}{C_{Fes} R_{PM-Fes}} \quad (2-11)$$

$$A_{21} = \frac{1}{C_W R_{W-Fes}} \quad (2-12)$$

$$A_{22} = -\frac{1}{C_W} \left( \frac{1}{R_{W-Fes}} + \frac{1}{R_{PM-W}} \right) \quad (2-13)$$

$$A_{23} = \frac{1}{C_W R_{PM-W}} \quad (2-14)$$

$$A_{31} = \frac{1}{C_{PM} R_{PM-Fes}} \quad (2-15)$$

$$A_{32} = \frac{1}{C_{PM} R_{PM-W}} \quad (2-16)$$

$$A_{33} = -\frac{1}{C_{PM}} \left( \frac{1}{R_{PM-Fes}} + \frac{1}{R_{PM-W}} + \frac{1}{R_{PM-A}} \right) \quad (2-17)$$

$$B = \begin{bmatrix} \frac{1}{C_{Fes}} & 0 & 0 & \frac{1}{C_{Fes}R_{Fes-C}} & 0 \\ 0 & \frac{1}{C_W} & 0 & 0 & 0 \\ 0 & 0 & \frac{1}{C_{PM}} & 0 & \frac{1}{C_{PM}R_{PM-A}} \end{bmatrix} \quad (2-18)$$

$$C = \begin{bmatrix} 1 & 0 & 0 \\ 0 & 1 & 0 \\ 0 & 0 & 1 \end{bmatrix} \quad (2-19)$$

$$D = \begin{bmatrix} 0 & 0 & 0 & 0 & 0 \\ 0 & 0 & 0 & 0 & 0 \\ 0 & 0 & 0 & 0 & 0 \end{bmatrix} \quad (2-20)$$

As can be seen from (2-6) to (2-20), the state vector  $x$  contains the node temperatures, whilst the input vector  $u$  represents the power loss of each node and the motor cooling system and ambient temperatures  $T_C$  and  $T_A$ . The state and input matrices  $A$  and  $B$  are  $3 \times 3$  and  $3 \times 5$  vectors, respectively, and they are the functions of the thermal resistances and capacitances. With regard to  $C$  and  $D$ , they are identity and zero matrices, because  $y$  is the observation of the states. It is worth mentioning that, the matrices  $A$ ,  $B$ ,  $C$  and  $D$  at this stage are independent of sampling time.

## 2.2.5 Model Discretization

For the purpose of real-time system identification, the discretization of the continuous-time model is required. The approach applied in discretizing the presented thermal model is the RK1 method. As a result, equation (2-4) now becomes (1-134) and hence the state transition and observation models are given by:

$$x(k+1) = (T_k A(k) + I)x(k) + T_k B(k)u(k) \quad (2-21)$$

$$y(k) = C(k)x(k) + D(k)u(k) \quad (2-22)$$

with:

$$x(k) = [T_{Fes}(k), T_W(k), T_{PM}(k)]^T \quad (2-23)$$

$$u(k) = [P_{Fes}(k), P_W(k), P_{PM}(k), T_C(k), T_A(k)]^T \quad (2-24)$$

Assuming  $\vartheta = T_k A(k) + I$ , and  $\varepsilon = T_k B(k)$ :

$$\vartheta = \begin{bmatrix} 1 - \frac{T_k}{C_{Fes}} \left( \frac{1}{\theta_1} + \frac{1}{\theta_2} + \frac{1}{\theta_3} \right) & \frac{T_k}{C_{Fes}\theta_2} & \frac{T_k}{C_{Fes}\theta_3} \\ \frac{T_k}{C_W\theta_2} & 1 - \frac{T_k}{C_W} \left( \frac{1}{\theta_2} + \frac{1}{\theta_4} \right) & \frac{T_k}{C_W\theta_4} \\ \frac{T_k}{C_{PM}\theta_3} & \frac{T_k}{C_{PM}\theta_4} & 1 - \frac{T_k}{C_{PM}} \left( \frac{1}{\theta_3} + \frac{1}{\theta_4} + \frac{1}{\theta_5} \right) \end{bmatrix} \quad (2-25)$$

$$\varepsilon = \begin{bmatrix} \frac{T_k}{C_{Fes}} & 0 & 0 & \frac{T_k}{C_{Fes}\theta_1} & 0 \\ 0 & \frac{T_k}{C_W} & 0 & 0 & 0 \\ 0 & 0 & \frac{T_k}{C_{PM}} & 0 & \frac{T_k}{C_{PM}\theta_5} \end{bmatrix} \quad (2-26)$$

where:

$$\theta_1 = R_{Fes-C} \quad (2-27)$$

$$\theta_2 = R_{W-Fes} \quad (2-28)$$

$$\theta_3 = R_{PM-Fes} \quad (2-29)$$

$$\theta_4 = R_{PM-W} \quad (2-30)$$

$$\theta_5 = R_{PM-A} \quad (2-31)$$

## 2.2.6 Parameter Identification

The thermal resistances in the LPTN are estimated using a measurement-informed parameter estimation procedure, based on the recursive Kalman Filter algorithm which is able to update continuously the values of the unknown state variables according to the minimization of the cost function  $J(x)$ :

$$\min_x J(x) \quad (2-32)$$

where:

$$J(x) = cov(e_x(k)) \quad (2-33)$$

$$cov(e_x(k)) = \sum_{k=1}^N e_x(k) e_x(k)^T \quad (2-34)$$

$$e_x(k) = \tilde{x}(k) - x(k) \quad (2-35)$$

The function  $cov(e_x(k))$  is the determinant of the covariance matrix of the state variable estimation errors  $e_x(k)$ . It is assumed that the system for which the states are to be estimated contains process noise and the observation noise is included in the measurements.

The Kalman Filter algorithm has numerous applications, such as navigation, target tracking, and has been widely used as the state observer in high performance PM motor drives in recent years. In [32], two low-order Kalman Filter models are proposed for the estimations of the winding resistance and PM flux linkage of a surface-mounted permanent magnet brushless AC (BLAC) motor under sensorless and sensed operations for rotor speed and position. The identification of the parameters only requires motor current and voltage measurements, and good estimation accuracy can be achieved. Furthermore, the models are of low computational demand and therefore can be relatively easily implemented in real-time.

The algorithm performs a two-step process: a) prediction step: the Kalman Filter calculates the state estimates at current time step, also known as ‘a priori’ estimates, using the estimates from the previous time step. The measurements are not used at this stage. b) Update step: the ‘a priori’ estimates are refined by taking account of the current measurement information. These improved estimates (‘a posterior’ state estimates) are then used for producing the new ‘a priori’ estimates at the next time step. From the description above, it is clear that the algorithm works with only the present input measurement(s) and the previously updated state(s) — no additional past information is required.

The identification problem can be formulated as a state observer with eight states. Other than the node temperatures, five additional states are included representing the unknown thermal resistances in the LPTN. The system has a nonlinear character due to the formulation where both temperatures and parameters are to be estimated. As a result, the extended Kalman Filter (EKF) which uses a continuously updated linearization is adopted to deal with the nonlinearity of the model.

The state-space models of a nonlinear system can be expressed as:

$$x_k = f(x_{k-1}, u_k) + w_k \quad (2-36)$$

$$z_k = h(x_k) + v_k \quad (2-37)$$

The process and measurement/observation noises  $w_k$  and  $v_k$  are assumed to be zero-mean white noises with covariances  $Q_k$  and  $R_k$  respectively. A standard assumption is that:

$$Q_k = w_k w_k^T \quad (2-38)$$

$$R_k = v_k v_k^T \quad (2-39)$$

The functions  $f$  and  $h$  are nonlinear and cannot be applied to the covariance estimations as the linear state-transition and observation models. Hence the Jacobian matrices are computed to linearize the nonlinear functions around the current state. The following equations describe the two-phase estimation process at each sampling time for the EKF algorithm:

- Predict

$$\hat{x}_{k|k-1} = f(\hat{x}_{k-1|k-1}, u_k) \quad (2-40)$$

$$P_{k|k-1} = F_k P_{k-1|k-1} F_k^T + Q_k \quad (2-41)$$

- Update

$$\hat{y}_k = z_k - h(\hat{x}_{k|k-1}) \quad (2-42)$$

$$S_k = H_k P_{k|k-1} H_k^T + R_k \quad (2-43)$$

$$K_k = P_{k|k-1} H_k^T S_k^{-1} \quad (2-44)$$

$$\hat{x}_{k|k} = \hat{x}_{k|k-1} + K_k \hat{y}_k \quad (2-45)$$

$$P_{k|k} = (I - K_k H_k) P_{k|k-1} \quad (2-46)$$

where the Jacobians are defined as:

$$F_k = f'(x)|_{\hat{x}_{k-1|k-1}, u_k} \quad (2-47)$$

$$H_k = h'(x)|_{\hat{x}_{k|k-1}} \quad (2-48)$$

In the prediction step, the EKF computes the current state estimates  $\hat{x}_{k|k-1}$  based on the state function  $f$ , and the covariance matrix  $P_{k|k-1}$ , using the state-transition Jacobian  $F_k$  — a matrix of partial derivatives linearizing the system function. The update phase provides the improved estimates  $\hat{x}_{k|k}$  by adding a corrective term  $K_k \hat{y}_k$  to the ‘a priori’ estimates in order to take into account the current measurement information. The Kalman gain matrix  $K_k$  is derived from the minimization of the trace of the ‘a posteriori’ estimate covariance matrix  $P_{k|k}$ . The block diagram representing the two-step estimation process is shown in Fig. 2-2.

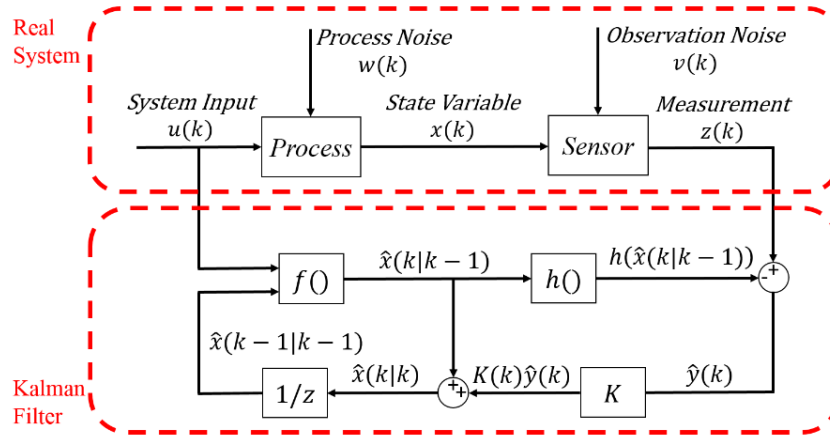


Fig. 2-2: Extended Kalman Filter algorithm block diagram

Concerning the aforementioned thermal network with eight states of the node temperatures and thermal resistances, the nonlinear functions  $f$  and  $h$  can be written as:

$$f = \begin{bmatrix} x_1 - \frac{T_k x_1}{C_{Fes}} \left( \frac{1}{x_4} + \frac{1}{x_5} + \frac{1}{x_6} \right) + \frac{T_k x_2}{C_{Fes} x_5} + \frac{T_k x_3}{C_{Fes} x_6} + \frac{T_k u_1}{C_{Fes}} + \frac{T_k u_4}{C_{Fes} x_4} \\ \frac{T_k x_1}{C_W x_5} + x_2 - \frac{T_k x_2}{C_W} \left( \frac{1}{x_5} + \frac{1}{x_7} \right) + \frac{T_k x_3}{C_W x_7} + \frac{T_k u_2}{C_W} \\ \frac{T_k x_1}{C_{PM} x_6} + \frac{T_k x_2}{C_{PM} x_7} + x_3 - \frac{T_k x_3}{C_{PM}} \left( \frac{1}{x_6} + \frac{1}{x_7} + \frac{1}{x_8} \right) + \frac{T_k u_3}{C_{PM}} + \frac{T_k u_5}{C_{PM} x_8} \\ x_4 \\ x_5 \\ x_6 \\ x_7 \\ x_8 \end{bmatrix} \quad (2-49)$$

$$h = \begin{bmatrix} x_1 \\ x_2 \\ x_3 \\ x_4 \\ x_5 \\ x_6 \\ x_7 \\ x_8 \end{bmatrix} \quad (2-50)$$

where:

$$[x_1, x_2, x_3, x_4, x_5, x_6, x_7, x_8]^T = [T_{Fes}, T_W, T_{PM}, \theta_1, \theta_2, \theta_3, \theta_4, \theta_5]^T \quad (2-51)$$

$$[u_1, u_2, u_3, u_4, u_5]^T = [P_{Fes}, P_W, P_{PM}, T_C, T_A]^T \quad (2-52)$$

Thus the state-transition and observation Jacobian matrices are:

$$F = \begin{bmatrix} 1 - \frac{T_k}{C_{Fes}} \left( \frac{1}{x_4} + \frac{1}{x_5} + \frac{1}{x_6} \right) & \frac{T_k}{C_{Fes}x_5} & \frac{T_k}{C_{Fes}x_6} \\ \frac{T_k}{C_Wx_5} & 1 - \frac{T_k}{C_W} \left( \frac{1}{x_5} + \frac{1}{x_7} \right) & \frac{T_k}{C_Wx_7} \\ \frac{T_k}{C_{PM}x_6} & \frac{T_k}{C_{PM}x_7} & 1 - \frac{T_k}{C_{PM}} \left( \frac{1}{x_6} + \frac{1}{x_7} + \frac{1}{x_8} \right) \dots \\ 0 & 0 & 0 \\ 0 & 0 & 0 \\ 0 & 0 & 0 \\ 0 & 0 & 0 \end{bmatrix} \quad (2-53)$$

$$\dots \begin{bmatrix} \frac{T_k(x_1 - u_4)}{C_{Fes}x_4^2} & \frac{T_k(x_1 - x_2)}{C_{Fes}x_5^2} & \frac{T_k(x_1 - x_3)}{C_{Fes}x_6^2} & 0 & 0 \\ 0 & \frac{T_k(x_2 - x_1)}{C_Wx_5^2} & 0 & \frac{T_k(x_2 - x_3)}{C_Wx_7^2} & 0 \\ 0 & 0 & \frac{T_k(x_3 - x_1)}{C_{PM}x_6^2} & \frac{T_k(x_3 - x_2)}{C_{PM}x_7^2} & \frac{T_k(x_3 - u_5)}{C_{PM}x_8^2} \\ 1 & 0 & 0 & 0 & 0 \\ 0 & 1 & 0 & 0 & 0 \\ 0 & 0 & 1 & 0 & 0 \\ 0 & 0 & 0 & 1 & 0 \\ 0 & 0 & 0 & 0 & 1 \end{bmatrix}$$

$$H = \begin{bmatrix} 1 & 0 & 0 & 0 & 0 & 0 & 0 & 0 \\ 0 & 1 & 0 & 0 & 0 & 0 & 0 & 0 \\ 0 & 0 & 1 & 0 & 0 & 0 & 0 & 0 \\ 0 & 0 & 0 & 1 & 0 & 0 & 0 & 0 \\ 0 & 0 & 0 & 0 & 1 & 0 & 0 & 0 \\ 0 & 0 & 0 & 0 & 0 & 1 & 0 & 0 \\ 0 & 0 & 0 & 0 & 0 & 0 & 1 & 0 \\ 0 & 0 & 0 & 0 & 0 & 0 & 0 & 1 \end{bmatrix} \quad (2-54)$$

Also, a relatively small sampling time  $T_k = 1s$  is selected to avoid significant prediction errors.

The process noise covariance  $Q$  and the observation noise covariance  $R$  are commonly used for tuning the EKF. Normally only  $Q$  is adjusted because  $R$  can be easily calculated from a series of measurements. It is obvious that the use of large  $Q$  results in a stronger weighting of the measurements, indicating that the variations in the actual states are large. The Kalman Filter gain  $K$  as a result is large in order to achieve that. However this results in more measurement noise, as the measurement residual  $\hat{y}_k$  includes the measurement noise  $v_k$ , which is amplified with a larger  $K$ . In conclusion, the general rule for the selection of  $Q$  is that, select the largest value without the estimates being overly noisy [94].

It is necessary to check whether the proposed thermal network is observable prior to the validation of the method. A state-space system is completely observable, only if the rank of the observability matrix  $M_o$ , defined as [94]:

$$M_o = \begin{bmatrix} C \\ CA \\ CA^2 \\ \vdots \\ CA^{n-1} \end{bmatrix} \quad (2-55)$$

is equal to the system order  $n_{so}$ . In (2-55),  $A$  and  $C$  are the state transition and observation matrices, which for nonlinear systems are the state and output Jacobians, respectively.

The observability matrix of the thermal network is computed using (2-53) and (2-54).  $M_o$  is a  $64 \times 8$  vector. It is confirmed that the rank of  $M_o$  is eight, the same as the order of the system model, and the number of the state variables.

## 2.3 Offline Validation

The model of the Motor-CAD existing traction IPMSM used in 2012 Nissan LEAF is employed for validation purpose, instead of the experimentally-tested SPMSM, which will be introduced in the following chapter, in order to evaluate the applicability of the presented method to different types of PMSMs. The motor schematic is shown in Fig. 2-3 (design parameters specified in Table II), and the simulation of the identification algorithm and the temperature estimation is performed in MATLAB/Simulink (see Appendix B the MATLAB function).

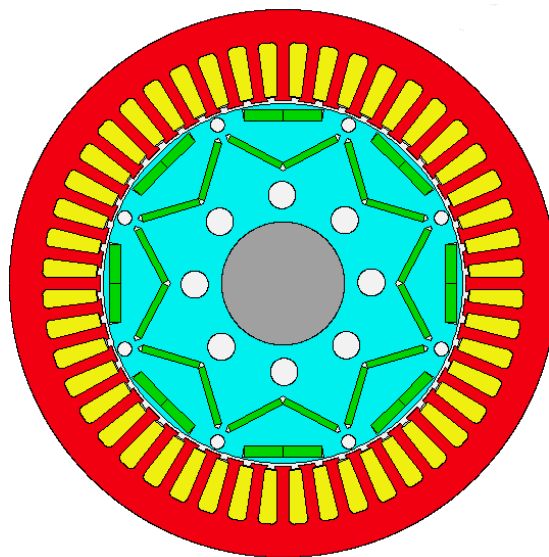


Fig. 2-3: Schematic of the PMSM used for offline validation

Table II: Parameters of the IPMSM

Quantity	Unit	Value
Max Speed	rpm	10,390
Peak Power	kW	80
DC Link Voltage	V	400
Peak Torque	Nm	280
No. of Pole-pairs	--	4
No. of Slots	--	48
Stator Resistance	$\Omega$	0.0112
<i>d</i> -axis Inductance	mH	0.2194
<i>q</i> -axis Inductance	mH	0.5371
PM Flux Linkage	Wb	0.088

### 2.3.1 Validation at Single Speed and Current

The validity of the proposed method is investigated under the conditions where the motor operates at the maximum rotor speed  $\omega_r = 6000rpm$  and stator current  $I = 189A$ . The motor losses are computed along with the temperatures of a detailed thermal network consisting of 48 nodes in Motor-CAD. For the presented low-order LPTN, the stator iron loss consists of the stator back iron and stator teeth losses, as well as a small amount of loss generated by the endcap. The winding loss is the sum of the active winding and end-winding losses. Due to the V-shaped interior PM being used, as illustrated in Fig. 2-3, the main contributor of loss in the rotor is the embedded magnet poles. The windage and bearing friction losses are also taken into account. The windage loss generated by the fluid movement in the air-gap is evenly distributed into the stator iron and PM nodes. The bearing loss is also separated equally into a stator iron and a rotor components, considering the friction between the bearing and the endcap and the shaft. The stator iron node temperature is assumed to be the average of the housing, endcap, stator back iron, and stator teeth temperatures, and the winding node temperature is considered the average temperature of the hot and cold winding spots. In respect of the rotor node temperature, it is regarded as the mean temperature of the rotor back iron, magnet and shaft. Fig. 2-4 and Fig. 2-5 show the thermal resistances and node temperatures estimated by the EKF. Fig. 2-6 shows the errors in the temperature estimations.

It can be seen from Fig. 2-5 and Fig. 2-6 that, the estimations by the EKF track the references rather well, suggesting that the estimated thermal model can offer a good degree of accuracy.

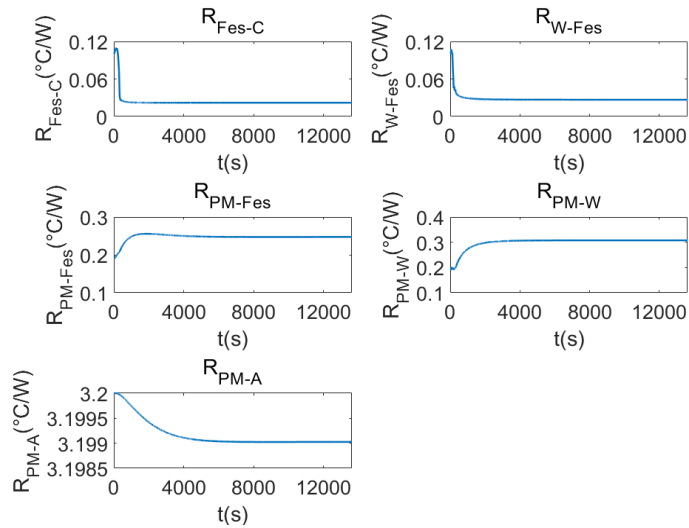


Fig. 2-4: Thermal resistances estimated by the EKF

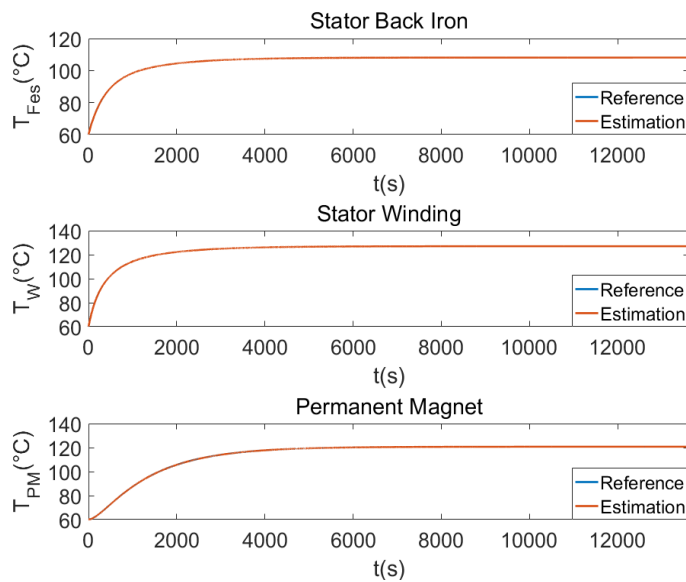


Fig. 2-5: Node temperatures estimated by the EKF

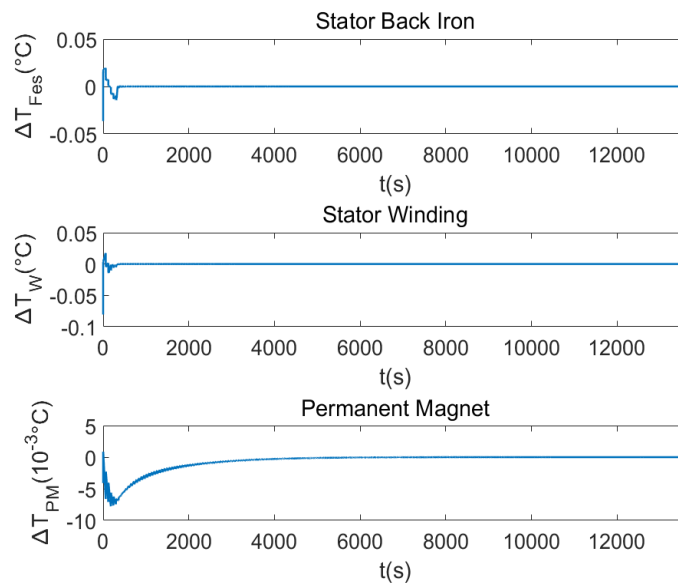


Fig. 2-6: Temperature estimation errors in Fig. 2-5

The estimation results of the thermal resistances are verified by performing an open-loop test, in which the node temperatures are calculated using (2-21)-(2-31), assuming that  $\theta_1$  to  $\theta_5$  are the values identified and shown in Fig. 2-4. Fig. 2-7 plots the estimated temperatures compared with the references and the corresponding errors are shown in Fig. 2-8.

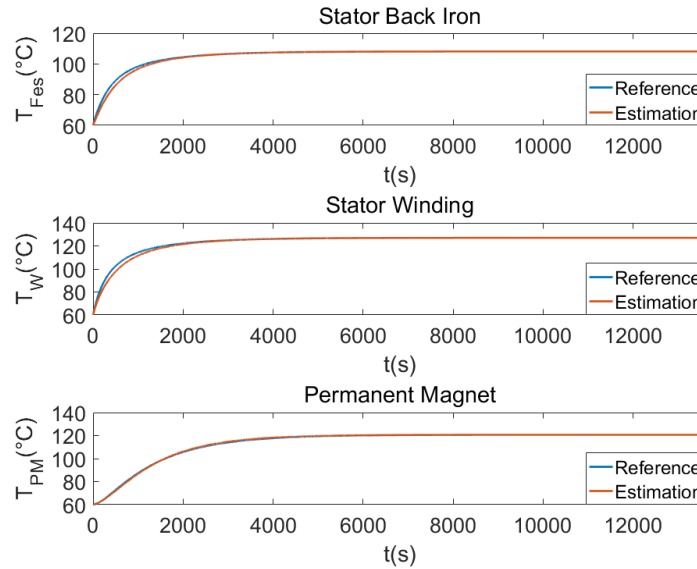


Fig. 2-7: Three-node temperature estimations using the identified thermal resistances

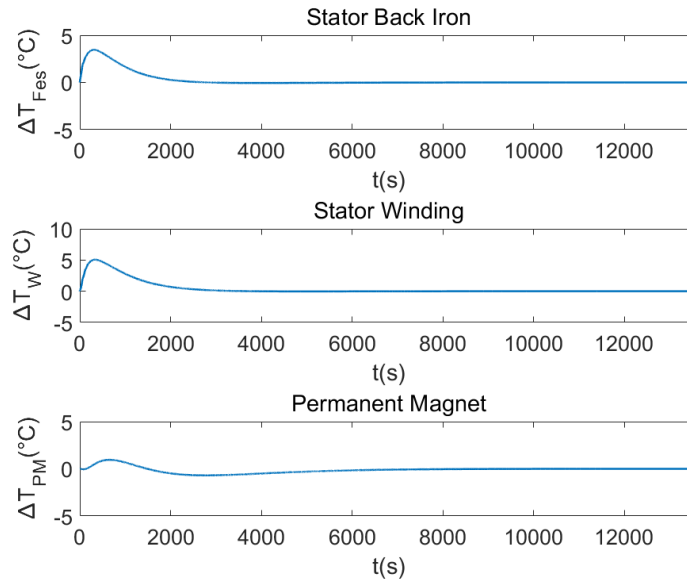


Fig. 2-8: Temperature estimation errors for the open-loop test

Less than 5.1°C errors in all three temperatures are shown, which may be due to the averaging of the Motor-CAD temperatures not being accurate. The proposed thermal network is highly simplified, meaning that each node represents a region within the motor and therefore the accuracy of the reference relies on the temperature of each motor component in the region, unless the temperatures are evenly distributed. In this case, the reference is approximated by

the average of the highest and lowest temperatures in the region for simplicity. It might not be particularly precise because the tested motor has an uneven temperature distribution. Also, the three-node, five-parameter structure is considered a reasonable abstraction of the major heat transfer processes in the most commonly used PMSMs. However it might be oversimplified for the IPMSM under test. Furthermore, the thermal resistances are identified only after the thermal equilibrium is reached, as shown in Fig. 2-4 and Fig. 2-5. This means the temperatures will be better estimated at steady-state unless the resistances during transient period are identical to those at steady-state, which might not be the case for the tested motor.

As an alternative to the use of the Kalman Filter, the identification of the thermal resistances is also performed using the nonlinear least squared optimization method based on the Levenberg-Marquardt algorithm [7] using the MATLAB estimation toolbox. This method locates the parameters  $\beta = (\beta_1, \beta_2 \dots \beta_n)$  of a nonlinear model curve  $y_\beta = f(x, \beta)$ , such that the sum  $S$  of the squares of the deviations between a set of observations and the model curve is minimized. Similarly to the EKF, the function  $f(x, \beta)$  is approximated by its linearization for the update of  $S$ . The algorithm is an iterative procedure. In each iteration, the parameters are refined by adjusting the damping factor  $\lambda_d$ , which controls the pace of the minimization of  $S$ . The iteration stops when  $S$  from the latest parameter estimations  $\beta_k$  is within the pre-defined limits, and  $\beta_k$  is considered the solution to the curve-fitting problem. With regard to the presented thermal network, the state variables  $x$  are assumed to be the node temperatures, whilst the unknown parameters correspond to the thermal resistances.

Fig. 2-9 shows the estimated temperatures alongside their corresponding references, and the power losses allocated into the temperature nodes. The ambient and cooling system temperatures are also included as they are the inputs of the thermal network. Only the steady-state temperatures are considered for the identification for the purpose of verifying the resistances shown in Fig. 2-4. Fig. 2-10 shows the value of the function  $S$  at each iteration before the optimization completed.

Fig. 2-11 shows the estimated thermal resistances. The resistances  $R_{Fes-C}$  and  $R_{W-Fes}$ , denoted as  $\theta_1$  and  $\theta_2$ , show approximately 0.04% and 2.22% difference respectively, compared to the results in Fig. 2-4. However the rotor-related resistances  $R_{PM-Fes}$ ,  $R_{PM-W}$ , and  $R_{PM-A}$  differ significantly from those estimated by the EKF. This is because these resistances have multiple solutions under the power loss profiles. With different algorithms, different ‘local optimal’

solutions around the initial guesses can be found which guarantee the minimum of the sum of the squared errors.

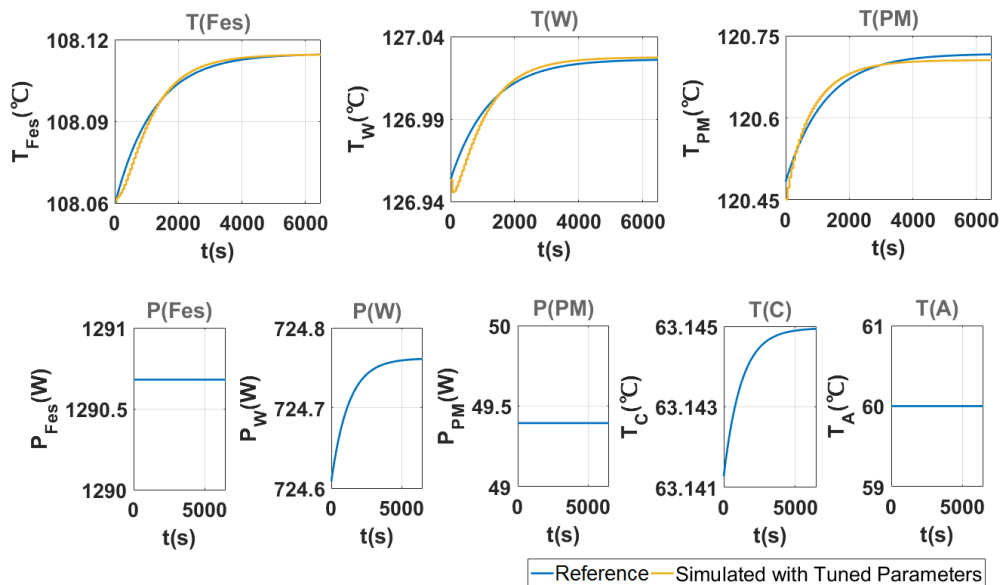


Fig. 2-9: Node temperatures estimated by the Levenberg-Marquardt algorithm, the power losses, the cooling system and ambient temperatures

Iteration	Cost Function
0	290.8621
1	6.6824
2	2.6395
3	0.3409
4	0.0048
5	$3.7584e^{-5}$
6	$1.0249e^{-6}$
7	$9.9462e^{-7}$

Fig. 2-10: Values of the cost function  $S$  before the iteration stops

Parameters	Levenberg-Marquardt	Extended Kalman Filter
$R_{Fes-C}$	0.021989	0.02198
$R_{W-Fes}$	0.02746	0.02685
$R_{PM-Fes}$	0.19172	0.2473
$R_{PM-W}$	0.17554	0.3073
$R_{PM-A}$	3.0761	3.199

Fig. 2-11: Thermal resistances estimated by the Levenberg-Marquardt and extended Kalman filter algorithms

The open-loop test is conducted estimating the node temperatures with the results displayed in Fig. 2-11. In spite of the nearly perfect estimation at the thermal steady-state, which affirms these resistances are indeed one of the many solutions that ensure the estimated temperatures approximately fit the references, over  $6^{\circ}\text{C}$  error in winding temperature and  $-5^{\circ}\text{C}$  error in rotor temperature can be observed in Fig. 2-12 and Fig. 2-13 during transient period, suggesting the results are not the best local optimal solutions for this particular application.

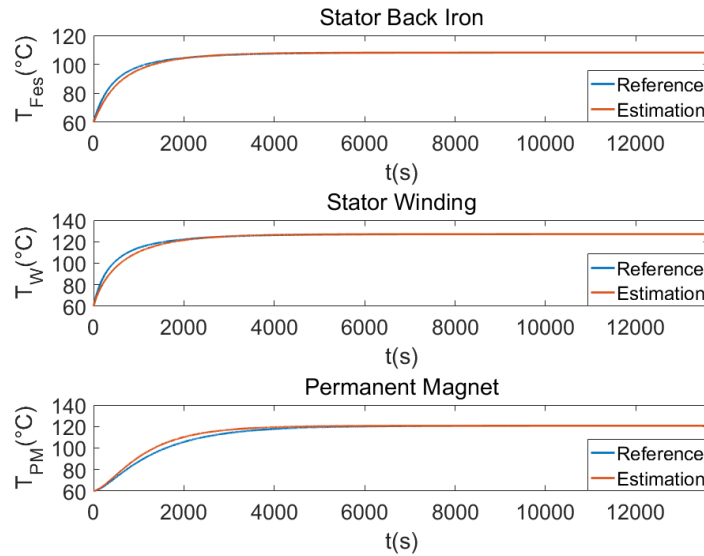


Fig. 2-12: Open-loop temperature estimations with the results in Fig. 2-11

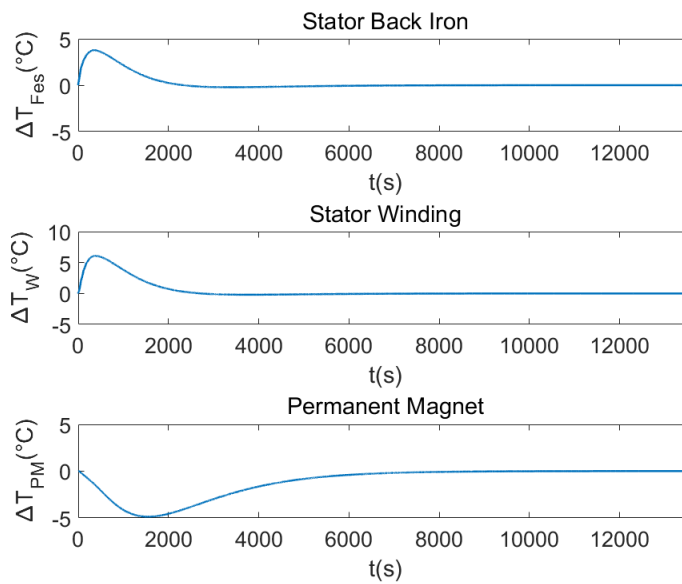


Fig. 2-13: Temperature estimation errors in Fig. 2-12

Fig. 2-14 demonstrates another local optimal solution estimated with a different set of initial guesses. Similarly to Fig. 2-11, the difference in the resistances connecting the rotor to the stator and ambient between using these two algorithms is evident. However the predicted node temperatures shown in Fig. 2-15 and Fig. 2-16 still match the temperature references rather well at steady-state. The maximum of 5°C error is shown in stator temperature estimations. Nonetheless, the rotor temperature is less accurately predicted compared to adopting the EKF algorithm.

Parameters	Levenberg-Marquardt	Extended Kalman Filter
$R_{Fes-C}$	0.021948	0.02198
$R_{W-Fes}$	0.026645	0.02685
$R_{PM-Fes}$	0.25994	0.2473
$R_{PM-W}$	0.42082	0.3073
$R_{PM-A}$	3.8181	3.199

Fig. 2-14: Thermal resistances estimated by the Levenberg-Marquardt algorithm with different initial conditions and the extended Kalman filter algorithm

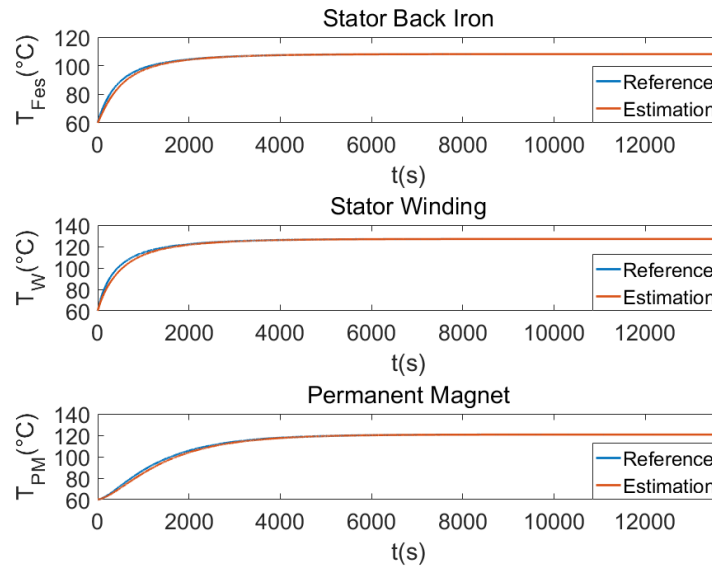


Fig. 2-15: Estimated node temperatures with the results in Fig. 2-14

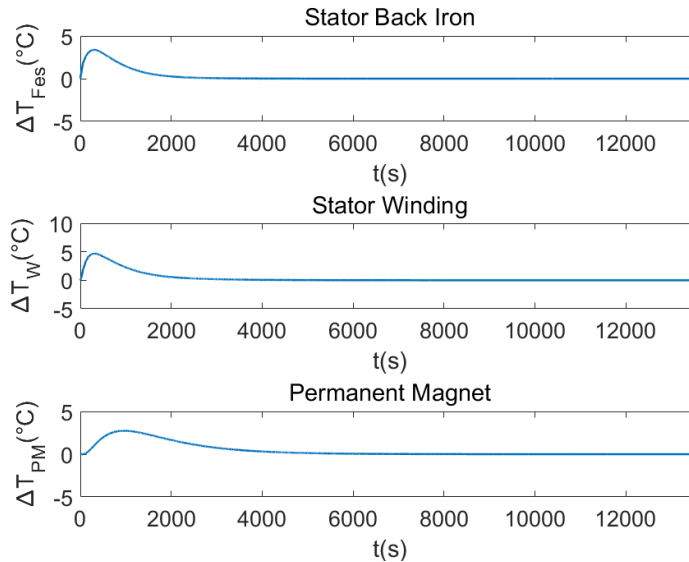


Fig. 2-16: Temperature estimation errors in Fig. 2-15

### 2.3.2 Validation at Multiple Speeds and Currents

The resistances related to rotor  $R_{PM-Fes}$ ,  $R_{PM-W}$ , and  $R_{PM-A}$  are assumed to be speed-dependent due to convection effects. Fig. 2-17 depicts the resistance estimations at multiple rotor speeds ranging from 1000rpm to 6000rpm, whilst the stator current is set to be its maximum.

It is clear that the thermal resistances between stator and rotor vary with rotor speed. However, the resistances  $R_{W-Fes}$  and  $R_{Fes-C}$  are expected to be constant, because a) rotor speed in theory does not affect heat conduction, b) the cooling system (housing water jacket) has a constant volume flow rate. The dependency on rotor speed can be simply explained by the fact that the resistances are estimated based upon the temperature predictions matching the temperature references and therefore have less physical meanings. The irregular variations in the values of  $R_{PM-A}$  may also be the result of it.

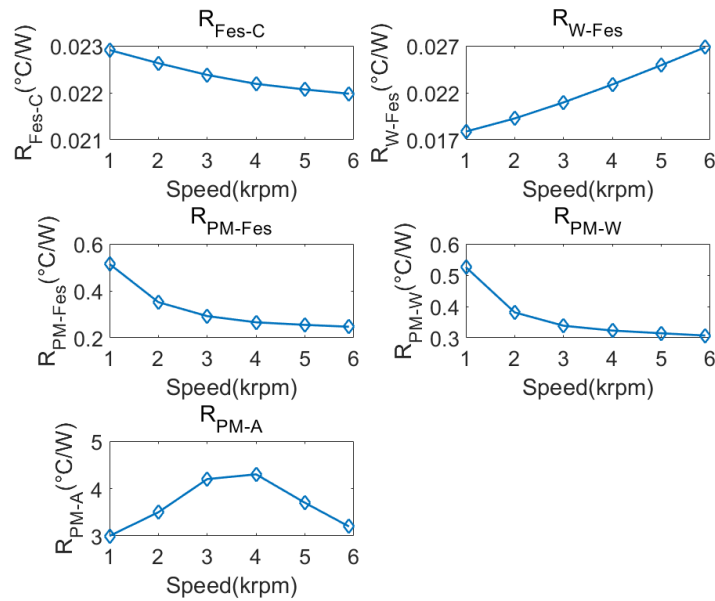


Fig. 2-17: Thermal resistances estimated at  $\omega_r = 1000rpm$ ,  $2000rpm$ ,  $3000rpm$ ,  $4000rpm$ ,  $5000rpm$ , and  $6000rpm$  and maximum current

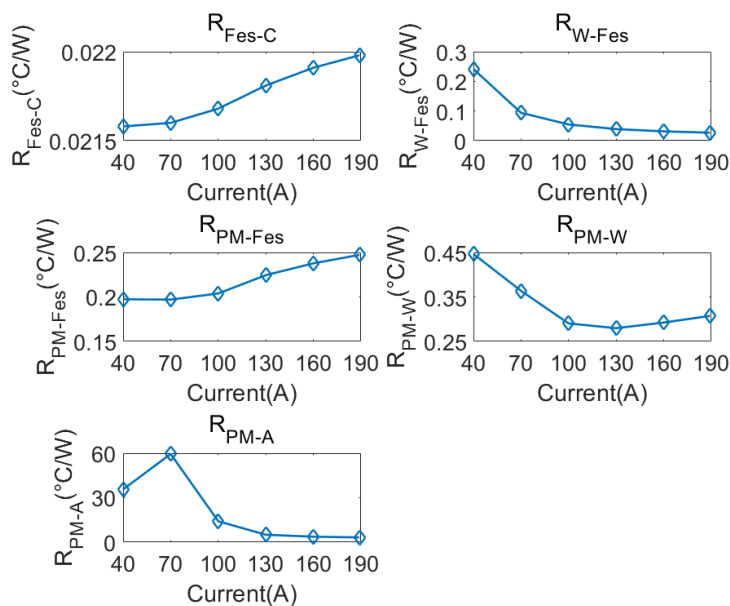


Fig. 2-18: Thermal resistance estimated at  $I = 40A$ ,  $70A$ ,  $100A$ ,  $130A$ ,  $160A$ , and  $189A$  and maximum speed

The identification procedure is also performed at different stator currents. Fig. 2-18 shows the predicted resistances when  $I = 40A, 70A, 100A, 130A, 160A,$  and  $189A$  are applied. The rotor speed remains constant at  $\omega_r = 6000rpm$ . The fact that the parameters still show some dependence on current supports the assumption that searching for the best fit to the temperature measurement points outweighs the physical meaning of the parameters for the EKF algorithm.

Fig. 2-19 to Fig. 2-23 demonstrate the resistances identified at several speed and current combinations. The data is written into five two-dimensional look-up tables (2-D LUT), with speed and current being the inputs, and the interpolated resistances being the outputs, for the purpose of temperature estimation. The non-uniform variation in the values of the resistances in a wide range of operating conditions confirms the aforementioned conclusions.

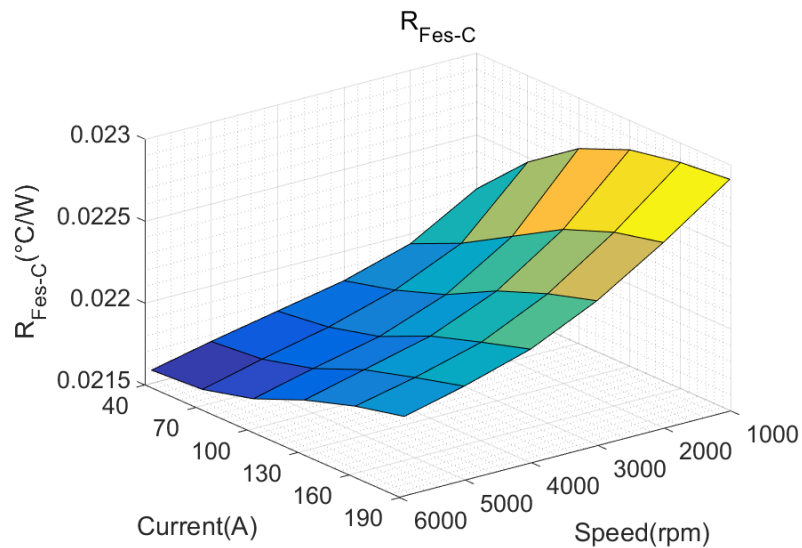


Fig. 2-19:  $R_{Fes-C}$  estimated at various speeds and currents

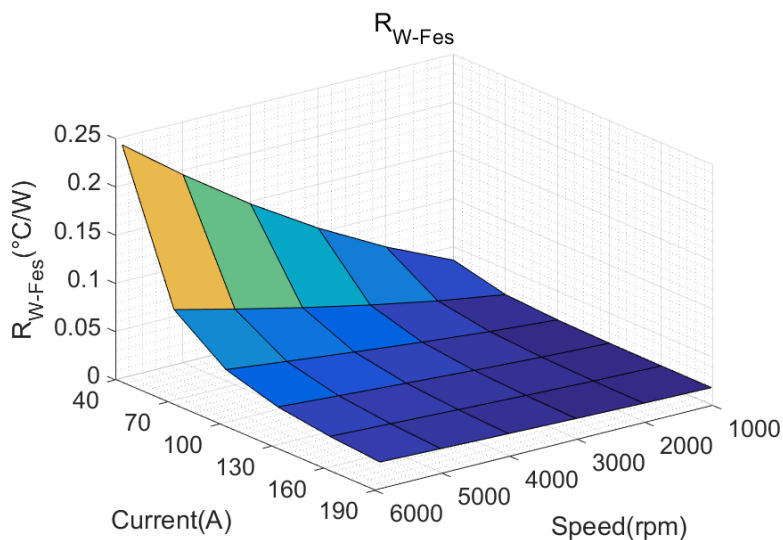


Fig. 2-20:  $R_{W-Fes}$  estimated at various speeds and currents

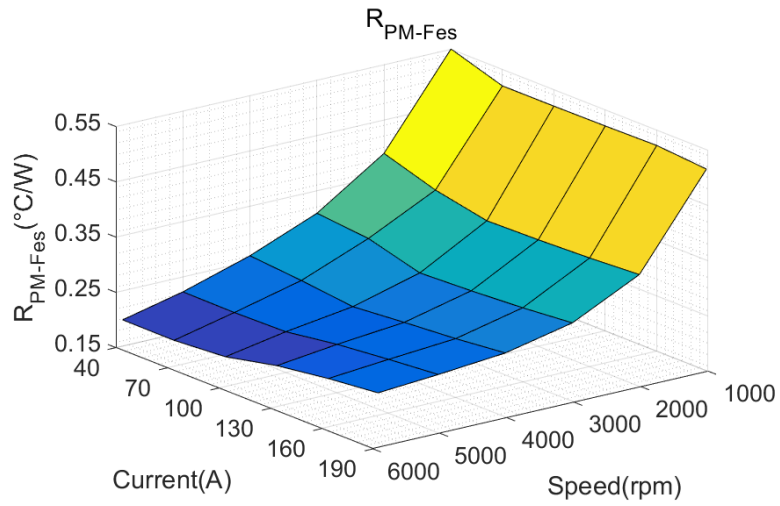


Fig. 2-21:  $R_{PM-Fes}$  estimated at various speeds and currents

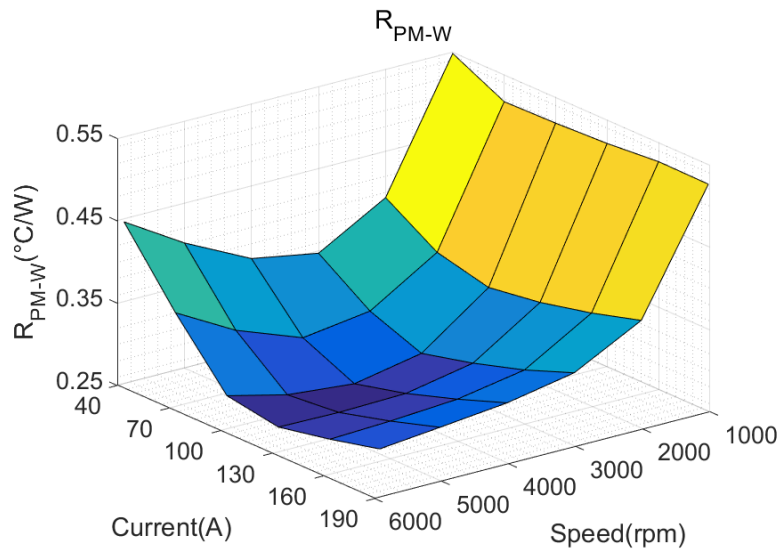


Fig. 2-22:  $R_{PM-W}$  estimated at various speeds and currents

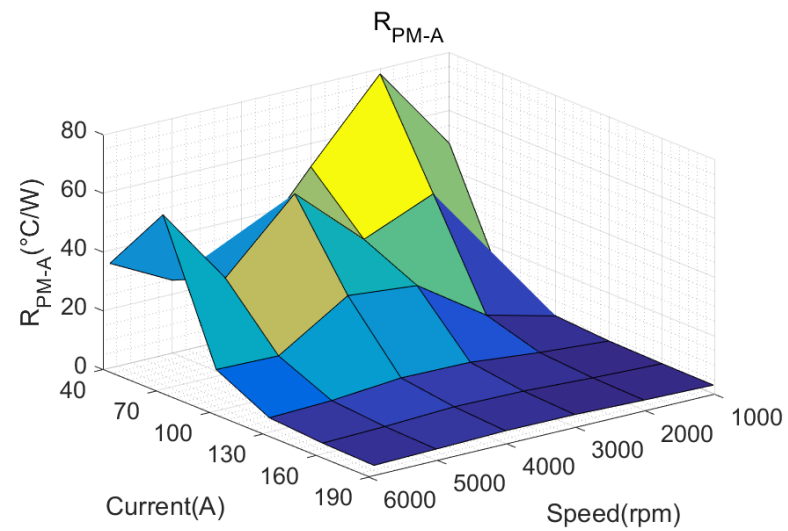


Fig. 2-23:  $R_{PM-A}$  estimated at various speeds and currents

A simplified driving cycle in which the motor speed and current vary in steps, as illustrated in Fig. 2-24, is used to generate a dynamic thermal transient. The node temperatures are estimated in the open-loop test. The thermal resistances are assumed to be dependent on both speed and current, and are interpolated using the 2-D LUTs. Fig. 2-25 shows the step-based resistances in response to the driving cycle, whereas Fig. 2-26 and Fig. 2-27 depict the estimated temperatures, and their deviations from the corresponding references, respectively. The errors are within 5.8°C for all predicted temperatures.

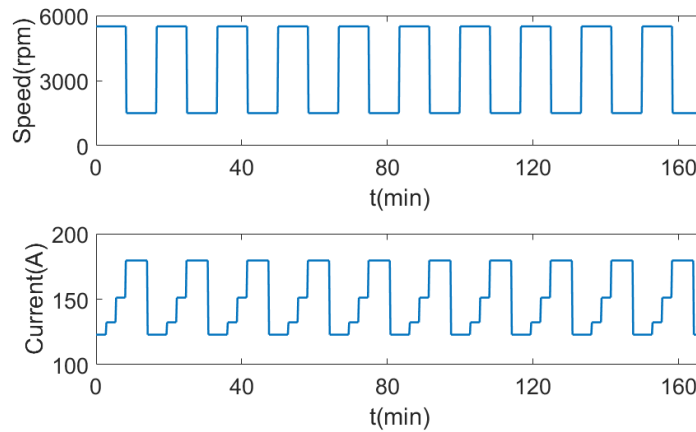


Fig. 2-24: Speed and current profiles of the transient test

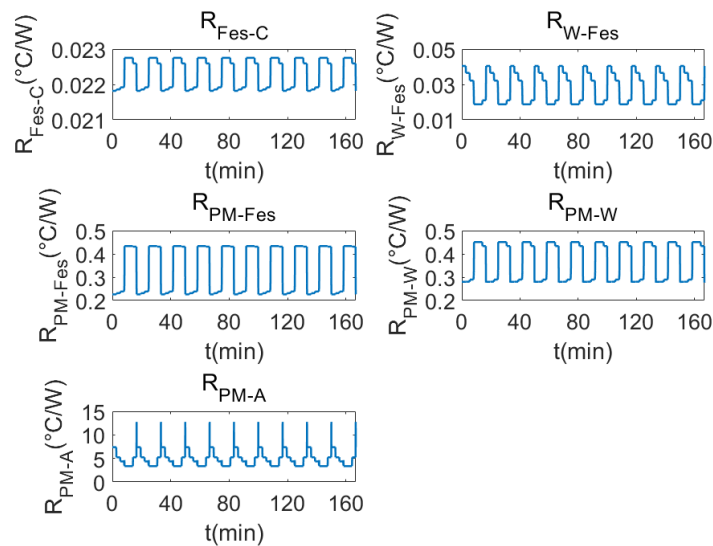


Fig. 2-25: Thermal resistances in response to the driving cycle

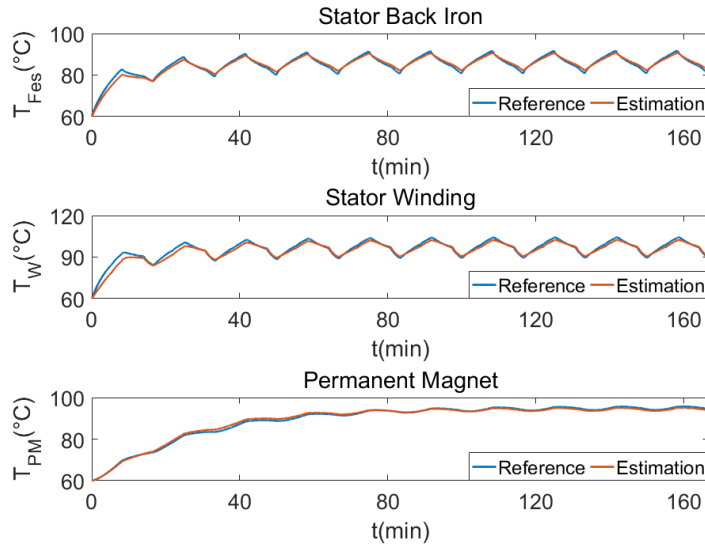


Fig. 2-26: Temperature estimation results according to the driving cycle

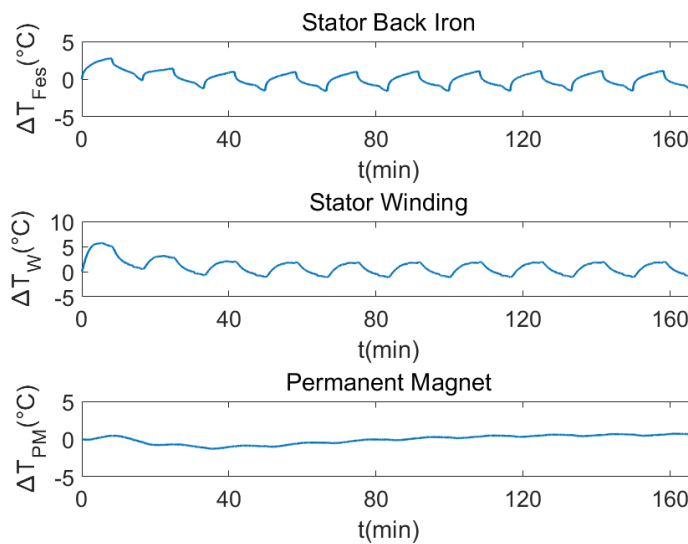


Fig. 2-27: Temperature estimation errors for the transient test

In Fig. 2-28, a load profile based on the standard WLTP Class 3 driving cycle for Nissan LEAF is considered. The thermal resistances used for temperature predictions are plotted in Fig. 2-29. The estimated three-node temperatures are shown in Fig. 2-30, together with the temperature references generated as a result of the employed duty cycle. Fig. 2-31 plots the estimation errors, where no more than  $\pm 3^\circ\text{C}$  difference between the references and estimations can be observed, showing the robustness of the system and accuracy of the identification results.

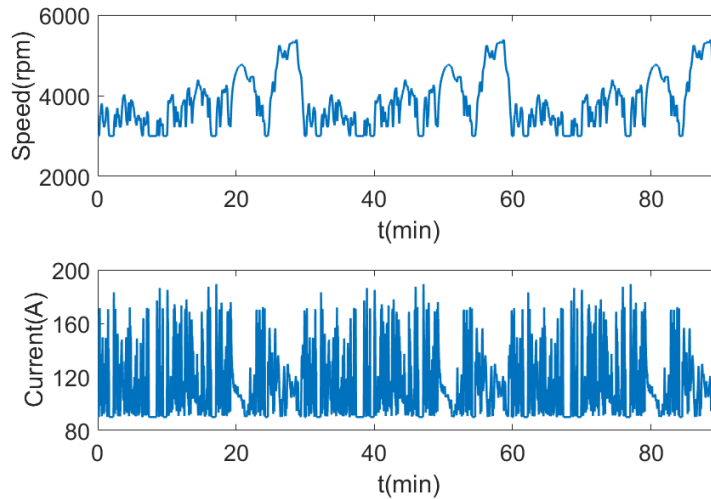


Fig. 2-28: Load profile based on the WLTP Class 3 driving cycle

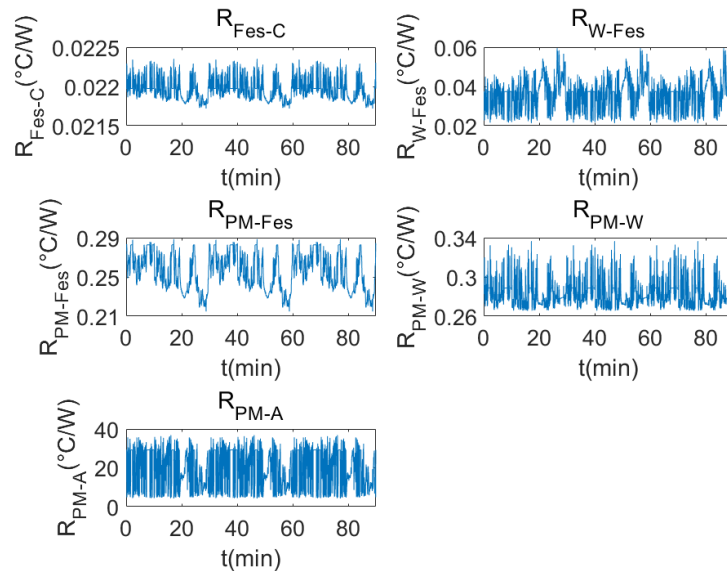


Fig. 2-29: Thermal resistances for temperature estimations

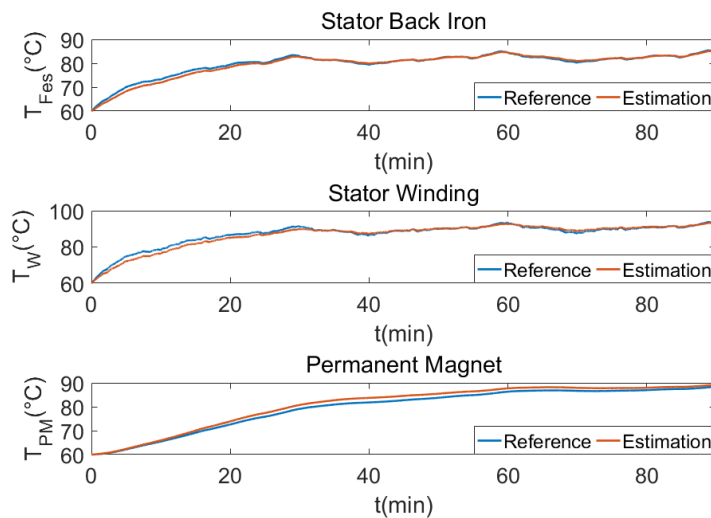


Fig. 2-30: Temperature estimations and the corresponding measurements

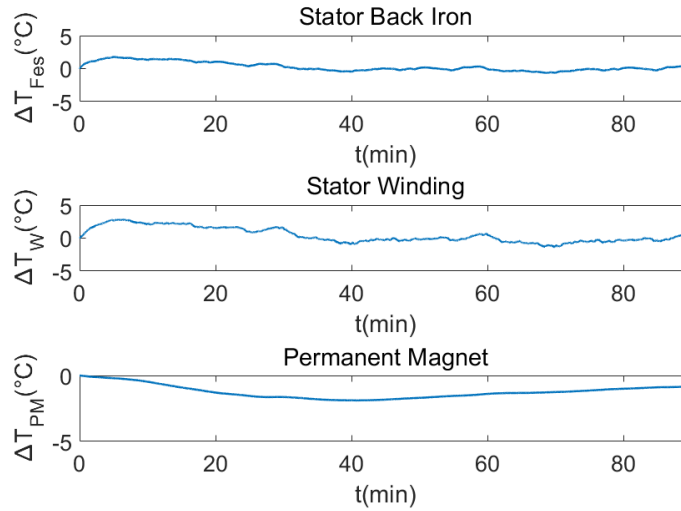


Fig. 2-31: Temperature estimation errors under the transient profiles

### 2.3.3 Loss Error Analysis

Practically, the accuracy of the presented method can be affected by motor losses. The effect of the errors in copper loss, iron loss and magnet loss on the identification algorithm, and the resulting temperature estimations is analysed in detail in the following section. The motor is assumed to operate at steady-state with  $\omega_r = 6000rpm$  and  $I = 189A$ .

#### 2.3.3.1 Copper Loss

The errors generated by current sensors and the estimation of the stator resistance are the sources of copper loss errors. This section provides a sensitivity analysis of the estimated thermal model parameters to loss uncertainties. The copper loss is changed between 50% and 250% of the Motor-CAD value. As can be seen from the result shown in Fig. 2-32, the resistance  $R_{W-Fes}$  becomes smaller with larger copper loss. It is because due to the temperatures remaining unchanged, according to Ohm's law, the resistance decreases as a result of the increased copper loss flowing into the stator iron node through heat conduction. The resistance  $R_{Fes-C}$  also decreases as the increased copper loss from the winding enhances the convection between the stator iron and cooling system. However the resistances  $R_{PM-Fes}$ ,  $R_{PM-W}$ , and  $R_{PM-A}$  are not sensitive to the change in copper loss. It could be because the convection between stator and rotor is not as dominant as the conduction in stator. Also, as mentioned earlier, the proposed method prioritises the temperature predictions best matching the references. Therefore the identified parameters do not necessarily represent the actual thermal resistances for this motor.

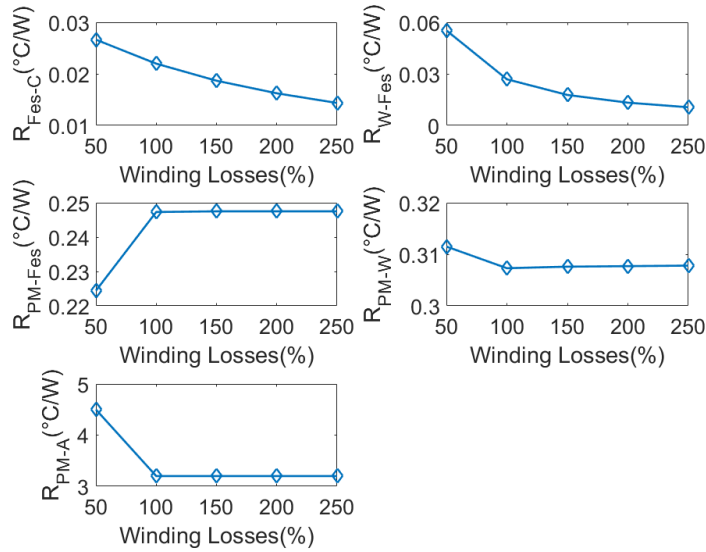


Fig. 2-32: Thermal resistances estimated with different copper losses  $P_w$  applied

### 2.3.3.2 Iron Loss

Iron loss error originates from the inaccurate iron loss modelling. Fig. 2-33 shows the estimated resistances with iron losses changed between 50% and 250%. It can be seen from Fig. 2-5 that the iron temperature at steady-state is lower than the winding and rotor temperatures, meaning that the increased iron loss only flows from the stator iron node through to the cooling system, resulting in the decrease in the estimated resistance  $R_{Fes-C}$ .

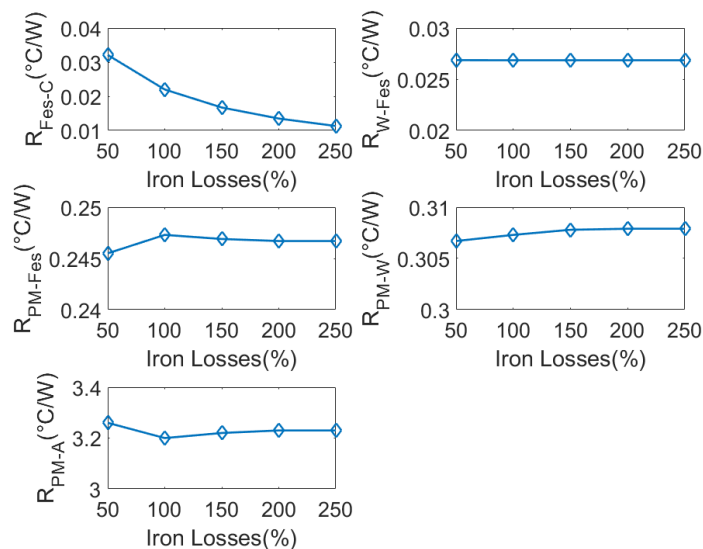


Fig. 2-33: Thermal resistances estimated with different iron losses  $P_{Fes}$  applied

### 2.3.3.3 Magnet Loss

The error in magnet loss estimation is also taken into consideration. The thermal resistances due to uncertainties in magnet losses are depicted in Fig. 2-34. The result suggests that the increased magnet losses intensify the heat transfer between rotor and ambient, while weakening the convection through air gap. It could be the reflection that the convection with ambient is predominant for rotor. It is also possible that the results are meaningful from the perspective of mathematics more than physics.

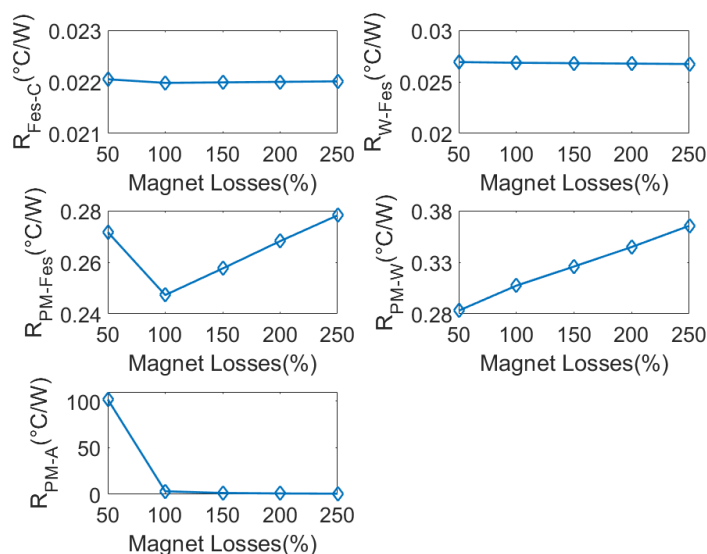


Fig. 2-34: Thermal resistances estimated with different magnet losses  $P_{PM}$  applied

### 2.3.3.4 Loss Effect on Temperature Estimation

It is expected that the node temperatures are better predicted towards the thermal steady-state where the resistances are identified. However the temperature estimations during the transient period may be affected as a result of the errors in losses. Fig. 2-35 to Fig. 2-37 show the maximum temperature errors under the influence of the winding, iron and magnet losses, respectively. In order to quantify the temperature errors produced only by the losses, it is assumed that the temperatures are perfectly estimated without the loss errors.

As can be seen from the figures below, the temperature estimation errors are generally proportional to the loss errors. At this particular motor operating condition, the stator iron contributes nearly 65% of the overall losses, and the maximum temperature error, as illustrated in Fig. 2-36, is close to  $-12^{\circ}\text{C}$ . On the other hand, the magnet loss is less than 5% of the iron loss, and no more than  $-4.5^{\circ}\text{C}$  errors in the temperature estimations are shown.

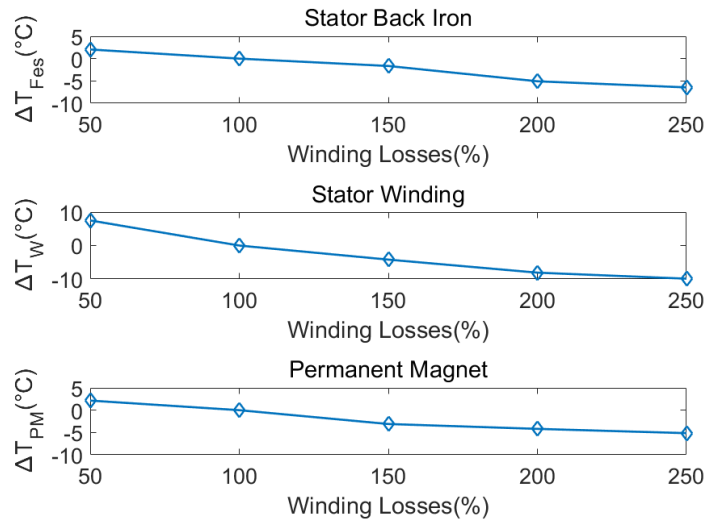


Fig. 2-35: Maximum node temperature errors with different  $P_W$  applied

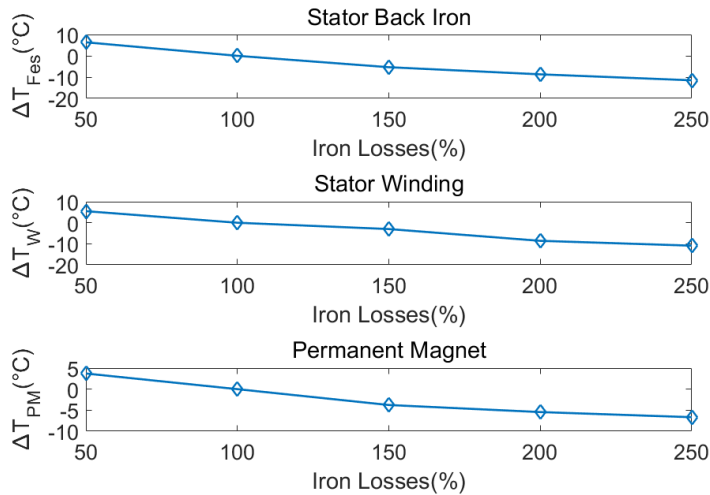


Fig. 2-36: Maximum node temperature errors with different  $P_{Fes}$  applied

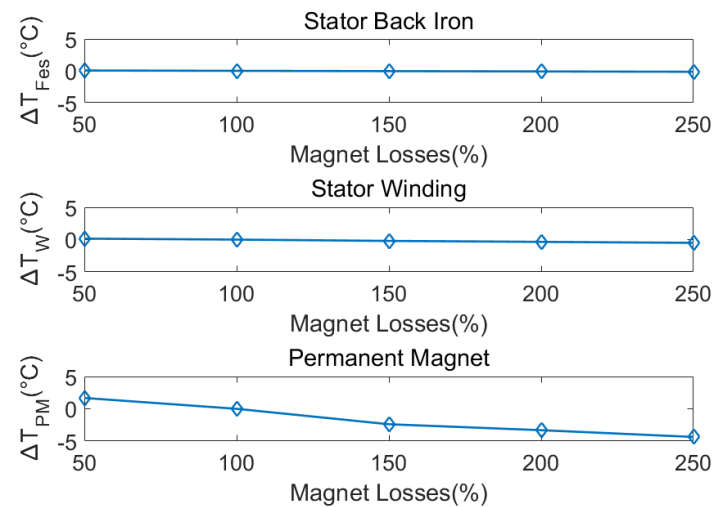


Fig. 2-37: Maximum node temperature errors with different  $P_{PM}$  applied

## 2.4 Conclusion

An empirical approach for monitoring the critical temperatures in PMSMs, based on a three-node LPTN representing stator iron, stator winding and PM, is introduced. The simplified thermal network can be described by state-space equations in which the losses and thermal capacitances can be obtained via Finite Element software, whereas the thermal resistances are predicted adopting a measurement-based parameter identification procedure. This method is computationally efficient due to the relatively simple thermal structure. Additionally, the detailed information such as the motor geometry and the thermal properties of the materials is not required. Extensive offline validation of the presented method under two driving cycles with different complexity is performed. The estimation results show relatively good match with the actual values in a broad region of speeds and currents.

Nevertheless, due to the difficulty in obtaining rotor temperature from temperature sensor in practice, an accurate estimation method which determines rotor temperature via PM flux linkage is desirable to provide the thermal network with a rotor temperature measurement. In chapter 3, an online flux linkage estimation method involving only simple electrical measurements is proposed, which is capable of estimating rotor temperature reliably and precisely. Chapter 4 demonstrates the critical temperatures in the tested motor predicted by the two methods combined, and the accuracy is satisfactory.

# Chapter 3: PWM-based Flux Linkage and Rotor Temperature Estimations for Permanent Magnet Synchronous Machines

## 3.1 Introduction

As stated in Chapter 2, direct rotor temperature measurement is particularly difficult in practice, since it is difficult to access temperature sensors on a rotating shaft. Nevertheless, rotor temperature can be obtained indirectly with the information of rotor magnet flux linkage, as permanent magnet remanence decreases with rotor temperature. The flux linkage is assumed to be dependent on temperature as:

$$\psi_m(T_{PM}) = \psi_m(T_{0,PM})[1 + \alpha_{\beta r}(T_{PM} - T_{0,PM})] \quad (3-1)$$

The temperature-dependent coefficient  $\alpha_{\beta r}$  for the most widely used NdFeB magnet is approximately  $-0.1\%/^{\circ}\text{C}$  [95]. The rotor temperature can then be calculated as:

$$T_{PM} = T_{0,PM} + \frac{1}{\alpha_{\beta r}} \left[ \frac{\psi_m(T_{PM})}{\psi_m(T_{0,PM})} - 1 \right] \quad (3-2)$$

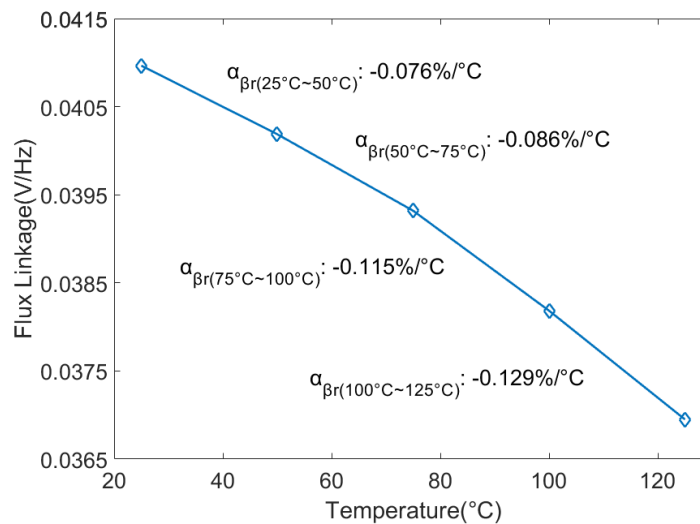


Fig. 3-1: The values of  $\alpha_{\beta r}$  at each temperature region for the tested motor

It is clear that the accuracy of the flux linkage estimation strongly influences the rotor temperature estimation due to the small temperature coefficient  $\alpha_{\beta r}$  at the denominator in (3-

2). Fig. 3-1 shows the magnet flux linkage as function of the temperature for the experimentally tested surface-mounted permanent magnet synchronous machines (SPMSM) in this chapter. The flux linkages are calculated via the back-EMFs measured at open-circuit condition at different rotor temperatures. It is clear that the temperature coefficient has a small nonlinearity with temperature which will need to be taken into account for accurate temperature prediction. Assuming a relatively small value of  $\alpha_{\beta r} = -0.076\%/^{\circ}\text{C}$ , an 1% error in flux linkage could result in a  $13^{\circ}\text{C}$  error in rotor temperature estimation.

This chapter introduces a relatively simple and accurate method for online flux linkage estimation for PMSM, which only involves the uses of motor voltages and currents in response to the standard space-vector pulse width modulation (SV-PWM). Similarly to [26], [28], knowledge of machine parameters, such as inductances, which may not be available, is not required for the estimation. In addition, this method does not need signal injection which creates undesirable disturbance to the system, as the excitation signal is intrinsic in the already-existing PWM voltage. The proposed methodology is applied to rotor temperature estimation using (3-2).

The basis of the method is presented in section 3.2, followed by the preliminary validation in offline simulation using an interior PMSM (IPMSM) model. A comprehensive real-time validation conducted using the Hardware-in-the-Loop (HIL) technique [96]-[104] is introduced in the following section. The most common issues with the practical implementation of this method, for instance, inverter non-linear effect, data acquisition sampling time, are analysed in detail as they may affect the precision of the rotor temperature estimation. Finally, the method is verified experimentally on a three-phase SPMSM. Relatively good results in a wide range of motor operating conditions are demonstrated, where the errors in the estimation of the rotor temperature are less than  $2^{\circ}\text{C}$ .

## 3.2 Fundamental Theory

The voltage equations of a PMSM represented in the rotating  $dq$ -reference frame are expressed as:

$$v_d = R_s i_d + L_d \frac{d}{dt} i_d - \omega_r L_q i_q \quad (3-3)$$

$$v_q = R_s i_q + L_q \frac{d}{dt} i_q + \omega_r (L_d i_d + \psi_m) \quad (3-4)$$

It is obvious that, rearranging the  $q$ -axis equation (3-4) it is possible to calculate the rotor flux  $\psi_m$ . This would require the measurement of voltages, currents as well as the knowledge of machine parameters  $R_s, L_d, L_q$ . However, with SV-PWM technique, voltage information can be obtained via the voltage reference vector, the location of which in relation to the active voltage vectors on the state vector diagram determines the generation of the PWM switching period [105], as shown in Fig. 3-2:

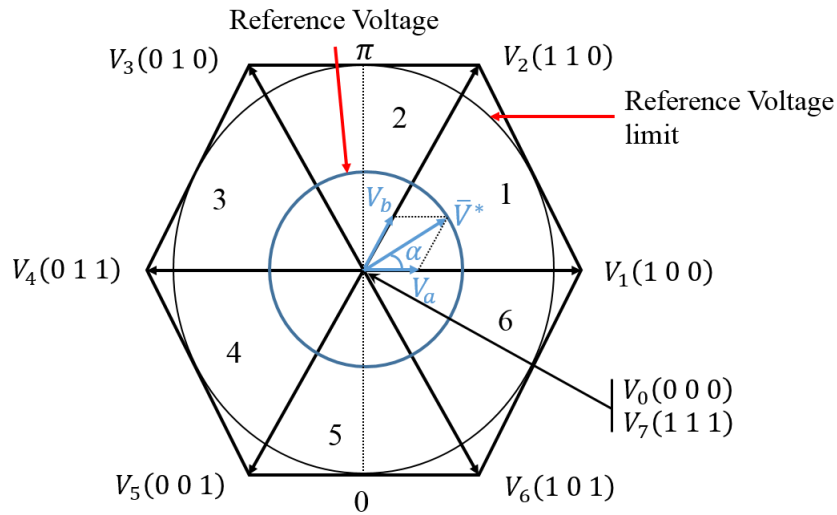


Fig. 3-2: Hexagon state vector diagram

The modulating voltage command is represented by the rotating space vector  $\bar{V}^*$ . The active state vectors  $V_1 \cdots V_6$  occupy the space with six  $60^\circ$  sectors denoted as 1  $\cdots$  6, and  $V_0$  and  $V_7$  are zero vectors. The voltage vector  $\bar{V}^*$  has two components  $\bar{V}_a$  and  $\bar{V}_b$  lying along each of the adjacent vectors, and the magnitudes of these two components reflect the amount of time the vectors are applied. Due to the voltage command being equal to the average PWM output, the following relationship can be obtained:

$$\bar{V}^* = \bar{V}_a + \bar{V}_b = \frac{\bar{V}_1 t_a + \bar{V}_2 t_b + (\text{either } \bar{V}_0 \text{ or } \bar{V}_7) t_0}{t_{\text{switching}}} \quad (3-5)$$

The voltage terms  $\bar{V}_a, \bar{V}_b$  are phase quantities. The remaining interval  $t_0$  in a switching period  $t_{\text{switching}}$  is filled with zero-voltage vector. Therefore:

$$t_a = \frac{|\bar{V}_a|}{|\bar{V}_1|} t_{\text{switching}} \quad (3-6)$$

$$t_b = \frac{|\bar{V}_b|}{|\bar{V}_2|} t_{\text{switching}} \quad (3-7)$$

$$t_0 = t_{switching} - t_a - t_b \quad (3-8)$$

Compared to [28] in which the injection of a zero-voltage vector is required, the use of the inherent SV-PWM zero-voltage period  $t_0$  for the estimation of the PM flux linkage is the novel contribution of the thesis. The voltage components  $|\bar{V}_a|$  and  $|\bar{V}_b|$  can be retrieved from the vector diagram. For the location of the reference vector  $\bar{V}^*$  shown in Fig. 3-2:

$$|\bar{V}_a| \sin \frac{\pi}{3} = |\bar{V}^*| \sin \left( \frac{\pi}{3} - \alpha \right) \quad (3-9)$$

$$|\bar{V}_b| \sin \frac{\pi}{3} = |\bar{V}^*| \sin \alpha \quad (3-10)$$

which lead to:

$$|\bar{V}_a| = \frac{2}{\sqrt{3}} |\bar{V}^*| \sin \left( \frac{\pi}{3} - \alpha \right) \quad (3-11)$$

$$|\bar{V}_b| = \frac{2}{\sqrt{3}} |\bar{V}^*| \sin \alpha \quad (3-12)$$

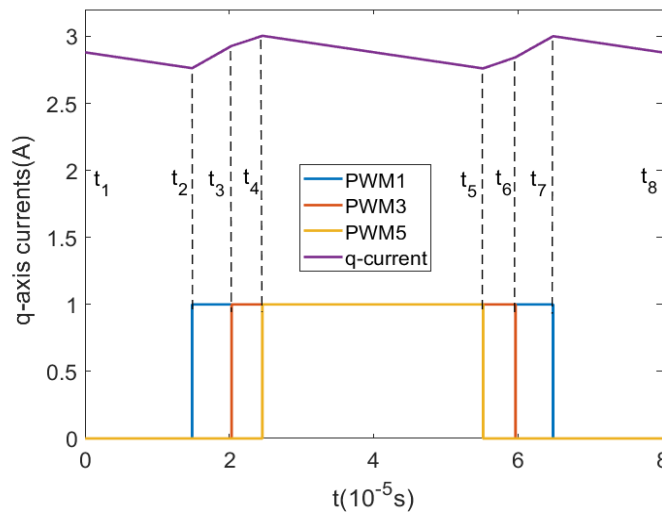


Fig. 3-3: Gate signals PWM1, PWM3, PWM5, and the corresponding current variation in a single switching period

Fig. 3-3 shows an example of a single PWM switching period with a duration of  $t_{switching} = 1/f_{sw}$ , PWM1, PWM3, PWM5 being the logic signals controlling the turn-on of the top three devices in a standard two-level voltage-source inverter.  $t_1 \dots t_8$  are the time instants at which a different voltage vector is applied. The  $q$ -axis equation (3-4) can be discretized with a

sampling time  $T_s \ll t_{switching}$ . The resultant relationships between two adjacent sampling points, assuming the  $d$ -axis current to be controlled to zero, are given as:

$$v_{q(t_1 \sim (t_1+T_s))} = R_s i_{q(t_1 \sim (t_1+T_s))} + L_q \frac{d}{dt} i_{q(t_1 \sim (t_1+T_s))} + \omega_r \psi_m \quad (3-13)$$

$$v_{q((t_1+T_s) \sim (t_1+2T_s))} = R_s i_{q((t_1+T_s) \sim (t_1+2T_s))} + L_q \frac{d}{dt} i_{q((t_1+T_s) \sim (t_1+2T_s))} + \omega_r \psi_m \quad (3-14)$$

⋮

$$v_{q((t_1+(n-2)T_s) \sim t_8)} = R_s i_{q((t_1+(n-2)T_s) \sim t_8)} + L_q \frac{d}{dt} i_{q((t_1+(n-2)T_s) \sim t_8)} + \omega_r \psi_m \quad (3-15)$$

Where  $t_1$  is the starting point of the PWM period in Fig. 3-3. It is worth noticing that, the total number of the sampling points  $n$  in the period must be an integer to guarantee an integer number of equations. The speed  $\omega_r$  is assumed to be constant during the switching period. The derivative term can be approximated by:

$$di_q/dt \approx \frac{i_{q(t_1+(k+1)T_s)} - i_{q(t_1+kT_s)}}{T_s} \quad (3-16)$$

with  $k = 0, 1 \dots n - 2$ . It is noted that the last sampling point in the period is  $t_8 = t_1 + (n - 1)T_s$ .

When the motor operates at steady-state, the current loop controller only responds to the currents measured at the beginning of the non-zero active voltage vectors, which are  $i_{q(t_2)}$  and  $i_{q(t_5)}$  and ensures that on average they remain constant in steady-state condition. This means  $i_{q(t_2)} = i_{q(t_5)}$ ,  $i_{q(t_4)} = i_{q(t_7)}$  and also  $i_{q(t_1)} = i_{q(t_8)}$ .

Multiplying the  $n - 1$  equations by the sampling time  $T_s$  gives:

$$T_s v_{q(t_1 \sim (t_1+T_s))} = T_s R_s i_{q(t_1 \sim (t_1+T_s))} + L_q (i_{q(t_1+T_s)} - i_{q(t_1)}) + T_s \omega_r \psi_m \quad (3-17)$$

$$\begin{aligned} T_s v_{q((t_1+T_s) \sim (t_1+2T_s))} \\ = T_s R_s i_{q((t_1+T_s) \sim (t_1+2T_s))} + L_q (i_{q(t_1+2T_s)} - i_{q(t_1+T_s)}) + T_s \omega_r \psi_m \end{aligned} \quad (3-18)$$

⋮

$$\begin{aligned} T_s v_{q((t_1+(n-2)T_s) \sim t_8)} \\ = T_s R_s i_{q((t_1+(n-2)T_s) \sim t_8)} + L_q (i_{q(t_8)} - i_{q(t_1+(n-2)T_s)}) + T_s \omega_r \psi_m \end{aligned} \quad (3-19)$$

Now adding each equation to the next, it yields:

$$T_s \sum_{j=1}^{n-1} v_{q(j)} = T_s R_s \sum_{j=1}^{n-1} i_{q(j)} + t_{switching} \omega_r \psi_m \quad (3-20)$$

where  $j$  is the  $j^{\text{th}}$  equation. It can be noticed that the inductance-related terms are eliminated.

With regard to the voltage terms, it is evident that the voltage sum  $T_s \sum_1^{n-1} v_{q(j)}$  is always equivalent to the average PWM output voltage:

$$T_s \sum_1^{n-1} v_{q(j)} = (t3 - t2)v_{q(t3-t2)} + (t4 - t3)v_{q(t4-t3)} + (t6 - t5)v_{q(t6-t5)} + (t7 - t6)v_{q(t7-t6)} \quad (3-21)$$

It can be easily verified that:

$$(t3 - t2)v_{q(t3-t2)} = (t7 - t6)v_{q(t7-t6)} \quad (3-22)$$

$$(t4 - t3)v_{q(t4-t3)} = (t6 - t5)v_{q(t6-t5)} \quad (3-23)$$

as the switching period consists of two symmetrical switching combinations. Therefore, equation (3-20) now becomes:

$$2[(t3 - t2)v_{q(t3-t2)} + (t4 - t3)v_{q(t4-t3)}] = T_s R_s \sum_1^{n-1} i_{q(j)} + t_{switching} \omega_r \psi_m \quad (3-24)$$

Also, the time differences  $(t3 - t2)$  and  $(t4 - t3)$  can be pre-calculated at the beginning of the SV-PWM based on the location of the rotating voltage reference vector on the space vector diagram, and  $v_{q(t3-t2)}$  and  $v_{q(t4-t3)}$  are the results of the switching vectors being transformed from  $\alpha\beta$ -reference frame to  $dq$ -reference frame. The MATLAB code of the derivation of the voltage term in (3-24) is shown in Appendix C. In conclusion, the rotor flux can be calculated as:

$$\psi_m = \frac{f_{sw}}{\omega_r} 2[(t3 - t2)v_{q(t3-t2)} + (t4 - t3)v_{q(t4-t3)}] - \frac{f_{sw}}{\omega_r} T_s R_s \sum_1^{n-1} i_{q(j)} \quad (3-25)$$

However, it is clear that this method is not able to estimate the flux linkage correctly under zero-speed condition, because the back-EMF term in (3-4) equals to zero. In addition, due to the fact that the derivation of (3-25) is based on the assumption of steady-state motor operation during one PWM switching period, the estimation would be incorrect with a high-dynamic load applied.

### 3.3 Offline Validation

The presented method is tested offline in MATLAB/Simulink, in which an IPMSM simulation model is controlled with a FOC, along with SV-PWM. The model parameters are listed in

Table III. The rotor position is derived from the motor electrical speed, which is the product of the motor mechanical speed and pole pairs.

Quantity	Unit	Value
Peak Torque	Nm	70
Rated Torque	Nm	35.5
Base Speed	r/min	1350
Max Speed	r/min	4500
Peak Power	kW	9.9
Rated Power	kW	5
DC Link Voltage	V	120
Peak Current	A	125
No. of Pole-pairs	--	3
No. of Slots	--	36
Active Stack Length	mm	118
Stator Outer Diameter	mm	150
Rotor Outer Diameter	mm	80
Stator Resistance	$\Omega$	0.0545
$d$ -axis Inductance	mH	0.8258
$q$ -axis Inductance	mH	1.8711
PM Flux Linkage	Wb	0.1121

Fig. 3-4 and Fig. 3-5 demonstrate the estimated flux linkages when the machine operates in a wide range of rotor speeds and stator currents. The results show a good agreement between the estimations and the nominal value. The small deviation ( $Error\% = \left(\frac{\hat{\psi}_m - \psi_m}{\psi_m}\right) \times 100$ ) exists because the small voltage drops across the power switches ( $0.001\Omega$  in resistance) and shunt resistors ( $0.01\Omega$ ) are taken into consideration in the inverter model, resulting in a slight mismatch between the command and PWM voltages.

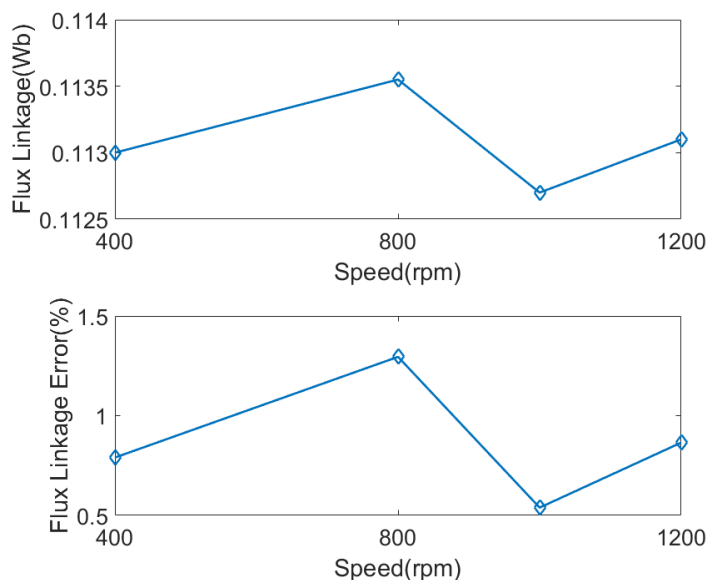


Fig. 3-4: Flux linkage estimations (top) and the corresponding errors (bottom) at 400rpm, 800rpm, 1000rpm, and 1200rpm rotor speeds

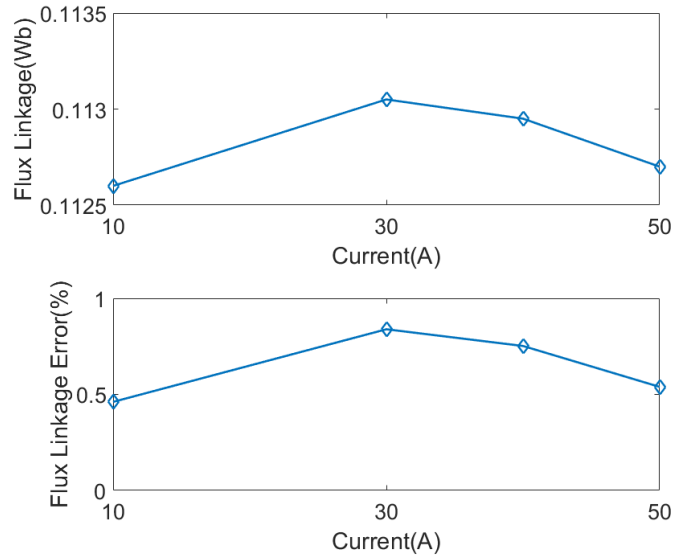


Fig. 3-5: Flux linkage estimations (top) and the corresponding errors (bottom) at  $i_q = 10A, 30A, 40A,$  and  $50A$

Fig. 3-6 and Fig. 3-7 compare the voltage commands with the PWM voltages at the same operating conditions as in Fig. 3-4 and Fig. 3-5. It is confirmed that the small error in voltage command, is the main contributor to the error in flux linkage estimation.

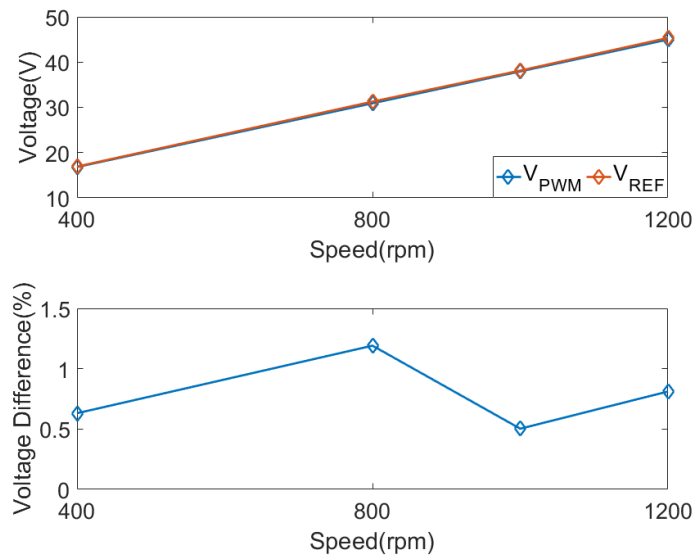


Fig. 3-6: Command and PWM voltages (top) and their differences (bottom) at  $400rpm, 800rpm, 1000rpm,$  and  $1200rpm$  rotor speeds

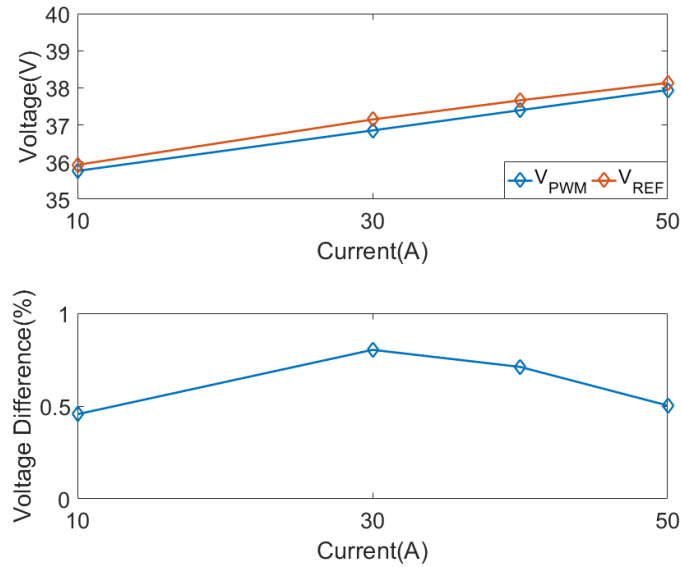


Fig. 3-7: Command and PWM voltages (top) and their differences (bottom) at  $i_q = 10A, 30A, 40A,$  and  $50A$

Fig. 3-8 shows the results of the flux linkage and rotor temperature estimations after a step-based profile is applied to the rotor temperature, which generates the step variations in the flux linkage according to (3-2). A 4<sup>th</sup> order Butterworth low-pass filter with the passband edge frequency of  $1Hz$  is employed after the flux linkage estimation in order to extract its average value. This is found adequate in practice because the temperature varies only very slowly. It can be seen from Fig. 3-8 that, the estimation keeps good track of the nominal values, and the error in the flux linkage due to some inverter non-ideal effects is modest, leading to no more than  $8^{\circ}C$  error in the rotor temperature.

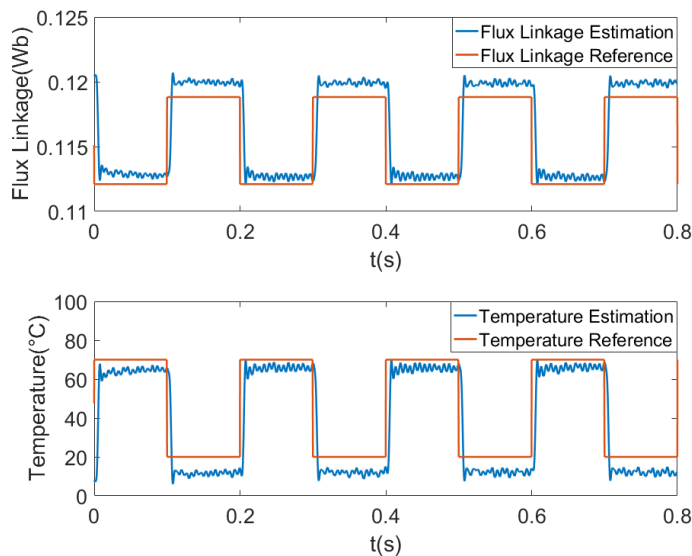


Fig. 3-8: Flux linkage (top) and rotor temperature (bottom) estimations according to the step-based profile

## 3.4 Real-time simulation

### 3.4.1 Experimental Setup

The proposed methodology is validated in real-time simulation on the IPMSM model. The HIL technique is adopted, which is able to precisely replicate the dynamics of the physical equipment with computer models running on real-time platforms and therefore is an excellent replacement to the expensive conventional testing. Fig. 3-9 describes the HIL implementation, in which machine and power converter are simulated on the FPGA-based National Instrument (NI) myRIO-1900 data acquisition and control platform. It is programmed with LabVIEW, which is an engineering software using graphical notations to create programs. The real-time modelling has been validated in [104]. A standard FOC along with SV-PWM and the proposed flux linkage estimation are implemented in the OPAL-RT 5600 platform, where the code is programmed through RT-LAB — a real-time simulation software fully integrated with MATLAB/Simulink.

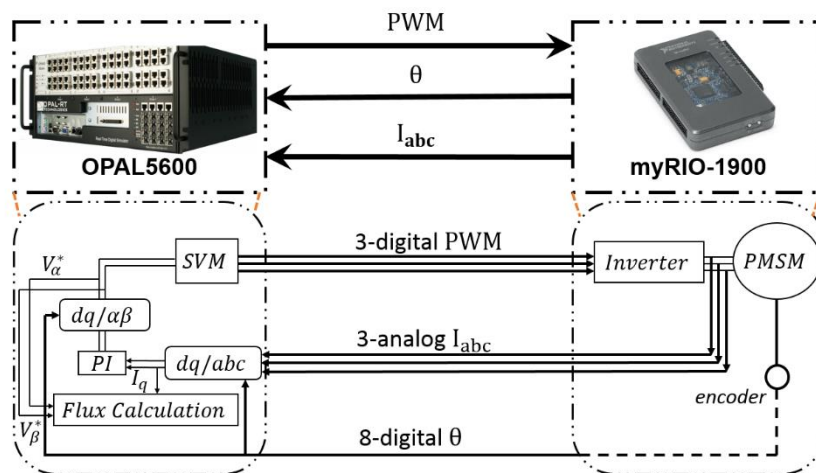


Fig. 3-9: HIL implementation scheme

The sampling time for myRIO-1900 is set to  $1\mu s$ , which is calculated by:

$$T_{second} = \frac{T_{count}}{f_{system}} \quad (3-26)$$

where  $T_{second}$  and  $T_{count}$  are the sampling time expressed in second and in FPGA clock ticks, which is determined by the system frequency  $f_{system}$ . With regard to OPAL-RT,  $10\mu s$  is used due to the requirement of completing relatively complex calculations (3-25) and the standard FOC algorithm within one sampling step.

The current is transferred from myRIO through the FPGA I/O Node. The data is represented in binary, and converted into the analog output in a range of  $[-10V, 10V]$ . On the other side, OPAL-RT receives the current signals via a 16-channel analog I/O module with the programmable range up to  $\pm 16V$ . Fig. 3-10 demonstrates the phase currents employed for the flux linkage estimation at  $i_{q\_command} = 2.9A$ .

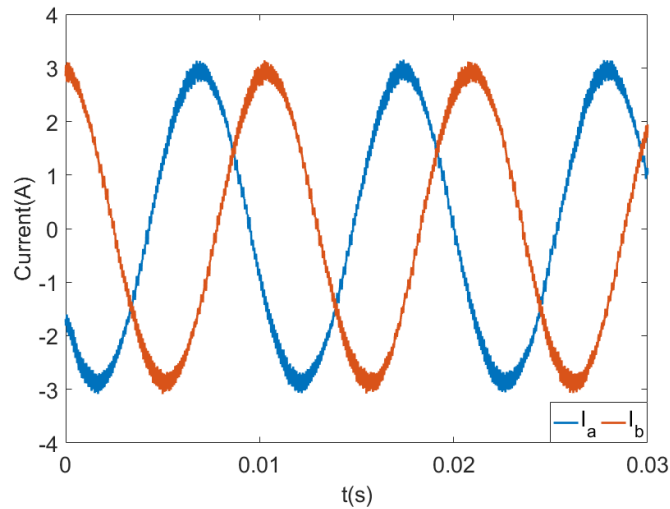


Fig. 3-10: Phase current at  $i_{q\_command} = 2.9A$

The rotor angle can be derived from the rotor speed, simply adopting:

$$\theta = \int \omega_r dt \quad (3-27)$$

in which  $dt$  is the sampling time  $1\mu s$ . The calculated angle is rescaled from  $[-\pi, \pi]$  to  $[-127, 127]$ , which following the conversion into a 7-bit signed binary number, is transferred into OPAL-RT with a 16-channel digital I/O module. Fig. 3-11 shows the rotor angle depicted in OPAL-RT.

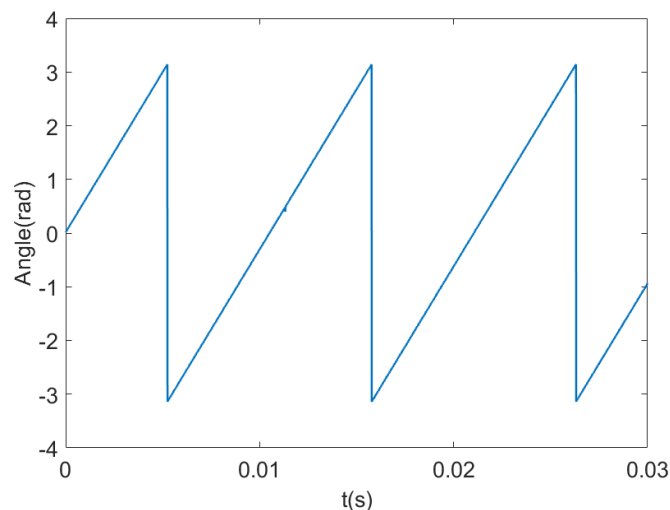


Fig. 3-11: Rotor angle in OPAL-RT

The Hardware-in-the-loop arrangement introduces a short delay between the two devices, resulting in errors in flux linkage estimation. In order to quantify this delay time, a simple test of the current of a first-order RL circuit responding to a pulse voltage signal, is carried out, emulating OPAL-RT generating three-phase PWM and acquiring current. The voltage is simulated in OPAL-RT and the data transferred into myRIO where the RL circuit is. An oscilloscope displays the voltage and the resulting current, which are shown in Fig. 3-12. It can be seen from Fig. 3-12 that, the responding time of the current to the voltage is approximately  $12\mu\text{s}$ , which is the delay time produced by myRIO. The current is transferred into OPAL-RT and plotted along with the pulse voltage in Fig. 3-13. The voltage and current are rescaled for a clear illustration of the time difference between them due to the delay from both myRIO and OPAL-RT.

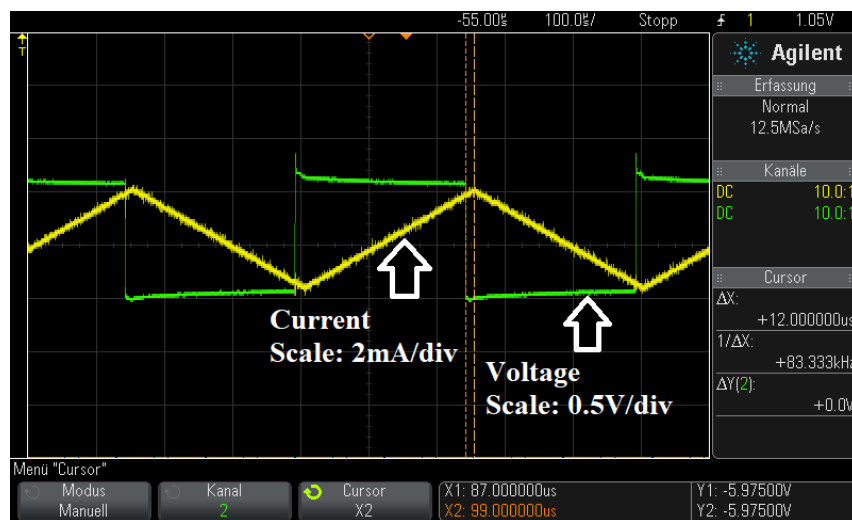


Fig. 3-12: Delay between the voltage (green) and current (yellow) in the first-order RL circuit test due to myRIO

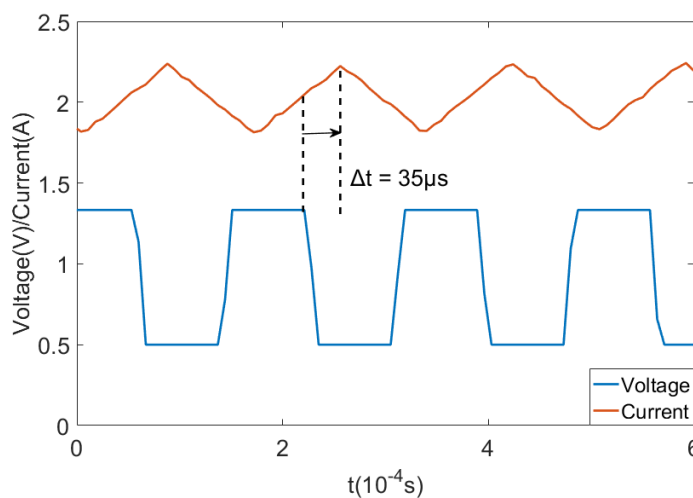


Fig. 3-13: Delay times due to myRIO and OPAL-RT

### 3.4.2 Steady-state Test

The theory upon which the proposed method is based, is tested in real-time simulation. Fig. 3-14 shows the  $q$ -axis current variation as well as the three PWM signals from SV-PWM. It can be seen that at steady-state conditions, the currents at the beginning of the non-zero voltage periods are always identical, as a result of PI controller regulating the average  $q$ -axis current.

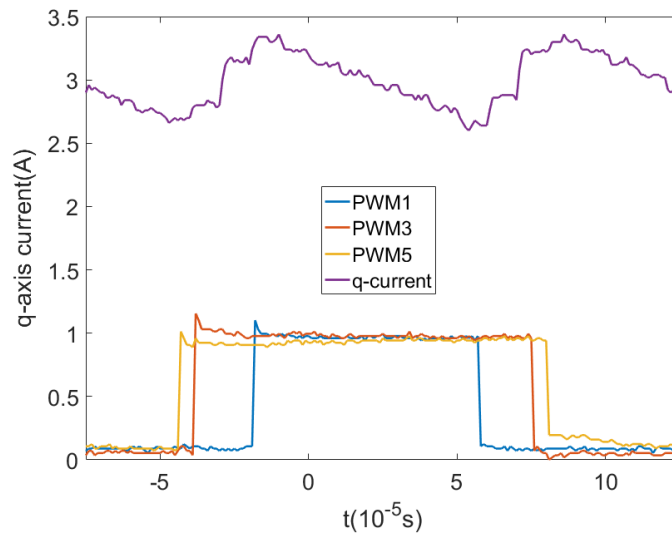


Fig. 3-14: PWM1, PWM3, PWM5 and the corresponding  $q$ -axis current variation within one switching period in real-time simulation

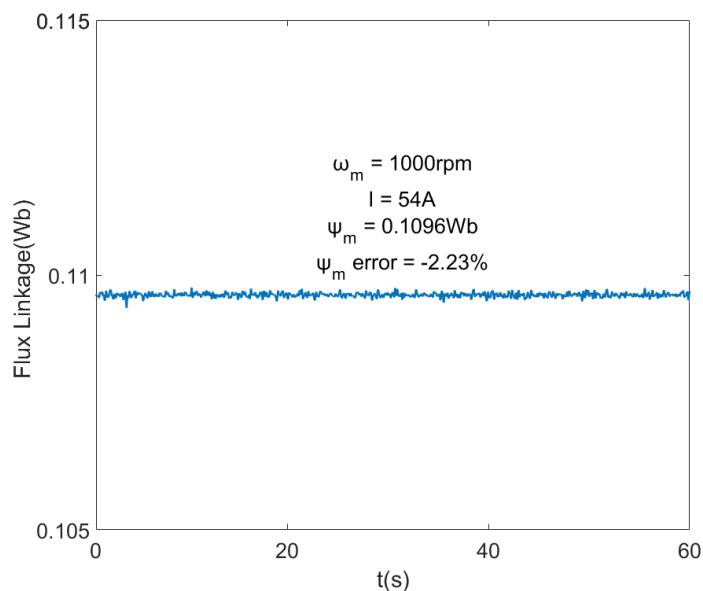


Fig. 3-15: Flux linkage estimation at  $1000\text{rpm}$  rotor speed and rated torque ( $I = 54\text{A}$ )

Fig. 3-15 depicts the flux linkage estimation when the motor operates at the rated torque and a relatively high speed ( $1000rpm$ ) at room temperature. It shows that the estimated flux linkage is approximately  $0.1096Wb$ , corresponding to  $-2.23\%$  estimation error with respect to the nominal value.

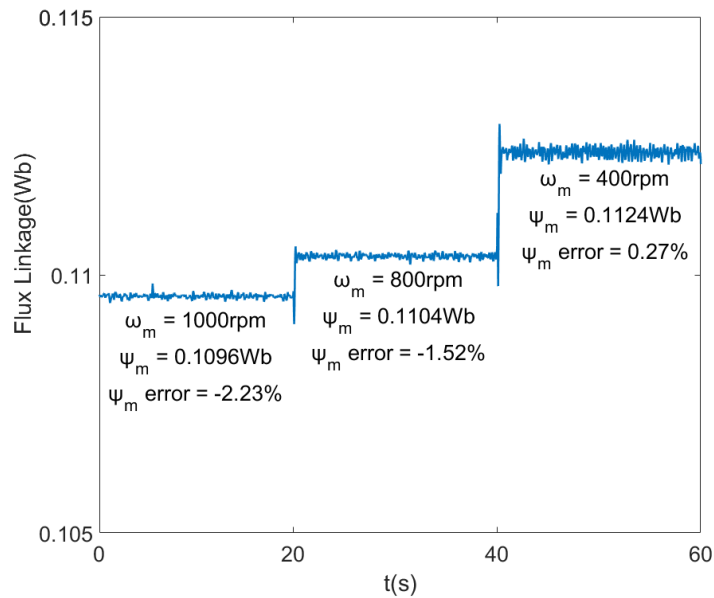


Fig. 3-16: Flux linkage estimations at  $1000rpm$ ,  $800rpm$ , and  $400rpm$  rotor speeds

Fig. 3-16 shows the estimated flux linkages under the operating conditions that torque (current) and room temperature remain unchanged while  $1000rpm$ ,  $800rpm$  and  $400rpm$  speeds are applied at  $t = 0s$ ,  $t = 20s$  and  $t = 40s$ , respectively. In comparison to the nominal value, the flux linkage errors are  $-1.52\%$  at  $800rpm$  and  $0.27\%$  at  $400rpm$ .

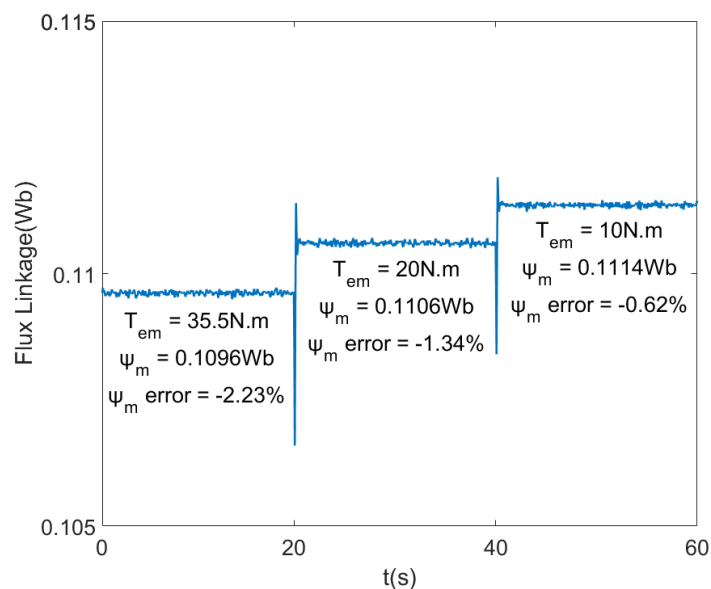


Fig. 3-17: Flux linkage estimations at  $35.5Nm$ ,  $20Nm$ , and  $10Nm$  electromechanical torques

Fig. 3-17 illustrates the results with three different values of torques (rated,  $20Nm$  and  $10Nm$ ) being imposed at  $t = 0s$ ,  $t = 20s$  and  $t = 40s$ , in which  $-1.34\%$  and  $-0.62\%$  deviations are observed at  $20Nm$  and  $10Nm$ .

The slight differences in the flux linkage estimations at different conditions are mainly due to the fact that the calculation uses command voltages which are slightly different from the voltages applied to the motor due to small inaccuracy in the real-time emulations.

Furthermore, the current signals used for the flux linkage calculation are acquired by the control unit with a sampling time of  $10\mu s$ , which is relatively large. A practical switching frequency of  $5kHz$  for SV-PWM is employed. The usage of  $10\mu s$  ensures the number of the sampling points, and thus the number of the equations, in a switching period is integer. With the relatively slow  $10\mu s$  sampling time, some errors in the ability to correctly capture variable voltages and currents are inevitable. However the effect on the precision of the method is relatively modest.

### 3.4.3 Transient Test

A simplified case is considered where the machine is controlled at the rated torque and a constant speed of  $500rpm$ , whereas a test cycle is used to generate a thermal transient which affects the rotor temperature and flux linkage. Excellent estimation results using the proposed method and the corresponding rotor temperature variations are shown in Fig. 3-18.

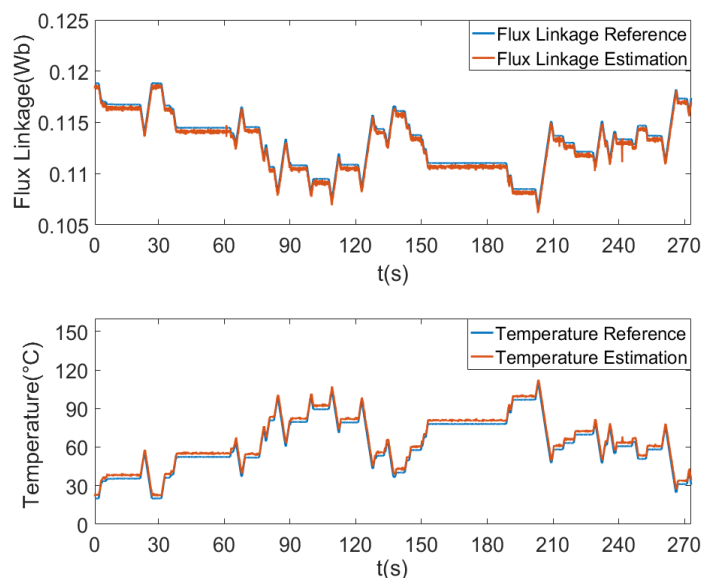


Fig. 3-18: Flux linkage (top) and rotor temperature (bottom) estimations at the rated torque and  $500rpm$  rotor speed, according to the transient test cycle

The errors of approximately 0.3% in flux linkage and  $-3^{\circ}\text{C}$  in rotor temperature are demonstrated in Fig. 3-19.

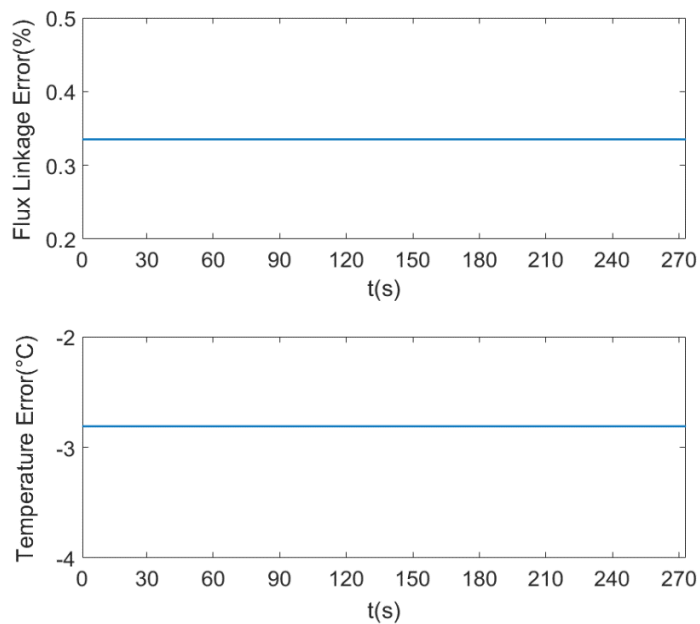


Fig. 3-19: Flux linkage (top) and rotor temperature (bottom) estimation errors for the test in Fig. 3-18

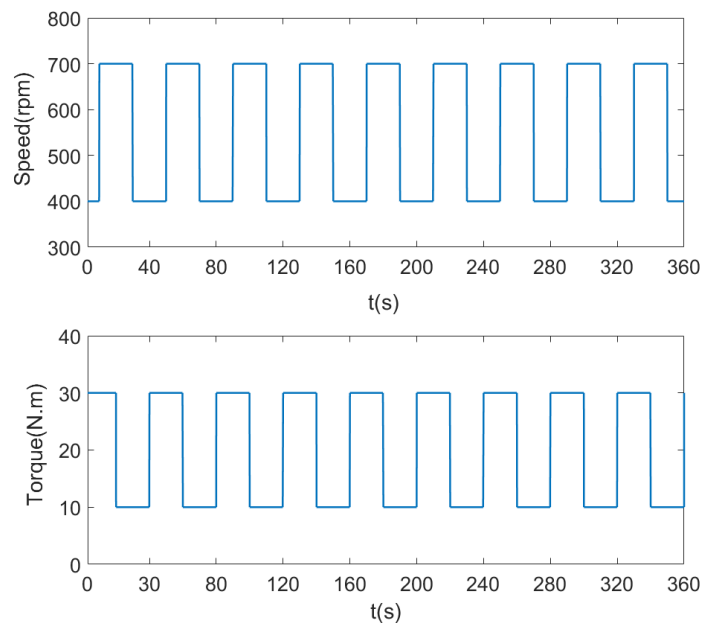


Fig. 3-20: Load profile

A three-node LPTN consisting of the stator iron, stator winding and PM nodes, as illustrated in Fig. 2-1 is also used for the thermal evaluation in the real-time simulations.  $P_W$  is the copper loss and simply calculated by  $P_W = I^2 R_s$ . The speed-dependent iron loss can be approximated by the sum of the losses for open-circuit and short-circuit conditions described by (1-82) and (1-83), and is allocated into the stator iron and PM nodes according to the proportion of the

iron utilized in stator and rotor [91]. In order to validate the proposed method in non-stationary conditions, a driving cycle with simple step variations in speed and torque as plotted in Fig. 3-20 is considered.

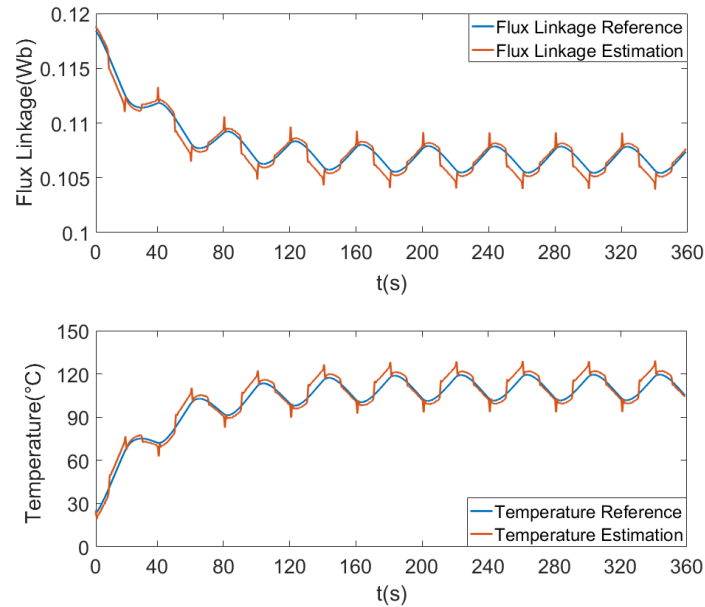


Fig. 3-21: Flux linkage (top) and rotor temperature (bottom) estimations, according to the test duty cycle used on the simplified three-node thermal network

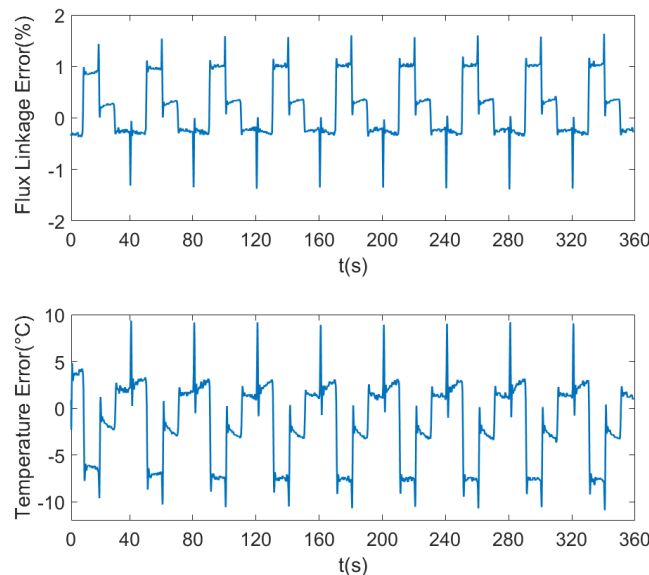


Fig. 3-22: Flux linkage (top) and rotor temperature (bottom) estimation errors in Fig. 3-21

It can be seen from Fig. 3-21 and Fig. 3-22 that, less than  $\pm 2\%$  errors in flux linkage estimation are obtained, and all estimated rotor temperatures lie within an approximately  $\pm 10^{\circ}\text{C}$  band around their corresponding nominal values. Unfortunately, a very small error in the flux linkage estimation is amplified in the estimation of temperature due to the very small temperature

coefficient  $\alpha_{\beta r}$ . Nevertheless, the error in the temperature estimation is contained within  $\pm 9\%$ . Some dependency of the estimation on the operating conditions (speed, current) is apparent. This is due to the relatively slow acquisition of  $10\mu s$  which creates small errors in the timing and current/voltage measurement that change with a variable modulation index. It is expected that these effects can be minimised with a faster acquisition unit.

### 3.5 Practical Implementation Error Analysis

In practice, flux linkage estimation could be inaccurate due to a number of sources of error. The effect of these errors on the proposed methodology can be potentially significant and therefore is evaluated in this section using a simulation model of the experimentally tested SPMSM controlled using a standard field-oriented motor control with SV-PWM. The motor parameters are specified in Table IV.

Table IV: Parameters of the SPMSM

Quantity	Unit	Value
Continuous Torque	Nm	0.2754
Max Speed	r/min	6000
DC Link Voltage	V	24
Peak Current	A	7.1
No. of Pole-pairs	--	4
No. of Slots	--	18
Stator Resistance	$\Omega$	0.36
$d$ -axis Inductance	mH	0.1569
$q$ -axis Inductance	mH	0.1569
PM Flux Linkage	V/Hz	0.0409

The voltage used for the calculation can be the command voltages generated by the controller in the standard FOC. However, due to the command voltages being affected by some motor control issues, such as inverter dead-times and voltage drops on the power switches, which will significantly affect the accuracy of the estimation, phase voltages are directly measured and the actual voltage command calculated from  $v_{abc}$  after suitable filtering with a 4<sup>th</sup> order Butterworth low-pass filter with the passband edge frequency of 10Hz in order to obtain the average  $v_{dq}$ .

In steady-state conditions and assuming  $i_d = 0$ , rearranging the  $q$ -axis equation (3-4) it is possible to calculate the rotor flux  $\psi_m$  as:

$$\psi_m = \frac{v_q - R_s i_q}{\omega_r} \quad (3-28)$$

This simple method, denoted as ‘averaged model’ in the following, requires the measurements of voltage, current as well as the knowledge of machine parameter  $R_s$ . It is evident that the precision of rotor flux estimation relies on the precise knowledge of  $R_s$  and the stator voltage. The following analysis compares the accuracy of rotor flux estimation based on (3-28) with the more accurate estimation based on the averaging of phase-voltage measurement during a PWM period, introduced in section 3.2.

### 3.5.1 Sampling Time

The estimation error in relation to limited sampling speed will be analysed in this section. The simulation is performed assuming the machine and control models are sampled every  $1\mu s$ , whereas the sampling rate for the estimation is set to  $1\mu s$ ,  $2\mu s$ ,  $5\mu s$ ,  $10\mu s$ , and  $20\mu s$ , respectively. The flux linkage results shown in Fig. 3-23 indicate that the error increases with larger sampling time. The switching frequency is assumed to be  $10\text{ kHz}$ . The error is also dependent on the operating conditions (speed, current). This is because different modulation indices result in different duration of the active vectors in the PWM period, i.e. the periods  $(t3 - t2)$ ,  $(t4 - t3)$ .

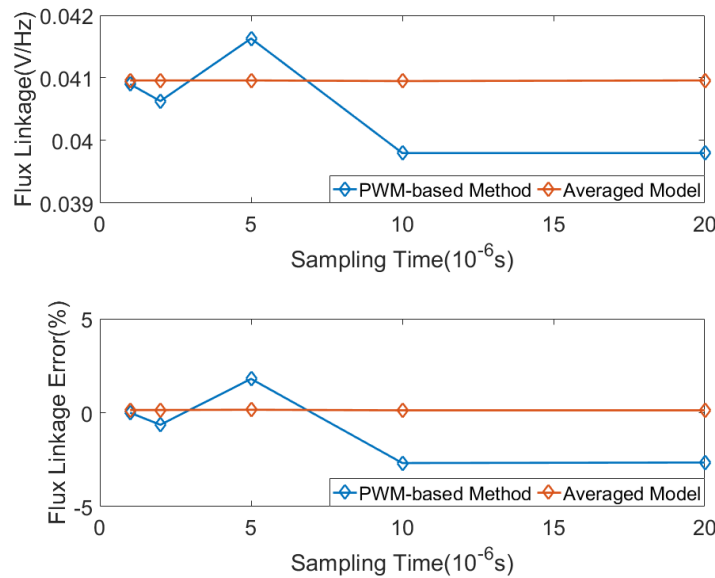


Fig. 3-23: Flux linkage estimations (top) and the corresponding errors (bottom) at  $1\mu s$ ,  $2\mu s$ ,  $5\mu s$ ,  $10\mu s$ , and  $20\mu s$  sampling times

Fig. 3-24 shows the PWM voltages as a result of the three phase voltages being sampled at  $1\mu s$ ,  $2\mu s$ ,  $5\mu s$ ,  $10\mu s$ , and  $20\mu s$ , respectively, and the command voltages at these sampling times. It can be concluded that, the error in voltage measurements, which reflect on  $(t3 - t2)$  and  $(t4 - t3)$ , largely contribute to the error in the flux linkage estimation. The voltage

command on the other hand is not influenced by sampling time, because it is calculated by the control per se. The current errors however are very small and only have minor effect on the estimation results as the average  $q$ -axis currents at different sampling rates remain the same.

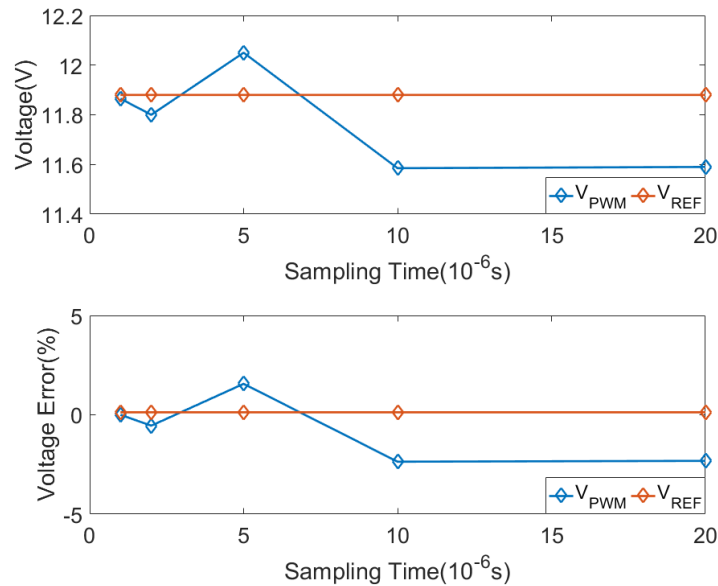


Fig. 3-24: Command and PWM voltages (top) and their corresponding errors (bottom) at  $1\mu s$ ,  $2\mu s$ ,  $5\mu s$ ,  $10\mu s$ , and  $20\mu s$  sampling times

### 3.5.2 Inverter Dead-time Effect

Inverter dead-time effect is the direct result of a delay time between the opening of the upper switch and the closing of the lower switch, altering the effective output voltage. Increased dead-time results in increased difference between the command voltage and the actual voltage. Several dead-times ranging from  $0.5\mu s$  to  $10\mu s$ , are applied manually between the three phase PWM and their corresponding complementary signals for the purpose of simulating this particular phenomenon. Fig. 3-25 plots the flux linkage estimations along with the errors in comparison to the nominal value.

As can be seen in the figure above, the accuracy of the estimation adopting the simplified method (3-28) is worsened as dead-time increases, which is the reflection of the increasing difference between the command voltage and the resulting PWM voltages. On the contrary, no more than  $\pm 0.01\%$  error results from the PWM-based method, for the reason that the voltage and current are measured and the ones used for motor operations.

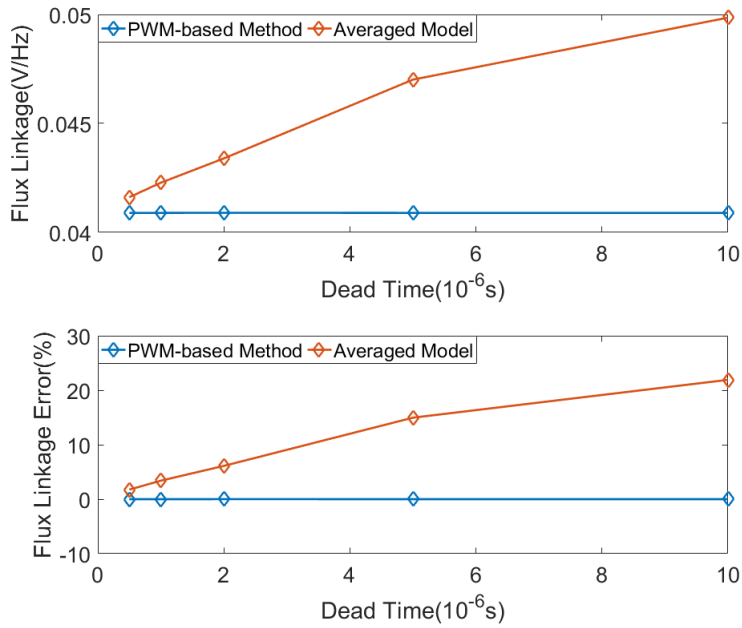


Fig. 3-25: Flux linkage estimations (top) and the corresponding errors (bottom) with  $0.5\mu s$ ,  $1\mu s$ ,  $2\mu s$ ,  $5\mu s$ , and  $10\mu s$  dead-times applied

### 3.5.3 PM Flux Linkage Harmonics

In reality, rotor flux linkage contains some high-order harmonics because of slotting effects and additional harmonics in the air gap magnetic field. This effect is investigated by adding a third-order harmonic to the PM flux linkage nominal value in three-phase quantity, such that:

$$\psi_{m\_ph} = \psi_m \sin \theta + m\psi_m \sin 3\theta \quad (3-29)$$

where:  $0 \leq m \leq 1$ .

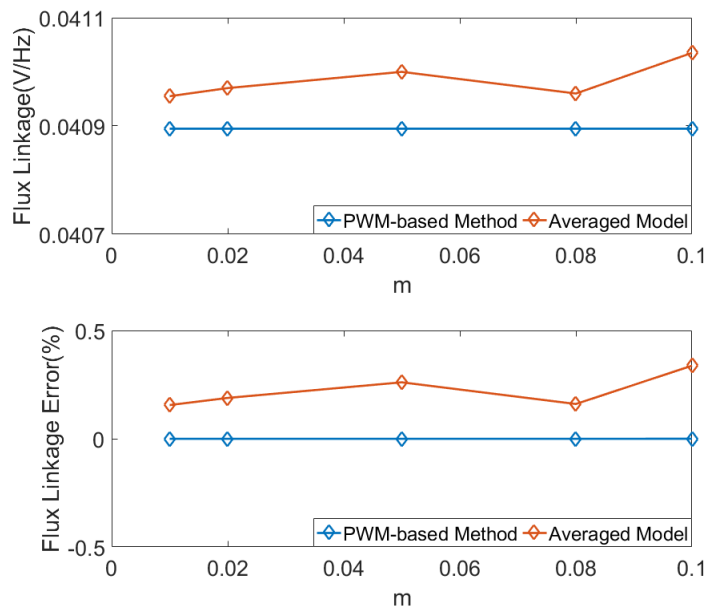


Fig. 3-26: Flux linkage estimations (top) and the corresponding errors (bottom) when  $m = 0.01$ ,  $0.02$ ,  $0.05$ ,  $0.08$ , and  $0.1$

The estimation results employing  $m = 0.01, 0.02, 0.05, 0.08,$  and  $0.1$  are depicted in Fig. 3-26, suggesting the injected harmonics only have small impact on the estimations with both methods. This is due to the use of the low-pass filter (4<sup>th</sup> order Butterworth with 1Hz passband edge frequency) which eliminates the high-order component originating from the voltage and current. The result using (3-30) shows higher level of error, because the voltage command is different from the output voltage as the phase currents flow through the power switches and shunt resistors, resulting in voltage distortion.

### 3.5.4 Inductance Saturation

Practically, the main inductances  $L_d$  and  $L_q$  of PMSMs could be subject to saturation at high current level. The existence of saturation means that the estimation is less precise as the  $q$ -axis inductance terms in the voltage equations can no longer be eliminated. The constant inductances in the machine model are replaced with two LUTs, which are obtained from the calculations using Finite Element software. The saturated inductances are shown in Fig. 3-27.

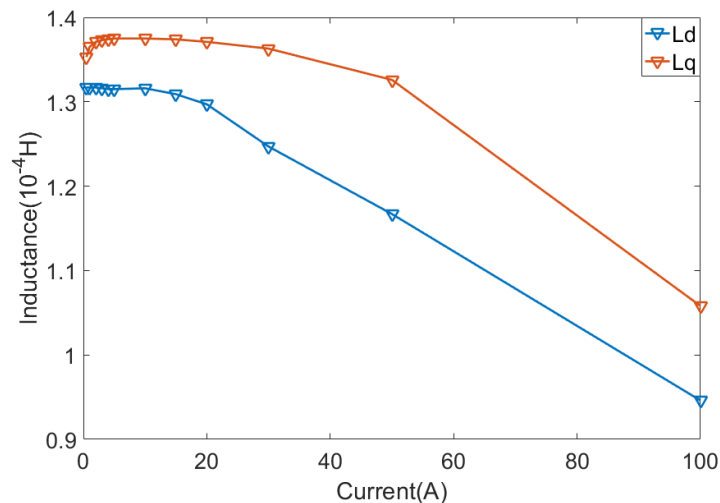


Fig. 3-27: Values of  $L_d$  and  $L_q$  in a wide range of currents

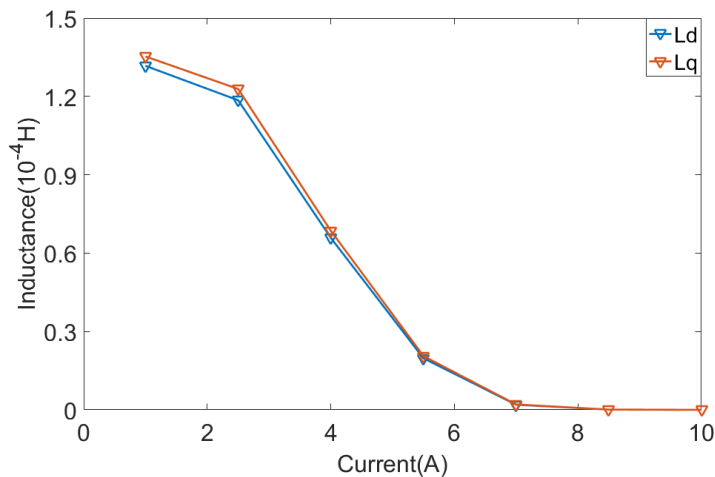


Fig. 3-28: Values of  $L_d$  and  $L_q$  after the modification

As Fig. 3-27 suggests, the inductances of the tested motor in applications in which the current is smaller than 10A do not change dramatically. However the data in the LUTs is modified such that the inductance at high current (5A) is less than 20% that at low current (0.5A) for the purpose of demonstration. Fig. 3-28 shows the inductances  $L_d$  and  $L_q$  after the modification.

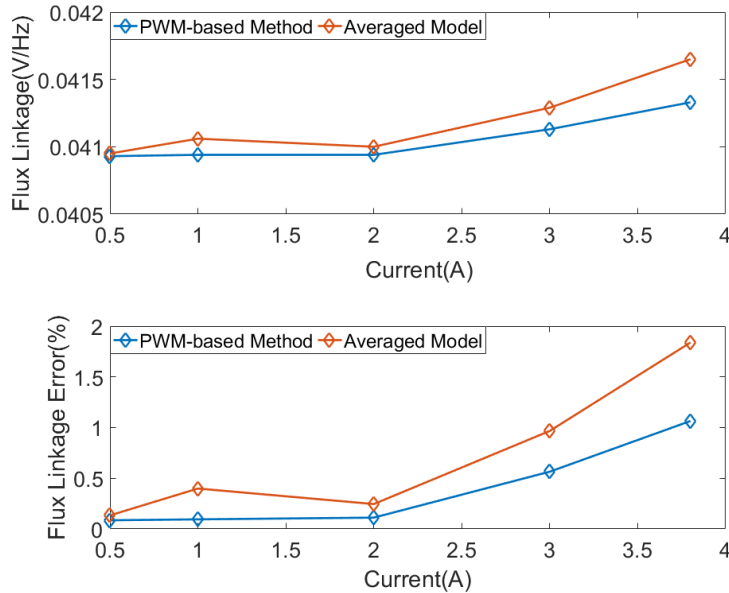


Fig. 3-29: Flux linkage estimations (top) and the corresponding errors (bottom) at  $i_{q\_command} = 0.5A, 1A, 2A, 3A,$  and  $3.8A$

Fig. 3-29 illustrates the estimation results at  $i_{q\_command} = 0.5A, 1A, 2A, 3A,$  and  $3.8A,$  respectively, showing slightly over 1% error with the PWM-based method and nearly 2% with the simplified method. Equations (3-30) and (3-31) compensate the voltage errors in (3-25) and (3-28), and are used for re-estimating the flux linkage:

$$\psi_m = \frac{f_{sw}}{\omega_r} 2[(t_3 - t_2)v_{q(t_3-t_2)} + (t_4 - t_3)v_{q(t_4-t_3)}] - \frac{f_{sw}}{\omega_r} T_s R_s \sum_1^{n-1} i_{q(j)} \quad (3-30)$$

$$- \frac{f_{sw}}{\omega_r} \sum_1^{n-1} L_{q(j)} (i_{q(k+1)} - i_{q(k)})$$

$$\psi_m = \frac{v_q - R_s i_q - \sum L_q \frac{i_{q(m)} - i_{q(m-1)}}{T_s}}{\omega_r} \quad (3-31)$$

In which:  $k$  is the  $k^{th}$  sampling point in one PWM switching period and  $j = k = 1, 2, \dots, n - 1,$  whereas  $m$  is the ‘current’ sampling point in real-time and  $m = 2, 3, \dots \infty.$   $L_{q(j)}$  can be acquired from the LUT. The results are shown in Fig. 3-30, where the improvement on the estimation for both methods is evident.

Additionally, assuming the inductance cross-coupling is included in the motor model, as shown in (1-10) to (1-15), the flux linkage estimation using (3-25) and (3-28) will be erroneous because the voltage contributions (i.e.  $L_{qq}^* \frac{di_q}{dt}$  and  $\omega_r L_{dq} i_q$  in (1-11)) as a result of this effect are not taken into account.

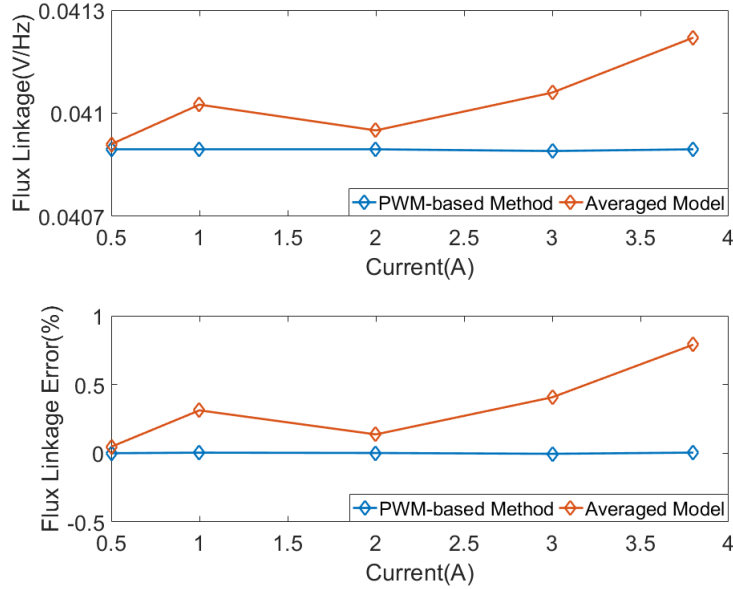


Fig. 3-30: Flux linkage estimations (top) and the corresponding errors (bottom) using (3-32) and (3-33)

### 3.5.5 Non-zero d-axis Current

At  $i_d \neq 0$ , the precision of the estimation is also affected due to the cancellation of the voltage term  $\omega_r L_d i_d$  in (3-4). The simulation results depicted in Fig. 3-31 after  $i_{d\_command} = -0.5A, -1A, -1.5A, -2A$  and  $-3A$  are imposed respectively, show more than  $-7\%$  error in flux linkage being introduced, using either method. It is assumed that  $L_d$  and  $L_q$  are their nominal values and remain constant. The estimation error can be compensated by adding the voltage term  $\omega_r L_d i_d$  into (3-25) and (3-28):

$$\psi_m = \frac{f_{sw}}{\omega_r} 2[(t_3 - t_2)v_{q(t_3-t_2)} + (t_4 - t_3)v_{q(t_4-t_3)}] - \frac{f_{sw}}{\omega_r} T_s R_s \sum_1^{n-1} i_{q(j)} \quad (3-32)$$

$$- f_{sw} T_s L_d \sum_1^{n-1} i_{d(j)}$$

$$\psi_m = \frac{v_q - R_s i_q}{\omega_r} - L_d i_d \quad (3-33)$$

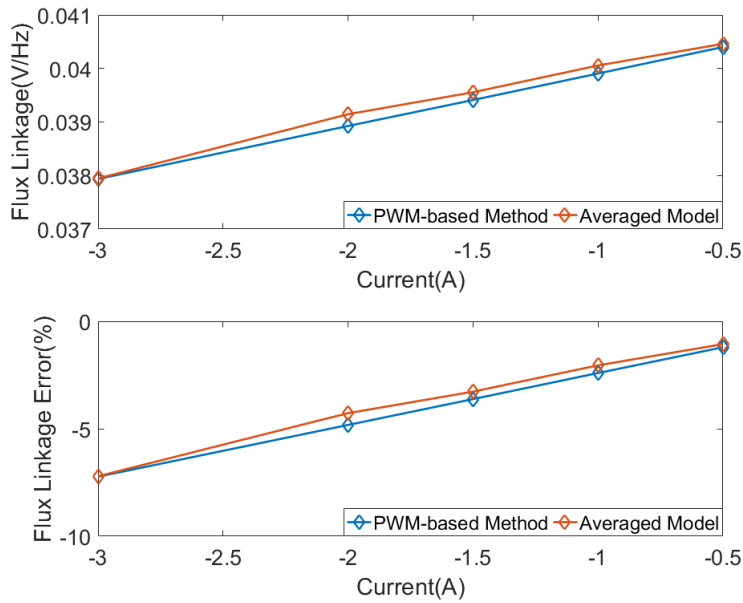


Fig. 3-31: Flux linkage estimations (top) and the corresponding errors (bottom) at  $i_{d\_command} = -0.5A, -1A, -1.5A, -2A,$  and  $-3A$

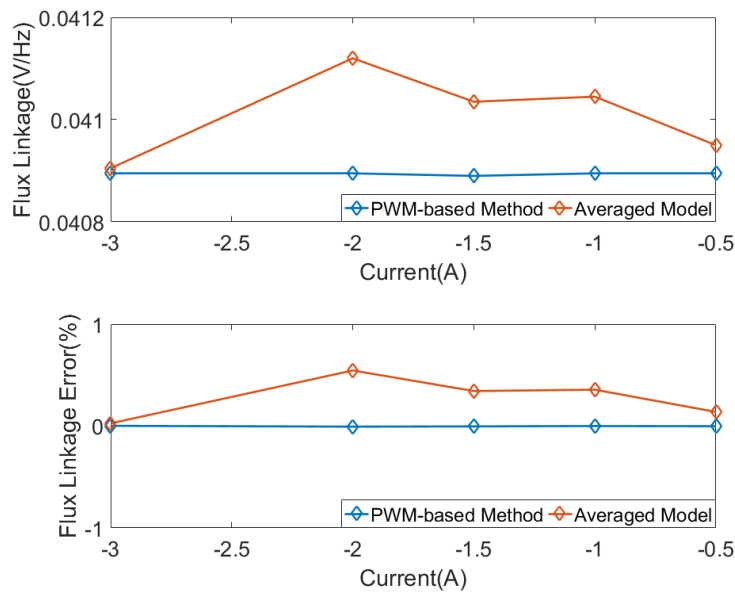


Fig. 3-32: Flux linkage estimations (top) and the corresponding errors (bottom) post-compensation

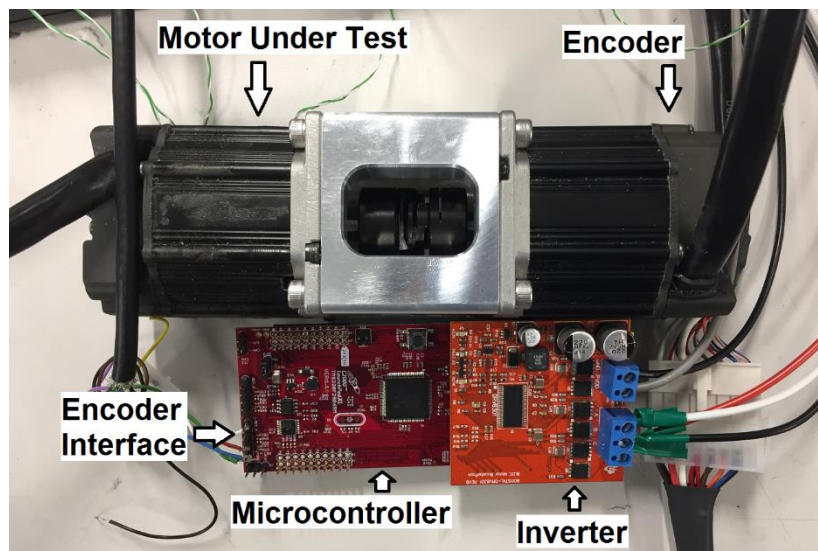
Fig. 3-32 shows the estimated flux linkages post-compensation, with less than  $\pm 0.01\%$  and  $0.6\%$  errors demonstrated adopting (3-32) and (3-33), respectively.

In conclusion, the PWM-based method utilizing phase-voltage measurement, with a proper sampling rate selected, is more desirable from the perspective of rotor temperature estimation, because with suitable compensation (i.e. saturation effect and non-zero  $d$ -axis current), the estimated flux linkage is not sensitive to the most common practical implementation errors.

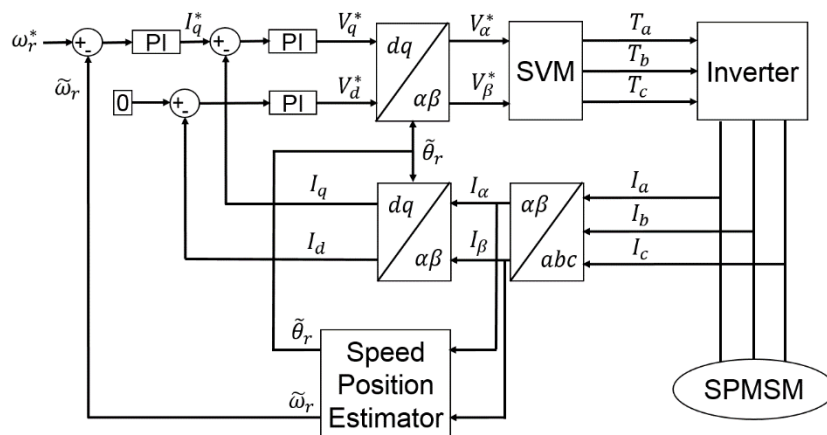
## 3.6 Experimental Validation

### 3.6.1 Experimental Setup

Extensive experimental validations are performed on a two motor dynamometer test rig built with a pair of three-phase PM servo-motors (Teknic M-2310P-LN-04K), with one connected to a three-phase MOSFET inverter and the second serving as a load and working as generator connected with a three-phase resistive load. A quadrature encoder with 4000 counts/rev resolution is used for position measurement. The motor is controlled using a Texas Instruments (TI) C2000 series FOC-enabled microcontroller LAUNCHXL-F28069M LaunchPad. The rig is shown in Fig. 3-33(a), alongside the diagram describing in detail the motor control scheme, which is illustrated in Fig. 3-33(b).



(a)



(b)

Fig. 3-33: (a) Tested motor, microcontroller and three-phase inverter and (b) motor control schematic diagram

The presented flux linkage estimation algorithm is performed on the FPGA-based data acquisition and control platform OPAL-RT 5600, as is seen in Fig. 3-34. The implementation of the estimation method is presented in Fig. 3-35.

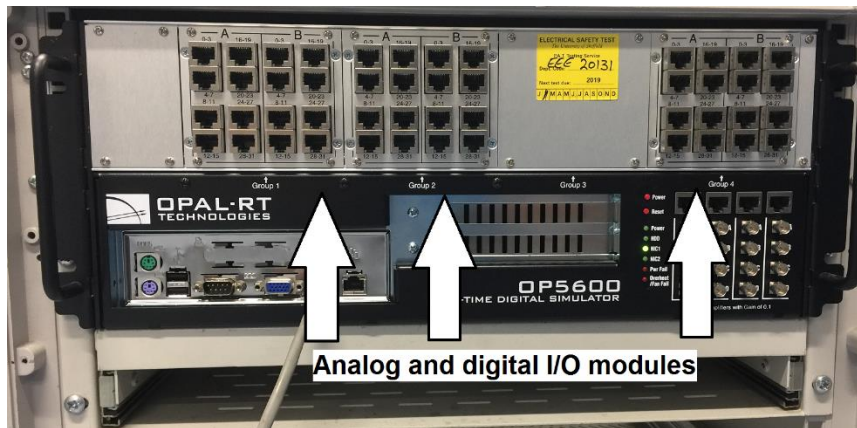


Fig. 3-34: Data acquisition unit OPAL-RT 5600

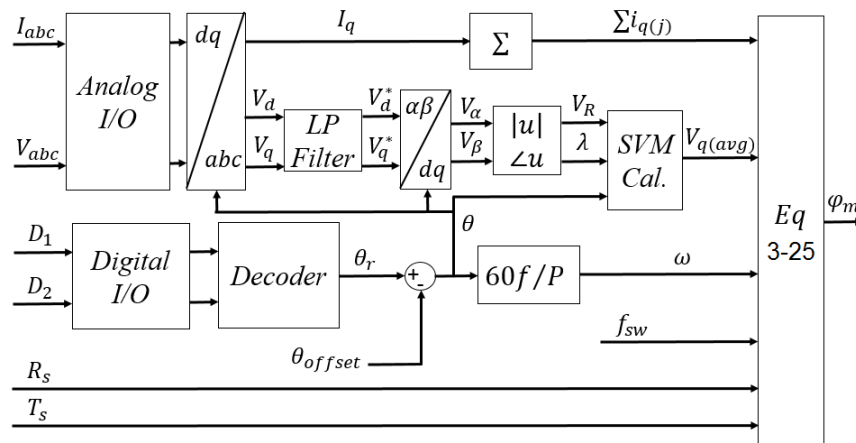


Fig. 3-35: Method implementation block diagram

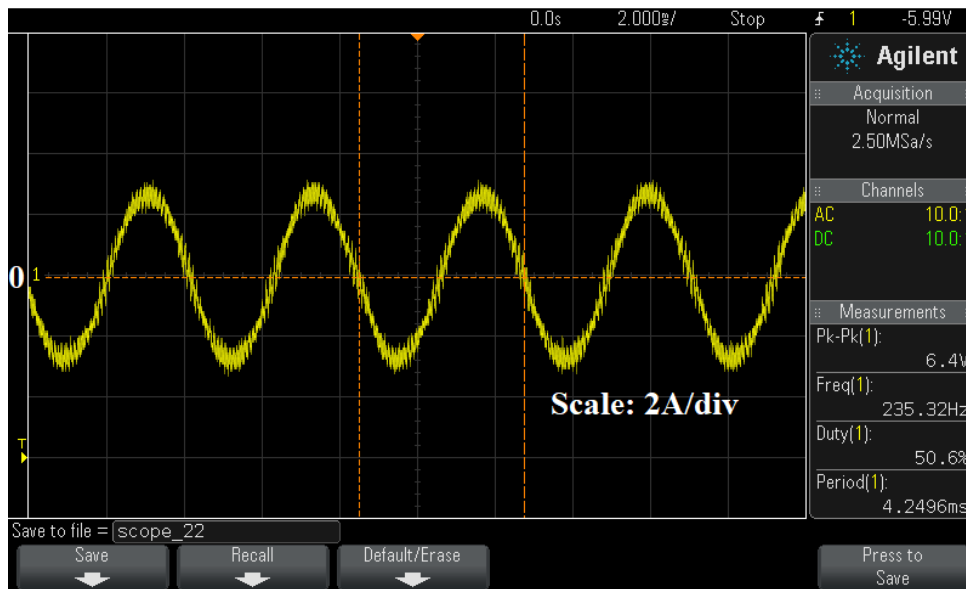
Current sensors are used for current measurement. The sensors are wrapped with wires and are connected to three resistors in star connection. The phase current is calculated by the measurement of the voltage across the resistor, which is described as:

$$I = \frac{V_{resistor} \times K_N}{N_T \times R_{resistor}} \quad (3-34)$$

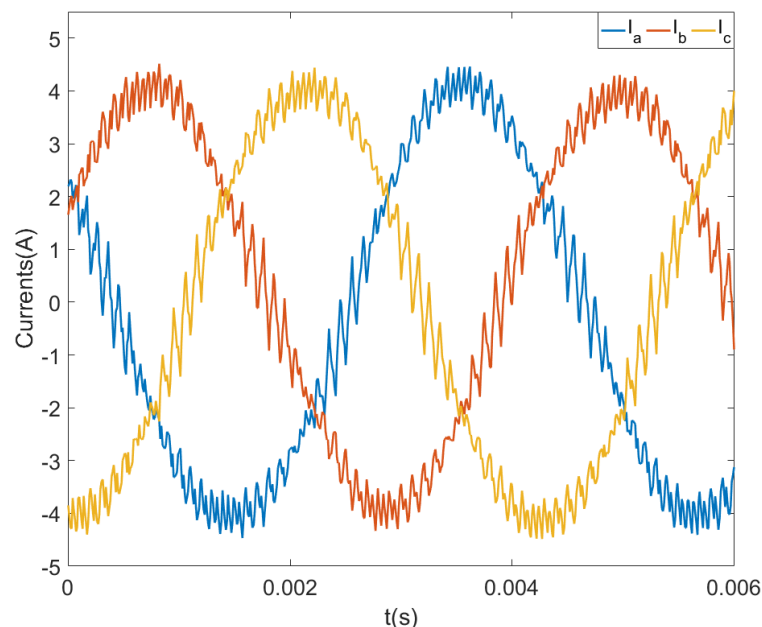
When  $K_N/(N_T \times R_{resistor}) = 1$ , the measured voltage equals to the current. For the current sensor (LEM LA 25-P) performing the current measurement,  $K_N = 1000$ ,  $N_T = 6$  and  $R_{resistor} = 100\Omega$ . This leads to  $K_N/(N_T \times R_{resistor}) > 1$  and compensation being made to the measured current.

Also, the sensors are calibrated by conducting a simple test, in which the sensors are connected in series with a  $6\Omega$  resistor and DC power supply, and the currents measured with the sensors

are recorded in OPAL-RT 5600 and compared to the actual  $I = V/R$  in order to determine their difference. Multiple voltage points in a range of  $[3V, 30V]$  are selected ensuring different current regions are taken into account. It is suggested from the result that the current is 14% higher measured by the sensors, regardless of current level. This error is considered by dividing the current measurement by 114%. Fig. 3-36 shows the phase current signal(s) displayed on oscilloscope and plotted in OPAL-RT 5600, at  $i_d = 0$  and  $i_q = 4A$  operating conditions.



(a)



(b)

Fig. 3-36: Phase current signal(s) on oscilloscope and (b) in the data acquisition unit at  $i_d = 0$  and  $i_q = 4A$

The  $q$ -axis current  $i_q$  measured for the estimation at the ‘current’ sampling time, is added to the sum of the currents at the ‘previous’ sampling times until the last sampling point of the switching period where the sum is triggered by an additional PWM signal and reset.

Voltage calibration is also carried out measuring the errors generated by the differential probes. The  $q$ -axis voltage error as a result of this effect is approximately  $0.1V$ , which leads to up to a 10% error in the flux linkage estimation at high speed and current. Phase voltage is not directly available as the three-phase load neutral cannot be accessed. Instead, line-to-line voltage is measured, from which phase voltage can be derived. Fig. 3-37 depicts at  $\omega_r = 3500rpm$  rotor speed the phase voltage. The value of it is shifted between  $\pm \frac{2V_{DC}}{3}$  ( $\pm 16V$ ), according to the inverter switching states which are determined by the location of the reference voltage space vector rotating on the space vector diagram.

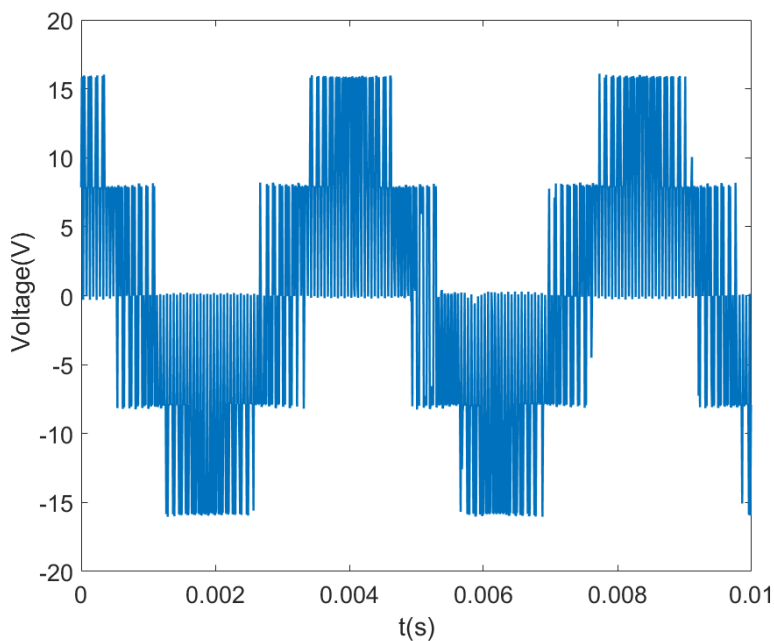


Fig. 3-37: Phase voltage at  $\omega_r = 3500rpm$

The phase voltages are transformed from the three-phase quantity  $v_{abc}$  into the rotating reference frame quantity  $v_{dq}$ , which after the low-pass filtering (i.e. 4<sup>th</sup> order Butterworth filter with the passband edge frequency of 10Hz), can be used as the voltage command. The averaged PWM output  $v_{avg}$  is computed with the knowledge of the time intervals  $(t3 - t2)$  and  $(t4 - t3)$  in Fig. 3-3, which can be retrieved from the voltage command in the form of a rotating space vector ( $\vec{V}^* = |\vec{V}^*| \angle \alpha$ ), and the sector where the space vector lands. The voltage calculation only takes place on one switching period basis.

The quadrature encoder uses three output channels,  $X_A$ ,  $X_B$  and  $X_Z$  (index) to sense position. The data acquisition device receives signals from the encoder via a 5-pin interface embedded on the microcontroller. The decoder only outputs the relative angular position  $\theta_r$  using  $X_A$  and  $X_B$ , due to the unavailability of the input signal  $X_Z$  for the decoder function. However, the absolute position of the rotor can be located by simply adding an constant value  $\theta_{offset}$  to the relative position, such that  $i_d = 0$ . The rotor speed is estimated, based on the fact that the motor fundamental frequency  $f_r$  equals to the reciprocal of the time the rotor travels  $360^\circ E$  in position, as Fig. 3-38 illustrates. Therefore, the rotor speed can be calculated by:

$$\omega_r = \frac{60f_r}{P} \quad (3-35)$$

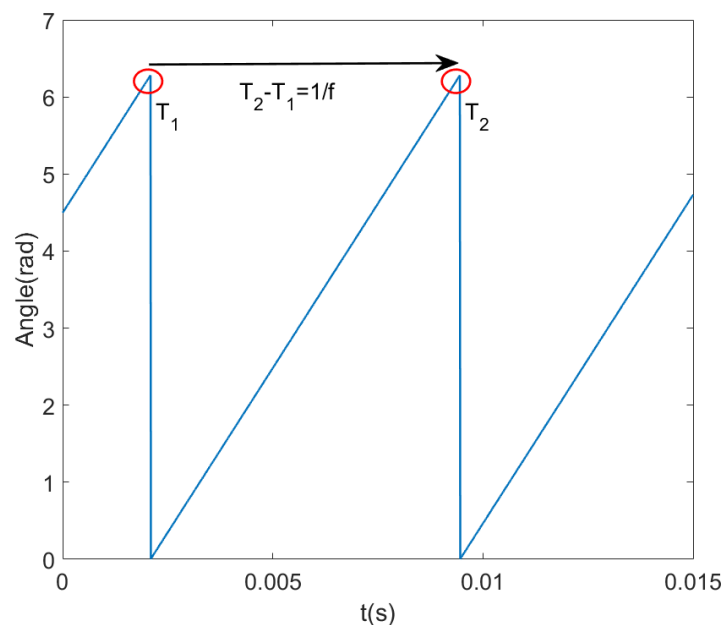


Fig. 3-38: Rotor angle and its relationship with motor fundamental frequency

It is necessary to point out that, the stator resistance  $R_s$  for the tested motor is not necessarily identical to the value provided by the manufacture datasheet.  $R_s$  can be estimated by connecting two of the three phase windings in series with the DC power supply. The voltage  $V$  across the resistors is measured with multi-meter or differential probe, whilst the current  $I$  can be the reading displayed on the power supply, provided that the current level is relatively high. As a result, the phase resistance  $R_s$  is expressed as:

$$R_s = \frac{V}{2I} \quad (3-36)$$

Also, the resistance of the wire from the inverter to the motor must be considered, which is approximately 7% the phase winding resistance of this motor and contributes a non-negligible proportion to the voltage measurement. It can be roughly calculated by subtracting the phase winding resistance from the overall resistance of the phase winding and wire in series connection.

### 3.6.2 Validation at Room Temperature

As with offline simulation, Fig. 3-39 exhibits the measured  $q$ -axis current variation and the three-phase PWM signals from PWM. It can be noticed that at steady-state conditions, the currents at the beginning of the non-zero voltage periods remain identical because the PI controller regulates the average  $q$ -axis current.

The steps shown in the  $q$ -axis current in Fig. 3-39 are the result of the fact that only ten current sampling points are acquired in one PWM switching period. Voltages and currents are acquired at 100  $kS/s$ . From the point of view of reducing current ripples, a large switching frequency, is preferable for this particular motor with small inductances. However 10  $kHz$  is employed which ensures that enough current points are sampled covering the entire switching period.

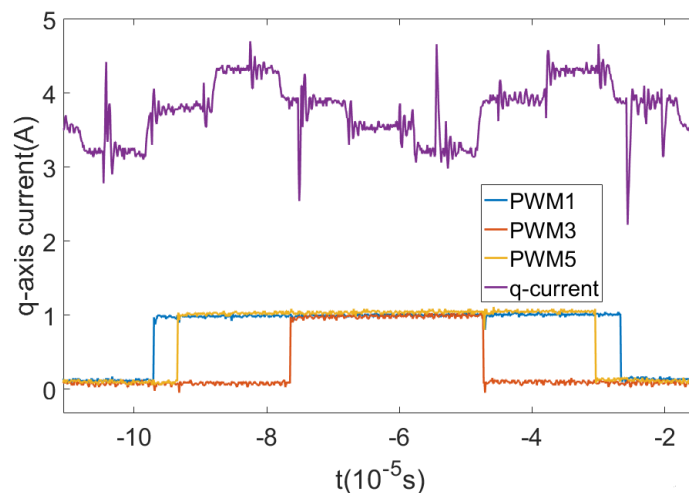


Fig. 3-39: Three-phase PWM signals and the corresponding  $q$ -axis current variation in one switching period in experimental testing

A set of dead-times 0.5 $\mu s$ , 1 $\mu s$ , 2 $\mu s$ , 5 $\mu s$ , and 10 $\mu s$ , are implemented in the inverter to verify the dead-time effect on the presented estimation method. The amount of dead-time is set in number of clock cycles, which is defined as:

$$T_{dead\_count} = T_{dead\_second} \times f_{system} \quad (3-37)$$

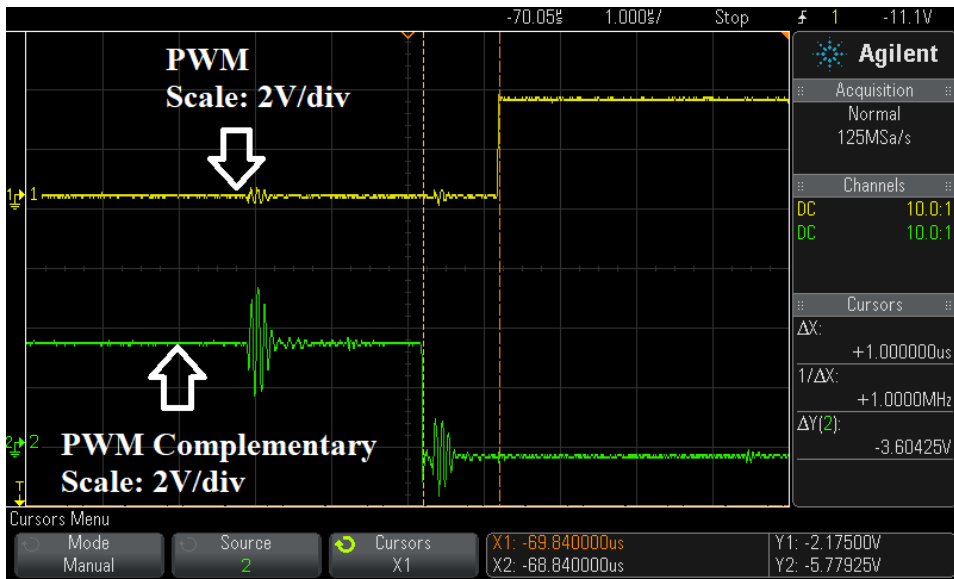
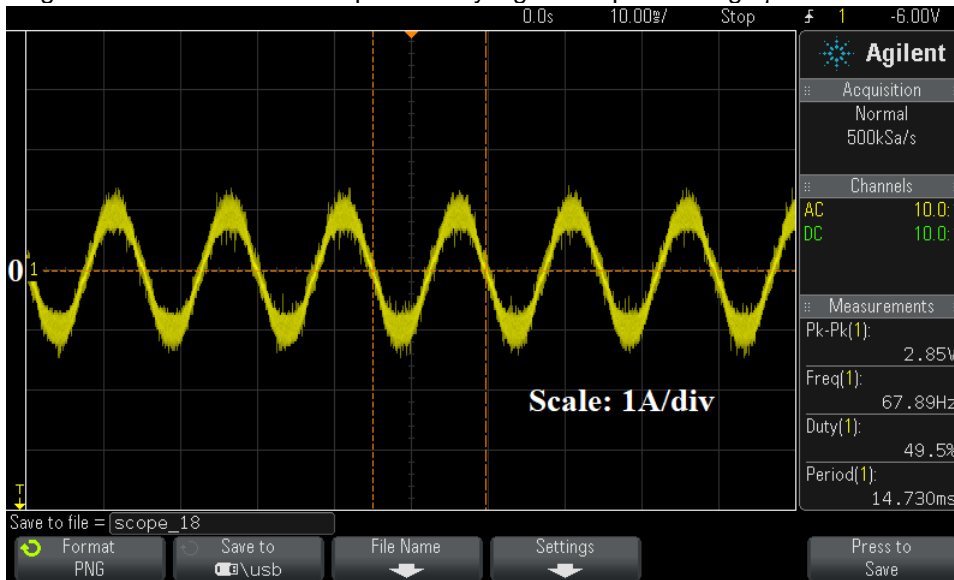
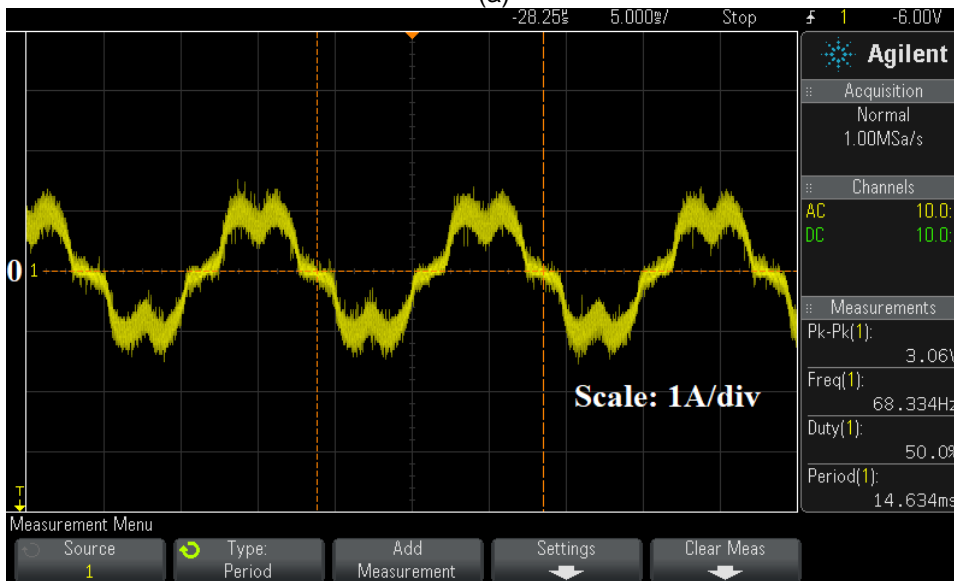


Fig. 3-40: PWM and its complementary signals implementing  $1\mu\text{s}$  dead-time



(a)



(b)

Fig. 3-41: Phase current applying (a)  $1\mu\text{s}$  and (b)  $10\mu\text{s}$  dead-times

Fig. 3-40 presents the PWM and the corresponding complementary signals following the implementation of  $1\mu s$  dead-time. The dead-times also impact on the motor current, as is shown in Fig. 3-41, where the distinction between applying  $1\mu s$  and  $10\mu s$  dead-times to the motor operating at  $I = 1.5A$  and  $\omega_r = 1020rpm$ , for instance, is visible.

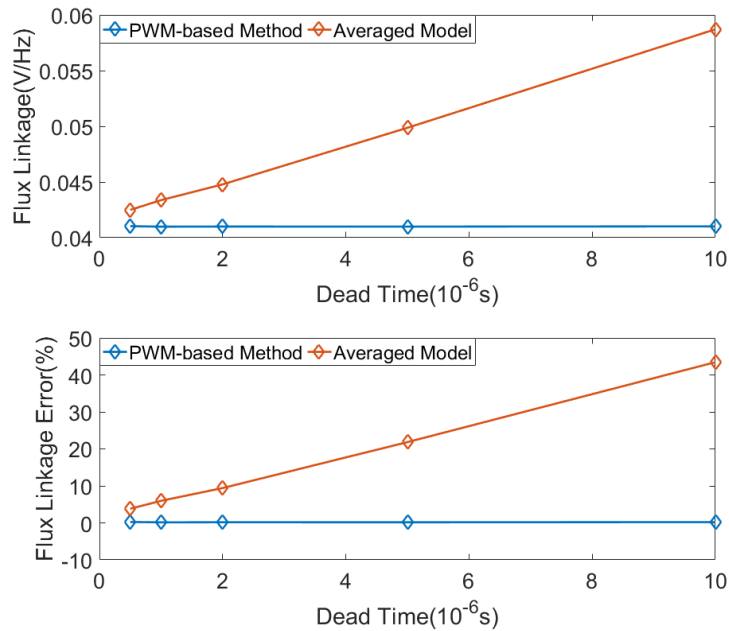


Fig. 3-42: Flux linkage estimations (top) and the corresponding errors (bottom) with  $0.5\mu s$ ,  $1\mu s$ ,  $2\mu s$ ,  $5\mu s$ , and  $10\mu s$  dead-times implemented experimentally at  $i_q = 3.6A$  and  $\omega_r = 3000rpm$

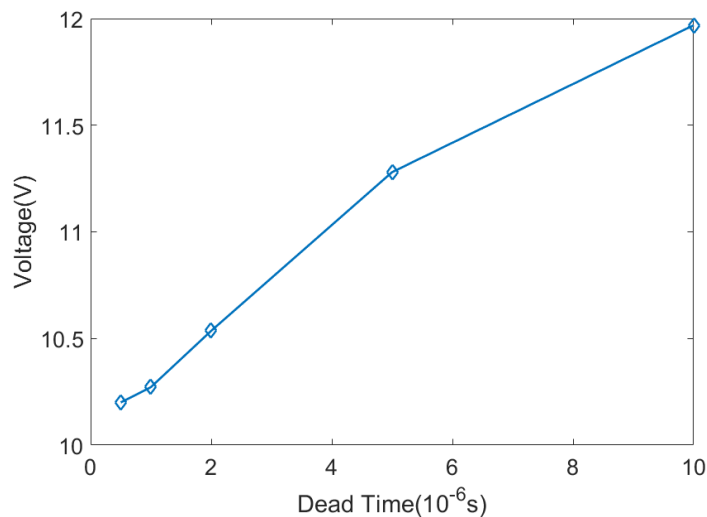


Fig. 3-43: Voltage commands with  $0.5\mu s$ ,  $1\mu s$ ,  $2\mu s$ ,  $5\mu s$ , and  $10\mu s$  dead-times implemented experimentally at  $i_q = 3.6A$  and  $\omega_r = 3000rpm$

As can be seen in Fig. 3-42, dead-time does not affect the accuracy of the estimation using the PWM-based method. The flux linkage can also be estimated using (3-28). The controller

graphic user interface roughly calculates the voltage and current commands, whereas in OPAL-RT 5600 the rotor speed and stator resistance, which with the motor rotating, slightly changes in value due to the inevitable loss-induced winding temperature change, are recorded. The results are consistent with Fig. 3-25, as the estimation deteriorates with larger dead-time.

Fig. 3-43 plots the voltage commands imposing these dead-times. The increase in voltage command at the same motor operating conditions (i.e.  $i_q = 3.6A$  and  $\omega_r = 3000rpm$ ) explains the increase in the flux linkage in Fig. 3-42.

### 3.6.3 Validation at Constant Temperatures

In order to perform tests at various temperatures, the motor is placed in a metal enclosure and wrapped around with two  $150\text{ mm} \times 50\text{ mm}$  silicone resistive heater mats powered by 30V DC voltage. The mats are connected with a power supply via a temperature controller in which the desired temperatures are set for approximately 30 minutes until the internal thermal equilibrium of the motor is reached. A K-type thermocouple with the sensing tip located at the motor winding is fitted into the controller input module to provide temperature measurement feedback. A simple hysteresis temperature controlled is implemented to reach and maintain the desired winding temperature set-point. This is achieved by using an electromechanical relay which is mounted within the controller and connected to the output pins.

The motor is then covered with a calcium-magnesium silicate thermal insulation sheet in order to keep the motor at elevated temperatures and emulate adiabatic thermal conditions. In this way, once thermal equilibrium is reached, it can be assumed that rotor temperature, which is not directly accessible, is very close to the winding temperature which can be directly measured. The setup is shown in Fig. 3-44.

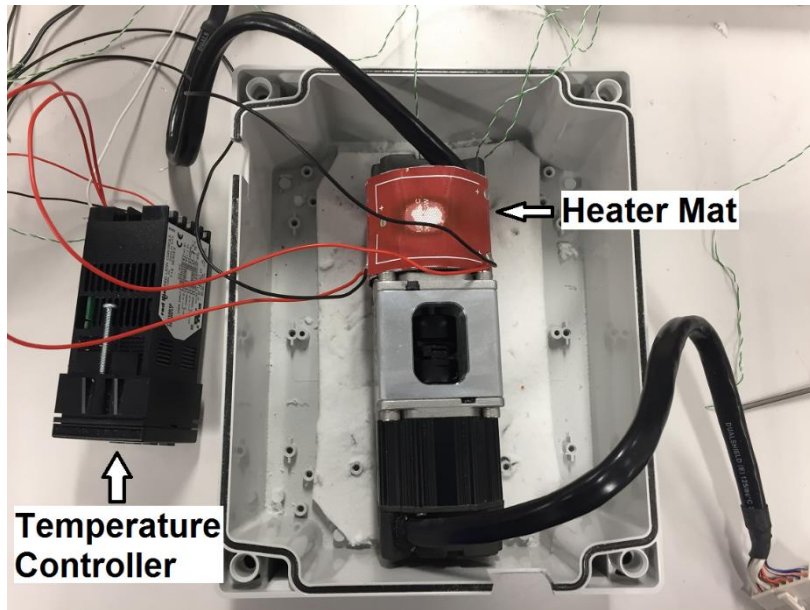
It is important that temperature dependence of stator winding resistance is taken into account in the estimation. Up to 3% error in flux linkage is detected otherwise at high motor temperatures. It is assumed that the temperature effect on winding resistance can be described as the following linear function:

$$R_s(T_W) = R_s(T_{0,W})[1 + \alpha_{cu}(T_W - T_{0,W})] \quad (3-38)$$

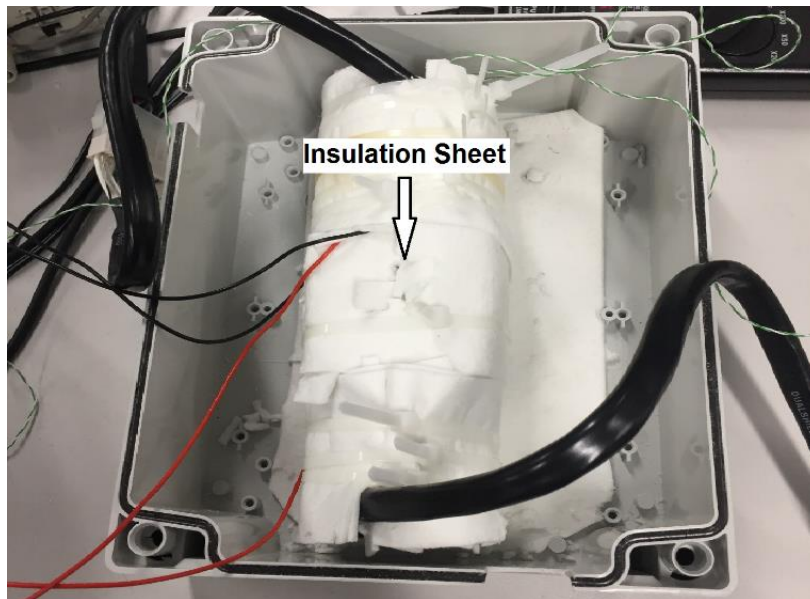
The temperature coefficient  $\alpha_{cu}$  for copper has the value of  $0.393\%/^{\circ}C$ .

Temperature also affects the B-H curve and permeability of stator core [106], [107], potentially affecting the accuracy of this method. However, as demonstrated in [106] and [107], the temperature effect on the magnetic properties of Silicon-Iron (SiFe) material, used for the

tested motor, is small in the typical operating temperatures range for electrical machines (i.e. 20°C to 120°C) and therefore neglected in the work presented here.



(a)



(b)

Fig. 3-44: (a) Motor wrapped with heater mat and (b) kit wrapped with insulation material

The estimated flux linkage is compared with its real value derived from the back-EMF measurements, which are the phase voltages at no-load condition for the tested motor acting as generator, expressed as:

$$v_q = v_{abc} = \omega_r \psi_m \quad (3-39)$$

Thus,

$$\psi_m = v_{abc}/\omega_r \quad (3-40)$$

Fig. 3-45 shows the estimated flux linkage at 4000rpm rotor speed and 25°C motor temperature, alongside the corresponding back-EMF measurements. The estimation error is less than -0.5%, showing a relatively good match with the measured value.

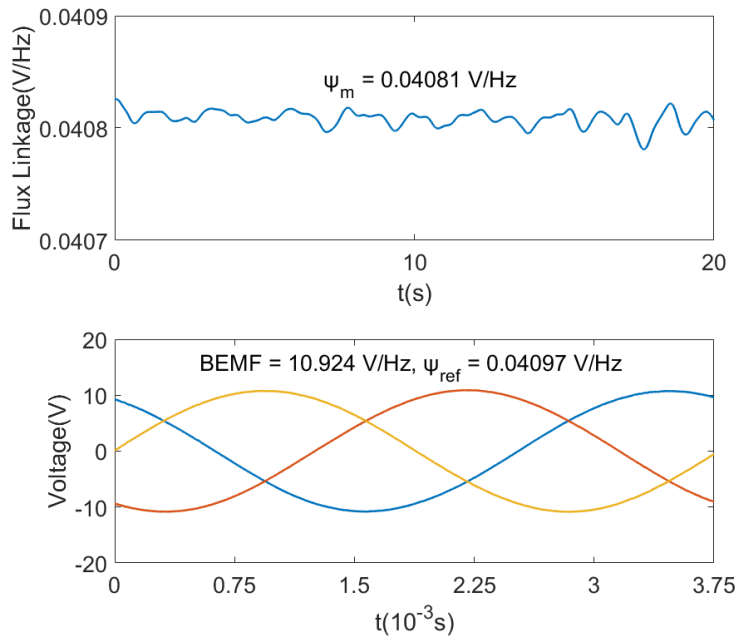


Fig. 3-45: Flux linkage estimation (top) and back-EMF measurements (bottom) at 4000rpm and 25°C motor temperature

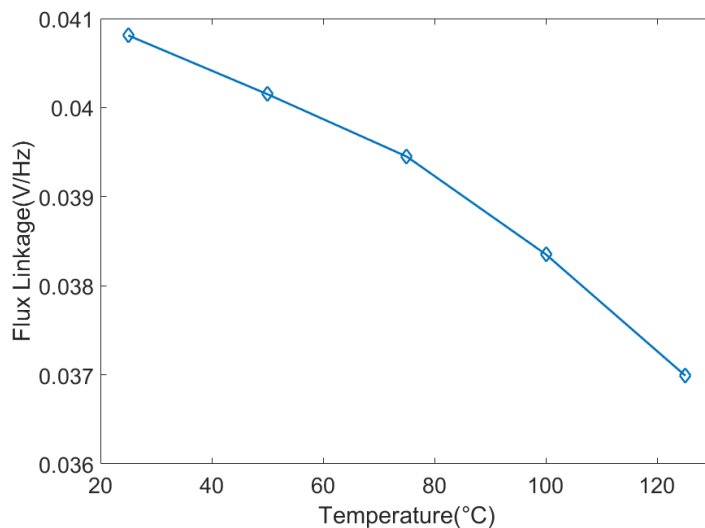


Fig. 3-46: Flux linkage estimations at 4000rpm and rising temperatures

The estimation results at 4000rpm and constant-step elevated motor temperatures starting from 25°C are plotted in Fig. 3-46, where the flux linkage variations are consistent with the

inverse relationship between flux linkage and rotor temperature. As shown in Fig. 3-47, the accuracy of the estimation shows some dependence on the motor operating condition (speed) and motor temperature, with the maximum error of  $-1.3\%$  detected at  $1000rpm$  and  $125^{\circ}C$ . Admittedly, the precision of the back-EMFs is limited by the resolution of the differential probes and the relatively slow acquisition of  $10\mu s$ , which creates some errors in the timing. Additional error and noise is also generated by current sensors.

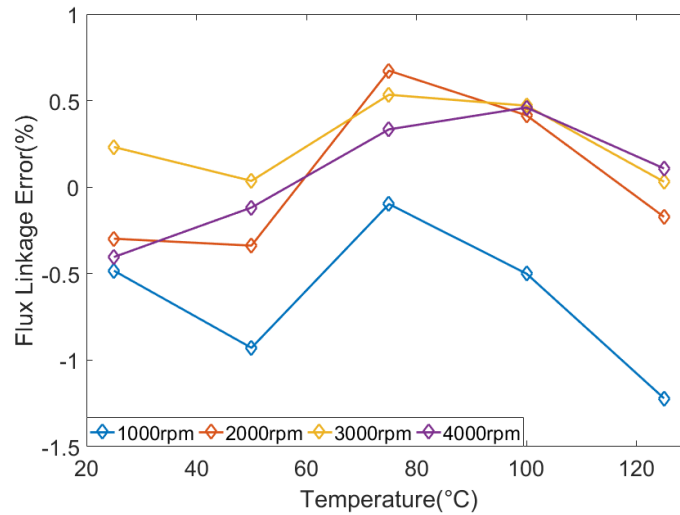


Fig. 3-47: Flux linkage errors at  $1000rpm$ ,  $2000rpm$ ,  $3000rpm$ ,  $4000rpm$ , and rising temperatures

### 3.6.4 Rotor Temperature Estimation

A calibration procedure is adopted to evaluate the coefficient  $\alpha_{\beta r}$  (see Fig. 3-1) by measuring the open-circuit back-EMF at different rotor temperatures as:

$$\alpha_{\beta r} = \frac{1}{\psi_m(T_{0,PM})} \left[ \frac{\psi_m(T_{PM}) - \psi_m(T_{0,PM})}{T_{PM} - T_{0,PM}} \right] \quad (3-41)$$

Fig. 3-1 depicts the flux linkage measurements at  $25^{\circ}C$ ,  $50^{\circ}C$ ,  $75^{\circ}C$ ,  $100^{\circ}C$ , and  $125^{\circ}C$ , respectively, along with  $\alpha_{\beta r}$  calculated using two adjacent temperature points. These values are selected for the estimation at each temperature region. The difference in  $\alpha_{\beta r}$  may be associated with the attribute of the material for the magnets.

A simple thermal steady-state test is conducted. The heater mats heat up the motor for a certain period of time during which the motor temperature climbs, reaches the set-point and the adiabatic state is maintained. The flux linkage and rotor temperature are then estimated using (3-25) and (3-2) with the motor operating at an arbitrary condition. Fig. 3-48 shows the

estimated rotor temperature along with the winding temperature controlled at  $60^{\circ}\text{C}$ . The winding temperature is a few degrees higher than expected due to the losses during the motor operation.

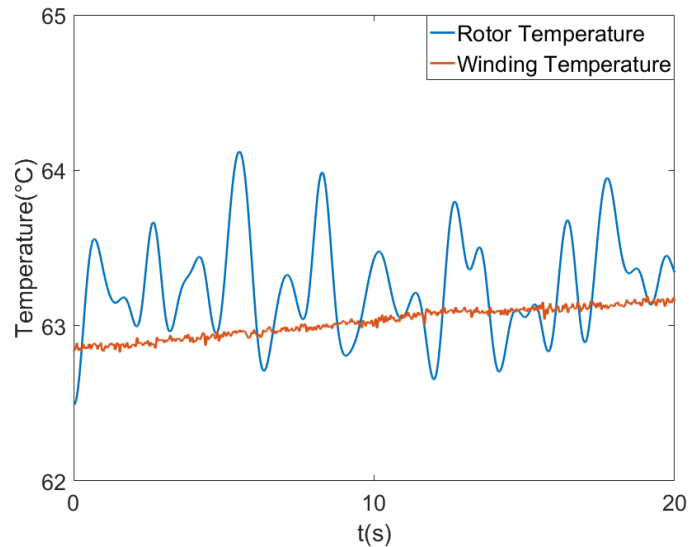


Fig. 3-48: Rotor temperature estimation and winding temperature measurement at  $T_{setpoint} = 60^{\circ}\text{C}$

Fig. 3-49 shows the rotor temperatures estimated at several set-point temperatures. The accuracy for the proposed method is demonstrated by the fact that no more than  $2^{\circ}\text{C}$  error is achieved for the rotor temperatures.

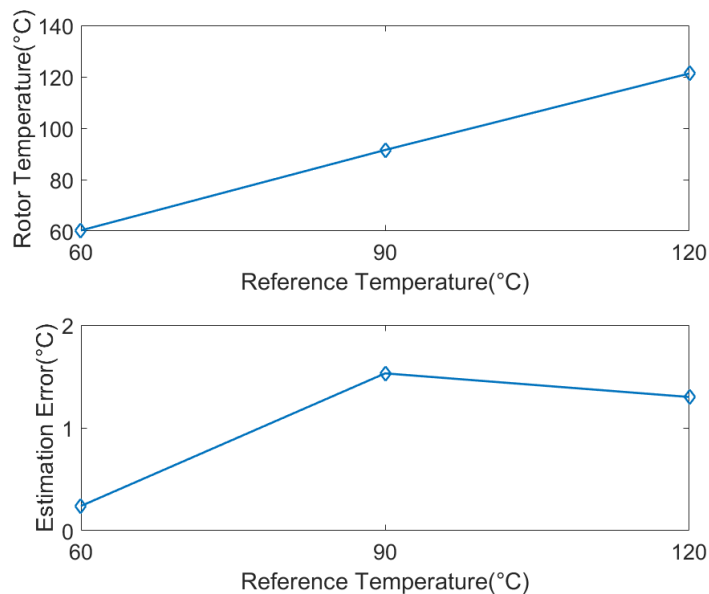


Fig. 3-49: Rotor temperature estimations (top) and the corresponding errors (bottom) at  $T_{setpoint} = 60^{\circ}\text{C}$ ,  $90^{\circ}\text{C}$ , and  $120^{\circ}\text{C}$

A transient test over four hours is performed in which the motor temperature increases and decreases in steps generated by the temperature controller, as Fig. 3-50 illustrates. In order to validate the presented method in non-stationary conditions, a simplified duty cycle applied on speed ( $\omega_{base} = 4500rpm$ ) and stator current ( $I_{base} = 5A$ ) is considered and shown in Fig. 3-51.

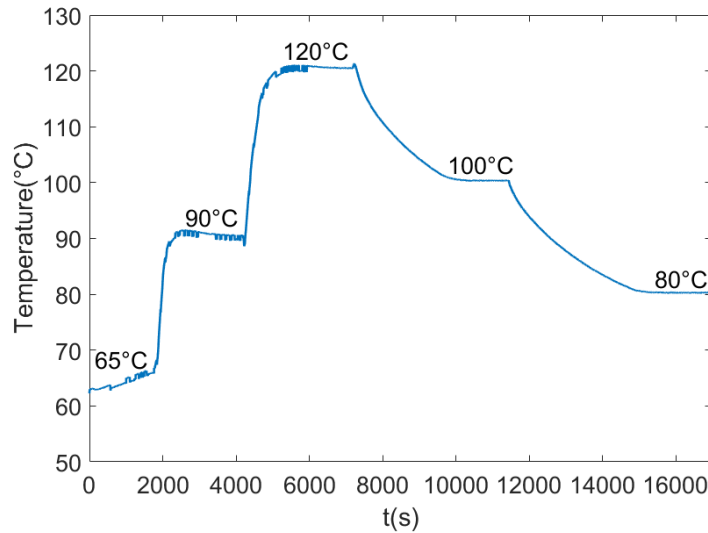


Fig. 3-50: Motor stator temperature profile during transient testing

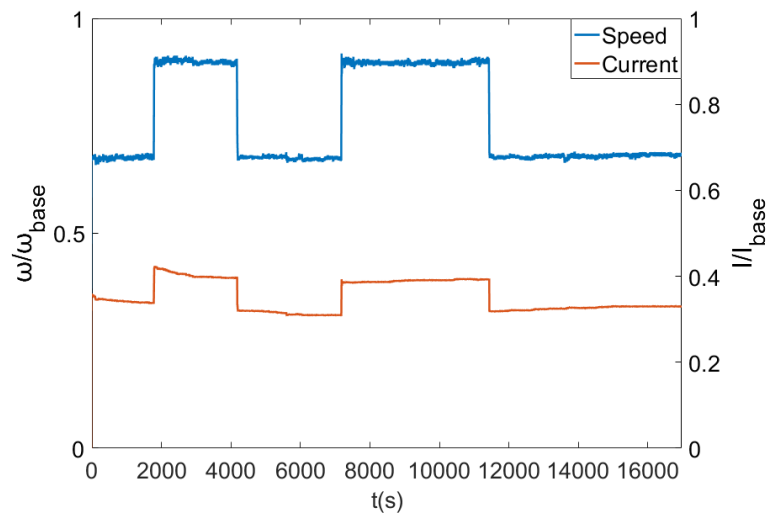


Fig. 3-51: Motor speed and current profiles of the transient testing

Less than  $1.7^{\circ}C$  differences in the steady-state temperatures between winding and rotor can be observed in Fig. 3-52. Unfortunately, it is difficult to provide measured temperatures for the estimations at the transient periods due to the challenge of obtaining the estimated flux linkage results and back-EMF measurements synchronously.

Also, the heater mat is slightly shorter in length than the motor circumference. Therefore, the heating distribution in the motor might not be uniform. Additionally, rotor temperature is

indirectly measured using stator windings temperature and assuming adiabatic and steady-state conditions, assuming that in these conditions stator and rotor have reached a thermal equilibrium. These ideal conditions might not be perfectly verified in practice.

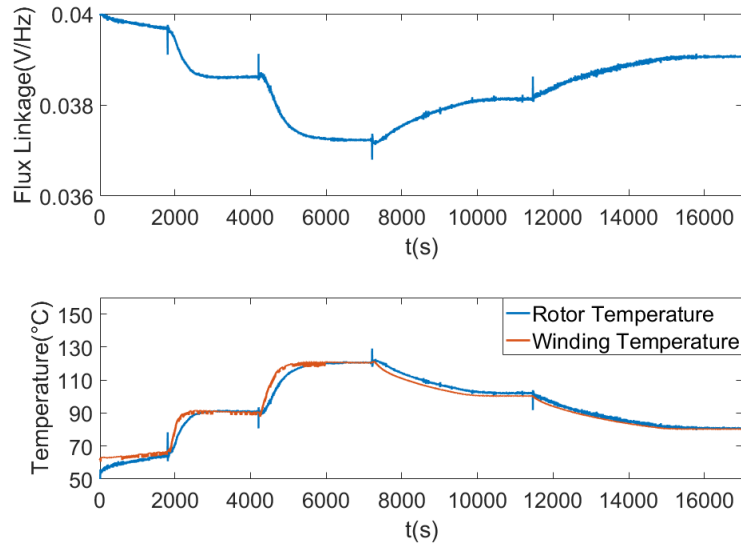


Fig. 3-52: Flux linkage (top) and rotor temperature (bottom) estimations under the transient profiles

### 3.7 Conclusion

This chapter presents a relatively simple and accurate method for online flux linkage and rotor temperature estimations of PMSMs, based on the current response to the standard SV-PWM which is commonly employed in most state-of-the-art power converter drive applications. This method is simple to implement and does not create additional disturbance to the machine as no additional signal injection is required. The method is also independent of machine inductances. A series of offline and real-time simulations, and experimental testing are presented to validate the proposed methodology. The results demonstrate good accuracy in rotor flux linkage and temperature estimations in a wide range of machine operating conditions. Extensive simulations and experimental validations are provided to evaluate the sensitivity of the method and evaluate its robustness to a number of parameters including sampling rate, dead-time, additional harmonics in the PM flux and saturation.

# Chapter 4: A PWM-based Low-order Thermal Network for Critical Temperatures Estimations for Permanent Magnet Synchronous Motors

## 4.1 Introduction

In chapter 2, a reduced-order LPTN is presented to monitor the critical temperatures in PMSMs, and good model performance is shown under ideal simulation conditions. However, this method requires rotor temperature measurement which is extremely difficult, in some applications even unrealistic, due to the challenge of placing temperature sensors on a rotating shaft. As a result, the relatively simple PWM-based estimation method proposed in chapter 3 is employed, which retrieves accurate rotor temperature information indirectly from motor PM flux linkage, and can be implemented in real-time.

The temperature estimation system integrating the two approaches is experimentally tested on the three-phase PM servo machine introduced in chapter 3. A thorough validation is conducted and the estimation errors are relatively small.

## 4.2 Experimental Validation

### 4.2.1 Loss Modelling

The losses of the tested motor are calculated based on motor speed and electric currents, which are commonly available in the motor controller. The three-phase copper loss generated by the active winding and end-winding of the motor can be calculated by (1-65). The stator resistance  $R_s$  is assumed to be linearly dependent on the winding temperature  $T_W$  as stated by (3-38). Therefore, the loss  $P_W$  for the winding node in the LPTN presented in chapter 2 is expressed as:

$$P_W = 1.5I_q^2 R_s(T_W) \quad (4-1)$$

where  $T_W$  is the average winding temperature obtained from temperature sensors and used as the temperature measurement for the winding node.

The on-load iron loss is assumed to be the superposition of the two modes of motor operations corresponding to two distinct flux paths — the main magnetizing flux path associated with the

PM and stator current, and the field weakening path relating to the demagnetizing current [91]. The iron loss models (1-82) and (1-83) are adopted, which after taking into consideration the dependence of the flux linkage on the load condition, the demagnetizing field and the magnet temperature  $T_{PM}$  ( $T_{0,PM} = 25^\circ\text{C}$ ), can be described as:

$$P_{CT} = a_h f_r \left( \frac{\sqrt{\psi_d^2(T_{PM}) + \psi_q^2(T_{PM})}}{\psi_m(T_{0,PM})} \right) + a_e f_r^2 \left( \frac{\sqrt{\psi_d^2(T_{PM}) + \psi_q^2(T_{PM})}}{\psi_m(T_{0,PM})} \right)^2 \quad (4-2)$$

$$P_{CP} = b_h f_r \left( \frac{|\psi_d(T_{PM}) - \psi_m(T_{PM})|}{\psi_m(T_{0,PM})} \right) + b_e f_r^2 \left( \frac{|\psi_d(T_{PM}) - \psi_m(T_{PM})|}{\psi_m(T_{0,PM})} \right)^2 \quad (4-3)$$

The total iron loss at a given operating condition is the sum of  $P_{CT}$  and  $P_{CP}$ . In this application, the motor is only controlled at the rated flux region, which means  $P_{CP} = 0$ . The constants ( $a_h$ ,  $a_e$ ) and ( $b_h$ ,  $b_e$ ) can be found using the FE analysis at open-circuit and short-circuit operations, respectively, and room temperature  $T_{0,PM}$ .  $\psi_d$  and  $\psi_q$  are the  $dq$ -axis flux linkages considering the demagnetizing field  $\psi_d^*$ , assuming  $i_d = 0$ :

$$\psi_d = \psi_m + \psi_d^* \quad (4-4)$$

$$\psi_q = L_q i_q \quad (4-5)$$

The specifications of the motor are shown in Table IV. The PMSM is modelled in the motor design software Motor-CAD, due to its: a) efficiency, as accurate modelling of the electromagnetic and thermal behaviours of the motor can be performed rather quickly, b) simplicity. Motor-CAD provides a template-based setup which simplifies the design process. As a result, only the most significant machine geometry and material information is required. Adobe Photoshop CC 2018 is used to obtain the radial and axial dimensions of the motor in an image, whereas the material information is available on the manufacture datasheet. In this application, the constants are obtained by performing the 2-D FEA at an arbitrary rotor speed in Motor-CAD Lab. These parameters for the servo-motor are summarized in Table V.

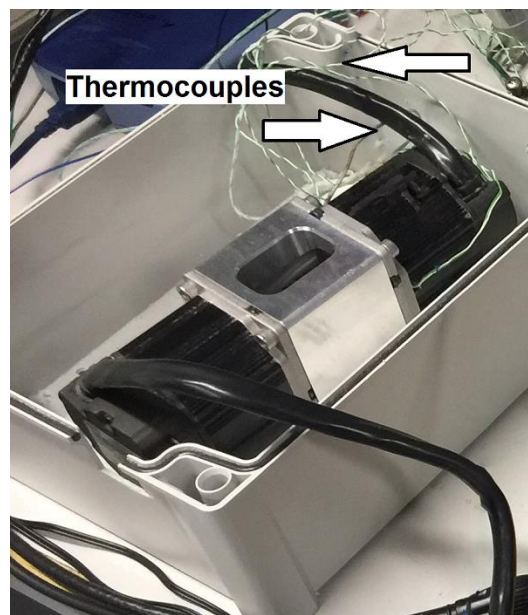
Table V: Parameters calculated by FEA

Quantity	Unit	Value
$a_h$	$W/Hz$	0.009311
$a_j$	$W/(Hz)^2$	$3.082e^{-5}$
$b_h$	$W/Hz$	0.001021
$b_j$	$W/(Hz)^2$	$5.508e^{-6}$

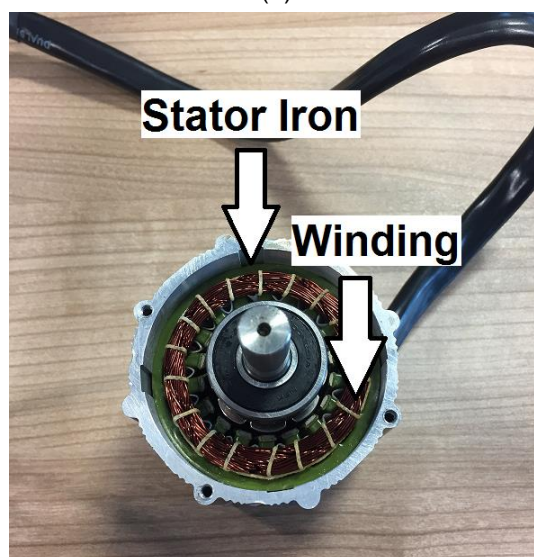
The loss  $P_{PM}$  for the PM node is neglected. According to the FEA simulation result, the rotor core iron and magnet, which are the main sources of the rotor loss for the tested machine, only produce very small amount of heat losses. Windage loss and friction loss are also assumed to be zero to simplify the modelling process.

## 4.2.2 Experimental Setup

The estimation method is experimentally validated on the motor shown in chapter 3. The motor under test is positioned in an enclosure and only cooled by natural convection. The resistances  $R_{Fes-C}$  and  $R_{PM-A}$  represent natural convection between the motor and ambient and their values are finite. The test rig is shown in Fig. 4-1(a).



(a)



(b)

Fig. 4-1: (a) test rig and (b) thermocouple locations

The generator is connected to a three-phase resistive load, with each phase consisting of multiple  $10\Omega$  resistors in parallel connection, in order to raise the level of the motor current, and therefore raise the levels of the copper loss and motor temperature. Due to the temperatures being relatively evenly distributed in the motor, only one K-type thermocouple is installed in the gap between the housing and stator yoke, and another inside the end-winding to obtain the temperature measurements for the stator iron and winding nodes, respectively. Fig. 4-1(b) demonstrates the locations of the thermocouples in the motor. The parameter estimation procedure introduced in chapter 2 is executed on the real-time platform OPAL-RT 5600, along with the PWM-based method presented in chapter 3, which provides an accurate rotor temperature measurement for the prediction of the thermal parameters. Fig. 4-2 shows the implementation of the EKF algorithm in a block diagram. A relatively small sampling time  $10\mu s$  is adopted for the rotor temperature estimation, whilst the acquisition of the measured temperatures and power losses for the computation of the thermal resistances takes place every 60s, because the temperature variation is rather slow. However it can be reduced to 1s, for instance, such that sudden changes in the operating conditions (speed/current) between two sampling points are able to be detected. The temperature measurements from the thermocouples are converted into voltage signals by two temperature amplifiers powered by 10V DC voltage, before being received by OPAL-RT where the following linear function is used to acquire temperature information:

$$T^m = (V_o - 1.25)/5mV \quad (4-6)$$

in which  $T^m$  and  $V_o$  are in Celsius and Volts. The open-loop temperature estimation is performed offline, after the identification process is completed.

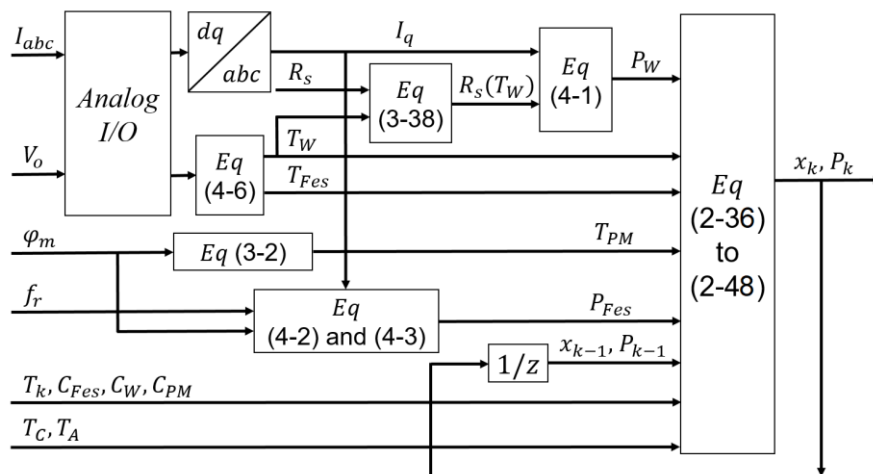


Fig. 4-2: EKF algorithm implementation block diagram

### 4.2.3 Validation at Single Speed and Current

The presented method is validated at  $\omega_r = 3200rpm$  and  $I = 3.4A$ . The test identifying the unknown thermal resistances of the motor is carried out for more than three hours, until after the thermal equilibrium is reached. The two thermocouples fixed into the motor are used to monitor the temperature change, and the data is accessed and displayed via a Pico TC-08 thermocouple data logger. The estimated resistances and temperatures using the EKF algorithm are shown in Fig. 4-3 and Fig. 4-4, and the corresponding temperature errors are plotted in Fig. 4-5.

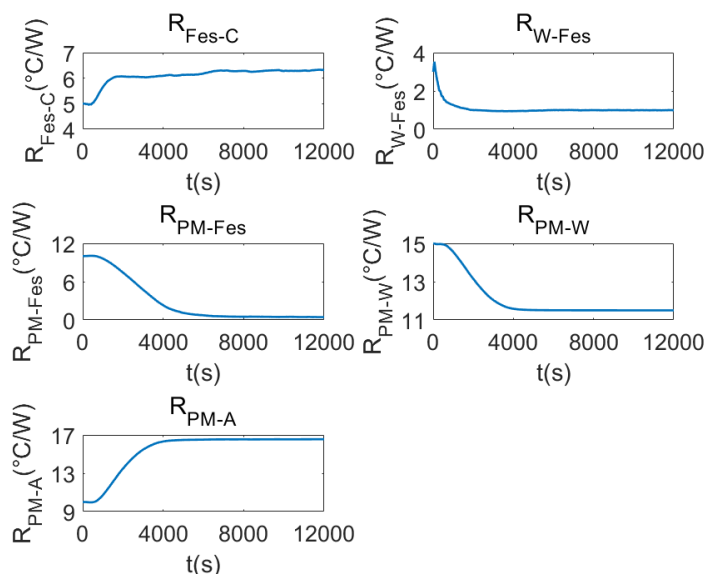


Fig. 4-3: Estimated thermal resistances at  $\omega_r = 3200rpm$  and  $I = 3.4A$

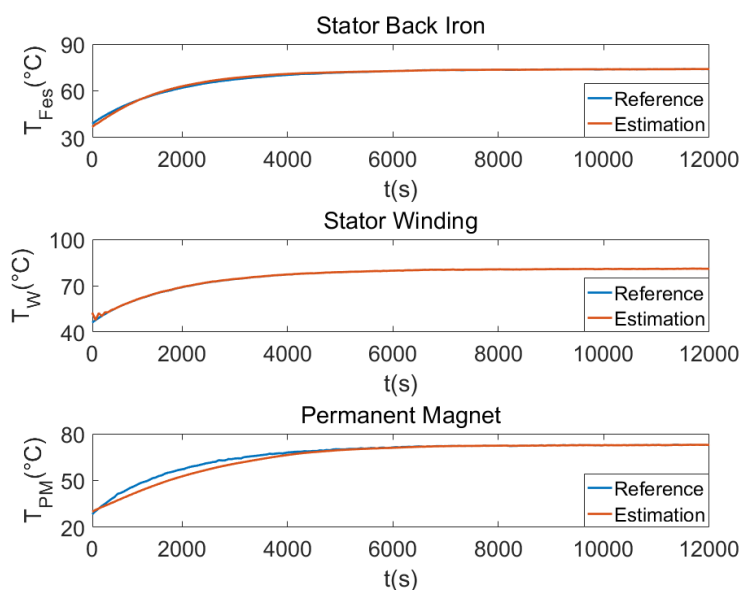


Fig. 4-4: Estimated three node temperatures at  $\omega_r = 3200rpm$  and  $I = 3.4A$

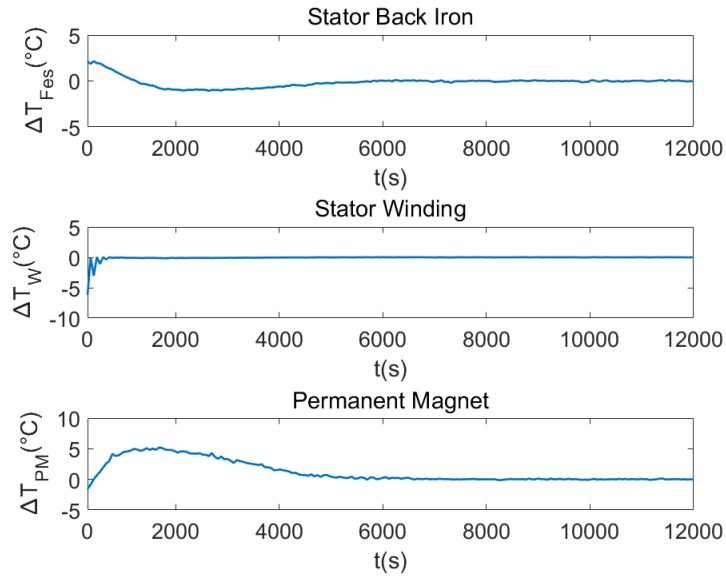


Fig. 4-5: Temperature estimation errors in Fig. 4-4

In Fig. 4-4 and Fig. 4-5, the estimated temperatures show good agreement with the corresponding measurements at the thermal steady-state. However, more than 5°C error appears in the rotor temperature estimation during transient period, because the rotor temperature measurement, which is predicted by the PWM-based approach, is less precise at lower temperature. This means the estimation will not be able to keep track of the real value unless a large process noise covariance  $Q$  is chosen which results in a stronger weight given to the measurement in the updating of the estimate. In this case, only a small  $Q = 0.05$  is used in order to reduce the measurement noise.

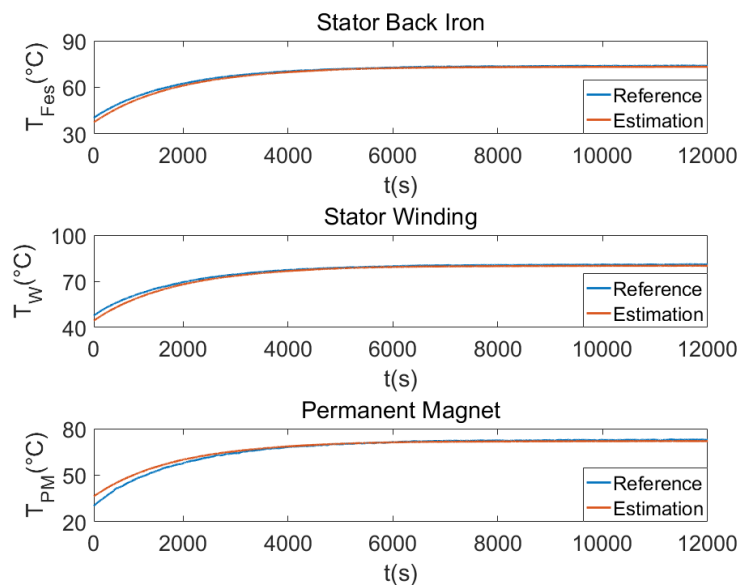


Fig. 4-6: Estimated node temperatures using the results in Fig. 4-3

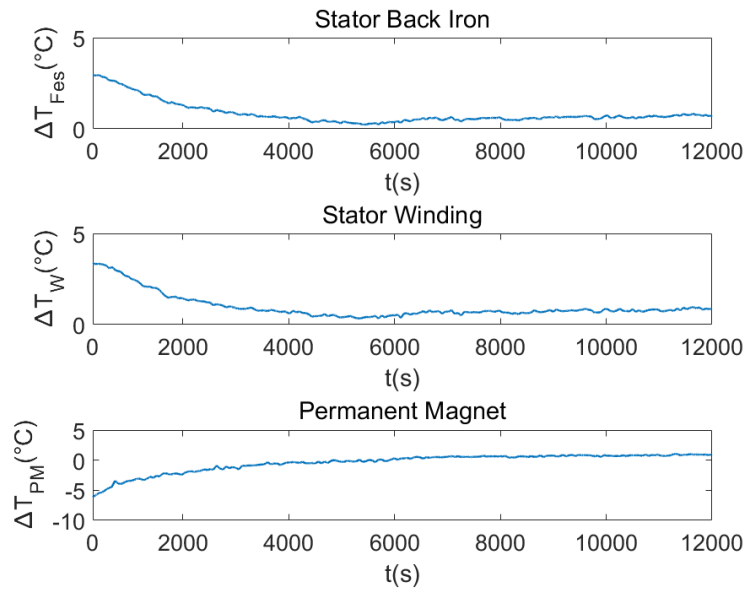


Fig. 4-7: Temperature estimation errors in Fig. 4-6

The open-loop test is conducted to validate the identified thermal resistances. Fig. 4-6 shows the temperature estimations alongside the temperature measurements, and the differences between them are shown in Fig. 4-7. The deviations are mainly due to the fact that the thermal parameters identified at steady-state do not take into account the error in rotor temperature estimation using the PWM-based method during the transient period. Also, the power losses might not be perfectly modelled, as the copper loss can be affected by the imprecision of the current measurement and stator resistance, and the ‘*OC + SC* model’ only provides reasonably accurate iron loss estimation. In addition, small errors might exist in the stator iron and winding temperature measurements as a result of only one measurement point being used for each node.

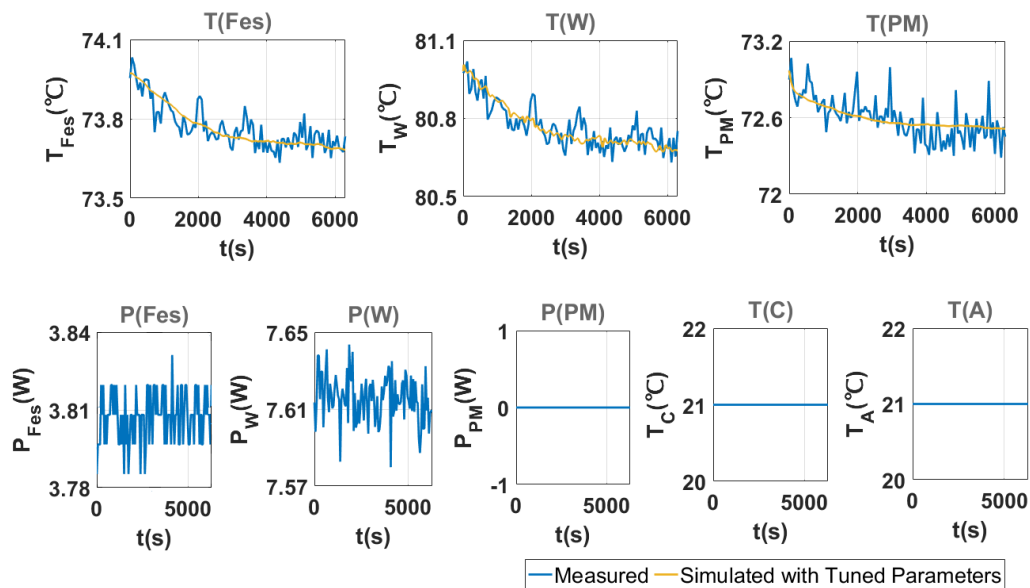


Fig. 4-8: Three-node temperatures predicted by the Levenberg-Marquardt algorithm, the power losses, the cooling system (natural convection) and ambient temperatures

Iteration	Cost Function
0	9.7830
1	0.0716
2	$4.5533e^{-4}$
3	$4.5485e^{-4}$
4	$4.5483e^{-4}$

Fig. 4-9: Cost function values during the estimation process

Parameters	Levenberg-Marquardt	Extended Kalman Filter
$R_{Fes-C}$	6.367	6.26
$R_{W-Fes}$	1.4309	0.994
$R_{PM-Fes}$	2.7496	0.524
$R_{PM-W}$	3.0006	11.5
$R_{PM-A}$	16.361	16.547

Fig. 4-10: Identified thermal resistances using the Levenberg-Marquardt and extended Kalman filter algorithm

The Levenberg-Marquardt least-squares algorithm is employed once again to estimate the thermal resistances which will be compared with the results based on the EKF method. The identification problem can be viewed as searching iteratively within the search domain for the set of resistances that ensures the temperature measurements best fit the nonlinear thermal model in the least square sense. The algorithm may converge to local minimum as more than one solution to the rotor-related resistances can be calculated depending on the initial guesses. Fig. 4-8 depicts the node temperature measurements and the temperature estimations as a result of using the identified resistances shown in Fig. 4-10. The power losses and ambient temperature, which in this case is also the temperature of the ‘cooling system’ due to the use of natural convection for the motor, are shown as well. Fig. 4-9 shows the minimization of the cost function during which the local optimum of the unknowns can be detected. The test is intended for validating the results presented in Fig. 4-3 and therefore only considers the steady-state condition.

The estimated temperatures show a good match with the measurements, suggesting the resistances are correctly identified and are one of the many solutions to the identification problem. The fact that the cost function after four iterations reduces to a relatively low level of  $10^{-4}$  confirms that the local minimum may have been reached. Parameter-wise, the values of  $\theta_1$ ,  $\theta_2$  and  $\theta_5$  corresponding to  $R_{Fes-C}$ ,  $R_{W-Fes}$  and  $R_{PM-A}$ , respectively, are similar to those in Fig. 4-3. Nevertheless, the deviations in  $\theta_3(R_{PM-Fes})$  and  $\theta_4(R_{PM-W})$  adopting these two methods are noticeable, which may be related to the difference in the optimization process of the algorithm.

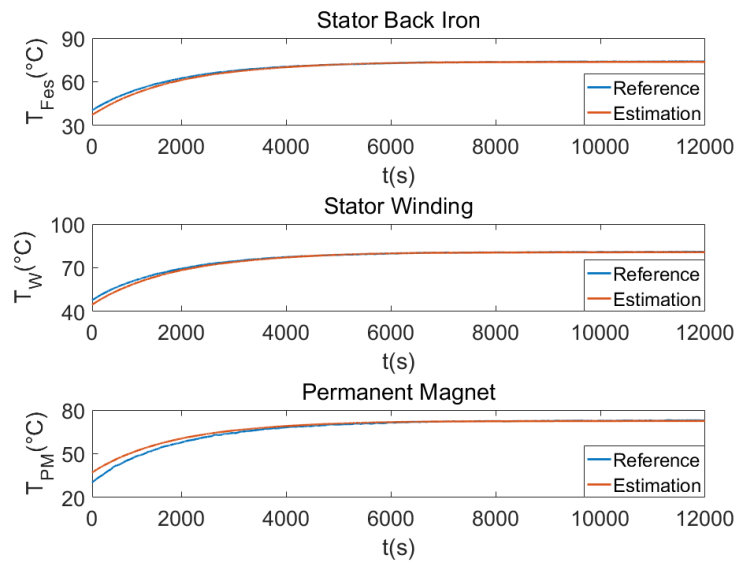


Fig. 4-11: Node temperatures estimated with the results in Fig. 4-10

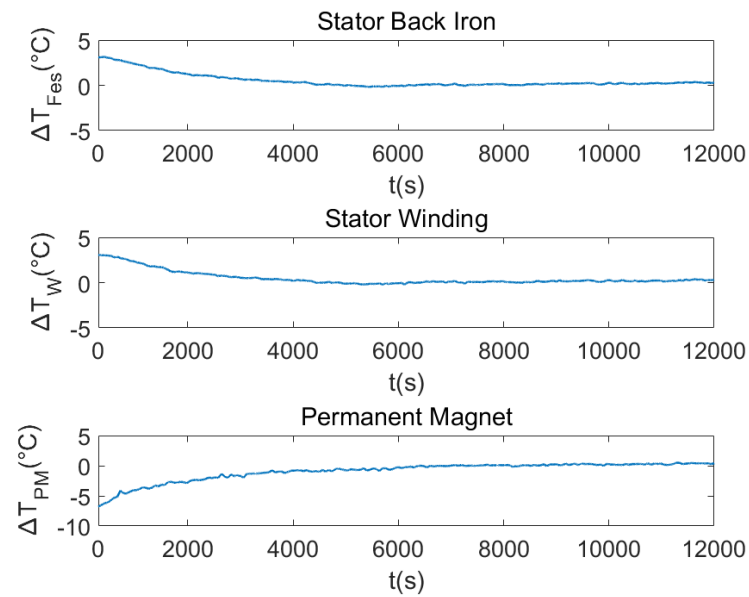


Fig. 4-12: Temperature errors in Fig. 4-11

Fig. 4-11 and Fig. 4-12 demonstrate the node temperatures which are predicted in the open-loop test with the parameters estimated by the Levenberg-Marquardt algorithm. Less than  $-7^{\circ}\text{C}$  error in rotor temperature and  $3.5^{\circ}\text{C}$  in the stator iron and winding temperatures can be observed, showing resemblance to Fig. 4-6 and Fig. 4-7, where the results are based on the EKF method. This further proves the identification problem has multiple local optima and that the solutions illustrated in Fig. 4-3 and Fig. 4-10 are equally correct.

## 4.2.4 Validation at Multiple Speeds and Currents

As mentioned in chapter 2, the thermal resistances may vary with motor operating conditions. Physically, the heat transfer coefficients between stator and rotor will be dependent on rotor speed. Additionally, the nonlinear least squared algorithms such as the EKF adopted here for parameter identification only search for parameters that guarantee the best fit between the mathematical function and the measurements. The identification of the thermal resistances is performed at  $\omega_r = 2000rpm, 2400rpm, 3200rpm,$  and  $3800rpm$ . As a result of the rotor speed and stator current not being decoupled in this particular application, speed is not independent from current. The motor accelerates as more current is required.

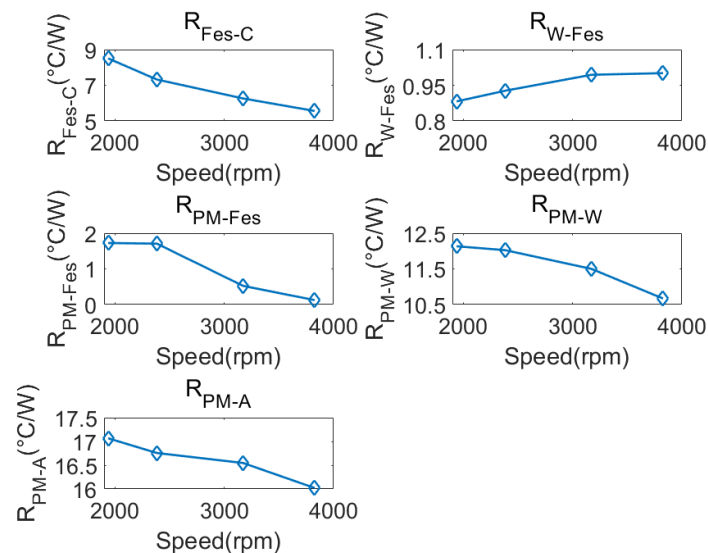


Fig. 4-13: Thermal resistance estimations under the conditions of  $\omega_r = 2000rpm, 2400rpm, 3200rpm,$  and  $3800rpm$  and their corresponding currents

The decrease in the thermal resistances connected with the rotor node may be linked with the speed-dependent convection effects. However the variation in the stator-related resistances, which in principle have no direct dependence on either the motor speed, or the stator current, are the result of the algorithm only considering the minimization of the cost function. Also, additional error is generated by the iron loss model, which has better accuracy at the speed where the constant parameters in (4-2) and (4-3) are calculated. The thermal resistances estimated with different current and speed conditions are shown in Fig. 4-14 to Fig. 4-18. The generator is connected to resistive loads, and the current level is dependent on the number of loads used. Therefore, the y-axis is set to be load condition instead of current.

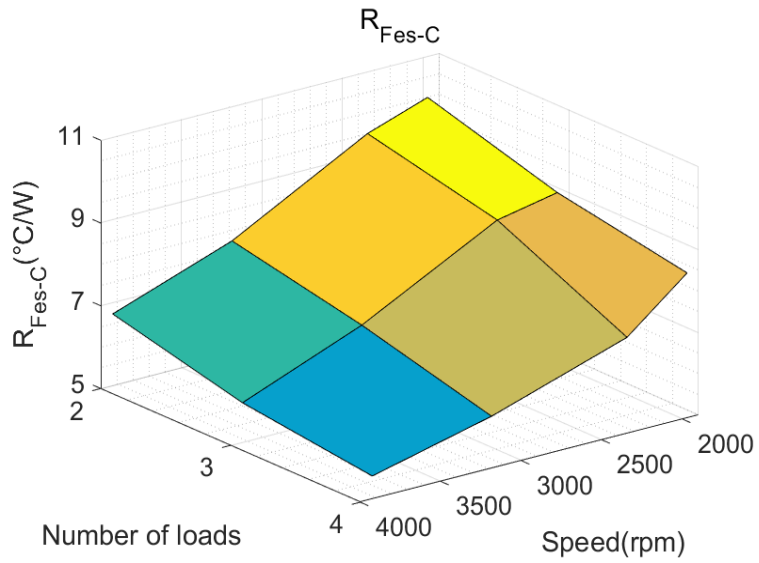


Fig. 4-14: Estimated thermal resistance  $R_{Fes-C}$  at different speeds and load conditions

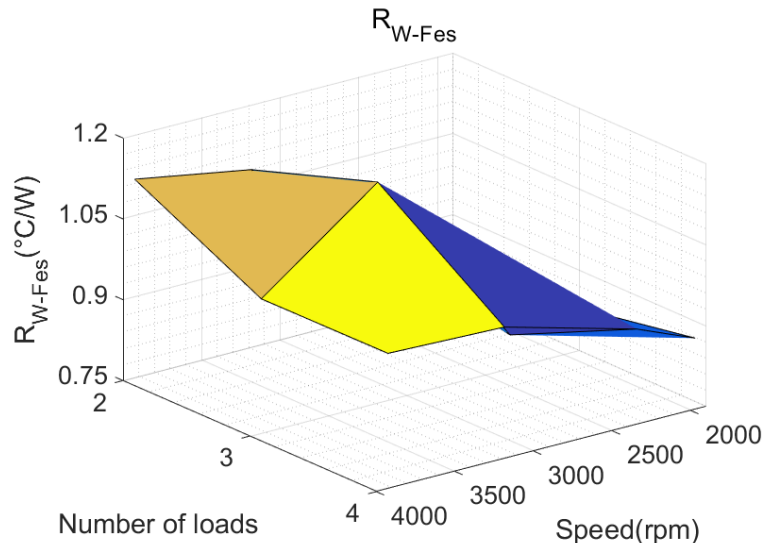


Fig. 4-15: Estimated thermal resistance  $R_{W-Fes}$  at different speeds and load conditions

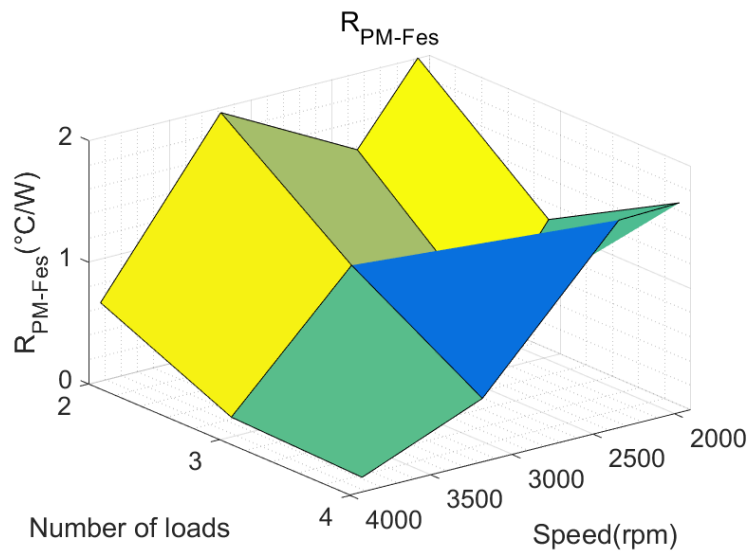


Fig. 4-16: Estimated thermal resistance  $R_{PM-Fes}$  at different speeds and load conditions

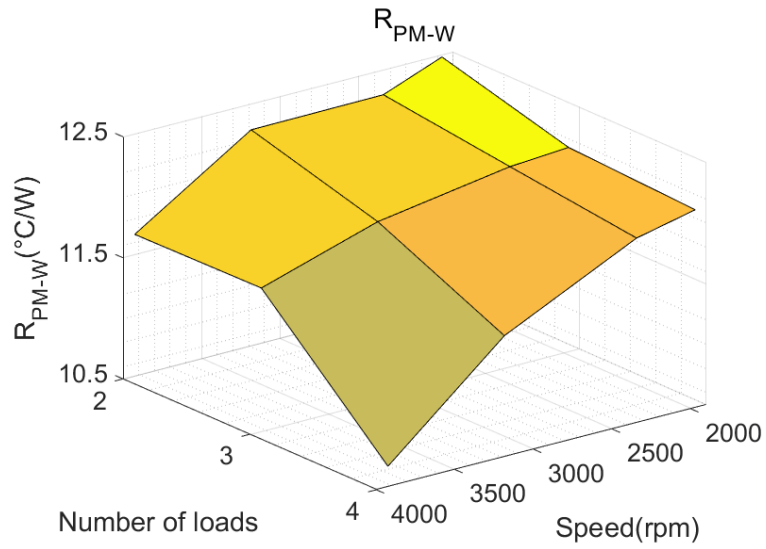


Fig. 4-17: Estimated thermal resistance  $R_{PM-W}$  at different speeds and load conditions

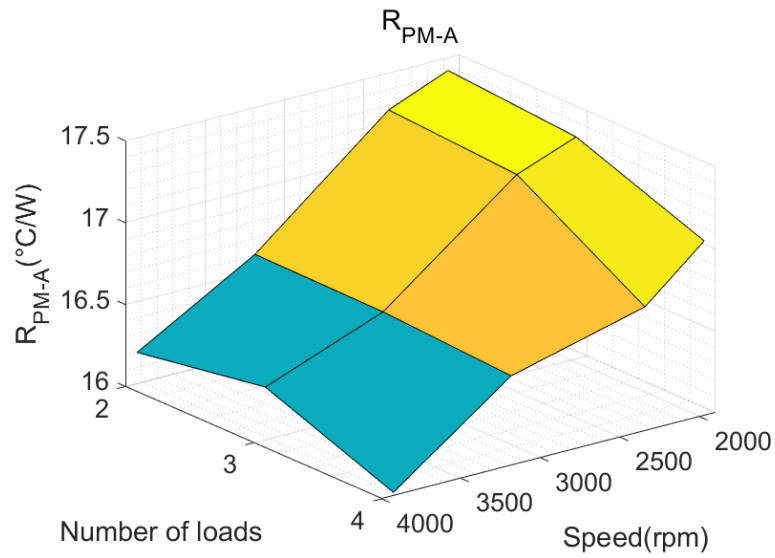


Fig. 4-18: Estimated thermal resistance  $R_{PM-A}$  at different speeds and load conditions

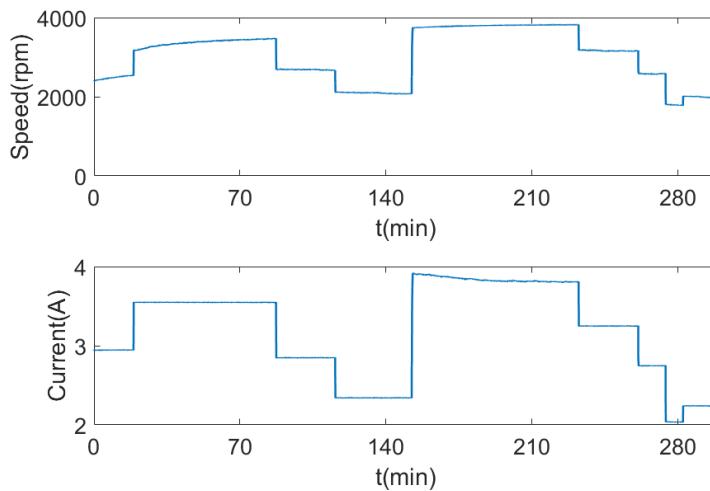


Fig. 4-19: Rotor speed and stator current profiles of the transient testing

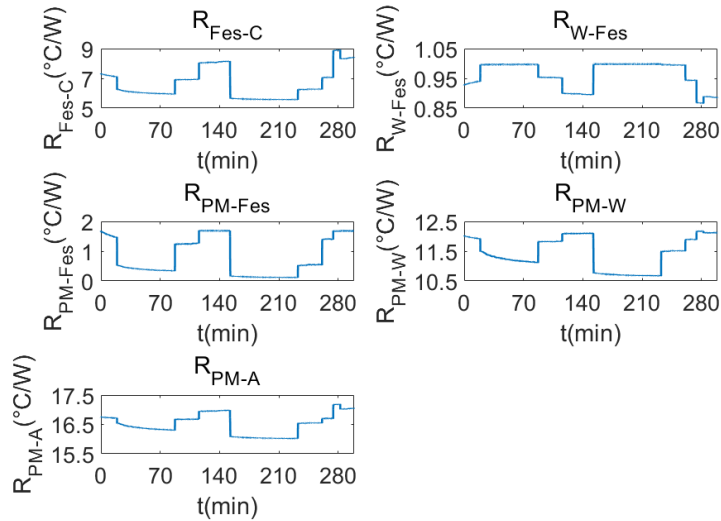


Fig. 4-20: Estimated thermal resistances according to the driving cycle

2-D LUTs with the identified parameters as the function of motor speed and number of loads are applied to estimate the node temperatures. A thermal transient test of slightly less than five hours is conducted, using a step-based duty cycle illustrated in Fig. 4-19. Fig. 4-20 depicts the dynamics of the thermal resistances. The maximum estimation error of no more than  $6^{\circ}\text{C}$  in all node temperatures is achieved, as can be seen in Fig. 4-21 and Fig. 4-22.

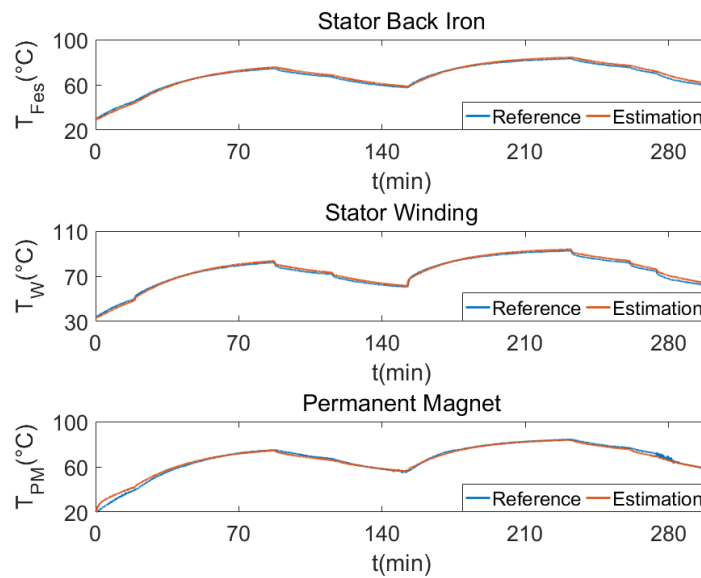


Fig. 4-21: Open-loop temperature estimations based on the transient driving cycle

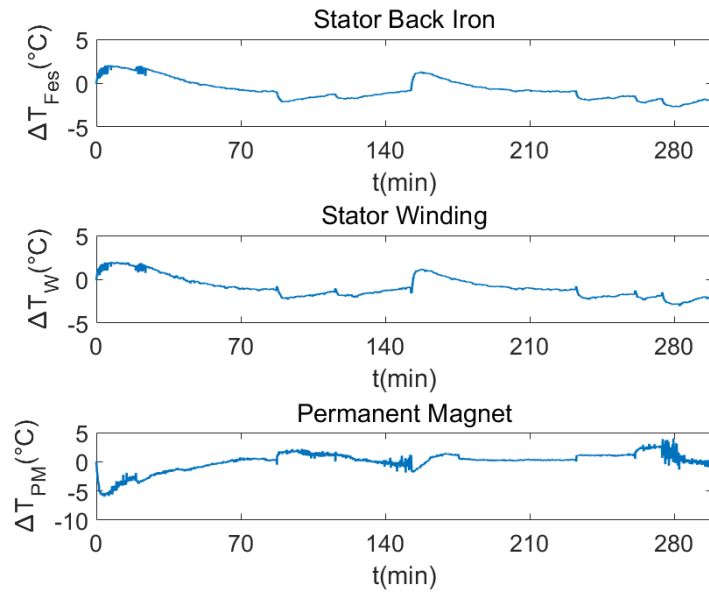


Fig. 4-22: Temperature estimation errors in Fig. 4-21

### 4.3 Conclusion

This chapter proposes a practical and relatively simple model-based methodology for the predictions of the stator iron, stator winding and PM temperatures in PMSMs, using a three-node thermal model featuring a PWM-based estimation algorithm as a replacement for rotor temperature measurement. The implementation of this method is rather simple as only the commonly measurable quantities, such as motor current, speed and stator temperatures, are required. The use of the PWM-based estimation avoids direct rotor temperature measurement, which is costly and practically difficult. Furthermore, the estimated temperatures contain low level of noise due to the filtering effect of the EKF algorithm. The experimental testing validates the presented method comprehensively on a typical SPMSM, and the result shows good precision in a variety of motor operating conditions.

# Chapter 5: Conclusion and Future Work

## 5.1 Conclusion

Temperature monitoring of PMSMs is of great importance because thermal stress is one of the main factors affecting their lifetimes. Whilst the implementation of direct temperature monitoring techniques on motor stator is relatively simple, rotor temperature measurement requires significant effort as it is difficult to place sensors on a rotating shaft. Alternatively, motor temperatures can be determined through temperature-dependent electrical parameters. However this method usually involves the use of an injected signal to the motor, which produces undesired ripples and losses disturbing motor operation. Besides, the accuracy of this method largely depends on that of the modelling of machine and inverter. Model-based approach based on lumped parameters equivalent thermal circuit can inform a thermal observer, which integrated with a robust loss model can also provide temperature estimation during real-time operation. Although a complex thermal network leads to more accurate temperature prediction, the information of motor dimension and material properties is required and the derivation of thermal parameters and coefficients using analytical formulas is hardly an easy task. The modelling depth of a reduced-order thermal model on the other hand is relatively low, as large regions of a motor can be lumped in several temperature nodes, and the thermal parameters can be computed in a measurement-informed identification procedure.

A simplified LPTN representing motor stator iron, stator winding, and permanent magnet is presented for the estimation of the critical temperatures in PMSMs. The heat conduction and convection in the motor are described in a compact style with a set of state-space equations. The losses and thermal capacitances of the motor are calculated via the Finite Element software, whereas an identification procedure based on the extended Kalman Filter algorithm is employed to estimate the unknown thermal resistances. As a result the analytical derivation is not necessary. This method is computationally efficient due to the simple three-node thermal structure. In addition, only little motor physical knowledge is required. However, the method is almost impossible to implement in practice due to the difficulty in accessing rotor temperature directly from temperature sensors. An approach able to estimate rotor temperature with high precision via PM flux linkage is one of the preferable solutions.

A relatively simple and accurate method for online flux linkage and rotor temperature estimations is then introduced, which is based on the response of motor current to the standard

space-vector pulse width modulation. It uses the already-existing PWM voltage as the excitation signal in order to avoid the need for additional signal injection, and knowledge of machine inductances which may vary as a result of saturation, is not required. A comprehensive validation is conducted in online simulation using the advanced Hardware-in-the-Loop technique which emulates the motor, power converter, field oriented control and proposed estimation algorithm in two separated FPGA-based data acquisition units. Also, extensive simulations and experimental validations are provided to evaluate the robustness of the method to a number of potential practical implementation errors, followed by the experimental testing in a wide range of motor temperatures. The results demonstrate no more than 2°C error in the predicted rotor temperatures, affirming that this method is suitable to provide the thermal model with a rotor temperature measurement.

The motor temperature estimation system integrating the three-node LPTN with the PWM-based rotor temperature estimation algorithm is experimentally validated and the maximum error in the estimated temperatures is approximately 6°C. In conclusion, this temperature estimation system is advantageous because: a) it is not computational-demanding as only the most dominant motor heat transfer processes are taken into consideration for the LPTN, b) its implementation is relatively simple, with only motor current, voltage, and stator temperature measurements required, c) direct rotor temperature measurement is avoided due to the use of the rotor temperature estimation method, d) the predicted motor temperatures are of low noise level because of the EKF's filtering effect.

## 5.2 Future Work

The main focus of the research in the future is to incorporate indirect stator temperature monitoring methods in the presented temperature estimation system in order to further reduce the number of temperature sensors required. Stator winding temperature can be predicted via temperature-dependent stator resistance. Online method based on signal injection technique, such as [26], where the stator resistance is relatively accurately determined using a full-rank motor model corresponding to  $i_d = 0$  and a  $i_d \neq 0$  signal injected into the motor, is one of the available options. Alternatively, parameter identification algorithm, such as the EKF algorithm proposed in [32], which updates the value of stator resistance continuously without involving the injection of an additional signal, can also be considered.

From the perspective of improving the estimation accuracy, future work should also be focused on the modification of the structure of the proposed LPTN, and the modelling of motor losses.

As mentioned in chapter 2, the oversimplification of the thermal network may be one of the major issues resulting in the temperature estimation errors, because the thermal resistance  $R_{PM-A}$  only considers the heat convection from the rotor to ambient through the rotor shaft. In fact, the rotor is also thermally connected to the end-cap, for instance, and to the generator via the metal frame mount. These heat paths should be modelled separately. Also, considering the temperature effect on the eddy-current iron loss may reduce the estimation errors. In addition, the rotor losses are rather small and therefore considered negligible in the experimental test in chapter 4. However, this assumption might lead to some errors in the rotor temperature estimation, because the cooling of the rotor can be difficult.

In chapter 3, the estimation of the rotor temperature requires the measurement of the stator terminal voltages, as the output voltage due to some inverter non-ideal effects such as dead-time is not solely determined by the voltage command. However standard commercial drives normally do not include voltage sensors, making the practical implementation of the method particularly difficult. In light of this issue, an inverter model compensating the difference between voltage command and PWM voltage should be used.

# APPENDICES

## Appendix A: list of publications

### Conference paper

- S. Xiao and A. Griffo, “PWM-based flux linkage estimation for permanent magnet synchronous machines,” in *proc. 9<sup>th</sup> IET Conf. Power Electron. Mach. Drives*, Apr. 2018, pp. 1-6.

### Journal

- S. Xiao and A. Griffo, “PWM-based flux linkage and rotor temperature estimations for permanent magnet synchronous machines,” *IEEE Trans. Power Electron.*, conditional acceptance.

## Appendix B: Parameter identification of three-node thermal network

The following Matlab function performs the identification of the unknown parameters in the three-node thermal network. The function contains 17 inputs, including:

- Losses generated by each temperature node, denoted as  $u(1)$ ,  $u(2)$  and  $u(3)$
- Cooling and ambient temperatures, denoted as  $u(4)$  and  $u(5)$
- Three node temperature measurements  $u(6)$ ,  $u(7)$  and  $u(8)$
- Three node temperatures predicted at the previous time step  $u(9)$ ,  $u(10)$  and  $u(11)$
- Thermal resistances estimated at the previous time step, used as the measurements for the estimation of the resistances at the current step and represented as  $u(12)$ ,  $u(13)$ ,  $u(14)$ ,  $u(15)$  and  $u(16)$
- Covariance matrix estimation  $P$  at the previous time step

The outputs are the present temperature, resistance and covariance predictions.

```
function [out,P_next] = fcn(u,P)
% system inputs: power, cooling and ambient temperatures
input = [u(1);u(2);u(3);u(4);u(5)];
% Temperature and resistance measurements
z_measured = [u(6);u(7);u(8);u(12);u(13);u(14);u(15);u(16)];
% System states: node temperatures and thermal resistances
x = [u(9);u(10);u(11);u(12);u(13);u(14);u(15);u(16)];
% Number of states
n = 8;
% Definition of process noise covariance
q = 0.1;
Q = q^2*eye(n);
% Definition of observation noise covariance
r = 0.1;
R = r^2*eye(n);
% Step 1/2: predict
x_next = f(x,input);
F = StateJacobian(x,input);
P_next = F*P*F'+Q;
```

```

% Step 2/2: update
H = OutputJacobian(x);
S = H*P_next*H' + R;
K = P_next*H'*inv(S);
z_predicted = h(x_next);
residual = z_measured - z_predicted;
P_next = (eye(n)-K*H)*P_next;
out = x_next + K*residual;
% Definition of nonlinear system
function funct = f(x,u)
% stator iron node capacitance calculated using Finite Element software
C_fe = 17694.48;
% stator winding node capacitance
C_w = 3667.72;
% permanent magnet node capacitance
C_pm = 6034.32;
% sampling time
Ts = 1;
funct = [(1-(Ts/C_fe)*((1/x(4))+1/x(5))+1/x(6)))*x(1)+(Ts/C_fe)*(1/x(5))*x(2)
+(Ts/C_fe)*(1/x(6))*x(3)+(Ts/C_fe)*u(1)+(Ts/C_fe)*(1/x(4))*u(4);
(Ts/C_w)*(1/x(5))*x(1)+(1-(Ts/C_w)*((1/x(5))+1/x(7)))*x(2)
+(Ts/C_w)*(1/x(7))*x(3)+(Ts/C_w)*u(2);(Ts/C_pm)*(1/x(6))*x(1)
+(Ts/C_pm)*(1/x(7))*x(2)+(1-(Ts/C_pm)*((1/x(6))+1/x(7))+1/x(8)))*x(3)
+(Ts/C_pm)*u(3)+(Ts/C_pm)*(1/x(8))*u(5);x(4);x(5);x(6);x(7);x(8)];
% Definition of observation
function HH = h(x)
HH = [x(1);x(2);x(3);x(4);x(5);x(6);x(7);x(8)];
% Definition of state-transition Jacobian
function J=StateJacobian(x,u)
C_fe = 17694.48;
C_w = 3667.72;
C_pm = 6034.32;
Ts = 1;
J = zeros(8);
J(1,1) = 1-(Ts/C_fe)*((1/x(4))+1/x(5))+1/x(6));

```

$J(1,2) = (Ts/C_{fe}) * (1/x(5));$   
 $J(1,3) = (Ts/C_{fe}) * (1/x(6));$   
 $J(1,4) = (Ts/C_{fe}) * ((x(1)-u(4))/(x(4)^2));$   
 $J(1,5) = (Ts/C_{fe}) * ((x(1)-x(2))/(x(5)^2));$   
 $J(1,6) = (Ts/C_{fe}) * ((x(1)-x(3))/(x(6)^2));$   
 $J(1,7) = 0;$   
 $J(1,8) = 0;$   
 $J(2,1) = (Ts/C_w) * (1/x(5));$   
 $J(2,2) = 1 - (Ts/C_w) * ((1/x(5)) + (1/x(7)));$   
 $J(2,3) = (Ts/C_w) * (1/x(7));$   
 $J(2,4) = 0;$   
 $J(2,5) = (Ts/C_w) * ((x(2)-x(1))/(x(5)^2));$   
 $J(2,6) = 0;$   
 $J(2,7) = (Ts/C_w) * ((x(2)-x(3))/(x(7)^2));$   
 $J(2,8) = 0;$   
 $J(3,1) = (Ts/C_{pm}) * (1/x(6));$   
 $J(3,2) = (Ts/C_{pm}) * (1/x(7));$   
 $J(3,3) = 1 - (Ts/C_{pm}) * ((1/x(6)) + (1/x(7)) + (1/x(8)));$   
 $J(3,4) = 0;$   
 $J(3,5) = 0;$   
 $J(3,6) = (Ts/C_{pm}) * ((x(3)-x(1))/(x(6)^2));$   
 $J(3,7) = (Ts/C_{pm}) * ((x(3)-x(2))/(x(7)^2));$   
 $J(3,8) = (Ts/C_{pm}) * ((x(3)-u(5))/(x(8)^2));$   
 $J(4,1) = 0;$   
 $J(4,2) = 0;$   
 $J(4,3) = 0;$   
 $J(4,4) = 1;$   
 $J(4,5) = 0;$   
 $J(4,6) = 0;$   
 $J(4,7) = 0;$   
 $J(4,8) = 0;$   
 $J(5,1) = 0;$   
 $J(5,2) = 0;$   
 $J(5,3) = 0;$   
 $J(5,4) = 0;$

$$J(5,5) = 1;$$

$$J(5,6) = 0;$$

$$J(5,7) = 0;$$

$$J(5,8) = 0;$$

$$J(6,1) = 0;$$

$$J(6,2) = 0;$$

$$J(6,3) = 0;$$

$$J(6,4) = 0;$$

$$J(6,5) = 0;$$

$$J(6,6) = 1;$$

$$J(6,7) = 0;$$

$$J(6,8) = 0;$$

$$J(7,1) = 0;$$

$$J(7,2) = 0;$$

$$J(7,3) = 0;$$

$$J(7,4) = 0;$$

$$J(7,5) = 0;$$

$$J(7,6) = 0;$$

$$J(7,7) = 1;$$

$$J(7,8) = 0;$$

$$J(8,1) = 0;$$

$$J(8,2) = 0;$$

$$J(8,3) = 0;$$

$$J(8,4) = 0;$$

$$J(8,5) = 0;$$

$$J(8,6) = 0;$$

$$J(8,7) = 0;$$

$$J(8,8) = 1;$$

% Definition of observation Jacobian

function Ja = OutputJacobian(x)

Ja = eye(8);

## Appendix C: Voltage calculation of the PWM-based flux linkage and rotor temperature estimations

The MATLAB functions carrying out voltage calculation in (3-25) are shown. Voltage input is assumed to be in the form of a rotating space vector expressed as  $\bar{V}^* = |\bar{V}^*| \angle \alpha$ . Rotor angle is also required to calculate the  $q$ -axis voltage components of active state vectors. The voltage calculation only takes place at the beginning of a PWM switching period, where the values of  $|\bar{V}^*|$ ,  $\alpha$  and rotor angle are triggered by an additional digital signal.

% V\_ref\_mag is reference voltage magnitude, V\_ref\_ang is the location of the reference vector in relation to the active voltage vectors on state vector diagram

function Vq = fcn(V\_ref\_mag, V\_ref\_ang, theta)

% Tc is half switching frequency, Vdc is inverter DC-link voltage, and mag is a constant for the calculation of the time intervals active state vectors are applied

Tc = (1/10000)/2;

Vdc = 24;

gain = Vdc/sqrt(3);

mag = (V\_ref\_mag/gain)\* Tc;

% Sector 1

if (V\_ref\_ang >= 0 && V\_ref\_ang < pi/3)

    T1 = mag \* sin(pi/3 - V\_ref\_ang);

    T2 = mag \* sin(V\_ref\_ang);

    Sector = 1;

else

% Sector 2

if (V\_ref\_ang >= pi/3 && V\_ref\_ang < 2\*pi/3)

    adv = V\_ref\_ang - pi/3;

    T2 = mag \* sin(pi/3 - adv);

    T1 = mag \* sin(adv);

    Sector = 2;

else

% Sector 3

if (V\_ref\_ang >= 2\*pi/3 && V\_ref\_ang < pi)

    adv = V\_ref\_ang - 2\*pi/3;

    T1 = mag \* sin(pi/3 - adv);

    T2 = mag \* sin(adv);



```

V1_beta = 0;
V1_q = -sin(theta)*V1_alpha + cos(theta)*V1_beta;
% V2
V2_alpha = 1*Vdc/3;
V2_beta = 1*Vdc/sqrt(3);
V2_q = -sin(theta)*V2_alpha + cos(theta)*V2_beta;
% V3
V3_alpha = -1*Vdc/3;
V3_beta = 1*Vdc/sqrt(3);
V3_q = -sin(theta)*V3_alpha + cos(theta)*V3_beta;
% V4
V4_alpha = -2*Vdc/3;
V4_beta = 0;
V4_q = -sin(theta)*V4_alpha + cos(theta)*V4_beta;
% V5
V5_alpha = -1*Vdc/3;
V5_beta = -1*Vdc/sqrt(3);
V5_q = -sin(theta)*V5_alpha + cos(theta)*V5_beta;
% V6
V6_alpha = 1*Vdc/3;
V6_beta = -1*Vdc/sqrt(3);
V6_q = -sin(theta)*V6_alpha + cos(theta)*V6_beta;
% Calculation of the voltage term in (3-25) and considering two symmetrical switching
combinations in one PWM switching period
if (Sector == 1)
    Vq = 2*T1*V1_q + 2*T2*V2_q;
else
    if (Sector == 2)
        Vq = 2*T1*V3_q + 2*T2*V2_q;
    else
        if (Sector == 3)
            Vq = 2*T1*V3_q + 2*T2*V4_q;
        else
            if (Sector == 4)
                Vq = 2*T1*V5_q + 2*T2*V4_q;

```

```
else
  if (Sector == 5)
    Vq = 2*T1*V5_q + 2*T2*V6_q;
  else
    if (Sector == 6)
      Vq = 2*T1*V1_q + 2*T2*V6_q;
    else
      Vq = 0;
    end
  end
end
end
end
end
end
```

## Reference

- [1] S. B. Lee, J. Yang, J. Hong, J.-Y. Yoo, B. Kim, K. Lee, J. Yun, M. Kim, K.-W. Lee, E. J. Wiedenbrug, and S. Nandi, "A new strategy for condition monitoring of adjustable speed induction machine drive systems," *IEEE Trans. Power Electron.*, vol. 26, no. 2, pp. 389-398, Feb. 2011.
- [2] R. R. Errabelli and P. Mutschler, "Fault-tolerant voltage source inverter for permanent magnet drives," *IEEE Trans. Power Electron.*, vol. 27, no. 2, pp. 500-508, Feb. 2012.
- [3] J. Hong, S. B. Lee, C. Karl, and A. Haumer, "Detection of airgap eccentricity for permanent magnet synchronous motors based on the d-axis inductance," *IEEE Trans. Power Electron.*, vol. 27, no. 1, pp. 2605-2612, May 2012.
- [4] S. Cheng, Y. Du, J. A. Restrepo, P. Zhang, and T. G. Habetler, "A nonintrusive thermal monitoring method for induction motors fed by closed-loop inverter drives," *IEEE Trans. Power Electron.*, vol. 27, no. 9, pp. 4122-4131, Sep. 2012.
- [5] Y. Da, X. Shi, and M. Krishnamurthy, "A new approach to fault diagnostics for permanent magnet synchronous machines using electromagnetic signature analysis," *IEEE Trans. Power Electron.*, vol. 28, no. 8, pp. 4104-4112, Aug. 2013.
- [6] X. Chen, J. Wang, and A. Griffio, "A high-fidelity and computationally efficient electro-thermally coupled model for interior permanent-magnet machines in electric vehicle traction applications," *IEEE Trans. Transport. Electrification.*, vol. 1, no. 4, pp. 336-347, Dec. 2015.
- [7] T. Huber, W. Peters, and J. Bocker, "A low-order thermal model for monitoring critical temperatures in permanent magnet synchronous motors," in *Proc. 7<sup>th</sup> IET Conf. Power Electron. Mach. Drives*, Oct. 2014, pp. 1-6.
- [8] A. Specht and J. Bocker, "Observer for the rotor temperature of IPMSM," in *Proc. 14<sup>th</sup> Int. Power Electron. Motion Control Conf.*, Sep. 2010, pp. T4-12 – T4-15.
- [9] J. Dymond, R. Ong, and N. Stranges, "Instrumentation, testing and analysis of electric machine rotor steady-state heating," *Petro. Chem. Ind. Conf., IEEE Ind. Appl. Soc. 48<sup>th</sup> Annu.*, Sep. 2001, pp. 297-303.

- [10] C. Mejuto, M. Mueller, M. Shanel, A. Mebarki, M. Reekie, D. Staton, "Improved synchronous machine thermal modelling," in *Proc. Int. Conf. Electrical Mach.*, Sep. 2008, pp. 1-6.
- [11] D. Reigosa, F. Briz, M. W. Degner, P. Garcia, and J. M. Guerrero, "Magnet temperature estimation in surface PM machines during six-step operation," *IEEE Trans. Ind. Appl.*, vol. 48, no. 6, pp. 2353-2361, Nov.-Dec. 2012.
- [12] C. Kral, A. Haumer, M. Haigis, H. Lang, H. Kapeller, "Comparison of a CFD analysis and a thermal equivalent circuit model of a TEFC induction machine with measurements," *IEEE Trans. Energy Convers.*, vol. 24, no. 4, pp. 809-818, Dec. 2009.
- [13] Z. Hou and G. Gu, "Wireless rotor temperature measurement system based on MSP430 and nRF401," in *Proc. Int. Conf. Electrical Mach. Systems*, Oct. 2008, pp. 858-861.
- [14] D. Fernandez, D. Reigosa, T. Tanimoto, T. Kato, and F. Briz, "Wireless permanent magnet temperature and field distribution measurement system for IPMSMs," in *Proc. IEEE Energy Convers. Cong. Expo.*, Sep. 2015, pp. 3996-4003.
- [15] M. Ganchev, H. Umschaden, and H. J. Kapeller, "Rotor temperature distribution measuring system," in *Proc. 37<sup>th</sup> Annu. Conf. IEEE Ind. Electron. Soc.*, Nov. 2011, pp. 2006-2011.
- [16] F. Briz, M. W. Degner, J. M. Guerrero, and A. B. Diez, "Temperature estimation in inverter-fed machines using high-frequency carrier signal injection," *IEEE Trans. Ind. Appl.*, vol. 44, no. 2, pp. 799-808, May-Jun. 2008.
- [17] D. Reigosa, P. Garcia, F. Briz, D. Raca, and R. D. Lorenz, "Modelling and adaptive decoupling of transient resistance and temperature effects in carrier-based sensorless control of PM synchronous machines," in *IEEE Ind. Appl. Soc. Annu. Meet.*, Oct. 2008, pp. 1-8.
- [18] D. Reigosa, F. Briz, P. Garcia, J. M. Guerrero, and M. W. Degner, "Magnet temperature estimation in surface PM machines using high-frequency signal injection," *IEEE Trans. Ind. Appl.*, vol. 46, no. 4, pp. 1468-1475, Jul.-Aug. 2010.
- [19] D. Reigosa, D. Fernandez, H. Yoshida, T. Kato, and F. Briz, "Permanent magnet temperature estimation in PMSMs using pulsating high frequency current injection," *IEEE Trans. Ind. Appl.*, vol. 51, no. 4, pp. 3159-3168, Jul.-Aug. 2015.

- [20] D. Reigosa, D. Fernandez, T. Tanimoto, T. Kato, and F. Briz, "Permanent magnet temperature distribution estimation in PMSMs using BEMF harmonics," in *Proc. IEEE Energy Convers. Cong. Expo.*, Sep. 2015, pp. 768-775.
- [21] D. Reigosa, D. Fernandez, T. Tanimoto, T. kato, and F. Briz, "Sensitivity analysis of high frequency signal injection based temperature estimation methods to machine assembling tolerances," in *Proc. IEEE Energy Convers. Cong. Expo.*, Sep. 2015, pp. 6122-6129.
- [22] M. Ganchev, C. Kral, H. Oberguggenberger, and T. Wolbank, "Sensorless rotor temperature estimation of permanent magnet synchronous motor," in *Proc. 37<sup>th</sup> Annu. Conf. IEEE Ind. Electron. Soc.*, Nov. 2011, pp. 2018-2023.
- [23] M. Ganchev, C. Karl, and T. Wolbank, "Identification of sensorless rotor temperature estimation technique for permanent magnet synchronous motor," in *Proc. Int. Symp. Power Electron. Electrical Drives Autom. Motion*, Jun. 2012, pp. 38-43.
- [24] M. Ganchev, C. Karl, and T. Wolbank, "Hardware and software implementation of sensorless rotor temperature estimation technique for permanent magnet synchronous motor," in *Proc. IEEE Int. Conf. ESARS*, Oct. 2012, pp. 1-6.
- [25] M. Ganchev, C. Karl, and T. Wolbank, "Compensation of speed dependence in sensorless rotor temperature estimation for permanent magnet synchronous motor," *IEEE Trans. Ind. Appl.*, vol. 49, no. 6, pp. 2487-2495, Nov.-Dec. 2013.
- [26] K. Liu, Z. Zhu, and D. Stone, "Parameter estimation for condition monitoring of PMSM stator winding and rotor permanent magnets," *IEEE Trans. Ind. Electron.*, vol. 60, no. 12, pp. 5902-5913, Dec. 2013.
- [27] K. Liu, Q. Zhang, J. Chen, Z. Zhu, and J. Zhang, "Online multiparameter estimation of nonsalient-pole PM synchronous machines with temperature variation tracking," *IEEE Trans. Ind. Electron.*, vol. 58, no. 5, pp. 1776-1788, May 2011.
- [28] G. Xie, K. Lu, S. K. Dwivedi, R. J. Riber, and W. Wu, "Permanent magnet flux online estimation based on zero-voltage vector injection method," *IEEE Trans. Power Electron.*, vol. 30, no. 12, pp. 6506-6509, Dec. 2015.
- [29] A. Specht, O. Wallscheid, and J. Bocker, "Determination of rotor temperature for an interior permanent magnet synchronous machine using a precise flux observer," in *proc. Int. Power Electron. Conf.*, May 2014, pp. 1501-1507.

- [30] O. Wallscheid, A. Specht, and J. Bocker, "Observing the permanent magnet temperature of synchronous motors based on electrical fundamental wave model quantities," *IEEE Trans. Ind. Electron.*, vol. 64, no. 5, pp. 3921-3929, May 2017.
- [31] O. Wallscheid and J. Bocker, "Fusion of direct and indirect temperature estimation techniques for permanent magnet synchronous motors," in *Proc. IEEE Int. Electric Mach. Drives Conf.*, Aug. 2017, pp. 1-8.
- [32] Z. Zhu, X. Zhu, P. Sun, and D. Howe, "Estimation of winding resistance and PM flux-linkage in brushless AC machines by reduced-order extended Kalman Filter," in *Proc. IEEE Int. Conf. Netw. Sens. Control*, Apr. 2007, pp. 740-745.
- [33] A. Piippo, M. Hinkkanen, and J. Luomi, "Adaptation of motor parameters in sensorless PMSM drives," in *Proc. 7<sup>th</sup> Int. Conf. Power Electron. Drive Syst.*, Nov. 2007, pp. 175-182.
- [34] X. Xiao, C. Chen, and M. Zhang, "Dynamic permanent magnet flux estimation of permanent magnet synchronous machines," *IEEE Trans. Appl. Supercond.*, vol. 20, no. 3, pp. 1085-1088, Jun. 2010.
- [35] S. J. Underwood and I. Husain, "Online parameter estimation and adaptive control of permanent magnet synchronous machines," *IEEE Trans. Ind. Electron.*, vol. 57, no. 7, pp. 2435-2443, Jul. 2010.
- [36] K. Liu, Z. Zhu, Q. Zhang, and J. Zhang, "Influence of nonideal voltage measurement on parameter estimation in permanent magnet synchronous machines," *IEEE Trans. Ind. Electron.*, vol. 59, no. 6, pp. 2438-2447, Jun. 2012.
- [37] K. Liu and Z. Zhu, "Online estimation of the rotor flux linkage and voltage-source inverter nonlinearity in permanent magnet synchronous machine drives," *IEEE Trans. Power Electron.*, vol. 29, no. 1, pp. 418-427, Jan. 2014.
- [38] K. Liu and Z. Zhu, "Mechanical parameter estimation of permanent magnet synchronous machines with aiding from estimation of rotor PM flux linkage," *IEEE Trans. Ind. Appl.*, vol. 51, no. 4, pp. 3115-3125, Jul.-Aug. 2015.
- [39] P. H. Mellor, D. Roberts, and T. R. Turner, "Lumped parameter thermal model for electrical machines of TEFC design," in *Proc. IEE Electric Power Appl.*, vol. 138, no. 5, Sep. 1991, pp. 205-218.

- [40] G. Kylander, "Thermal modelling of small cage induction motors," Ph.D. dissertation, School Electrical Comput. Eng., Chalmers Univ. Technol., Goteborg, Sweden, Tech. Rep. 265, Feb. 1995.
- [41] A. Boglietti, A. Cavagnino, M. Lazzari, and M. Pastorelli, "A simplified thermal model for variable-speed self-cooled industrial induction motor," *IEEE Trans. Ind. Appl.*, vol. 39, no. 4, pp. 945-952, Jul.-Aug. 2003.
- [42] A. M. El-Refaie, N.C. Harris, T. M. Jahns, and K. M. Rahman, "Thermal analysis of multibarrier interior PM synchronous machine using lumped parameter model," *IEEE Trans. Energy Convers.*, vol. 19, no. 2, pp. 303-309, Jun. 2004.
- [43] E. Andersson, *Real Time Thermal Model for Servomotor Applications*, ABB AB Corporate Research, Vasteras, Sweden, Feb. 2006.
- [44] J. Nerg, M. Rilla, and J. Pyrhonen, "Thermal analysis of radial-flux electrical machines with a high power density," *IEEE Trans. Ind. Electron.*, vol. 55, no. 10, pp. 3543-3554, Oct. 2008.
- [45] G. D. Demetriades, H. Z. de la Parra, E. Andersson, and H. Olsson, "A real-time thermal model of a permanent-magnet synchronous motor," *IEEE Trans. Power Electron.*, vol. 25, no. 2, pp. 463-474, Feb. 2010.
- [46] J. Fan, C. Zhang, Z. Wang, Y. Dong, C. E. Nino, A. R. Tariq, and E. G. Strangas, "Thermal analysis of permanent magnet motor for the electric vehicle application considering driving duty cycle," *IEEE Trans. Magn.*, vol. 46, no. 6, pp. 2493-2496, Jun. 2010.
- [47] T. Bauml, C. Jungreuthmayer, and C. Karl, "An innovative parametrization method for a thermal equivalent circuit model of an interior permanent magnet synchronous machine," in *Proc. 37<sup>th</sup> Annu. Conf. IEEE Ind. Electron. Soc.*, Nov. 2011, pp. 1746-1781.
- [48] F. Qi, M. Schenk, and R. D. Doncker, "Discussing details of lumped parameter thermal modelling in electrical machines," in *Proc. 7<sup>th</sup> Int. Conf. Power Electron. Mach. Drives*, Apr. 2014, pp. 1-6.
- [49] O. Wallscheid and J. Bocker, "Design and identification of a lumped parameter thermal network for permanent magnet synchronous motors based on heat transfer theory and

- particle swarm optimization,” in *Proc. 17<sup>th</sup> Eur. Conf. Power Electron. Appl.*, Sep. 2015, pp. 1-10.
- [50] A. Boglietti, A. Cavagnino, and D. Staton, “Determination of critical parameters in electrical machine thermal models,” *IEEE Trans. Ind. Appl.*, vol. 44, no. 4, pp. 1150-1159, Jul. 2008.
- [51] D. Staton and A. Cavagnino, “Convection heat transfer and flow calculations suitable for electric machines thermal models,” *IEEE Trans. Ind. Electron.*, vol. 55, no. 10, pp. 3509-3516, Oct. 2008.
- [52] D. A. Howey, A. S. Holmes, and K. R. Pullen, “Measurement of stator heat transfer in air-cooled axial flux permanent magnet machines,” in *Proc. 35<sup>th</sup> Annu. Conf. IEEE Ind. Electron.*, Nov. 2009, pp. 1197-1202.
- [53] D. A. Howey, A. S. Holmes, and K. R. Pullen, “Measurement and CFD prediction of heat transfer in air-cooled disc-type electrical machines,” *IEEE Trans. Ind. Appl.*, vol. 47, no. 4, pp. 1716-1723, Jul.-Aug. 2011.
- [54] X. Chen, J. Wang, B. Sen, P. Lazari, and T. Sun, “A high-fidelity, computationally efficient model for interior permanent magnet machines considering the magnetic saturation, spatial harmonics and iron loss effect,” *IEEE Trans. Ind. Electron.*, vol. 62, no. 7, pp. 4044-4055, Jul. 2015.
- [55] C. Karl, A. Haumer, and S. B. Lee, “Robust thermal model for the estimation of rotor cage and stator winding temperatures of induction machines,” in *Proc. 20<sup>th</sup> Int. Conf. Electrical Mach.*, Sep. 2012, pp. 1810-1816.
- [56] C. Karl, A. Haumer, and S. B. Lee, “A practical thermal model for the estimation of permanent magnet and stator winding temperatures,” *IEEE Trans. Power Electron.*, vol. 29, no. 1, pp. 455-464, Jan. 2014.
- [57] T. Huber, W. Peters, and J. Bocker, “Monitoring critical temperatures in permanent magnet synchronous motors using low-order thermal models,” in *Proc. Int. Power Electron. Conf.*, May 2014, pp. 1508-1515.
- [58] A. Boglietti, E. Carpaneto, M. Cossale, A. L. Borlera, D. Staton, and M. Popescu, “Electrical machine first order short-time thermal transients model: measurements and parameters evaluation,” in *Proc. 40<sup>th</sup> Annu. Conf. IEEE Ind. Electron. Soc.*, Oct.-Nov. 2014, pp. 555-561.

- [59] O. Wallscheid and J. Bocker, "Design and empirical identification of a lumped parameter thermal network for permanent magnet synchronous motors with physically motivated constraints," in *Proc. IEEE Int. Electric Mach. Drives Conf.*, May 2015, pp. 1380-1386.
- [60] O. Wallscheid and J. Bocker, "Global identification of a low-order lumped-parameter thermal network for permanent magnet synchronous motors," *IEEE Trans. Energy Convers.*, vol. 31, no. 1, pp. 354-365, Mar. 2016.
- [61] S. W. Allison, M. R. Cates, B. W. Noel, and G. T. Gillies, "Monitoring permanent-magnet motor heating with phosphor thermometry," *IEEE Trans. Instrum. Measurem.*, vol. 37, no. 4, pp. 637-641, Dec. 1988.
- [62] P. Zheng, S. Pan, and Y. Li, "The research on the network optical fibre sensor of the surface temperature measurement for a large rotor based on IEEE1451.2," in *Proc. Int. Conf. Electrical Mach. Syst.*, Sep. 2005, pp. 2434-2436.
- [63] D. J. Tilak Siyambalapitiya, P. G. McLaren, and P. P. Acarnley, "A rotor condition monitor for squirrel-cage induction machines," *IEEE Trans. Ind. Appl.*, vol. IA-23, no. 2, pp. 334-340, Mar. 1987.
- [64] H. Yahoui, and G. Grellet, "Measurement of physical signals in rotating part of electrical machine by means of optical fibre transmission," in *Proc. IEEE Instrum. Measurem. Technol. Conf.*, Jun. 1996, pp. 591-596.
- [65] Z. Lazarevic, R. Radosavljevic, and P. Osmokrovic, "A new thermal observer for squirrel-cage induction motor," in *Proc. IEEE Instrum. Measurem. Technol. Conf.*, Jun. 1996, pp. 610-613.
- [66] X. Xue, V. Sundararajan, and W. P. Brithinee, "The application of wireless sensor networks for condition monitoring in three-phase induction motors," in *Proc. Electrical Insul. Conf. Electrical Manuf. Expo*, Oct. 2007, pp. 445-448.
- [67] H. Hafezi, and A. Jalilian, "Design and construction of induction motor thermal monitoring system," in *Proc. 41<sup>st</sup> Int. Univ. Power Eng. Conf.*, Sep. 2006, pp. 674-678.
- [68] J. Guo, H. Guo, and Z. Hou, "Rotor temperature monitoring technology of direct-drive permanent magnet wind turbine," in *Proc. Int. Conf. Electrical Mach. Syst.*, Nov. 2009, pp. 1-4.

- [69] S. B. Lee and T. G. Habetler, "An online stator winding resistance estimation technique for temperature monitoring of line-connected induction machines," *IEEE Trans. Ind. Appl.*, vol. 39, no. 3, pp. 685-694, May-Jun. 2003.
- [70] P. Zhang, B. Lu, and T. G. Habetler, "A remote and sensorless stator winding resistance estimation method for thermal protection of soft-starter-connected induction machines," *IEEE Trans. Ind. Electron.*, vol. 55, no. 10, pp. 3611-3618, Oct. 2008.
- [71] S. D. Wilson, P. Stewart, and B. P. Taylor, "Methods of resistance estimation in permanent magnet synchronous motors for real-time thermal management," *IEEE Trans. Energy Convers.*, vol. 25, no. 3, pp. 698-707, Sep. 2010.
- [72] A. Piippo, M. Hinkkanen, and J. Luomi, "Adaption of motor parameters in sensorless PMSM drives," *IEEE Trans. Ind. Appl.*, vol. 45, no. 1, pp. 203-212, Jan.-Feb. 2009.
- [73] R. Krishnan and P. Vijayraghavan, "Fast estimation and compensation of rotor flux linkage in permanent magnet synchronous machines," in *Proc. IEEE Int. Symp. Ind. Electron.*, Jul. 1999, pp. 661-666.
- [74] K. W. Lee, D. H. Jung, and I. J. Ha, "An online identification method for both stator resistance and back-EMF coefficient of PMSMs without rotational transducers," *IEEE Trans. Ind. Electron.*, vol. 51, no. 2, pp. 507-510, Apr. 2004.
- [75] S. Morimoto, M. Sanada, and Y. Takeda, "Mechanical sensorless drives of IPMSM with online parameter identification," *IEEE Trans. Ind. Appl.*, vol. 42, no. 5, pp. 1241-1248, Sep.-Oct. 2006.
- [76] R. Ramakrishnan, R. Islam, M. Islam, and T. Sebastian, "Real time estimation of parameters for controlling and monitoring permanent magnet synchronous motors," in *Proc. IEEE Int. Electric Mach. Drives Conf.*, May 2009, pp. 1194-1199.
- [77] U. Schaible and B. Szabados, "Dynamic motor parameter identification for high speed flux weakening operation of brushless permanent magnet synchronous machines," *IEEE Trans. Energy Convers.*, vol. 14, no. 3, pp. 486-492, Sep. 1999.
- [78] T. Senjyu, Y. Kuwae, N. Urasaki, and K. Uezato, "Accurate parameter measurement for high speed permanent magnet," in *Proc. 32<sup>nd</sup> Annu. Power Electron. Spec. Conf.*, Jun. 2001, pp. 772-777.

- [79] M. A. Jabbar, J. Dong, and Z. Liu, "Determination of machine parameters for internal permanent magnet synchronous motors," in *Proc. 2<sup>nd</sup> Int. Conf. Power Electron. Mach. Drives*, Mar.-Apr. 2004, pp. 805-810.
- [80] H. Polinder and M. J. Hoeijmakers, "Eddy-current losses in permanent magnet of a PM machine," in *Proc. 8<sup>th</sup> Int. Conf. Electrical Mach. Drives*, Sep. 1997, pp. 138-142.
- [81] B. Widrow and M. A. Lehr, "30 years of adaptive neural networks: Perceptron, madaline, and backpropagation," *Proc. IEEE*, vol. 78, no. 9, pp. 1415-1442, Sep. 1990.
- [82] F. Deng, "An improved iron loss estimation for permanent magnet brushless machines," *IEEE Trans. Energy Convers.*, vol. 14, no. 4, pp. 1391-1395, Dec. 1999.
- [83] G. R. Slemon and X. Liu, "Core losses in permanent magnet motors," *IEEE Trans. Magn.*, vol. 26, no. 5, pp. 1653-1655, Sep. 1990.
- [84] K. J. Tseng and S. B. Wee, "Analysis of flux distribution and core losses in interior permanent magnet motor," *IEEE Trans. Energy Convers.*, vol. 14, no. 4, pp. 969-975, Dec. 1999.
- [85] C. Mi, G. R. Slemon, and R. Bonert, "Modelling of iron losses of permanent-magnet synchronous motors," *IEEE Trans. Ind. Appl.*, vol. 39, no. 3, pp. 734-742, May-Jun. 2003.
- [86] R. Rabinovici and T. J. E. Miller, "Eddy-current losses of surface-mounted permanent magnet motors," *Proc. Electric Power Appl.*, vol. 144, no. 1, pp. 61-64, Jan. 1997.
- [87] R. Rabinovici, "Eddy current losses of permanent magnet motors," *Proc. Electric Power Appl.*, vol. 141, no. 1, pp. 7-11, Jan. 1994.
- [88] T. J. E. Miller and R. Rabinovici, "Back-EMF waveforms and core losses in brushless DC motors," *Proc. Electric Power Appl.*, vol. 141, no. 3, pp. 144-154, May 1994.
- [89] G. Bertotti, "General properties of power losses in soft ferromagnetic materials," *IEEE Trans. Magn.*, vol. 24, no. 1, pp. 621-630, Jan. 1988.
- [90] D. M. Ionel, M. Popescu, S. J. Dellinger, T. J. E. Miller, R. J. Heideman, and M. I. McGilp, "On the variation with flux and frequency of the core loss coefficients in electrical machines," *IEEE Trans. Ind. Appl.*, vol. 42, no. 3, pp. 658-667, May-Jun. 2006.

- [91] P. H. Mellor, R. Wrobel, and D. Holliday, "A computationally efficient iron loss model for brushless AC machines that caters for rated flux and field weakened operation," in *Proc. IEEE Int. Electric Mach. Drives Conf.*, May 2009, pp. 490-494.
- [92] C. Schulte and J. Bocker, "Co-simulation of an electric traction drive," in *Proc. Int. Electric Mach. Drives Conf.*, May 2013, pp. 974-978.
- [93] D. A. Howey, P. R. N. Childs, and A. S. Holmes, "Air-gap convection in rotating electrical machines," *IEEE Trans. Ind. Electron.*, vol. 59, no. 3, pp. 1367-1375, Mar. 2012.
- [94] F. Haugen, *Kompendium for Kyb. 2*, ved Høgskolen i Oslo, Telemark Univ. Coll., Dept. Electrical Eng., Inform. Technol. Cybernetics, Porsgrunn, Norway, 2016.
- [95] M. –D. Calin and E. Helerea, "Temperature influence on magnetic characteristics of NdFeB permanent magnets," in *Proc. 7<sup>th</sup> Int. Symp. Adv. Topics Electrical Eng.*, May 2011, pp. 1-6.
- [96] C. Dufour, J. Belanger, S. Abourida, and V. Lapointe, "FPGA-based real-time simulation of finite-element analysis permanent magnet synchronous machine drives," in *Proc. IEEE Power Electron. Spec. Conf.*, Jun. 2007, pp. 909-915.
- [97] C. Dufour, S. Cense, T. Yamada, R. Imamura, and J. Belanger, "FPGA permanent magnet synchronous motor floating-point models with variable-DQ and spatial harmonic Finite-Element Analysis solvers," in *Proc. 15<sup>th</sup> Int. Power Electron. Motion Control Conf.*, Sep. 2012, pp. LS6b.2-2 – LS6b.2-10.
- [98] A. Griffio, D. Salt, R. Wrobel, and D. Drury, "Computationally efficient modelling of permanent magnet synchronous motor drives for real-time Hardware-in-the-Loop simulation," in *Proc. 39<sup>th</sup> Annu. Conf. IEEE Ind. Electron. Soc.*, Nov. 2013, pp. 5368-5373.
- [99] A. Hasanzadeh, C. S. Edrington, N. Stroupe, and T. Bevis, "Real-time emulation of a high-speed microturbine permanent-magnet synchronous generator using multiplatform hardware-in-the-loop realization," *IEEE Trans. Ind. Electron.*, vol. 61, no. 6, pp. 3109-3118, Jun. 2014.
- [100] A. Schmitt, J. Richter, U. Jurkewitz, and M. Braun, "FPGA-based real-time simulation of nonlinear permanent magnet synchronous machines for power hardware-in-the-loop

- emulation systems,” in *Proc. 40<sup>th</sup> Annu. Conf. IEEE Ind. Electron. Soc.*, Oct.-Nov. 2014, pp. 3763-3769.
- [101] N. R. Tavana and V. Dinavahi, “A general framework for FPGA-based real-time emulation of electrical machines for HIL applications,” *IEEE Trans. Ind. Electron.*, vol. 62, no. 4, pp. 2041-2053, Apr. 2015.
- [102] N. R. Tavana and V. Dinavahi, “Real-time FPGA-based analytical space harmonic model of permanent magnet machines for hardware-in-the-loop simulation,” *IEEE Trans. Magn.*, vol. 51, no. 8, pp. 1-9, Aug. 2015.
- [103] F. Alvarez-Gonzalez and A. Griffo, “High-fidelity modelling of permanent magnet synchronous motors for real-time Hardware-in-the-Loop simulation,” in *Proc. 8<sup>th</sup> IET Int. Conf. Power Electron. Mach. Drives*, Apr. 2016, pp. 1-6.
- [104] F. Alvarez-Gonzalez, A. Griffo, B. Sen, and J. Wang, “Real-time hardware-in-the-loop simulation of permanent-magnet synchronous motor drives under stator faults,” *IEEE Trans. Ind. Electron.* vol. 64, no. 9, pp. 6960-6969, Sep. 2017.
- [105] B. K. Bose, *Modern power electronics and AC drives*, 1<sup>st</sup> ed., ser. 1. Upper Saddle River: Prentice Hall PTR, ch. 5, pp. 224-229, 2002.
- [106] N. Takahashi, M. Morishita, D. Miyagi and M. Nakano, “Examination of magnetic properties of magnetic materials at high temperature using a ring specimen,” *IEEE Trans. Magn.*, vol. 46, no. 2, pp. 548-551, Feb. 2010.
- [107] M. Morishita, N. Takahashi, D. Miyagi and M. Nakano, “Examination of magnetic properties of several magnetic materials at high temperature,” *Przegląd Elektrotechniczny (Electrical Review)*, vol. 87, no. 9b/2011, pp. 106-110, 2011.